



**HAL**  
open science

# Bioevaluation of aza-BODIPYs versatility for cancer NIR-II fluorescence imaging and Boron Neutron Capture Therapy application

Ghadir Kalot

► **To cite this version:**

Ghadir Kalot. Bioevaluation of aza-BODIPYs versatility for cancer NIR-II fluorescence imaging and Boron Neutron Capture Therapy application. Human health and pathology. Université Grenoble Alpes [2020-..], 2021. English. NNT : 2021GRALV054 . tel-04276363

**HAL Id: tel-04276363**

**<https://theses.hal.science/tel-04276363v1>**

Submitted on 9 Nov 2023

**HAL** is a multi-disciplinary open access archive for the deposit and dissemination of scientific research documents, whether they are published or not. The documents may come from teaching and research institutions in France or abroad, or from public or private research centers.

L'archive ouverte pluridisciplinaire **HAL**, est destinée au dépôt et à la diffusion de documents scientifiques de niveau recherche, publiés ou non, émanant des établissements d'enseignement et de recherche français ou étrangers, des laboratoires publics ou privés.

## THÈSE

Pour obtenir le grade de

**DOCTEUR DE L'UNIVERSITE GRENOBLE ALPES**

Spécialité : **BIOTECHNOLOGIE**

Arrêté ministériel : 25 mai 2016

Présentée par

**Ghadir KALOT**

Thèse dirigée par **Lucie SANCEY**

préparée au sein du **Laboratoire IAB: Institute for Advanced Biosciences (UGA / Inserm U1209 / CNRS UMR 5309)**  
dans **l'École Doctorale Chimie et Sciences du Vivant**

**Evaluation biologique d'aza-BODIPYs pour l'imagerie NIR-II des cancers et la thérapie par capture neutronique du Bore**

**Bioevaluation of aza-BODIPYs versatility for cancer NIR-II fluorescence imaging and Boron Neutron Capture Therapy application**

Thèse soutenue publiquement le **30 novembre 2021**,  
devant le jury composé de :

**Madame Lucie SANCEY**

DIRECTEUR DE RECHERCHE, Institute for Advanced Biosciences,  
Directrice de thèse

**Monsieur Wolfgang SAUERWEIN**

PROFESSEUR, Essen University Hospital, Rapporteur

**Monsieur Nicolas TSAPIS**

DIRECTEUR DE RECHERCHE, Institut Galien Paris-Saclay, Président

**Madame Christine GOZE**

MAITRE DE CONFERENCE HDR, Université Bourgogne Franche-Comté, Examinatrice

**Madame Anne-Laure BULIN**

CHARGE DE RECHERCHE, UA7 INSERM, University Grenoble Alpes,  
Examinatrice





# Acknowledgment

## **First of all, I would like to express my gratitude to:**

My thesis director Lucie Sancey. Thank you, Lucie, for your scientific guidance, trust, support, enthusiasm, and positive vibes during all my thesis duration.

The thesis jury members Wolfgang Sauerwein, Nicolas Tsapis, Christine Goze and Anne-Laure Bulin. Thank you for accepting to judge my work and for the time you will spend reviewing it.

The members of the thesis advancement committee, H  l  ne Elleaume, and Laurence Lafannech  re. Thank you for your comments, opinions, and suggestions.

## **I would like to sincerely thank all our collaborators:**

At ICMUB (Institut de Chimie Mol  culaire de l'Universit   de Bourgogne, Dijon, France), Franck Denat, Ewen Bodio, Christine Goze and Am  lie Godard for the aza-BODIPY project. At CERMAV (Centre de Recherches sur les Macromol  cules V  g  tales, Grenoble, France), Rachel Auz  ly and Simon Coninx for the nanogel project. Thomas Gautier (Lipids Nutrition Cancer laboratory, Dijon, France) for the lipoprotein project. Ulli K  ster for setting up the neutron beam line at the ILL (Institut Laue-Langevin, Grenoble, France). It was a great pleasure to work with you.

## **I would like to thank the financial supporters/ research institutes:**

The FRM (Fondation pour la Recherche M  dicale) for funding my doctoral studies (FRM ECO201806006861), the GDR 2073 AIM for granting me a mobility grant, and the IDEX program of Grenoble Alpes university for granting me the master scholarship. The Institute for Advanced Biosciences in which I carried out my research work and Grenoble Alpes University.

## **I would like to warmly thank:**

All the members of team 2 and 5 for being more than family, Amandine, Amani, Beatrice, Benoit, Camilla, Fabien, Julienne, Laetitia, Malika, Mans, Maxime, Morgane, Nathalie, Pierre, Sean, Sule, Sylvie, Thibault, Theo, Triston, Virginie, Veronica, Veronique<sup>2</sup> and Xavier. The members who left, Benjamin, Estelle, Jonathon, Mehdi, Melanie and Zaynab. A special thanks to our team leader Jean-Luc Coll.

My friends Ali, Amal, Areej, and Israa<sup>2</sup> for the great moments in Lebanon. Abir, Amani, Heba, Mohamad, Mansor, Maryam, Rouba, and Zakya for sharing my first year in France, for their care and joy.

My family back in Lebanon, especially my mother, father, three brothers, and my young sister. Thank you for your unlimited support.

My Husband Ali...

**I would like to have this manuscript in the honor of my grandparents.**



# Table of Contents

<b>Outline</b>	<b>8</b>
<b>1 Cancer: an overview</b>	<b>9</b>
1.1 Importance of cancer management	9
1.2 Cancer and carcinogenesis	9
1.3 Cancer Hallmarks	10
1.3.1 Sustaining proliferative signaling	11
1.3.2 Evading growth suppressors	11
1.3.3 Resisting cell death	11
1.3.4 Enabling replicative immortality	11
1.3.5 Inducing angiogenesis	12
1.3.6 Activating invasion and metastasis	13
1.3.7 Reprogramming energy metabolism	14
1.3.8 Evading immune destruction	15
1.4 Cancer targeting	16
1.4.1 EPR effect-mediated tumor targeting/ Passive targeting	16
1.4.2 Active targeting: example of HER2 receptor	17
<b>2 Preclinical cancer models</b>	<b>21</b>
2.1 <i>In vitro</i> tumor models: (2D) and (3D) tumor cell cultures	21
2.2 <i>In ovo</i> tumor model: chorioallantoic membrane (CAM) assay	22
2.3 <i>In vivo</i> tumor models: mouse tumor models	23
2.3.1 Xenograft mouse cancer model	23
2.3.1.1 Ectopic xenograft model	23
2.3.1.2 Orthotopic xenograft model	24
2.3.1.3 Patient derived xenograft (PDX) model	24
2.3.2 Syngeneic mouse cancer model	25
2.3.3 Genetically engineered mouse cancer model	26
2.3.4 Chemically-induced mouse cancer model	26
2.4 Conclusion	27
<b>3 Cancer diagnosis</b>	<b>30</b>
3.1 Fluorescence Imaging: Principle	31
3.2 <i>In vivo</i> fluorescence imaging: Light/Photon interaction with biological tissues	31
3.3 From visible to NIR-I fluorescence imaging	34
3.4 NIR-I fluorophores: for <i>in vivo</i> tumor imaging	34
3.4.1 "Always On" fluorophores	34
3.4.1.1 Non-targeted fluorophores	34
3.4.1.2 Targeted Fluorophores	36
3.4.2 Activable probes	37

3.5	From NIR-I to NIR-II fluorescence imaging .....	39
3.6	NIR-II fluorescence imaging: Requirements .....	40
3.6.1	NIR-II window detectors/cameras .....	40
3.6.2	NIR-II fluorophores: for <i>in vivo</i> tumor imaging .....	40
3.6.2.1	In-organic NIR-II fluorophores .....	41
3.6.2.1.1	Single-walled carbon nanotubes (SWCNTs) .....	41
3.6.2.1.2	Quantum dots (QDs) .....	42
3.6.2.1.3	Rare-earth doped NIR-II nanoparticles .....	43
3.6.2.2	Organic fluorophores .....	45
3.6.2.2.1	Donor-acceptor-donor (DAD) systems .....	45
3.6.2.2.2	Polymethine/Cyanine dyes .....	46
3.7	Conclusion .....	48

## **4 Cancer Therapy..... 49**

4.1	BNCT: Principle.....	49
4.2	BNCT: History .....	50
4.3	BNCT: Boron compounds.....	51
4.3.1	Clinically available boron compounds .....	51
4.3.1.1	Clinically available boron compounds: Limitations .....	52
4.3.1.2	Clinically available boron compounds: possible solutions .....	52
4.3.2	Theranostic boron compounds .....	52
4.3.2.1	Clinical example: <sup>18</sup> F-BPA .....	52
4.3.2.2	Preclinical examples.....	53
4.3.2.2.1	Small boron-containing molecules: .....	53
4.3.2.2.2	Large boron carriers:.....	55
4.4	BNCT: Neutron source .....	60
4.5	BNCT: Clinical evidence of efficacy .....	61
4.5.1	Newly diagnosed Glioblastoma (NDGB) .....	61
4.5.2	Recurrent Head and Neck malignancies (rHNM) .....	62
4.5.3	High-grade meningiomas.....	62
4.5.4	Recurrent Malignant gliomas .....	63
4.6	Conclusion .....	64

## **5 BODIPY fluorophores and their derivatives for cancer diagnosis and therapy .....65**

5.1	BODIPY fluorophores and their derivatives for cancer fluorescence imaging .....	65
5.1.1	Aza-BODIPYs for NIR-I cancer fluorescence imaging .....	65
5.1.2	aza-BODIPYs for NIR-II cancer fluorescence imaging .....	67
5.2	BODIPYs fluorophores and their derivatives for cancer therapy: BNCT in particular .....	70

<b>Thesis work</b> .....	<b>72</b>
<b>Article 1: Water-Soluble Aza-BODIPYs: Biocompatible Organic Dyes for High Contrast <i>In vivo</i> NIR-II Imaging</b> .....	<b>73</b>
<b>Article 2: Lipoproteins interaction with water-soluble NIR-II emitting aza-BODIPYs boosts the fluorescence signal and favors selective tumor targeting</b> .....	<b>83</b>
Lipoproteins.....	84
1. Lipoproteins: General Overview .....	84
2. Lipoprotein pathways .....	85
3. Lipoprotein receptors .....	88
3.1. LDL receptor (LDLR) .....	88
3.2. LDL receptor related protein (LRP).....	89
3.3. Class B, type I scavenger receptor (SR-BI) .....	89
3.4. ATP-Binding Cassette Transporter A1 (ABCA1).....	90
3.5. ATP-Binding Cassette Transporter G1 (ABCG1) .....	90
4. Lipoproteins in cancer targeting.....	90
<b>Article 3: Bioconjugated aza-BODIPYs NIR-II probes for selective imaging of HER2-positive ovarian cancer</b> .....	<b>111</b>
<b>Article 4: Aza-BODIPY: A New Vector for Enhanced Theranostic Boron Neutron Capture Therapy Applications</b> .....	<b>144</b>
<b>General Conclusion</b> .....	<b>174</b>
<b>References</b> .....	<b>175</b>



# Outline

This manuscript begins with an overview of cancer disease, describing its major hallmarks, with a specific focus on tumor aberrant vasculature and overexpressed receptors, that can enable respectively passive and active targeting of tumor diagnostic and therapeutic molecules. A brief presentation of the available preclinical tumor models, including those utilized during the thesis, is then provided. Two major sections regarding cancer diagnosis and cancer therapy follow. In the cancer diagnosis section, *in vivo* tumor fluorescence imaging technique is considered in detail, starting with the well-known fluorescence imaging in the first near infra-red (NIR-I) window (700-900 nm) and its clinical application as fluorescence-guided surgery (FGS). An extensive description of the emerging fluorescence imaging field in the second near infra-red (NIR-II) region (1000-1700 nm) and its main requisites is then presented, and its superiority over NIR-I imaging is demonstrated in preclinical rodent models. This section is concluded by restating the need for biocompatible NIR-II fluorophores with high quantum yields, for *in vivo* tumor imaging application. In the cancer therapy section, a targeted form of radiotherapy called Boron Neutron Capture Therapy (BNCT) is described. Its history, main requirements being the boron compounds and neutron sources, and its clinical efficacy, are presented. A subsection is dedicated to describing clinically available theranostic boron compounds and their limitations, followed by examples of theranostic compounds still in preclinical studies, and concluded by reinforcing the necessity for optimal theranostic boron compounds to achieve more efficient BNCT. Considering the use of aza-BODIPYs during the thesis, a section is devoted to the state of the art of aza-BODIPYs use in fluorescence tumor imaging field, NIR-II imaging in particular, and BNCT field, in addition to the required adjustments. To address the need for optimal NIR-II dyes, the first water-soluble aza-BODIPY emitting in the NIR-II window was developed and its capacity for *in vivo* tumor imaging is demonstrated in article 1. The mechanism of aza-BODIPY significant tumor accumulation is then deciphered in article 2. The bioconjugation of aza-BODIPY to an antibody and its selective tumor targeting potential is demonstrated in article 3. The efficacy of this bioconjugated aza-BODIPY, and our next steps regarding the proof of concept of its efficacy for NIR-II FGS, are discussed. In an attempt to develop an optimal theranostic boron compound, the synthesis, tumor accumulation, and BNCT potential of a theranostic boron compound made up of aza-BODIPY fluorophore coupled to a clinically used boron cage, is presented in article 4. Enhancing the water-solubility of this compound and linking it to radioisotopes is then deliberated. The manuscript is concluded with a brief description of the attained results and future perspectives.

# 1 Cancer: an overview

## 1.1 Importance of cancer management

Cancer poses a major clinical, social, and economic burden worldwide, among all other human diseases [1]. It presents the second cause of death after ischemic heart disease, and it is predicted to bypass it by 2030 (WHO) [2]. In 2020, 19.3 million cancer cases and 10 million cancer deaths have been reported by the International Agency for Research on Cancer (IARC) in the world [3]. Cancer incidence and mortality are expected to further rise to 30.2 million cases and 16.3 million deaths, by 2040 [4] (Figure 1). Considering these progressing epidemiological data regarding cancer frequency and mortality, the significant social consequences on cancer patients and their caregivers [5], and the huge economic expenses of cancer that were estimated by 1.16 trillion \$ in 2010 [2], clearly demonstrate the necessity for national and international organizations to cooperate and reinforce cancer prevention, diagnosis, treatment, and management. Promoting scientific research against cancer is a key pillar for establishing this efficient and sustainable strategy to combat cancer. Accordingly, my thesis work presents a humble attempt in this battle.

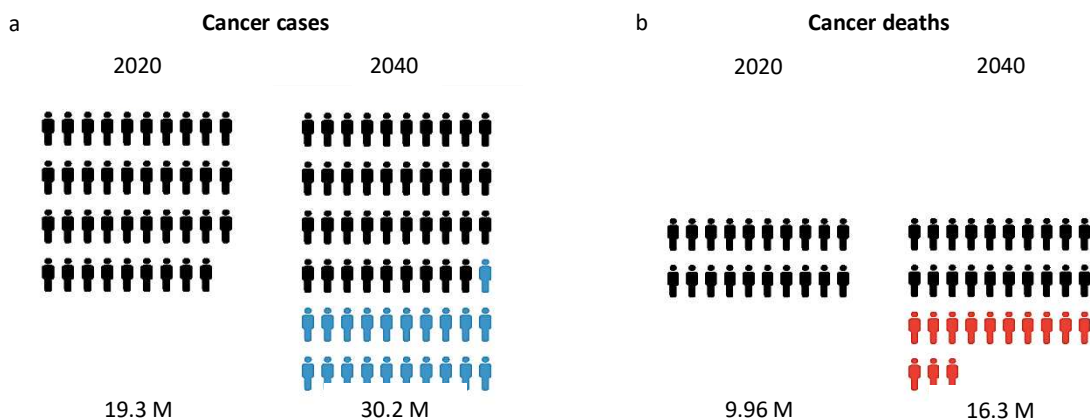


Figure 1: Estimated number of new cancer cases (a) and cancer deaths (b), in both sexes worldwide, from 2020 to 2040 [4].

## 1.2 Cancer and carcinogenesis

According to the National Cancer Institute (NIH), cancer is defined as a disease in which certain body cells can uncontrollably grow and spread to other body parts [6].

Focusing on solid cancers, they can no longer be designated as insular masses of proliferating cancer cells, they are rather considered as complex tissues composed of both: proliferating cancer cells and recruited normal cells that form the tumor-associated stroma (endothelial cells, pericytes, immune inflammatory cells, cancer-associated fibroblasts) and contribute to the tumor development [7, 8] (Figure 2).

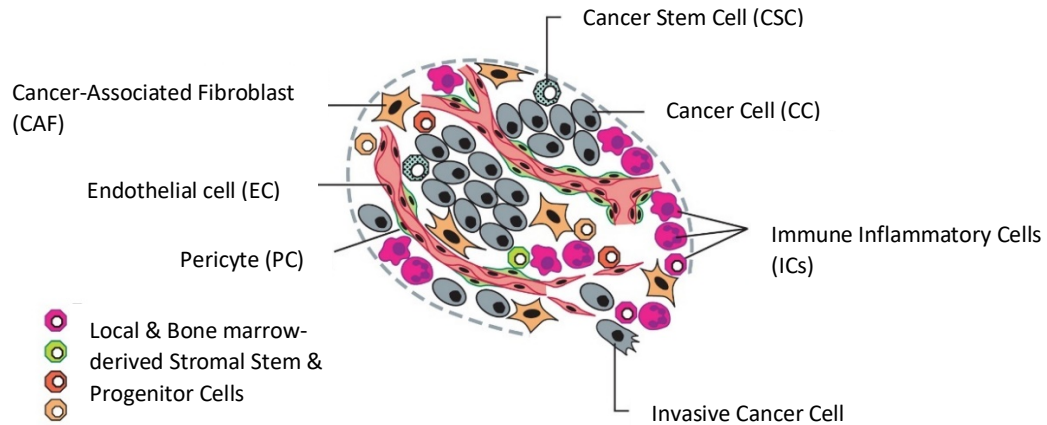


Figure 2: Schematic presentation of solid tumor and its microenvironment [8].

Accordingly, cancer development or carcinogenesis can be defined as the ability of cancer cells, present within a unique cancer microenvironment, to acquire fundamental traits called “the hallmarks of cancer”. These hallmarks include sustaining proliferative signaling, evading growth suppressors, resisting cell death, enabling replicative immortality, inducing angiogenesis, activating invasion and metastasis, reprogramming energy metabolism, and evading immune destruction [7, 8] (Figure 3). These hallmarks are briefly discussed below.

### 1.3 Cancer Hallmarks

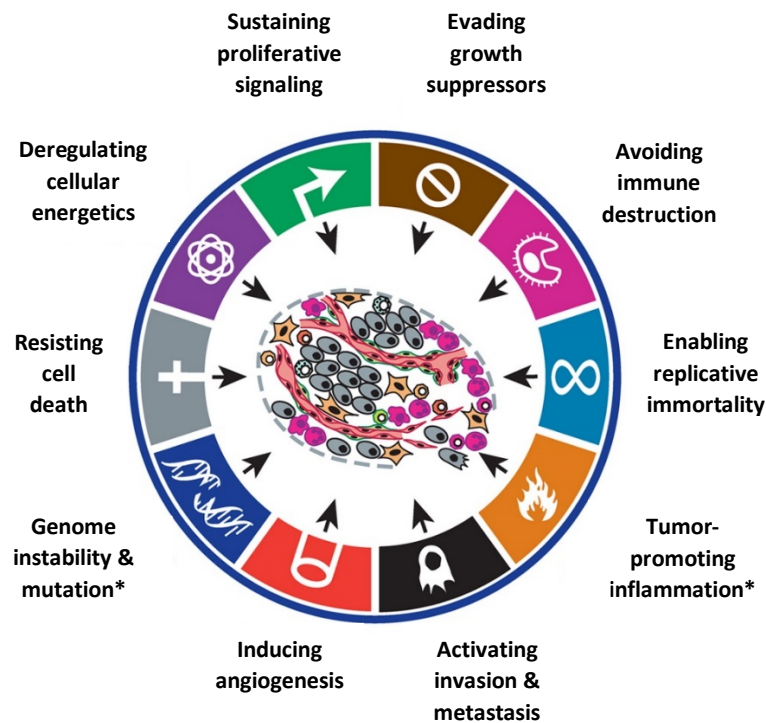


Figure 3: The emerging hallmarks and the enabling characteristics of cancer (\*) [8].

### 1.3.1 Sustaining proliferative signaling

Compared to normal cells that carefully control growth-promoting signals, cancer cells deregulate them. These growth signals majorly involve growth factors binding to cell surface receptors, that can induce through their intracellular domain, signaling pathways of cell cycle division and growth. To sustain proliferative signaling, cancer cells tend to produce their growth factors and respond to them by expressing/overexpressing suitable surface receptors, a phenomenon called autocrine proliferative stimulation [8]. They can also stimulate cells of tumor stroma to supply them with the various growth factors [9].

Another approach to maintain proliferative signaling is through growth factor independent constitutive activation of the receptors or the signaling pathways downstream of these receptors induced by somatic mutations. Mutation in the PI<sub>3</sub>-kinase, a downstream receptor kinase, for example, hyperactivates its signaling pathway [10]. In addition, defects in the negative-feedback mechanisms that normally attenuate proliferative signaling can otherwise enhance them. A notable example of a negative-feedback mechanism is PTEN phosphatase that counteracts PI<sub>3</sub>-kinase activity. However, mutations in PTEN can amplify PI<sub>3</sub>-kinase activity and thus promote tumorigenesis in cancer models [10].

### 1.3.2 Evading growth suppressors

Dozens of tumor suppressors have been identified, and their ability to limit cell growth and proliferation, and induce apoptosis has been discovered. RB (retinoblastoma-associated) protein presents a typical example of a tumor suppressor encoded protein that can integrate extracellular and intracellular signals, and decide whether a cell can proceed or not into cell division. Cancer cells with defects in this suppressor pathway permit persistent cell proliferation [8, 11].

### 1.3.3 Resisting cell death

Programmed cell death via apoptosis is usually triggered either by DNA damages sensed by TP<sub>53</sub> tumor suppressor [12], or insufficient survival signals e.g. inadequate levels of insulin-growth factor 1/2 (Igf1/2) in epithelial cells, or excessive oncogene signaling by Myc, for example [13]. To bypass apoptosis, cancer cells evolve unique strategies including loss of function of TP<sub>53</sub> damage sensor, increasing the expression of survival signals (e.g. Igf1/2 growth factor), and antiapoptotic regulators (e.g. Bcl-2) that counterbalance the hyperactive oncoprotein signaling [8].

### 1.3.4 Enabling replicative immortality

Normal cells can pass a limited number of successive cell divisions before entering into a non-proliferative state called senescence or becoming apoptotic. This is because after each cell division, telomeres - tandem hexanucleotide repeats protecting the ends of the chromosomes - shorten progressively and thus lose their ability to protect chromosomal DNA from end-to-end fusions that threaten cell viability (Figure 4a).

To counteract the continuous telomere erosion and the subsequent induction of senescence or apoptosis observed in normal cells, cancer cells express telomerase enzyme that adds telomere repeats at the end of the DNA. This telomerase activity permits unlimited replication of cancer cells, without senescence or apoptosis triggering, a process called immortalization [8, 14] (Figure 4b). It is worth noting that telomerase is almost absent in normal quiescent cells.

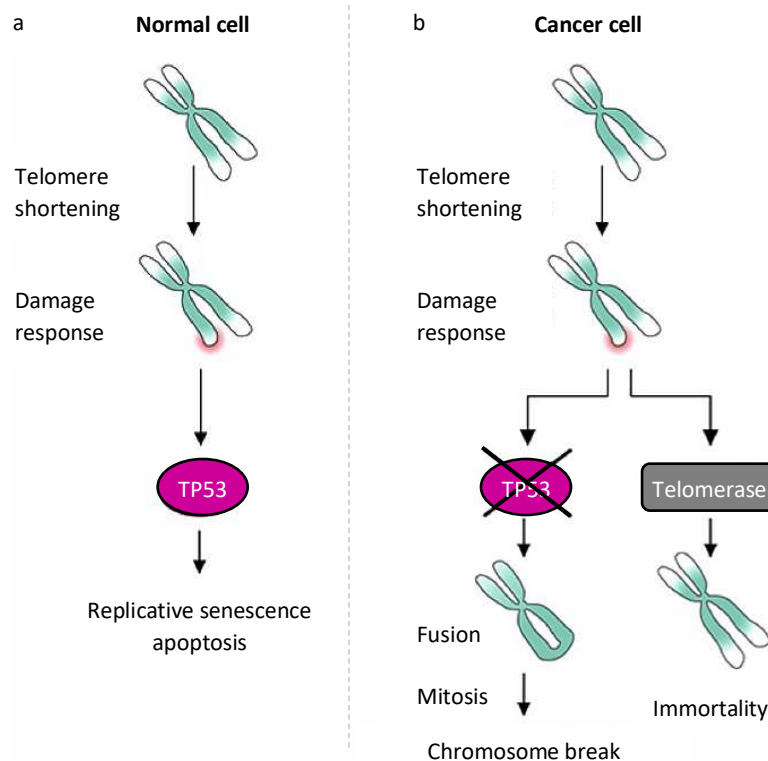


Figure 4: How cancer cells enable replicative immortality. (a) Telomere shortening attained following successive normal cell divisions induces senescence or apoptosis. (b) To overcome these later events, tumor cells express telomerase, an enzyme maintaining telomere length [15].

### 1.3.5 Inducing angiogenesis

Similar to normal tissues, cancer lesions require access to nutrients and oxygen as well as the need to evacuate metabolic wastes and carbon dioxide. To address these requirements, new vessels are generated at the tumor site via a process called angiogenesis. The angiogenic switch takes place early in tumor development and is governed by stimulatory and inhibitory angiogenic regulators, such as the vascular endothelial growth factor-A (VEGF-A) and Thrombospondin-1 (TSP-1), respectively. These regulators bind to cell-surface receptors displayed on vascular endothelial cells, and can subsequently evoke stimulatory or inhibitory angiogenic signals [16].

It is worth noting that the imbalance in these angiogenic signals leads to the generation of tumor vasculature (neovasculature) with all its components, endothelial cells, pericytes, and the surrounding basement membrane, being highly bizarre. Tumor vasculature possesses irregular size and shape and lacks the arteriole-capillaries-venules organization. Endothelial cells lack tight connections leading to leakiness (Figure 5), and pericytes being loosely attached to the

endothelial cells weaken the vessel walls and increase hemorrhage risk. In addition, the surrounding basement membrane owns irregular thickness, focal holes, and extension into the tumor stroma [17].

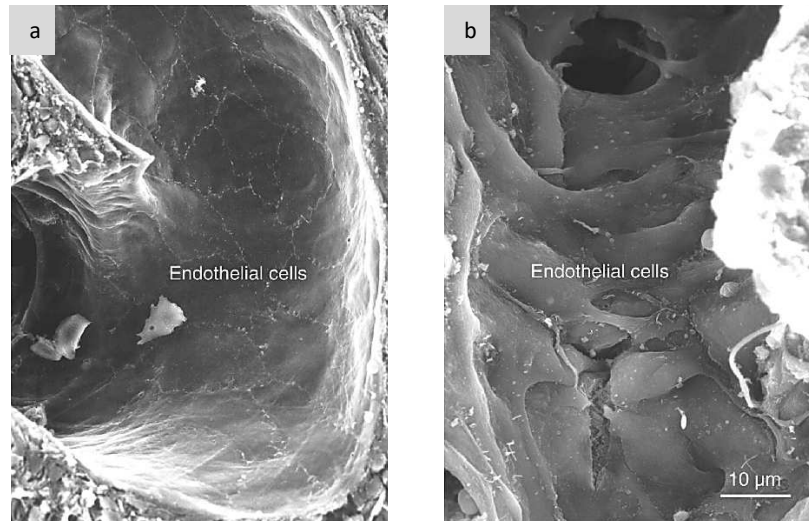
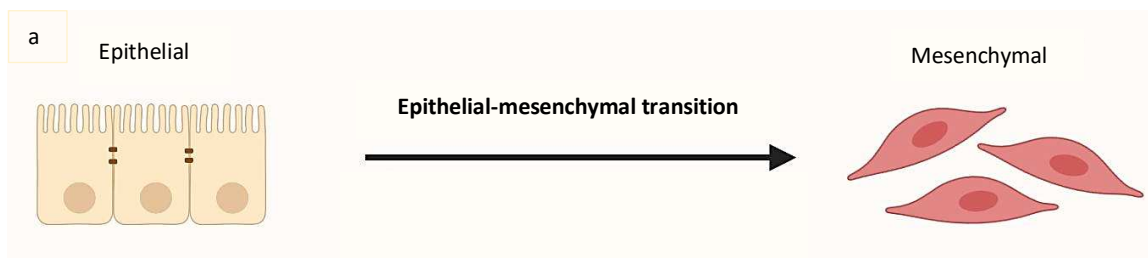


Figure 5: Scanning electron micrographs of normal (a) and tumor blood (b) vessels demonstrating that the smooth, tight endothelial cells monolayer is hugely disabled in tumor vasculature. Scale bar indicates 10 µm [17].

### 1.3.6 Activating invasion and metastasis

As cancer progress into high-grade malignancy, an epithelial-mesenchymal transition (EMT) is implicated in the induction of invasion and metastasis. EMT transition involves alteration in cancer cells shape (from polygonal/epithelial to spindly/fibroblastic morphology), loss of cell-cell and cell-extracellular matrix attachment (e.g. the downregulation or mutational inactivation of E-cadherin cell-to-cell adhesion molecule that is responsible for epithelial cells sheets assembly) (Figure 6a), and the expression of matrix-degrading enzymes [8, 18]. As a result of this transition, a multistep invasion-metastasis process is triggered (Figure 6b), starting by cancer cells local invasion, intravasation into the blood and lymphatic vessels, circulation within these vessels, arrest in capillary beds, extravasation into distant tissues parenchyma, formation of small micrometastases and their growth into macroscopic tumors, by a process called colonization [19].



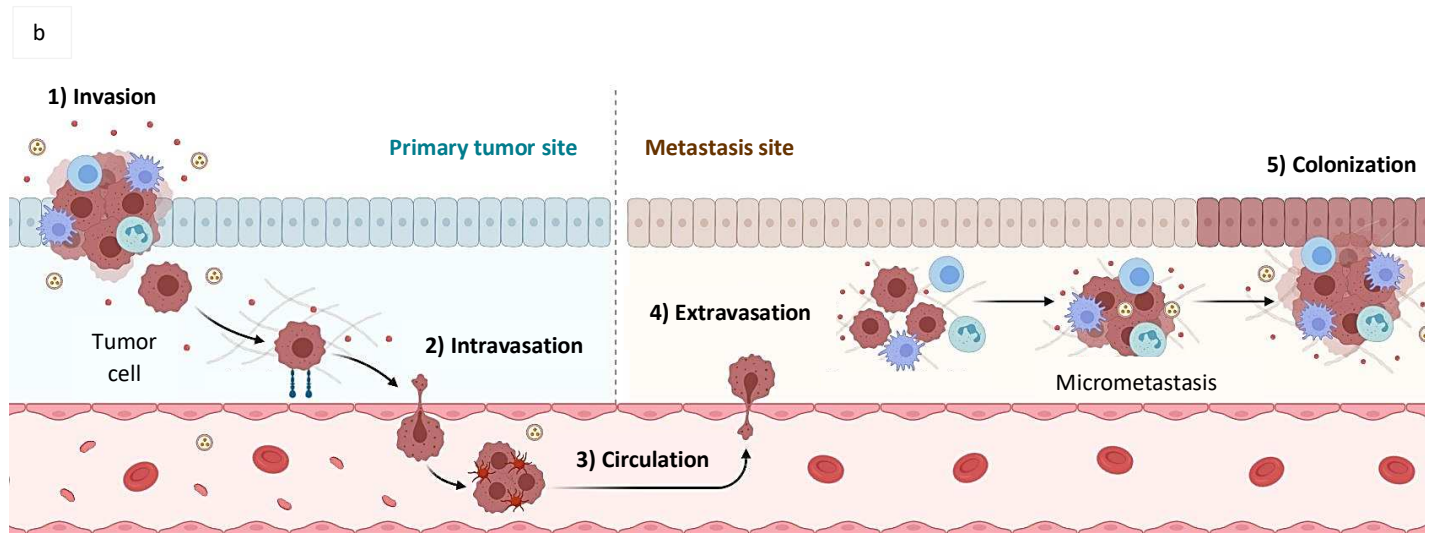


Figure 6: Schematic view presenting the epithelial-mesenchymal transition (a) and the multistep metastasis process including cancer cells invasion, intravasation, circulation, extravasation, and colonization (b) [20].

### 1.3.7 Reprogramming energy metabolism

The unlimited proliferation of cancer cells requires adjustment in cell energy metabolism, to fuel these excessive cell divisions. Under aerobic conditions, normal cells process glucose into pyruvate via glycolysis, then ATP is produced by mitochondrial oxidative phosphorylation. Under anaerobic conditions, glycolysis is favored and a low amount of pyruvate is transferred into the mitochondria. However, in cancer cells even in the presence of oxygen, glucose metabolism is reprogrammed and glycolysis is favored [21] (Figure 7). This metabolic switch involves the upregulation of glucose transporters (e.g. GLUT1) [22] and is explained by the hypothesis that the glycolytic intermediates are implicated in nucleosides and amino acids generation, which are required for the biosynthesis and the assembly of new cells [23].

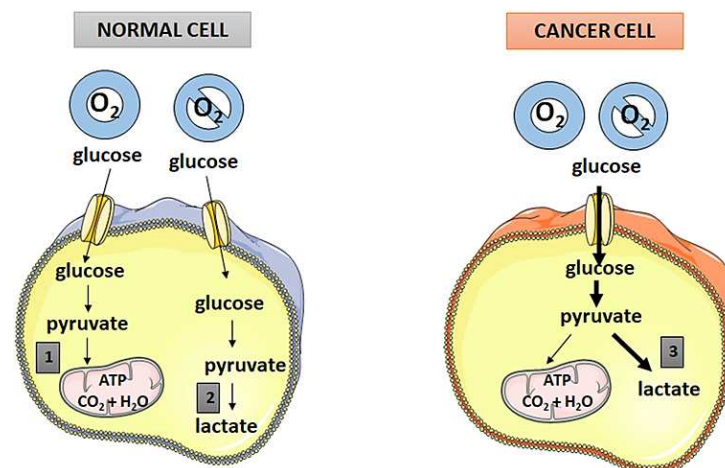


Figure 7: Glucose metabolism in normal and cancer cells. 1: Oxidative phosphorylation, 2: Anaerobic glycolysis, 3: Aerobic glycolysis [24].

### 1.3.8 Evading immune destruction

Considering the theory that body cells and tissues are under continuous immune surveillance, the development of tumors implies that tumor cells were able to evade immune destruction. This could be achieved by recruiting immunosuppressive inflammatory cells such as regulatory T cells [25] and secreting TGF- $\beta$  (Transforming Growth Factor Beta) that paralyze cytotoxic T-lymphocytes and natural killers' activities [26], for example (Figure 8).

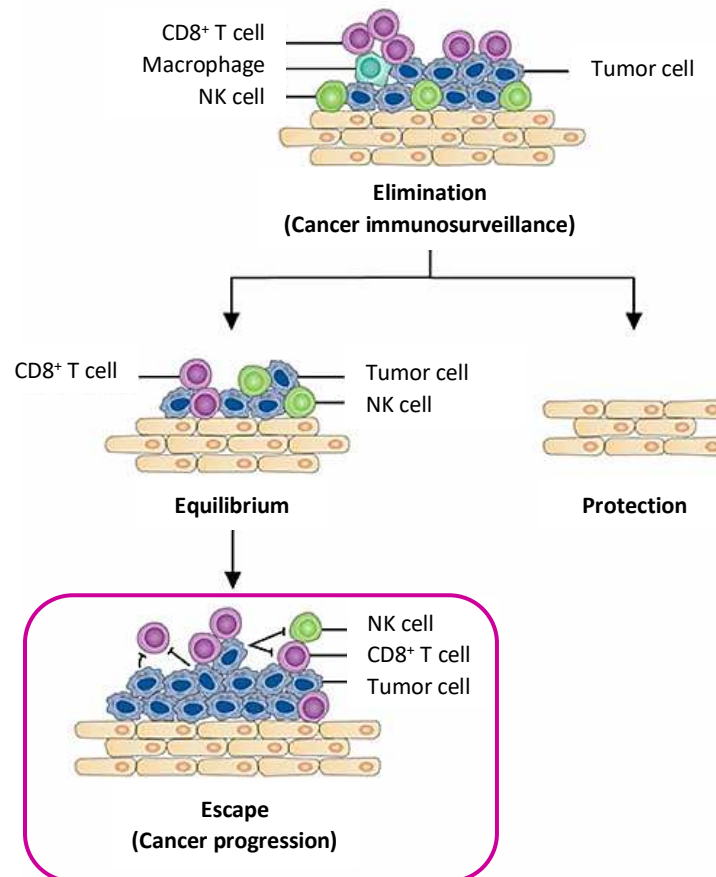


Figure 8: Schematic illustration of immune system evasion by cancer cells [27].

To conclude, the discussed hallmarks describe the capabilities acquired by tumors during their multistep development and provide a solid basis for the understanding of tumors/cancers/carcinogenesis complexity.

## 1.4 Cancer targeting

Considering the different cancer hallmarks, it is evident that tumors possess unique, peculiar characteristics compared to normal tissues. These distinctive characteristics can provide major targets for diagnostic and therapeutic approaches.

### 1.4.1 EPR effect-mediated tumor targeting/ Passive targeting

Given the aberrant tumor vasculature discussed earlier, the notion of “enhanced permeability and retention (EPR) effect” was discovered, and described as the preferential tumor accumulation of molecules and their prolonged retention, due to leaky tumor vasculature and poor lymphatic drainage respectively [28] (Figure 9). Several antitumor therapeutics have their tumor-targeting capacities mediated by the EPR effect, such as Doxil<sup>®</sup>, an FDA-approved liposome encapsulating doxorubicin, used for AIDS-related Kaposi's sarcoma, ovarian cancer, and multiple myeloma treatment [29].

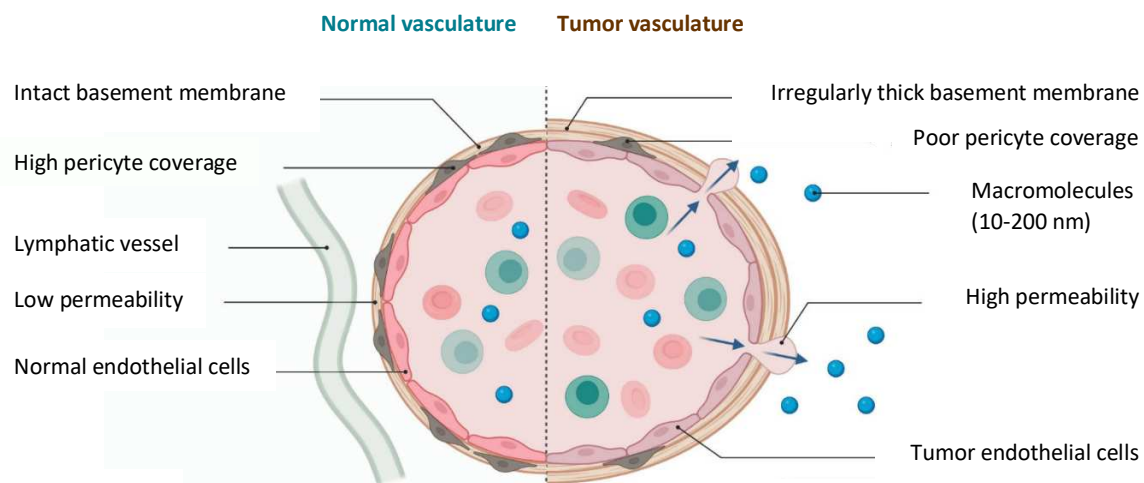


Figure 9: Schematic illustration of the enhanced permeability and retention (EPR) effect present within tumors, due to leaky tumor vasculature and poor lymphatic drainage [30].

Yet, EPR effect-mediated tumor-targeting provides variable response rates and modest tumor specificity (20-30% increase in tumor delivery compared to normal tissues) [31]. This sub-optimal efficiency is attributed to the intra- and inter-tumor heterogeneity in size, type, and vasculature status. Highly vascularized tumors such as hepatocellular carcinoma exhibit a greater EPR effect compared to tumors with a low vascular density such as prostate cancer. Additionally, large tumor masses with necrotic cores could induce a low EPR effect due to their damaged vasculature [32]. On the other hand, molecules' size, shape, and surface charge can greatly affect their EPR-targeting capacity. Molecules of 10-200 nm diameter (or 40-800 kDa [29]) are considered of optimal size, to avoid renal excretion (molecules <6 nm) and limit liver/ reticuloendothelial system (RES) uptake (molecules >300 nm) [31]. In addition, molecules with neutral net charges are more favorable, as highly charged molecules could be recognized by the RES [31]. Therefore, an appropriate design of molecules for EPR-mediated tumor targeting is required to maintain longer circulation time, avoid rapid clearance, target well the tumor and attain optimal diagnostic or therapeutic efficacy.

## 1.4.2 Active targeting: example of the HER2 receptor

Bearing in mind the cancer hallmarks, several receptors, growth factors, and downstream receptor kinases become overexpressed or mutated during carcinogenesis [8]. These tumor-specific alterations provide significant molecular targets for cancer diagnosis and therapy [33]. Focusing on tumor overexpressed receptors, active targeting of tumors could be achieved using ligands possessing high specificity to these overexpressed receptors, including small molecules (e.g. folic acid targeting folic acid receptor), peptides (e.g. RGD peptide targeting  $\alpha_v\beta_3$  integrin), proteins (e.g. transferrin targeting transferrin receptor), and antibodies (e.g. Trastuzumab antibody targeting HER2 receptor) [29] (Figure 10).

Compared to passive targeting, active targeting provides selective accumulation at the target site while reducing non-specific events. It can also contribute to 75% of tumor-targeting compared to 25% achieved by the EPR effect alone [29].

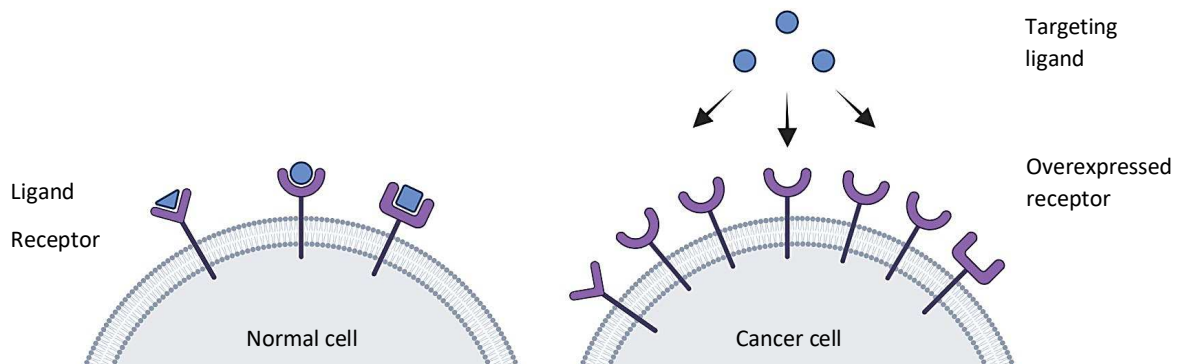


Figure 10: Schematic illustration of receptor-mediated active targeting of tumors, governed by tumor cells overexpression of surface receptors (Created with BioRender.com).

HER2 is a member of the human epidermal growth factor receptor family (HER family) consisting of HER1, 2, 3, and 4. It is a transmembrane tyrosine kinase receptor whose activation results in the induction of cell survival and proliferation signaling pathways, such as the mitogen-activated protein kinase (MAPK) pathway and the phosphoinositide-3-kinase (PI3K/Akt) pathway [34]. Overexpression of HER2 has been reported in 25-30% of breast and ovarian cancers, and it was associated with worse biological behavior/patient prognosis [35]. Accordingly, researchers have focused on the development of tumor diagnostic and therapeutic approaches via HER2 receptor targeting [36, 37].

Regarding therapy, several HER2-targeted therapies are clinically available. Trastuzumab, a HER2 specific antibody was developed and FDA approved for the treatment of HER2-overexpressing breast cancers, in 1998 [38]. The anticancer activity of trastuzumab was attributed to the inhibition of HER2 dimerization and subsequent signaling pathways [39] (Figure 11a), the down regulation of HER2 receptor by endocytosis (Figure 11b), and the induction of cell lysis via antibody-dependent cellular cytotoxicity (ADCC) [40] (Figure 11c). Despite the clinical significance of Trastuzumab, some patients experienced progression and others developed resistance. This led to the development of the antibody-drug conjugate i.e. Trastuzumab-DM1, by coupling Trastuzumab to a microtubule disrupting drug (DM1). Trastuzumab-DM1 was able to selectively

deliver DM1 into HER2-overexpressing cells thus inducing apoptosis (Figure 12b). It was also able to maintain HER2 signaling inhibition (Figure 12a) and ADCC induction (Figure 12c). Thus, Trastuzumab-DM1 was effective for patients developing Trastuzumab resistance [41]. On the other hand, Lapatinib a small molecule inhibitor of HER2 tyrosine kinase phosphorylation has been also FDA approved for the treatment of breast cancer patients [42] (Figure 13).

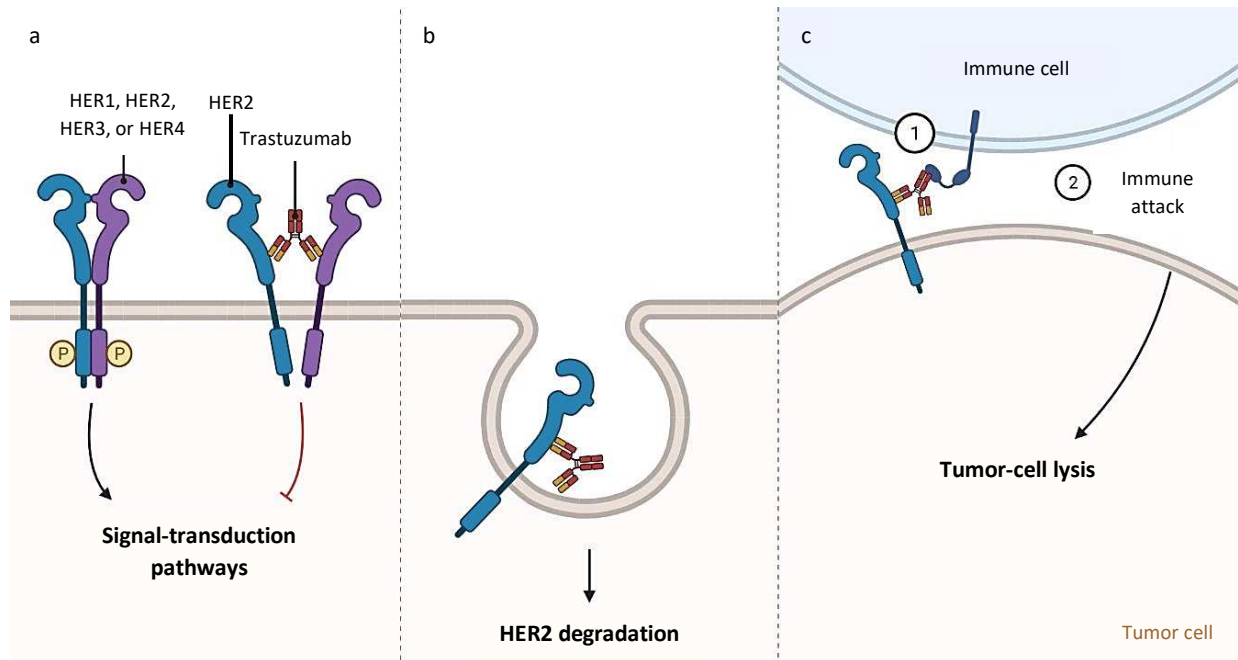


Figure 11: Trastuzumab, a monoclonal antibody specific to the HER2 receptor, mechanisms of action. (a) Trastuzumab can prevent the dimerization of HER2 receptors thus inhibiting downstream signaling pathways involved in cell survival and proliferation. (b) Trastuzumab can downregulate HER2 expression by endocytosis. (c) It can also recruit immune cells that induce antibody-dependent cellular cytotoxicity and lysis [43].

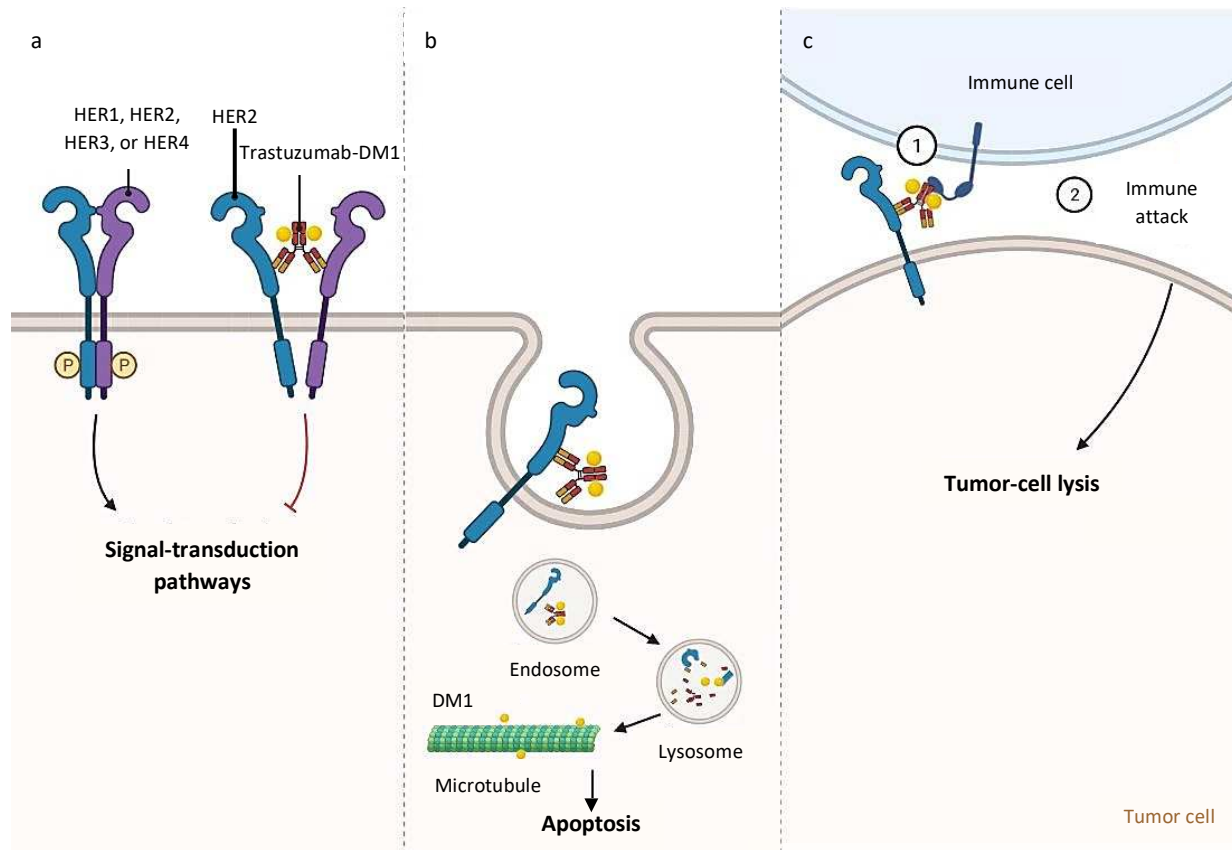


Figure 12: Trastuzumab-DM1, a conjugate of trastuzumab monoclonal antibody with the microtubule disrupting drug DM1, mechanisms of action. Similar to trastuzumab, (a) trastuzumab-DM1 can prevent the dimerization of HER2 receptor and the downstream signaling, (c) and it can induce antibody-dependent cellular cytotoxicity and lysis. (b) Trastuzumab-DM1 can be also internalized and degraded, releasing DM1 drug into the cytoplasm, thus inhibiting microtubule polymerization and inducing apoptosis (Created with BioRender.com).

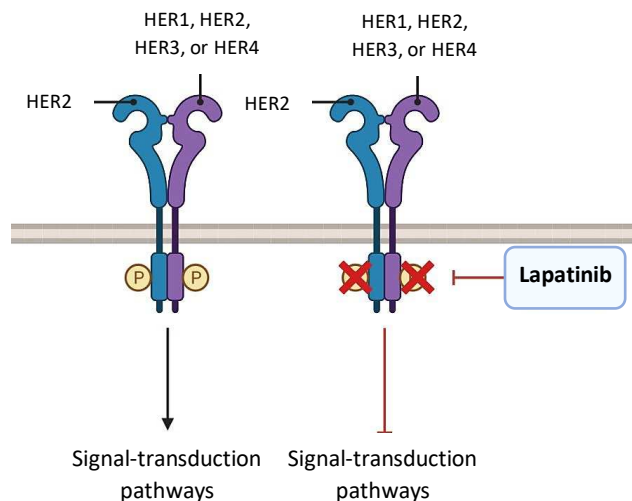


Figure 13: Lapatinib, a small molecule inhibitor of the HER2 receptor, mechanism of action. Upon HER receptors dimerization, ATP-mediated autophosphorylation activates signaling pathways involved in cell proliferation and survival. Lapatinib prevents phosphorylation and the subsequent signaling events, thus inhibiting cell proliferation and inducing apoptosis (Created with BioRender.com).

For HER2-targeted therapy to succeed, HER2 expression status should be accurately characterized first. Nowadays, HER2 status is determined by immunohistochemistry and fluorescence in situ hybridization techniques, performed on biopsied tissues [44]. In addition to being invasive, these small-sized biopsies may not be representative of the heterogeneity between various tumor lesions within the patient. Thus, the need for more accurate, non-invasive techniques to assess HER2 status, favored the development of radiolabeled Trastuzumab that can be visualized using radiological molecular imaging techniques (positron emission tomography PET, single photon emission computed tomography SPECT). The first-in-human clinical trial of  $^{89}\text{Zr}$ -Trastuzumab PET imaging demonstrated excellent tumor uptake and visualization of HER2-positive breast cancer metastatic lesions [45] (Figure 14). Other radiolabeled antibodies and antibody fragments have been also reported for HER2 PET and SPECT imaging [36].

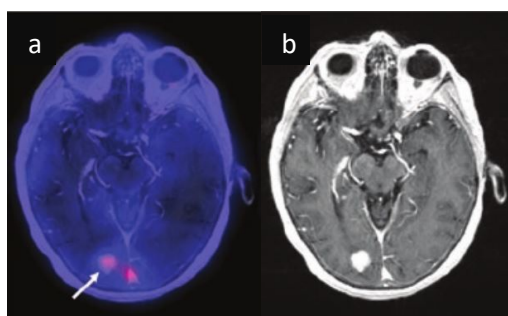


Figure 14: A HER2 positive brain lesion revealed by  $^{89}\text{Zr}$ -Trastuzumab PET imaging (a) and confirmed by MRI imaging (b) [45].

During the thesis work, both passive and active targeting, through HER2 receptor, of tumor diagnostic and therapeutic molecules were implicated

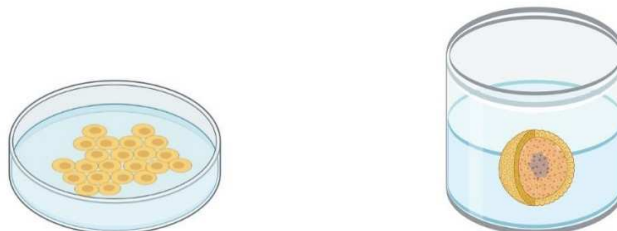
## 2 Preclinical cancer models

Preclinical cancer models have been developed to decipher and better understand cancer biology, as well as to assess novel diagnostic and therapeutic approaches [46]. No ideal cancer model exists, each model has its advantages and drawbacks, and the appropriate choice depends on the scientific question to be answered. The available tumor models, with their positive and negative sides, are discussed below.

### 2.1 *In vitro* tumor models: (2D) and (3D) tumor cell cultures

In two-dimensional (2D) cell cultures, tumor cells grow as a monolayer adhering to flat plastic surfaces such as culture flasks or petri dishes (Figure 15a). The simplicity, reproducibility, and low cost of this model allowed its wide use. However, the absence of cell-cell and cell-extracellular environment interactions, the unlimited availability of oxygen, nutrients, and metabolites, and the alterations of cellular morphology, polarity, phenotype, and function, rendered it far away from mimicking the natural tumor structure and microenvironment. To overcome these pitfalls, three-dimensional (3D) cell cultures have been developed, based on the ability of tumor cells to form spheroid-like structures of multiple cellular layers, when cultured in non-adherent plates, or cultures of gel-like substances, or on scaffolds [47] (Figure 15b). These 3D cultures mimic well the morphology, polarity, and behavior of solid tumor masses *in vivo* [47, 48]. However, being more expensive, time, and labor-consuming compared to 2D cultures, limits their extensive use (Table 1).

Table 1: Comparison between 2D and 3D tumor cell cultures characteristics [47].



	2D tumor cell culture	3D tumor cell culture
<b>Culture quality</b>	Simple, reproducible, easy to interpret	Challenging to carry out, limited reproducibility, difficult to interpret
<b>Cost</b>	Cheap	More expensive requirements
<b>Duration of culture formation</b>	Minutes to a few hours	Few hours to days
<b><i>In vivo</i> mimicking</b>	Do not mimic natural tumor architecture	Mimic tumor architecture
<b>Cell interactions</b>	Absence of cell-cell and cell-extracellular interactions	Presence of cell-cell and cell-extracellular interactions
<b>Cell characteristics</b>	Altered morphology, phenotype, and polarity	Preserved morphology, phenotype, and polarity
<b>Access to essential elements</b>	Unlimited access to nutrients, oxygen, and metabolites	Variable access to nutrients, oxygen, and metabolites

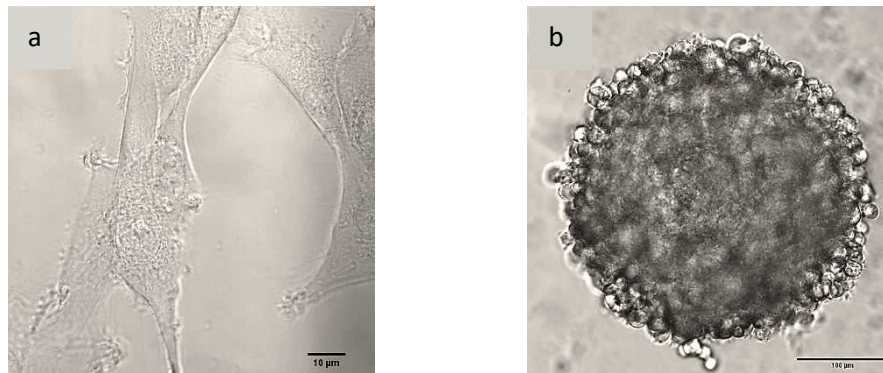


Figure 15: Bright field images of U87MG tumor cells cultured in 2D (a) and 3D (b). Scale bars represent 10 and 100  $\mu\text{m}$  respectively.

## 2.2 *In ovo* tumor model: chorioallantoic membrane (CAM) assay

In this model, tumor cells (tumor cell lines or patient-derived tumor cells) are implanted on the nutrient-rich membrane surrounding chicken embryos, named the chorioallantoic membrane (CAM) (Figure 16). Rapid tumor growth within 3-4 days can be achieved, with close resemblance to patients' tumors, in terms of the established tumor microenvironment (extracellular matrix, stromal cells, tumor vasculature). This fast tumor development is owed to the highly vascularized CAM membrane, responsible for gas, nutrients, and electrolyte exchange, in addition to the non-well-established immune system [49]. Being a cheap, quick, and easy to manipulate *in vivo* system that doesn't require ethical approval (CAM assay is not considered as an animal experiment), presents its main advantages. Despite this, the limited time window before egg hatching (21 days being the entire egg development lifespan), the extreme sensitivity to environmental factors (oxygen availability, pH, temperature), and contamination risks, are the main drawbacks of this model [50, 51] (Table 2).

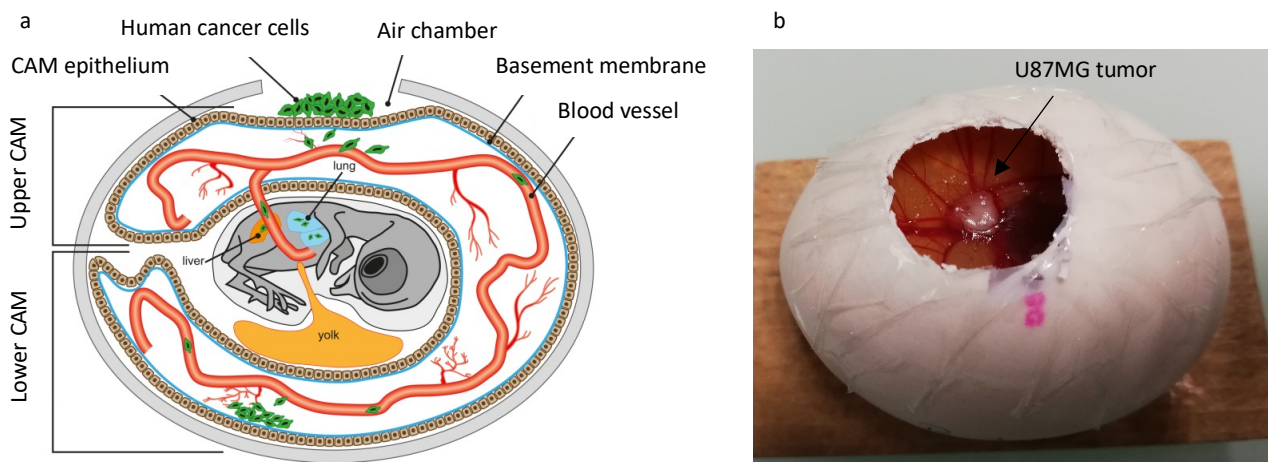


Figure 16: (a) Schematic representation of the *in ovo* CAM tumor model [51]. (b) Photograph of a fertilized chicken egg-bearing U87MG tumor on the upper CAM, at day 15, four days following tumor cells implantation.

Table 2: Comparison between the *in ovo* CAM and mice tumor models [51].

	<i>In ovo</i> tumor model	<i>In vivo</i> mouse tumor model
<b>Duration of tumor development</b>	3-5 days, maximum 7 days	> 4 weeks
<b>Cost</b>	Low cost (3-4 €/egg)	High cost (40-120 €/mouse)
<b>Ethical permission</b>	No approval from the ethics committee needed	Approval from the ethics committee needed
<b>Throughput</b>	High throughput with a large number of samples	A limited number of samples
<b><i>In vivo</i> tumor resemblance</b>	+	+ / ++ (depending on the mouse model)
<b>Life span</b>	Very short (21 days)	Long (1-3 years)
<b>Robustness</b>	Sensitive/ fragile	Robust

## 2.3 *In vivo* tumor models: mouse tumor models

Compared to other animal tumor models, mouse tumor models have been widely utilized in cancer research due to their superior advantages, including their small size, inexpensive maintenance, rapid production, large litters, and their ability to be genetically modified [52]. Mouse tumor models can be divided into xenograft, syngeneic, chemically induced, and genetically engineered cancer models.

### 2.3.1 Xenograft mouse cancer model

In standard mouse xenograft cancer models, established human tumor cell lines are implanted into immunocompromised/immune-deficient mice, and according to their implantation site, ectopic and orthotopic models can be defined.

#### 2.3.1.1 Ectopic xenograft model

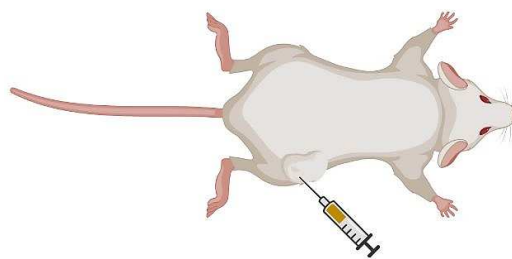


Figure 17: Schematic view of ectopic (subcutaneous) glioblastoma xenograft, generated by implanting human glioblastoma cell line under the skin of an immunocompromised mouse (Created with BioRender.com).

In ectopic models, human tumor cell lines are implanted in a different location than the natural tumor development site, mainly under the skin of immune-deficient mice (Figure 17). Being cost- and time-effective, reproducible, and suitable for a wide range of tumor cell types, allowed its use for early-stage pharmacological screening, and evaluation of drugs' anti-tumor efficacy.

Despite these uses, ectopic models possess limited clinical predictability due to the cancer cell lines histological and genetic dissimilarities with primary tumors, in addition, to the non-physiological location of tumor growth, and the absence of tumor interaction with stroma microenvironment (endothelial cells, inflammatory cells, tumor-associated fibroblasts, matrix proteins) [53, 54].

### 2.3.1.2 Orthotopic xenograft model

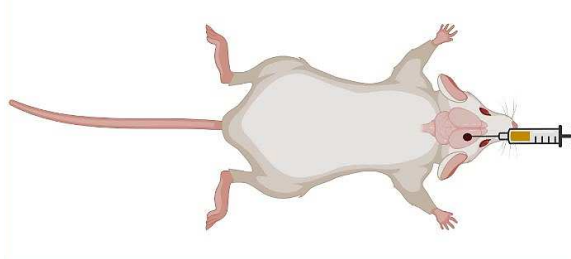
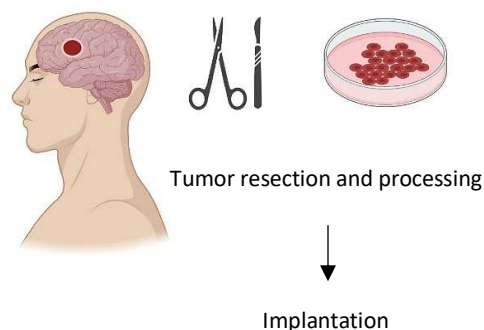


Figure 18: Schematic view of an orthotopic glioblastoma xenograft, generated by implanting a human glioblastoma cell line into the brain of an immunocompromised mouse (Created with BioRender.com).

In orthotopic models, human tumor cell lines are implanted in the organ of tumor origin, of immune-deficient mice (Figure 18). This provides a better resemblance to the pathological phenotype/physiology and allows an accurate reconstitution of the tumor microenvironment, which in turn influences tumor proliferation, angiogenesis, invasion, and metastasis. Accordingly, orthotopic models can offer moderate clinical predictability as compared to ectopic ones and can be used for the mid-late stages of drug discovery. Yet, orthotopic models still suffer from the use of tumor cell lines, the technical difficulties encountered during tumor implantation and monitoring (imaging is required), the long tumor development time, and possible animal losses during surgical implantations that might be complex/painful (e.g. brain, head and neck, bone tumors...) [53, 54].

### 2.3.1.3 Patient-derived xenograft (PDX) model



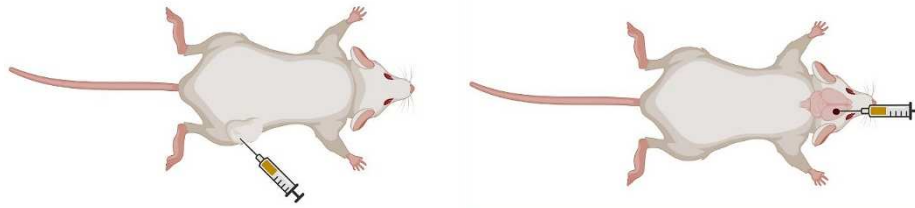


Figure 19: Schematic view of patient-derived glioblastoma xenograft model, generated by implanting processed human tumors into ectopic or orthotopic sites of immunocompromised mice (Created with BioRender.com).

To address the issues of using established tumor cell lines, patient-derived xenograft (PDX) model has been developed. PDX model is based on transplanting primary tumors directly isolated from patients into immune-deficient mice (Figure 19). This model can be maintained by passing the tumor from one mouse to another, with a recommended passage number (<10), to maintain the genetic integrity of the original tumor. Both ectopic and orthotopic PDX can be developed. The consistency of genetics, morphology, response to therapy between PDX and primary tumors, and the maintenance of stroma-tumor interaction have demonstrated the high predictive capacity of the PDX model for mid-late drug discovery stages. Yet, the access to fresh primary tumors, the high cost, the required passage skills, the long latency period (2-12 months) required for PDX establishment, the variable engraftment rates (23-75%), and the fact that most established PDX models are of high-grade late-stage tumors, have limited its wide spread [54-56].

All the discussed xenograft models possess a common characteristic which is the lack of immune system surveillance.

### 2.3.2 Syngeneic mouse cancer model

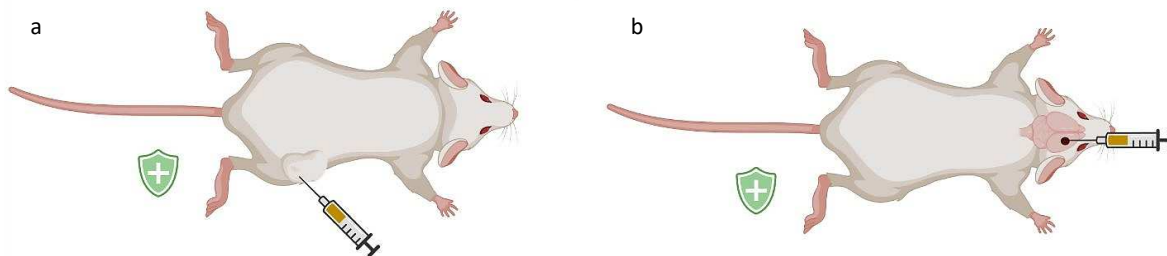


Figure 20: Schematic view of ectopic (a) and orthotopic (b) glioblastoma syngeneic mouse models, generated by implanting mouse glioblastoma cell line under the skin or into the brain of immunocompetent mice, respectively (Created with BioRender.com).

In the syngeneic cancer model, mouse tumor cells or fragments are implanted into immunocompetent mice of the same genetic background [57]. Both ectopic and orthotopic implantations can be achieved (Figure 20). These models are mainly utilized to study the influence of the immune system on tumor development and tumor response to therapies [54]. The main limitation of this model is the use of mouse tumor cells.

### 2.3.3 Genetically engineered mouse cancer model

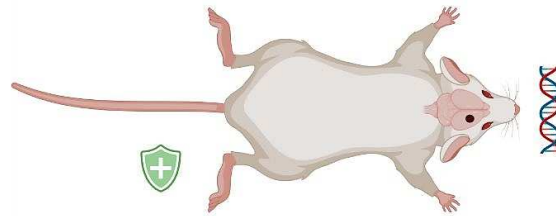


Figure 21: Schematic view of genetically engineered glioblastoma mouse model, generated in an immunocompetent mouse (Created with BioRender.com).

Spontaneous cancers can develop in immune-competent mice by genetic activation of tumor oncogenes or genetic inactivation of tumor suppressor genes [52, 58] (Figure 21). Due to the presence of tumor-stroma interactions and an active immune system, this model resembles human cancers under physiological conditions, thus providing a predictive tumor model. However, the heterogeneity in tumor frequency and development time, the high cost and effort, and the need for imaging systems to monitor tumor growth have restricted its use for mid-late stages of drug discovery [54].

### 2.3.4 Chemically-induced mouse cancer model

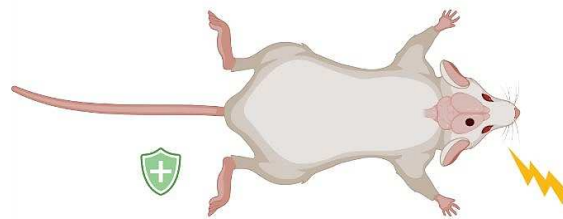


Figure 22: Schematic view of chemically induced glioblastoma model, generated in an immunocompetent mouse (Created with BioRender.com).

This model induces specific cancers by exposing immunocompetent mice to carcinogens [58] (Figure 22). It provides a clinically relevant model for time-dependent, multi-stage monitoring of tumor pathogenesis. This relevance is owed to the histological, molecular, and phenotypic similarities with human cancers, the availability of stroma-tumor interactions, and immune surveillance. However, the long-time frame (5-50 weeks), the cost of animal maintenance, the need for imaging modalities to monitor tumor lesions and sequencing to identify the induced mutation, and the safety concerns regarding carcinogen handling, have limited its use to late-stage drug discovery [54].

Companion animals (e.g. dogs, cats) [58] and non-human primates (e.g. rhesus macaques) [59] present valuable late-stage preclinical tumor models, that bridge the gap between early preclinical tumor models and human clinical investigations.

As early preclinical tumor models, i.e. *in vitro*, *in ovo*, and *in vivo* mouse models were the only utilized models during the thesis, late-stage preclinical tumor models will not be described in this manuscript.

## 2.4 Conclusion

To conclude, each preclinical tumor model possesses unique strengths and weaknesses in mimicking human tumors (Table 1, Table 2, Table 3), tumor-associated mechanisms (angiogenesis, invasion, metastasis), and response to diagnostic and therapeutic molecules. These models should be viewed as a set of biological tools that can be optimally utilized at the various stages of drug discovery, and that the appropriate model selection depends on its clinical predictability, data relevance, cost, time, and effort required for its establishment (Figure 23).

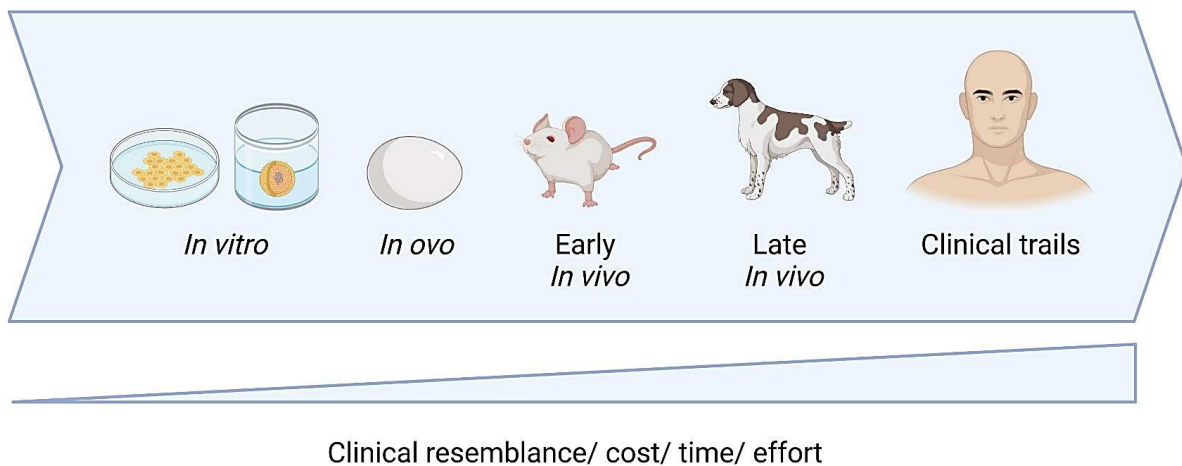


Figure 23: Tumor models utilized during drug discovery (Created with BioRender.com).

Table 3: The different mouse cancer models: characteristics and applications in oncology and drug discovery [54].

Cancer Mouse Model	Type	Host	Primary features	Strengths	Weaknesses	Utility	Clinical predictability	Stage of drug (diagnostic, therapeutic molecule) discovery
<b>Xenograft Cancer model</b>	Ectopic	Immuno-deficient mice	Implantation of human tumor cells in a different location than the natural tumor development site	<ul style="list-style-type: none"> <li>- Cost- and time-effective</li> <li>- Reproducible</li> <li>- Suitable for a wide range of tumor cell types</li> </ul>	<ul style="list-style-type: none"> <li>- Cancer cell lines histological and genetic dissimilarities, and heterogeneity loss compared to primary tumors</li> <li>- Non-physiological location of tumor growth</li> <li>- Absence of tumor interaction with stroma microenvironment</li> <li>- Low or absent metastatic rate</li> </ul>	<ul style="list-style-type: none"> <li>- Assessment of pharmacokinetics/ pharmacodynamics, and anti-tumor efficacy of new molecules</li> </ul>	Limited clinical predictability	Early-stage
	Orthotopic	Immuno-deficient mice	Implantation of human tumor cells in the organ of tumor origin	<ul style="list-style-type: none"> <li>- Reconstitution of the tumor microenvironment and stroma-tumor interactions</li> <li>- High metastatic rate</li> </ul>	<ul style="list-style-type: none"> <li>- Cancer cell lines histological and genetic dissimilarities, and heterogeneity loss compared to primary tumors</li> <li>- Technical difficulties in tumor implantation and monitoring (imaging is required)</li> <li>- Possible animal loss during surgical implantation</li> </ul>	<ul style="list-style-type: none"> <li>- Evaluation of new molecules effects on primary tumors (within proper microenvironment) and metastatic ones</li> </ul>	Moderate clinical predictability	Mid-late stages of drug discovery (especially for metastatic disease)
<b>Syngeneic</b>	Ectopic/ Orthotopic	Immuno-competent mice	Implantation of mouse tumor cells/fragments in mice of same genetic background, at tumor origin or different location	<ul style="list-style-type: none"> <li>- Immune system surveillance</li> </ul>	<ul style="list-style-type: none"> <li>- The use of mouse tumor cell lines which are genetically different from human cells</li> </ul>	<ul style="list-style-type: none"> <li>- Assessment of immune system influence on cancer development and response to therapies</li> </ul>	Limited (ectopic)/ Moderate (orthotopic) clinical predictability	Early (ectopic)/ Mid-late stage (orthotopic)

<b>Patient-derived xenograft model</b>	Ectopic/ Orthotopic	Immuno-deficient mice	Implantation of primary tumors directly isolated from patients, at the organ of tumor origin or different location	<ul style="list-style-type: none"> <li>- Consistency of genetics, morphology, and response to therapy between the PDX tumors and primary tumors</li> <li>- Maintenance of stromal components of the primary tumor</li> <li>- Metastatic potential</li> </ul>	<ul style="list-style-type: none"> <li>- Access for fresh primary tumors</li> <li>- High cost</li> <li>- Skills required for tumor passing</li> <li>- Long latency period (2-12 months) for PDX establishment</li> <li>- Variable engraftment rates (23-75%)</li> </ul>	<ul style="list-style-type: none"> <li>- Evaluation of new molecules' effects on the original human tumors.</li> </ul>	Highly predictive capacity	Mid-late drug discovery stages
<b>Genetically engineered model</b>		Immuno-competent mice	Development of spontaneous specific cancers by genetic activation of tumor oncogenes or genetic inactivation of tumor suppressor genes	<ul style="list-style-type: none"> <li>- Presence of tumor-stroma interactions and active immune system</li> <li>- Resemblance to human cancers under physiological conditions</li> </ul>	<ul style="list-style-type: none"> <li>- Heterogeneity in tumor development time and frequency</li> <li>- High cost and effort</li> <li>- The need for imaging systems to monitor tumor growth</li> </ul>	<ul style="list-style-type: none"> <li>- Evaluation of new molecules' effects on tumor progression and immune system under physiological conditions.</li> </ul>	Predictive tumor model	Mid-late stages of drug discovery
<b>Chemically-induced model</b>		Immuno-competent mice	Induction of specific cancers by exposure to carcinogen molecules	<ul style="list-style-type: none"> <li>- Similarity with human cancers</li> <li>- Availability of stroma-tumor interaction and immune surveillance.</li> </ul>	<ul style="list-style-type: none"> <li>- Long-time frame (5-50 weeks)</li> <li>- Costs of animal maintenance</li> <li>- The need for imaging modalities to monitor tumor lesions, and sequencing to identify the induced mutation</li> <li>- Safety concerns of handling carcinogenic agents</li> </ul>	<ul style="list-style-type: none"> <li>- Time-dependent multi-stage monitoring of tumor pathogenesis</li> <li>- Determination of the most relevant stage for therapeutic intervention.</li> </ul>	Predictive tumor model	Late-stage drug discovery

### 3 Cancer diagnosis

Cancer is a worldwide health concern that is progressively growing. Early tumor detection and diagnosis are key for increasing cure chances, maintaining good life quality, and reducing mortality and healthcare costs [60]. Non-invasive biomedical imaging has been one of the main pillars for tumor diagnosis, besides invasive biopsies. It has served in the accurate identification and characterization of tumor lesions (staging), establishment of appropriate treatment plans, and monitoring response rates. The prime clinical imaging techniques include X-ray computed tomography (CT), magnetic resonance imaging (MRI), ultrasound imaging, positron-emission tomography (PET), and single-photon-emission CT (SPECT) [61]. Each imaging system possesses its strengths and limitations regarding resolution, sensitivity, tissue penetration depth, safety, and cost (Table 4). In addition, considering the different information (anatomical, physiological, functional, or molecular) they can provide, the most suitable technique is selected.

Unlike early mentioned techniques, optical imaging and in particular fluorescence imaging has been extensively used in preclinical studies. However, its clinical translation is currently under evaluation [62] [63], in the form of fluorescence-guided surgery (FGS), thanks to the favorable clinical trials data. FGS, based on the use of fluorescent contrast agents, has proved its utility for real-time *in vivo* identification of fluorescently-labeled tumors, and guided the surgeons in the precise detection of surgical margins, thus permitting complete tumor resection. Fluorescence imaging high sensitivity, low cost, real-time monitoring, ease of operation, absence of ionizing radiation, and the availability of a wide range of fluorophores, that are under continuous development, have supported its translation [64].

In the following sections, fluorescence imaging principle, *in vivo* fluorescence imaging main limitation, and possible solution using fluorophores emitting in the first near infra-red (NIR-I) window (700-900 nm), is discussed with evidence of clinical investigations. An emerging fluorescence imaging field within the second near infra-red (NIR-II) window (1000-1700 nm) is then highlighted, and its superior performance compared to NIR-I fluorescence imaging, is demonstrated in preclinical animal models.

Table 4: Comparison of the common bioimaging techniques [61, 64].

	X-ray CT	MRI	PET	SPECT	Ultrasound	Fluorescence
<b>Source</b>	X-ray	Magnetic field and radiofrequency	$\beta^+/\gamma$ -emission	$\gamma$ -emission	Sound	Light
<b>Radiation</b>	Ionizing	Non-ionizing	Ionizing	Ionizing	Non-ionizing	Non-ionizing
<b>Contrast agent</b>	Heavy element, e.g. I, Ba	Magnetizable materials as $\text{Fe}_3\text{O}_4$ , Gd chelates	Radionuclide as $^{18}\text{F}$ , $^{11}\text{C}$ , $^{13}\text{N}$ , $^{15}\text{O}$ , $^{64}\text{Cu}$ , $^{68}\text{Ga}$	Radionuclide as $^{111}\text{In}$ , $^{99\text{m}}\text{Tc}$	Microbubble, emulsion, micelle	Fluorescent dye
<b>Spatial resolution</b>	50-200 $\mu\text{m}$	25-100 $\mu\text{m}$	1.2 mm	>2 mm	50-500 $\mu\text{m}$	1-5 mm
<b>Sensitivity (mol/L)</b>	$10^{-3}$	$10^{-3}$ - $10^{-5}$	$10^{-10}$ - $10^{-12}$	$10^{-10}$ - $10^{-12}$	Not characterized	$10^{-9}$ - $10^{-12}$
<b>Penetration depth</b>	No limit	No limit	No limit	No limit	Several cm	<1 cm

Obtained Information*	A and P	A, P, and M	P and M	P and M	A, P, and M	P and M
Cost	€€	€€€	€€€	€€	€€	€
Advantages	High resolution, no depth limit	High spatial resolution, no radiation, no depth limit	High sensitivity to probes, no depth limit	High sensitivity to probes, no depth limit	Easy, fast, no ionizing radiation, cost-effective	Easy, fast, no radiation, sensitive to probe dose, cost-effective
Drawbacks	Radiation, poor soft tissue delineation, low sensitivity to probes	Poor sensitivity to probes, expensive	Radiation, expensive, low resolution	Radiation, expensive, low resolution	Depth limit (cm), poor contrast, not suitable for air-containing organs	Low depth penetration, low resolution

\**In vivo* information: A: anatomical, P: physiological, and M: molecular

### 3.1 Fluorescence Imaging: Principle

In fluorescence imaging, a light source of an appropriate wavelength excites a molecule (fluorophore) from the ground state into a higher energetic state. Upon relaxing back into its stable ground state, the fluorescent molecule emits light of a longer wavelength and lower energy [65]. This instantaneous process called fluorescence is illustrated by the Jablonski diagram (Figure 24). Fluorescence is then visualized thanks to a sensitive cooled charged coupled device (CCD) camera, accompanied with specific filters, that can collect emitted light only.

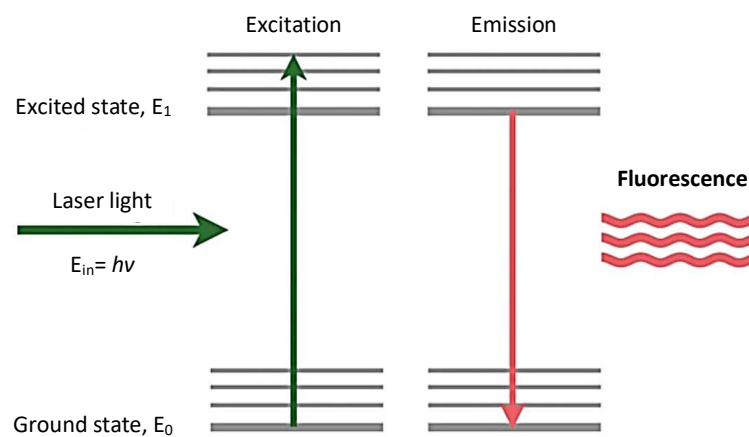


Figure 24: Simplified Jablonski diagram explaining the fluorescence phenomenon [66].

### 3.2 *In vivo* fluorescence imaging: Light/Photon interaction with biological tissues

As incident excitation light impinges the biological tissue and travels through it, several photon-tissue interactions will be encountered, limiting the photon tissue penetration. Similar events will impact the fluorescence emitted light (Figure 25). These interaction events include:

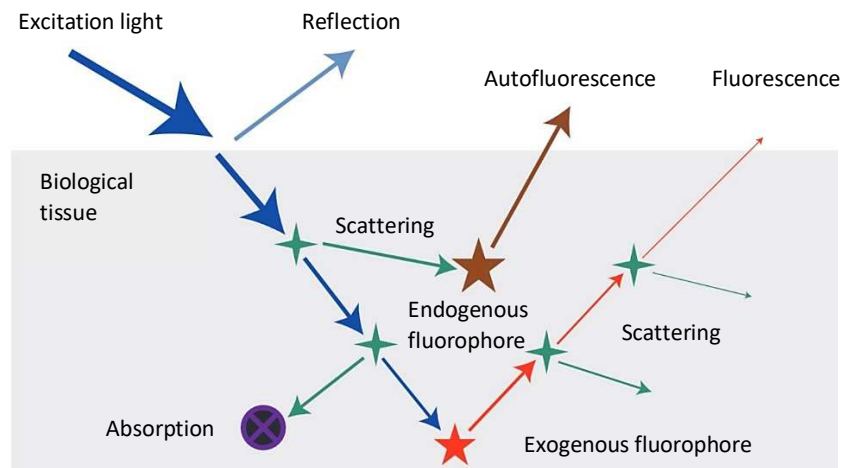


Figure 25: Light-tissue interactions resulting from light excitation of biological tissues. These interactions include light reflection, scattering, absorption, and endogenous fluorophores autofluorescence. Fluorescence can be obtained once light excites administered exogenous fluorophore [67].

**Photon reflection:** Due to the different refractive indices between air and imaged tissue, a part of the incident excitation light will be reflected. This phenomenon is not wavelength-dependent and normally doesn't lead to signal loss.

**Photon scattering:** Non-reflected photons can penetrate tissues, and encounter some scattering events due to the variable refractive indices of tissue components. Scattering events induce photon deviation from their original path, thus increasing background noise. Since scattering is inversely proportional to the light wavelength, a reduced scattering can be achieved using light sources with longer wavelength [67] (Figure 26).

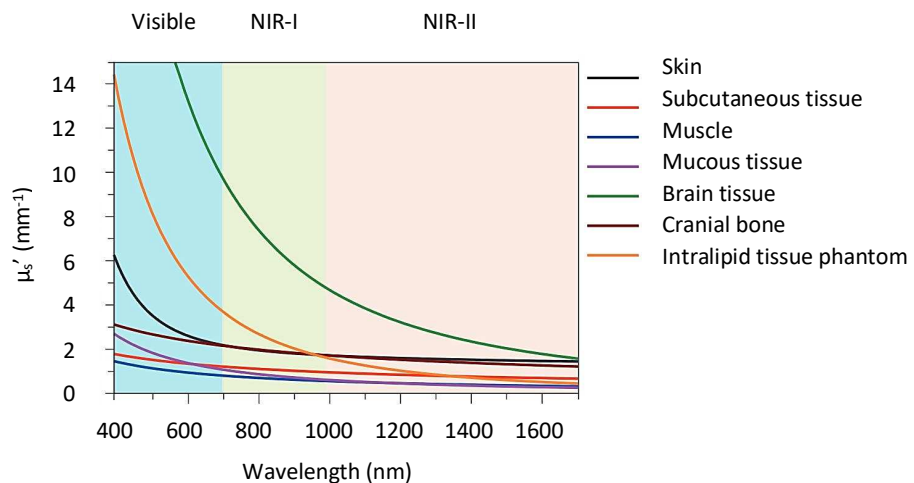


Figure 26: Scattering coefficient of various biological tissues and intralipid tissue phantom as a function of wavelength (400-1700nm), covering the visible, NIR-I, and NIR-II regions [67].

**Photon absorption:** As light passes through biological tissues, it can be absorbed by endogenous chromophores like hemoglobin, water, lipids, and melanin, leading to an exponential reduction in the number of photons reaching deep tissues [68]. As presented in Figure 27, the NIR region

benefits from minimal chromophores absorption and thus better photon penetration, compared to the visible region.

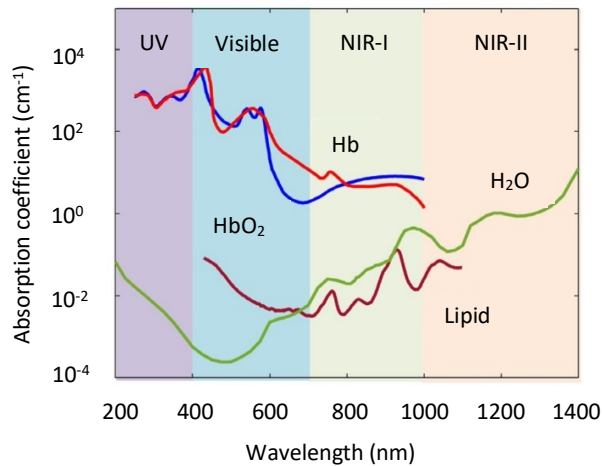


Figure 27: Absorption coefficient of endogenous chromophores (oxyhemoglobin  $\text{HbO}_2$ , deoxyhemoglobin  $\text{Hb}$ ,  $\text{H}_2\text{O}$ , and lipids) as a function of wavelength (200–1400 nm), covering UV, visible, NIR-I, and NIR-II optical windows [69].

**Autofluorescence:** defines the fluorescence signal/background obtained from exciting endogenous components present within biological tissues, including aromatic amino acids, NAD(P)H, flavins, and lipopigments [70]. Those latter act as endogenous fluorophores emitting mainly in the visible spectrum. Autofluorescence, being wavelength-dependent, is reduced using longer wavelength light sources and detectors [71] (Figure 28).

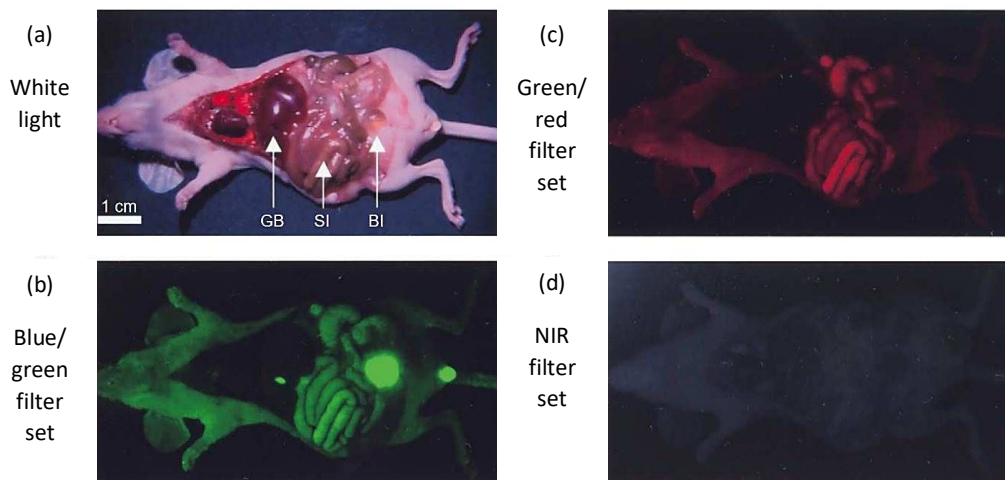


Figure 28: Autofluorescence of a sacrificed mouse imaged using different excitation/emission filters: (b) blue/green (460–500 nm/505–560 nm); (c) green/red (525–555 nm/590–650 nm); and (d) NIR (725–775 nm/790–830 nm) filters. Reduced autofluorescence is attained using longer wavelength excitation/emission filters. A white light image of the mouse is shown in (a). The location of the gallbladder (GB), small intestine (SI), and bladder (BI) is indicated by arrows [71].

To conclude, photon-tissue interactions, (scattering, absorption, and autofluorescence) that restrict photon penetration *in vivo*, can be strongly reduced using light sources and camera detectors of increased wavelength.

### 3.3 From visible to NIR-I fluorescence imaging

Using fluorophores emitting in the visible spectrum (400-700 nm), *in vivo* fluorescent imaging has been limited by photon-tissue interaction phenomena, leading to poor photon penetration (1-3 mm) into deep tissues [72], and resulting in images of reduced resolution and contrast in depth. The need to attain deep-tissue fluorescence imaging has then driven the development of new fluorophores with improved spectral properties, capable of emitting in another spectral window called the first near infra-red (NIR-I) window (700-900 nm). Within this optical window, photon scattering (Figure 26), absorption (Figure 27), and tissues autofluorescence (Figure 28) are hugely reduced, hence achieving deep imaging (5-7 mm) with an enhanced signal-to-noise ratio [72]. NIR-I window, also named “biological transparency window” presents the ideal optical region for biomedical fluorescence imaging [67, 71].

### 3.4 NIR-I fluorophores: for *in vivo* tumor imaging

NIR-I tumor imaging fluorophores can be classified according to their fluorescent status into “always on” or “activable” probes, and according to their tumor specificity into non-targeted and targeted fluorophores. A representative example of each NIR-I fluorophore group, assessed within clinical trials, is presented.

#### 3.4.1 “Always On” fluorophores

They are fluorophores whose fluorescent signal is always present. They are divided into non-targeted and targeted fluorophores.

##### 3.4.1.1 Non-targeted fluorophores

These dyes have no specificity to certain cellular or molecular target, and their tumor accumulation is mainly based on the enhanced permeability and retention (EPR) effect. Indocyanine green (ICG) presents one of the main examples of this group.

ICG (Figure 29a) was FDA-approved for determining cardiac output, hepatic function, and ophthalmic angiography. Recently, ICG NIR emission at  $\sim 822$  nm has permitted its use for sentinel lymph nodes mapping [73]. This application paved the way then towards using ICG for tumor detection and intraoperative fluorescence-guided surgery. Due to its passive tumor accumulation, ICG has succeeded, in clinical trials, to identify several tumor types including hepatocellular carcinoma [74] and colon cancers [75], distinguish malignant from benign breast lesions [76], and estimate gastric tumors invasivity [77].

Because ICG is well metabolized and excreted by healthy liver, ICG was able to identify all the microscopically confirmed hepatocellular carcinoma (HCC) and colorectal cancer metastasis (CRC) [78], in a clinical assay dedicated to liver cancer detection. Well-differentiated HCC presented a uniform total fluorescence (Figure 29b), whereas less differentiated HCC and CRC presented a fluorescence rim around the tumor (Figure 29c, d). Uniform tumor fluorescence was explained by the dysfunction of biliary excretion in progressing HCC. However, fluorescence rim

staining was explained by biliary excretion disorders in the surrounding non-cancerous cells that were compressed by the tumor. In addition, ICG fluorescence was able to recognize tumors that weren't evident without imaging (Figure 29e, f). These results demonstrated the ability of ICG-fluorescence imaging to identify HCC lesions, delineate poorly differentiated HCC and CRC metastasis, and detect small non-recognizable tumors, with secured negative tumor margins [79], thus improving the accuracy of intraoperative tumor resections.

Regardless of non-targeted fluorophores' clinical potential, high background signal, non-specific binding, and relatively fast clearance that limits optimal surgery time are the main drawbacks [62]. Particularly, ICG suffers from its short half-life and difficult bioconjugation.

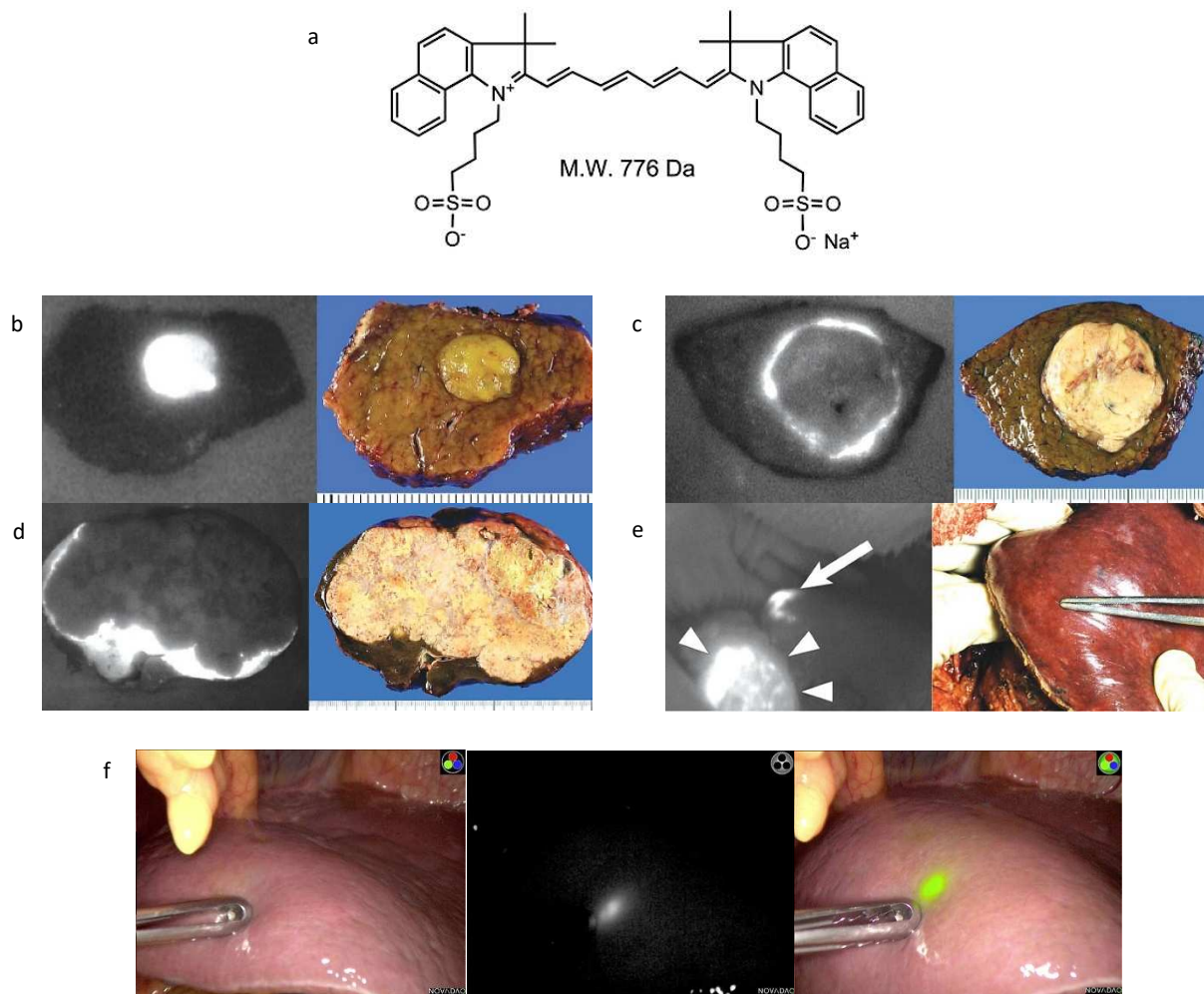


Figure 29: (a) Chemical structure of ICG [73]. ICG fluorescence pattern identified in liver cancer specimens: (b) well-differentiated HCC, (c) poorly differentiated HCC, and (d) CRC. A white light image is provided for each specimen, on the right side of each panel. (e) ICG Intraoperative fluorescence imaging identifying HCC on the liver surface, HCC lesion is indicated by a white arrow. It is worth noting that this lesion was not recognized by visible inspection (right side panel) or palpation. Arrows heads indicate the colon that was fluorescent due to ICG excretion in the stool [78]. (f) Laparoscopic colored image, NIR-fluorescence image, and colored-NIR fluorescence overlaid image of colorectal liver metastasis, that was not identified by visual inspection or preoperative diagnosis [79].

### 3.4.1.2 Targeted Fluorophores

These probes have specificity to certain cellular or molecular target overexpressed in tumor cells. They are usually made up of a fluorescent moiety linked to a ligand possessing affinity to the overexpressed cellular/ molecular target. The ligand could be a small molecule, peptide, antibody, or affibody, for example.

Here, the first clinical study of a fluorescently labeled antibody for tumor identification is discussed [80]. Cetuximab, a monoclonal antibody specific to the epidermal growth factor receptor (EGFR), was labeled with IRDye800 fluorophore ( $\lambda_{em}=795$  nm) (Figure 30) and administrated to patients undergoing resection of squamous cell carcinoma of the head and neck. No adverse events were observed with dose escalation of Cetuximab-IRDye800. Intraoperative fluorescent imaging demonstrated the success of Cetuximab-IRDye800 in the precise identification of tumors expressing EGFR from normal tissues, with a tumor-to-background ratio of 5.2 for the highest dose (Figure 31). Cetuximab-IRDye800 is now in phase 2 clinical trial to assess tumor margins during intraoperative fluorescence-guided surgery [81].

Using targeted fluorophores have several advantages that include, obtaining a high signal-to-noise ratio SNR (lower background), using less fluorophore dose, and improving tumor accumulation due to the prolonged fluorophore circulation time. On the other side, targeted fluorophores possess several drawbacks including the high production cost, and the target expression by normal tissues adjacent to the tumors, making it difficult to delineate tumors with low target expression. In addition, the variability of target expression in tumors and between tumor types, suggests that using targeted fluorophores is beneficial for tumors overexpressing the target, not to a wide range of tumors [62].

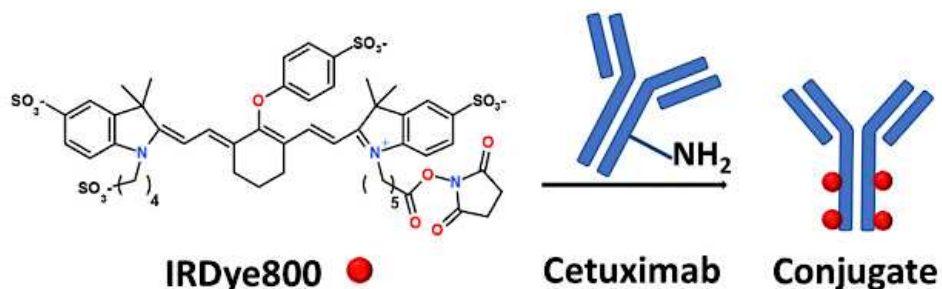


Figure 30: Schematic illustration of Cetuximab-IRDye800 conjugate synthesis through the conjugation of IRDye800-NHS to Cetuximab antibody [82].

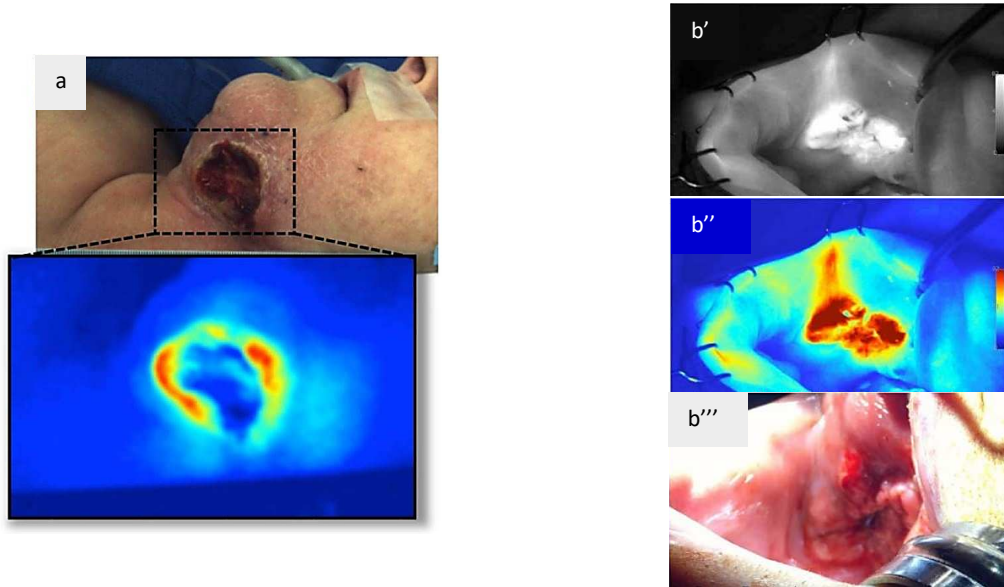


Figure 31: (a) White light and fluorescence image of a patient with head and neck tumor, injected with 25 mg/m<sup>2</sup> dose of Cetuximab-IRDye800 and imaged with a wide-field NIR imaging system. (b) Intraoperative fluorescence imaging of a patient injected with 25 mg/m<sup>2</sup> dose of Cetuximab-IRDye800, before a wide local excision of the buccal mucosa. Grayscale fluorescence image (b'), color map fluorescence image (b''), and the corresponding brightfield image (b''') were acquired using a wide-field NIR imaging system [80].

### 3.4.2 Activable probes

In their inactive state, activable probes are dark. Following specific tumor stimulus (enzyme cleavage, pH changes), the fluorophores recover their fluorescence signal. Their tumor-specific activity is based on the notion that tumors overexpress certain enzymes, and possess an acidic environment as compared to healthy tissues.

The first-in-human clinical trial to assess a protease-activated fluorescent probe, for intraoperative imaging, was published by Whitley et al. [83]. LUM015 (Figure 32a) composed of a fluorescence quencher linked by a peptide to polyethylene glycol (PEG) and Cy5 fluorophore was developed. The cleavage of the peptide by cathepsins protease, overexpressed in tumors, activates Cy5. LUM015 was well tolerated following its intravenous injection into soft tissue sarcoma (STS) and breast cancer patients. *Ex vivo* fluorescent imaging of resected tissues demonstrated a higher fluorescence signal in tumors as compared to healthy tissues (Figure 32b, c). Recently, LUM015 has completed phase 2 clinical trial [84] and robust performance in residual breast cancer detection during intraoperative fluorescence imaging was demonstrated, with a mean tumor/normal tissue signal ratio of 3.81-5.69 [85].

Compared to the previous fluorophores' types, activable probes have the advantage of low background, as they are only activated and detected at the target site. However, interpatient variability in enzymatic activities and expression levels that can affect the fluorescence signal is one of its limitations [62].

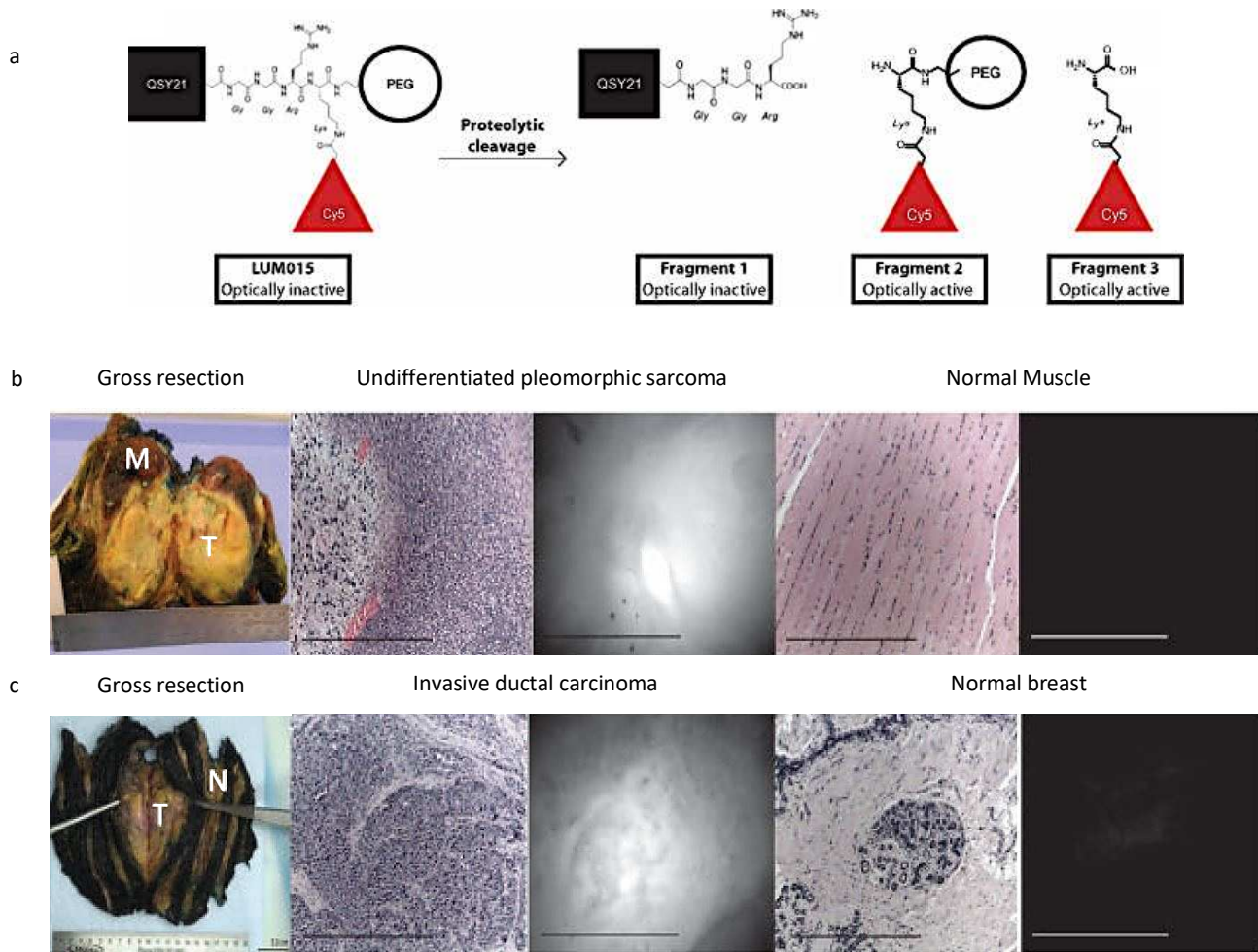


Figure 32: LUM015 probe and its cleavage products: the optically inactive fragment 1 containing QSY21 quencher, and the optically active fragments 2 and 3 containing Cy5 fluorophore (a). Representative undifferentiated pleomorphic sarcoma (UPS) of the thigh (b) and invasive ductal carcinoma (IDC) of the breast (c), obtained from patients that had received LUM015 before gross resection. From left to right: white light image of the gross resected tissue containing the tumor (T), normal muscle (M) or normal breast (N), hematoxylin and eosin (H&E) staining and fluorescence images of the tumors (UPS or IDC), followed by H&E staining and fluorescence images of normal tissues (muscle or breast). These Images demonstrate the tumor-selective fluorescence of LUM015 [83].

Altogether these examples demonstrated the potential of NIR-I fluorescence imaging in recognizing tumors and guiding precise resection.

### 3.5 From NIR-I to NIR-II fluorescence imaging

Yet, more favorable optical properties can be achieved in the spectral window ranging from 1000-1700 nm, named the second near infra-red (NIR-II) window. Benefiting from further diminished photon scattering [86] (Figure 33a) and exponentially reduced autofluorescence [87] (Figure 33b), NIR-II imaging can outperform NIR-I imaging by providing clearer images and better signal-to-noise ratio (Figure 34). NIR-II fluorescence imaging is a recent field. In 2009, the first *in vivo* fluorescence imaging of mice, in the NIR-II range, using single-walled carbon nanotubes (SWCNTs), marked the beginning of the NIR-II bioimaging era [88]. It was able to resolve tumor vessels under the skin with low autofluorescence. Since then, NIR-II imaging has been an active progressing field.

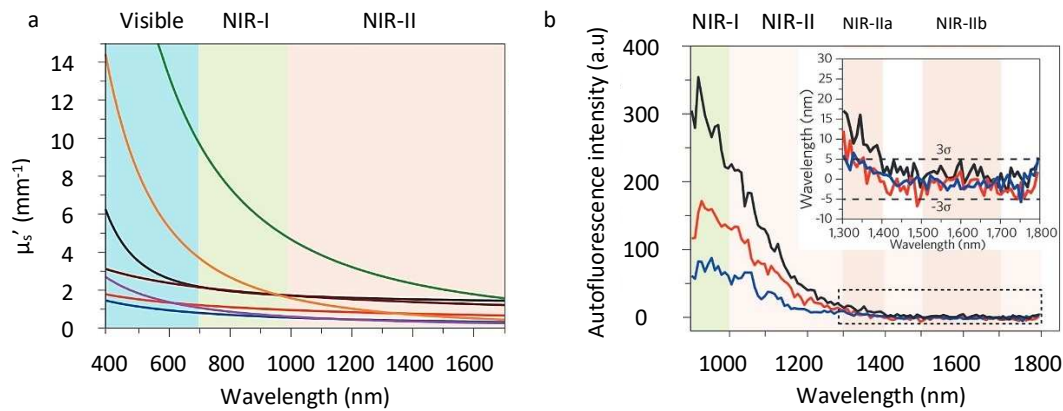


Figure 33: (a) Scattering coefficient of various biological tissues including brain (green), skin (black), cranial bone (brown), mucous tissue (purple), subcutaneous tissue (red), muscle (blue), and intralipid tissue phantom (orange) as a function of wavelength (400-1700nm), covering the visible, NIR-I and NIR-II regions. (b) Autofluorescence of ex vivo mouse liver (black), spleen (red), and heart tissue (blue) as a function of wavelength, showing the absence of autofluorescence beyond 1,500 nm [67].

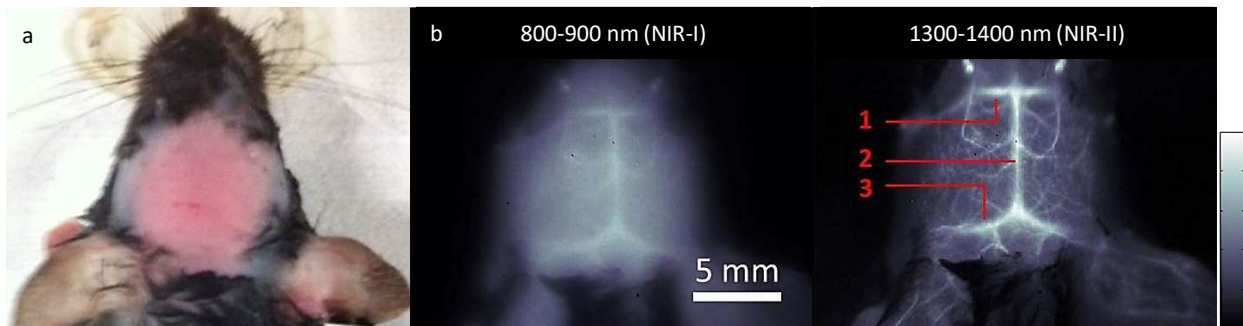


Figure 34: NIR-I and NIR-II *in vivo* fluorescence imaging of a mouse brain following SWNT-IRDye800 administration. (a) White light image of a C57B1/6 mouse head with the hair removed. (b) NIR-I and NIR-II images of the same mouse head. The inferior cerebral vein, the superior sagittal sinus, and the transverse sinus are indicated by 1, 2, and 3 respectively [89].

## 3.6 NIR-II fluorescence imaging: Requirements

NIR-II fluorescence imaging requires sensitive detectors/cameras and efficient fluorophores that can detect and emit within the NIR-II window, respectively.

### 3.6.1 NIR-II window detectors/cameras

Silicon (Si) cameras are the most commonly used detectors in fluorescence imaging. They are sensitive to fluorescence emission in the NIR-I region, however, they are not suitable for wavelength beyond 1000 nm. Indium-gallium-arsenide (InGaAs) cameras, having a high quantum efficiency in the NIR-II window, can detect fluorescence signals beyond 1000 nm with high sensitivity [90] (Figure 35). The need for high-quality and affordable InGaAs cameras is one of the limitations of NIR-II fluorescence imaging development. Recently, the combination of military and industrial imaging applications, allowed the InGaAs cameras to become more commercially available and with lower costs [91].

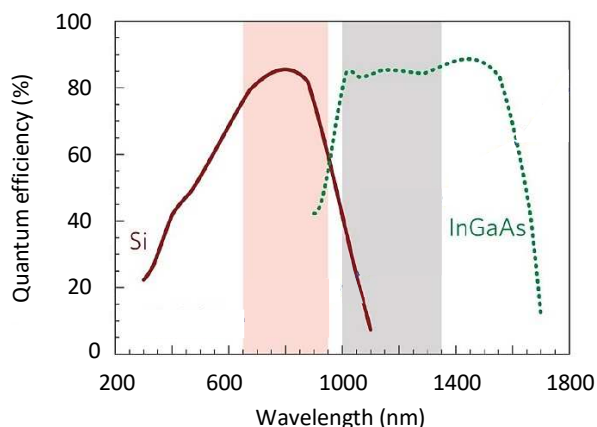


Figure 35: Sensitivity curves for silicon (Si) and indium gallium arsenide (InGaAs) based cameras. Si and InGaAs cameras are sensitive within the NIR-I and NIR-II windows, respectively. Adapted from [90].

### 3.6.2 NIR-II fluorophores: for *in vivo* tumor imaging

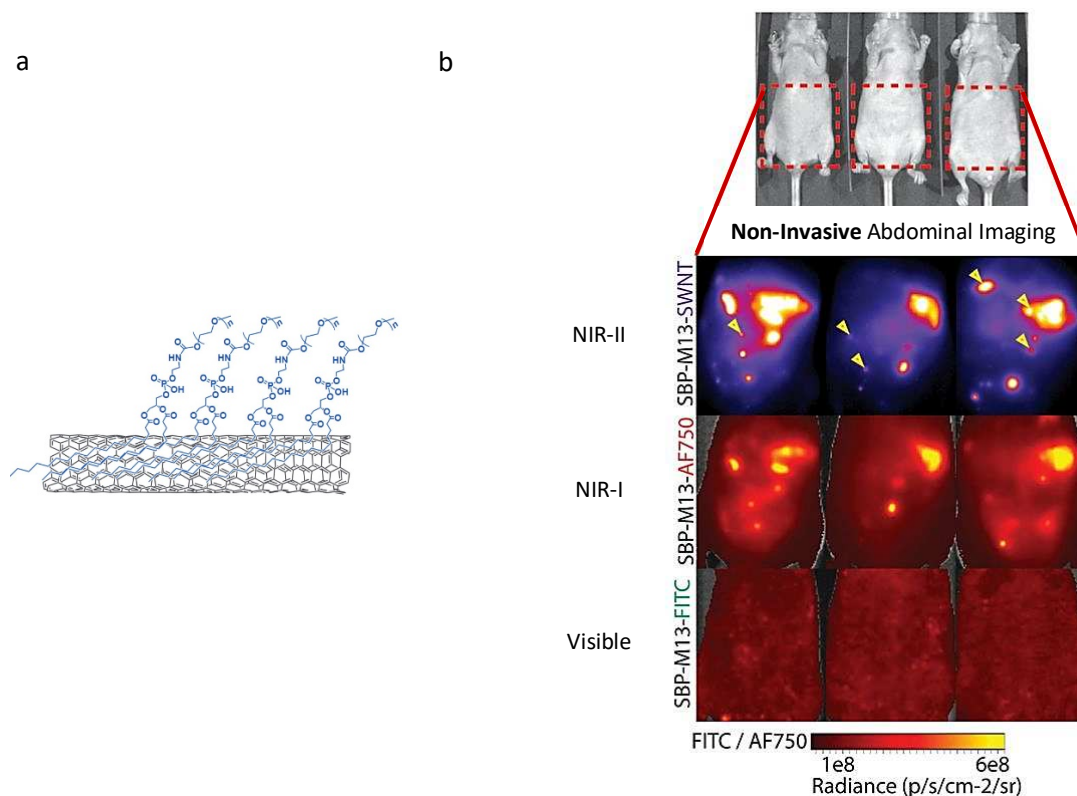
The development of fluorophores with NIR-II emission, high quantum yield - number of emitted photons relative to the number of absorbed ones-, biocompatibility, and solubility in aqueous/biological fluids, is a requisite for *in vivo* NIR-II tumor bioimaging. Several inorganic and organic NIR-II fluorophores have been developed and assessed for their tumor-targeting capacity within preclinical animal models. A representative example of each fluorophore class is discussed below.

### 3.6.2.1 In-organic NIR-II fluorophores

#### 3.6.2.1.1 Single-walled carbon nanotubes (SWCNTs)

SWCNTs possess significant fluorescent properties due to a phenomenon called the van Hove transition across bandgaps [92]. When SWCNTs are excited in the NIR-I window, they fluoresce in the NIR-II window. Considering their hydrophobic character, SWCNTs require coating with biocompatible and water-soluble polymers for *in vivo* application [88] (Figure 36a). Carbon-nanotubes contrast agents have been used for several bioimaging applications including specific tumor imaging.

A targeted form of SWCNTs, published by Ghosh et al., is discussed here [93]. M13 bacteriophage stabilized SWCNT targeting SPARC (secreted protein, acidic and rich in cysteines) expressing tumors were developed and administered intraperitoneally to mice bearing orthotopic human ovarian cancer. This probe was able to selectively target and visualize infiltrating tumor nodules, that were not detected with visible and NIR-I dyes of the same complex (Figure 36b). Using NIR-II imaging to guide tumor resection, led to the identification of submillimeter tumors (<1 mm) that were not recognized by surgery without guidance (Figure 36d,e). Altogether these findings demonstrated the potential of M13-SWCNT for non-invasive NIR-II tumor imaging and image-guided surgery. However, the main limitation of SWCNTs remains their low fluorescence quantum yields (<1%) [94].



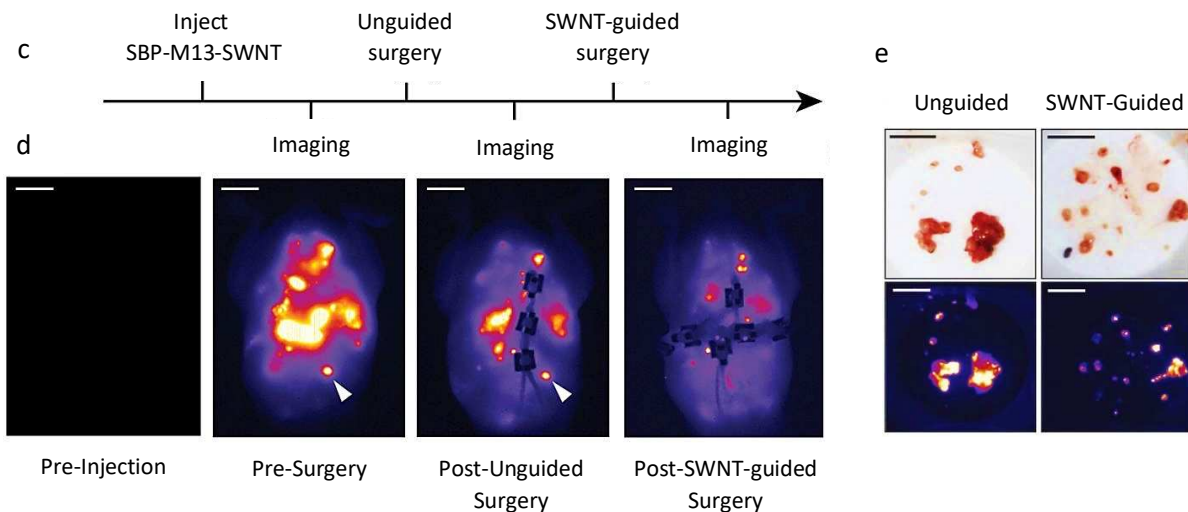


Figure 36: (a) Structure of SWCNTs functionalized with phospholipid-PEG for enhanced water-solubility and biocompatibility. (b) Non-invasive fluorescence imaging of ovarian tumors using M13-conjugated to SWCNTs (NIR-II), AlexaFluor750 (NIR-I), or FITC (visible) fluorophores. Arrows heads indicate tumor nodules that were only detected by M13-SWNTs (NIR-II). (c) Schematic view of the surgical procedure. (d) Whole abdomen NIR-II fluorescence imaging before M13-SWNT injection, before surgery, after un-guided surgery, and after subsequent M13-SWNT-guided surgery. (e) Photographs and NIR-II fluorescence images of excised tumor nodules, following un-guided and M13-SWNT-guided surgery [93].

### 3.6.2.1.2 Quantum dots (QDs)

Metal chalcogenide QDs such as  $\text{Ag}_2\text{S}$ ,  $\text{Ag}_2\text{Se}$ , and  $\text{PbS}$ , present a class of brightly fluorescent NIR-II fluorophores, with significantly high quantum yields as compared to SWCNTs [95]. Similar to carbon nanotubes, polymer coating is required for biological compatibility.  $\text{Ag}_2\text{S}$  QDs have been widely investigated due to their low toxicity compared to other QDs, high fluorescence quantum efficiency, and stability [94].

An  $\text{Ag}_2\text{S}$  QD functionalized with six-armed polyethylene glycol (PEG) was synthesized [96] (Figure 37A). It possessed fluorescence emission at 1200 nm, with an important fluorescence quantum efficiency of 15.5%, obtained following its excitation with an 808 nm diode laser. Intravenous injection of 6PEG- $\text{Ag}_2\text{S}$  QDs into mice bearing subcutaneous 4T1 breast tumors, led to a significant tumor accumulation of 10% of the injected dose, through the EPR effect. Tumor fluorescence signal increased from 30 min to 24h post-administration whereas other organs signal declined (Figure 37B). 6PEG- $\text{Ag}_2\text{S}$  QDs' high tumor uptake and long circulation time demonstrated its importance, yet genotoxicity and reproductive toxicity studies are required. A further enhanced tumor uptake ( $31 \pm 2$  % of ID/g of tumor) was reported using  $\text{Ag}_2\text{Te}$  QDs, assembled with poly(lactic-co-glycolic acid) and coated within 4T1 tumor cell-membrane derived vesicles [97]. In addition to  $\text{Ag}_2\text{Te}$  QDs bright and stable NIR-II fluorescence, coating with 4T1 tumor cell-membrane derived vesicles, provided good biocompatibility and homotypic tumor-targeting ability *in vivo*. However, accumulation in the reticuloendothelial organs (liver and spleen) was the main drawback of both QDs systems.

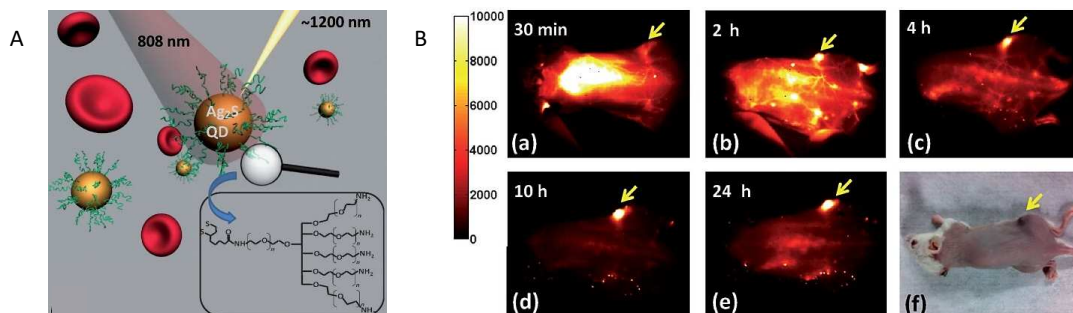


Figure 37: (A) NIR-II fluorescence-emitting  $\text{Ag}_2\text{S}$  QDs functionalized with six-armed PEG to render it water-soluble and biocompatible. Inset: chemical structure of the six-armed PEG. (B) NIR-II fluorescence images of 4T1 tumor-bearing mouse, 30 min (a), 2 h (b), 4 h (c), 10 h (d), and 24 h (e) post-injection of 6PEG- $\text{Ag}_2\text{S}$  QDs. Optical/white light image of the corresponding mouse is presented in (f). 4T1 tumor is indicated by yellow arrows [96].

### 3.6.2.1.3 Rare-earth doped NIR-II nanoparticles

Rare-earth (RE) doped nanoparticles provide another class of NIR-II fluorophores with exceptional emission, tunable according to the RE metal ion used [98] (Figure 38). Down-converting nanoparticles (DCNPs) tend to fluoresce in the NIR-II spectrum following NIR-I light excitation [94]. They are commonly made up of a RE ion-doped to an inorganic crystalline lattice (e.g.,  $\text{NaYF}_4$ ,  $\text{NaLuF}_4$ , and  $\text{CaF}_2$ ) [99]. Multi-shell core-shell RE nanoparticles have been also developed [94]. Similar to other NIR-II fluorophore classes, RE doped nanoparticles possess high photostability and require surface modification for *in vivo* application.

A targeted NIR-II emitting DCNP was developed from a luminescent  $\text{NaGdF}_4$ : 5% Nd core coated with an inert  $\text{NaGdF}_4$  shell [100] (Figure 39). This latter was functionalized with PEG and complementary DNA (L1 or L2), for *in vivo* nanoparticles assembly. Folic-stimulating hormone ( $\text{FSH}_\beta$ ) peptide was further anchored to the nanoparticles to favor ovarian cancer targeting. Sequential administration of DCNPs-L1- $\text{FSH}_\beta$  and DCNPs-L2- $\text{FSH}_\beta$  to a mice model of human ovarian adenocarcinoma peritoneal metastases, allowed accurate identification of large and small metastatic lesions, with a high tumor-to-normal tissue ratio  $\sim 11$ , surpassing that of the NIR-I ICG probe  $\sim 5$  and NIR-II carbon nanotubes  $\sim 6$ . In addition, prolonged tumor retention of 6h, provided an optimal surgical time window to precisely resect eye invisible metastasis  $< 1\text{mm}$ . These findings demonstrated the benefits of DCNPs-L1/2- $\text{FSH}_\beta$ , a targeted RE doped nanoparticles, for intraoperative NIR-II fluorescence-guided ovarian metastasis resection.

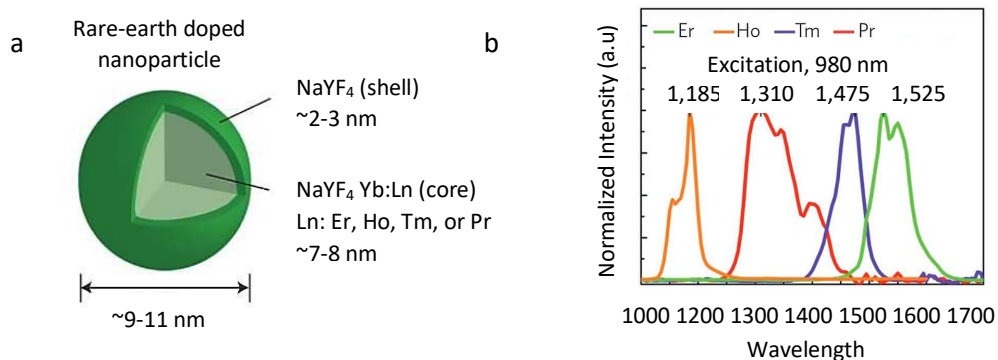


Figure 38: (a) Structure of a NIR-II emitting rare-earth-doped nanoparticle. Different rare-earth ions: Er, Ho, Tm, Pr can be doped in its core. (b) NIR-II fluorescence emission spectra of rare-earth-doped nanoparticles, showing different emissions with different doped rare-earth ions [98].

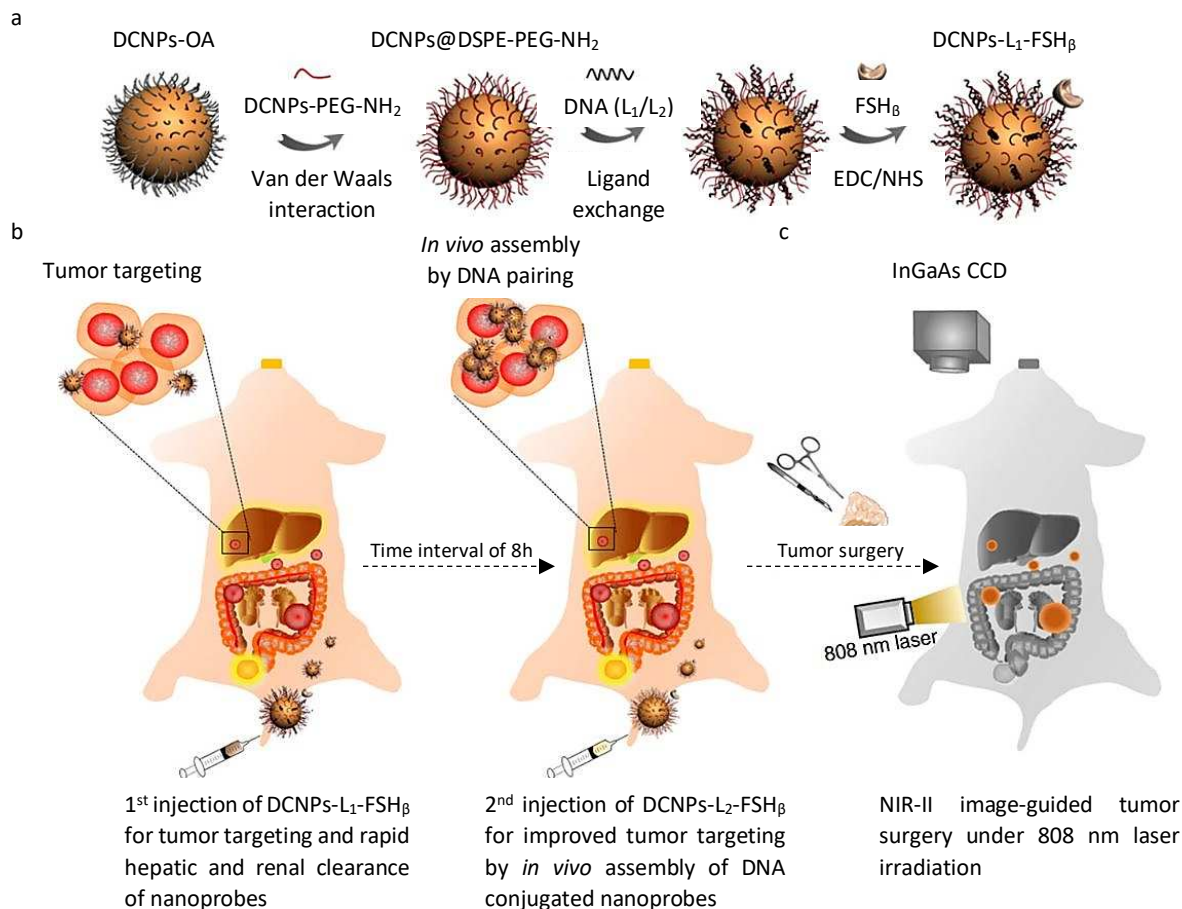


Figure 39: Schematic illustration of NIR-II nanoprobe fabrication for ovarian metastasis surgery, under NIR-II bioimaging guidance. (a) Schematic illustration of the step-wise fabrication of DNA and FSH $\beta$  modified DCNPs (DCNPs-L1-FSH $\beta$ ). (b) *In vivo* assembly of DCNPs-L1-FSH $\beta$  (first injection) and DCNPs-L2-FSH $\beta$  (second injection) results in improved tumor targeting and rapid hepatic and renal clearance. (c) Metastatic ovarian tumors can be clearly observed and precisely removed using NIR-II image-guided surgery [100].

To conclude, inorganic NIR-II fluorophores comprise the majority of NIR-II fluorophores due to their intrinsic NIR-II emission. Their excellent optical properties have offered deeper-tissue imaging, and further precise tumor delineation as compared to NIR-I imaging, in pre-clinical animal models [89, 93]. However, their slow excretion kinetics, long retention within reticuloendothelial systems, and concerns of long-term toxicity have currently hindered their clinical translation [101, 102], in addition to the low quantum yields and emission intensities of SWCNTs and RE-doped nanoparticles respectively [94, 103]. Thus, the development of organic NIR-II fluorophores, with improved pharmacokinetics, lower toxicities, and enhanced optical properties have then emerged.

### 3.6.2.2 Organic fluorophores

#### 3.6.2.2.1 Donor-acceptor-donor (DAD) systems

They consist of strong electron-donating groups connected through  $\pi$ -bridging to a central strong electron accepting group. This configuration serves to shrink the energy gap between the molecular orbital levels, thus shifting the fluorescence towards the NIR-II spectrum [67].

CH1055-PEG, a DAD compound emitting at 1055 nm, was functionalized with PEG for enhanced water solubility [104] (Figure 40a). A fast-renal excretion (90% of injected dose) was achieved within 24h. CH1055-PEG presented a passive tumor accumulation and was able to unambiguously label orthotopic glioblastoma tumors present 4 mm below intact skull (Figure 40b).

In addition, coupling CH1055-PEG to an anti-epidermal growth factor receptor (EGFR) affibody, allowed specific targeting of human squamous cell carcinoma xenografts in mice (Figure 40d,e). A tumor-to-normal tissue ratio of  $\sim 15$  was attained six hours post-injection, permitting an accurate image-guided tumor resection in mice. This achieved ratio was five times higher than those obtained by NIR-I fluorophores-affibody complexes. Although CH1055-PEG combines all the requisites for an ideal NIR-II emitting fluorophore (water solubility, biocompatibility, tumor targeting), its low quantum yield (0.3%) requires improvement. Tuning the structure of DAD compound (electron-donating/accepting groups) is required to enhance the quantum yield and red-shift the emission towards the deep NIR-II window.

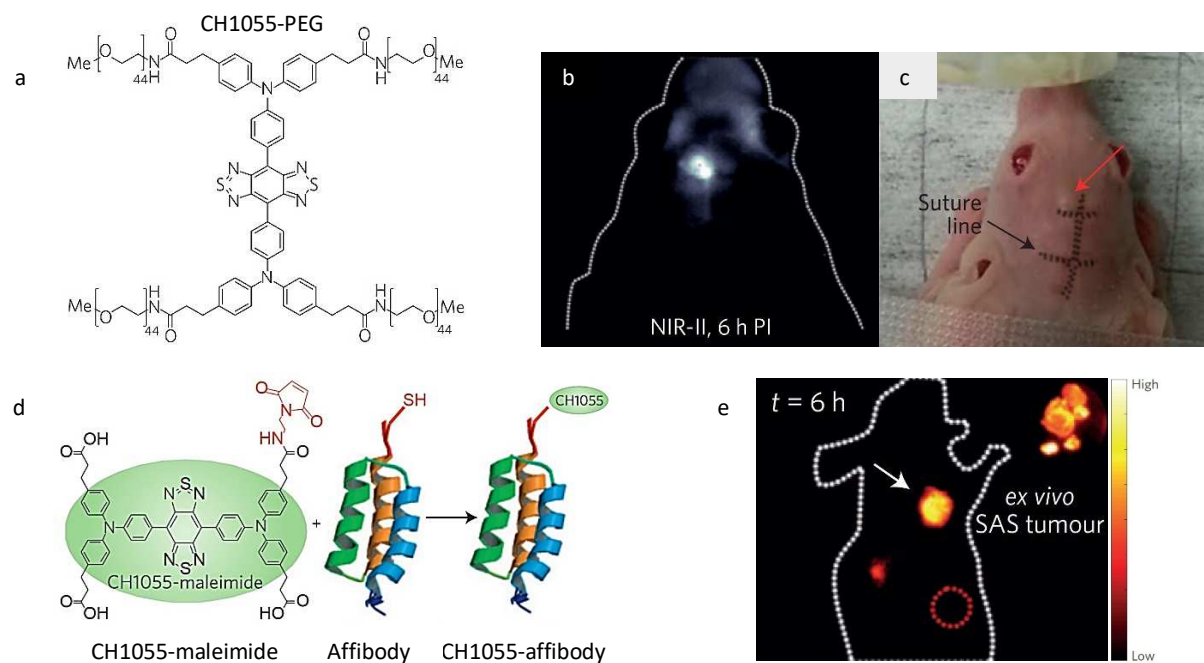


Figure 40: (a) Chemical structure of the NIR-II emitting DAD system, PEGylated CH1055. (b) NIR-II fluorescence image showing strong fluorescence of orthotopic glioblastoma brain tumor, localized 4 mm deep under the skull, 6h post CH1055-PEG administration. (c) The corresponding colored photograph of the nude mouse head, with the suture line and tumor position indicated by black and red arrows respectively. (d) A schematic illustration of CH-1055-affibody synthesis. (e) NIR-II fluorescence image of a mouse bearing squamous cell carcinoma (SAS) xenograft, 6h following CH-1055-anti-EGFR-affibody administration. The white arrow and the dotted red circle indicate the SAS tumor and normal tissue, respectively. The inset displays an ex vivo SAS tumor following its excision [104].

### 3.6.2.2.2 Polymethine/Cyanine dyes

Tuning the chemical composition and the length of conjugated structures in polymethine dyes, permit their NIR-II emission. Commercially available NIR-II polymethine dyes include IR-26, IR-1061, and IR-1048 [105]. These dyes have low water solubility requiring encapsulation within hydrophilic matrices [94].

An activable NIR-II emitting polymethine dye is discussed here. Coupling IR-1048 to a nitroimidazole group (2-(2-nitroimidazolyl) ethylamine) MZ results in IR-1048 fluorescence quenching and solubility/ biocompatibility enhancement (Figure 41a). When MZ is reduced by nitroreductase enzyme (NTR), overexpressed in hypoxic environments, IR-1048 NIR-II fluorescence is restored (Figure 41a). Following IR-1048-Mz intravenous injection into mice bearing subcutaneous A549 hypoxic tumors, that overexpress NTR, IR-1048-Mz permitted tumor-selective identification with a high tumor-to-background ratio of  $\sim 30$  (Figure 41b). This significant ratio was 3.8 times higher than the ratio achieved by the NIR-I NTR-sensitive probe. Yet, the low quantum yield (0.6%) was the main limitation [106], similar to DAD systems.

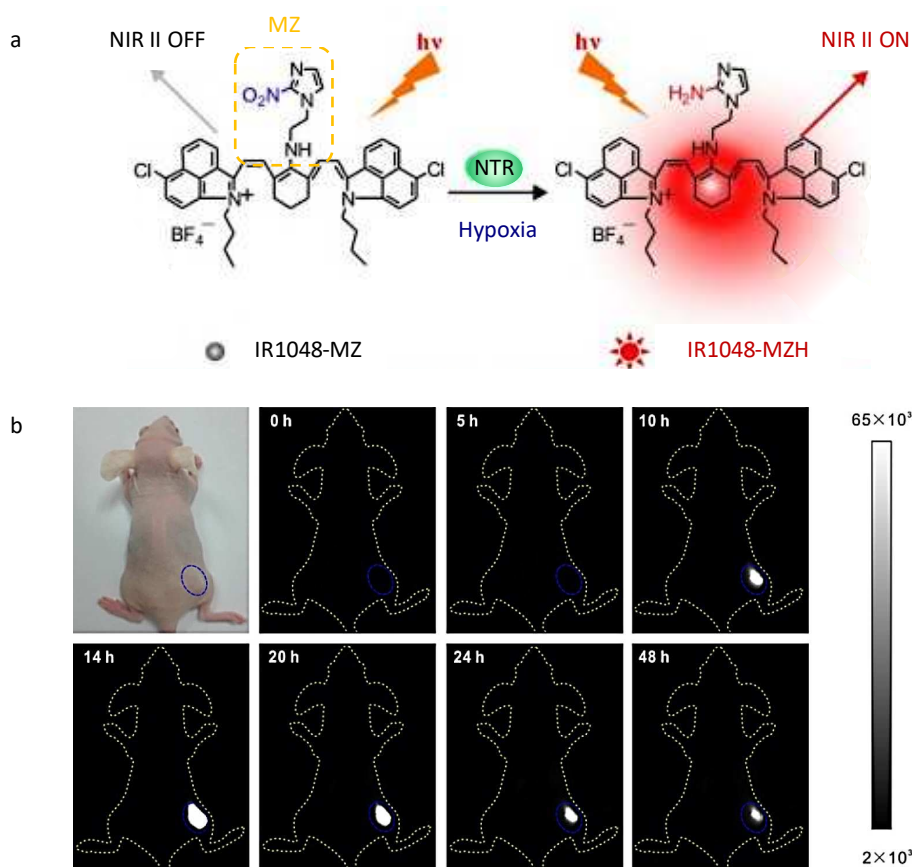


Figure 41: (a) Schematic illustration of the NTR-responsive NIR-II fluorescent probe: IR1048-MZ. In the presence of NTR, the MZ group is reduced enabling the restoration of the IR-1048 NIR-II fluorescence. Adapted from [106]. (b) NIR-II fluorescence imaging of a mouse bearing subcutaneous A549 tumor, before and after intravenous injection of IR-1048-Mz. Images were acquired at several time points (0, 5, 10, 14, 20, 24, and 48 h) post-injection. The tumor is indicated with a dotted blue circle. A colored photograph of the imaged mouse is presented in the first left panel [106].

Another attempt was to use the NIR-II emission tail of NIR-I fluorophores. In 2017, the ICG NIR-II fluorescence emission tail was characterized. ICG NIR-II imaging provided images with better resolution, more details, and twice enhancement in contrast-to-noise ratios as compared to the NIR-I region, in mice [107] (Figure 42A). In addition, coupling ICG to an anti-vascular endothelial growth factor (VEGF) antibody Bevacizumab (Bev) (Figure 42B), permitted a real-time identification of colorectal tumors in an orthotopic colorectal cancer rat model, using a NIR-II endoscopy system [108] (Figure 42C). Considering the ICG FDA approval, clinical translation of NIR-II imaging can be accelerated. However, this doesn't eliminate the need to develop efficient NIR-II organic dyes with elevated quantum yields to overcome ICG pitfalls (low efficiency of photon utilization in the NIR-II window, low photostability, and fast clearance) [109].

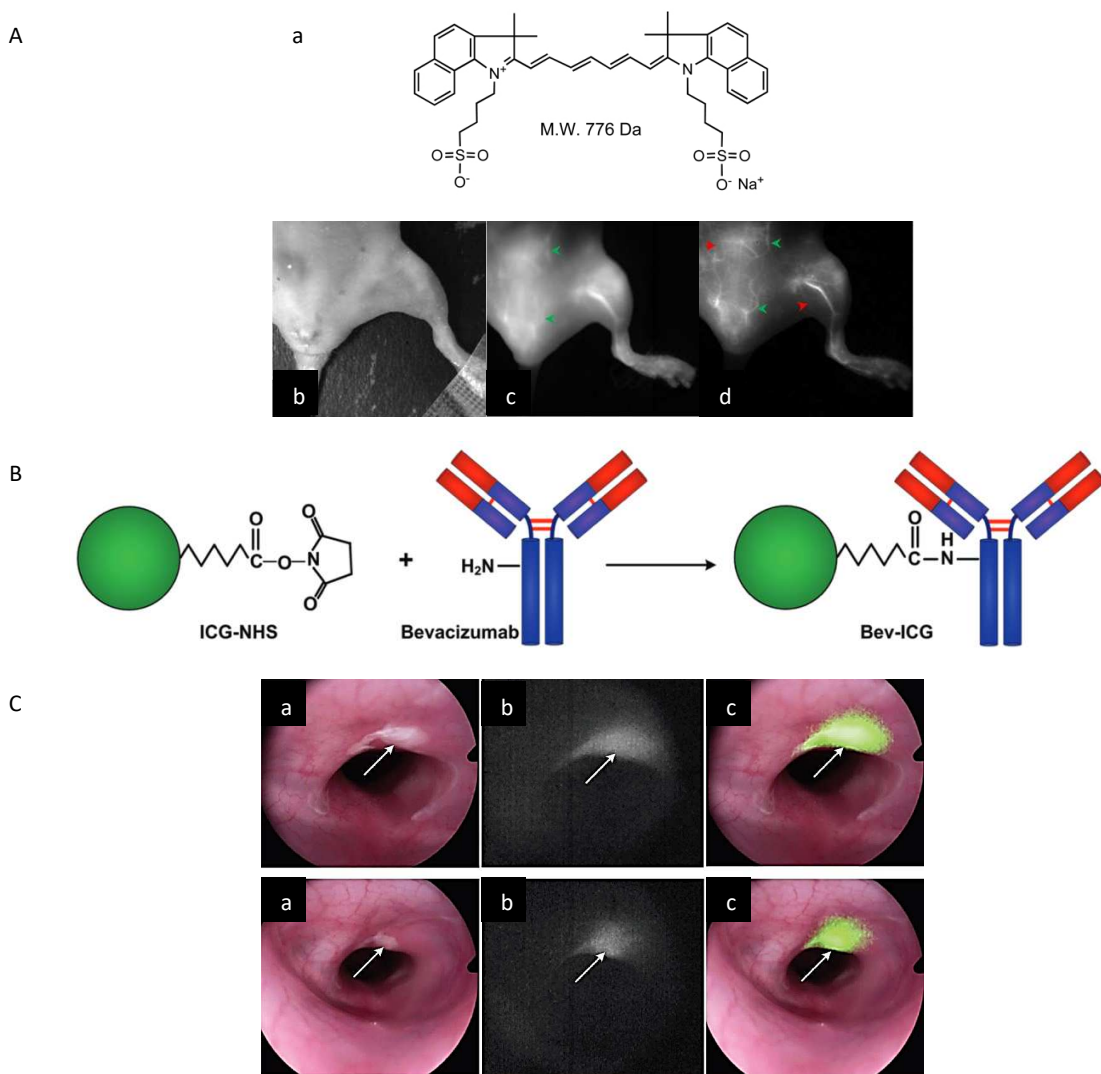


Figure 42: (A) (a) Chemical structure of ICG. Visible (b), NIR-I (c), and NIR-II (d) fluorescence imaging of a mouse hind limb following ICG intravenous administration [107]. (B) Schematic illustration of Bevacizumab-ICG (Bev-ICG) synthesis through the conjugation of ICG-NHS to Bevacizumab. (C) White light (a), fluorescence (b), and white light-fluorescence overlaid images (c) of representative colorectal tumors of a rat model, obtained using a NIR-II endoscope system. Bev-ICG fluorescent signal accurately stains the tumors [108].

At present, most of the NIR-II organic dyes possess poor water solubilities and low quantum yields. A careful design of NIR-II dyes is required. It is worth noting that modifying the molecule's functionalized groups or space configuration would greatly affect its solubility, biocompatibility, and fluorescence properties.

### 3.7 Conclusion

NIR-I fluorescence imaging, especially NIR-I fluorescence image-guided surgery, has been rapidly progressing towards clinical implementation, due to the improved cancer surgery outcomes, decreased time of anesthesia, and reduced health care costs [110]. On the other hand, NIR-II fluorescence imaging, still in its infancy stage, was able to prove its superior benefits over NIR-I imaging, in preclinical animal models [89, 93]. Yet, its clinical assessment requires further development in the NIR-II detector systems, particularly for clinical use, and NIR-II fluorophores. The integration of InGaAs cameras within existing imaging navigation platforms will grant NIR-II imaging within surgical practice [105]. Regarding NIR-II fluorophores, until now there is no ideal NIR-II fluorophore. Existing NIR-II dyes, inorganic and organic ones, suffer from toxicity and low quantum yields respectively [94]. Hence, a careful design of biocompatible NIR-II emitting dyes, with enhanced quantum yields and fast clearance, is required for NIR-II fluorescence imaging advancement. Organic dyes, possessing promising translational potential and safety as compared to their inorganic counterparts, present a suitable platform for NIR-II fluorophores synthesis [109].

Developing such optimal NIR-II fluorophores for NIR-II tumor imaging *in vivo* will be addressed in articles 1, 2, and 3 of the thesis work section.

## 4 Cancer Therapy

Following tumor diagnosis, a specific therapeutic modality or modalities will be selected and applied, depending on the diagnosed tumor type and stage (local or metastasized), and the patient health status.

Conventional cancer therapies include surgery, chemotherapy, and radiotherapy. As surgery can fail in recognizing microscopic tumors [111], it is often accompanied by chemotherapy or radiotherapy.

Traditional chemotherapy acts non-specifically on rapidly-proliferating cells, both tumor cells and fast-dividing healthy cells, such as hair follicles and gastrointestinal tract cells, inhibiting their cell division and leading to systemic toxicities [112]. To address these side effects, targeted anti-cancer agents have been developed, acting precisely on tumor cells [37].

Radiotherapy, being highly cost-effective (requiring less than 10% of cancer total budget) [113], accounting for 50% of cancer patients treatment plans and contributing to 40% of the curative effect [114], makes it an important cancer treatment modality, especially with the continuous technological advances that led to optimal dose delivery to tumors without exceeding the tolerance dose of healthy tissues.

To selectively irradiate tumor cells while sparing normal ones, an innovative developing form of radiotherapy, called Boron Neutron Capture Therapy (BNCT) was described. BNCT principle, history, its two major requirements *i.e.* suitable boron compounds and neutron irradiation sources, in addition to clinical evidence of success, will be discussed in the following section. BNCT's main limitations and possible solutions for daily clinical implantation will be also addressed.

### 4.1 BNCT: Principle

Boron Neutron Capture Therapy or “BNCT” is a targeted form of radiotherapy. It is based on the high propensity of the non-radioactive  $^{10}\text{B}$  nuclide to capture thermal neutrons, leading to the release of high linear energy transfer particles:  $\alpha$  particle ( $\approx 150 \text{ keV} \cdot \mu\text{m}^{-1}$ ) and  $^7\text{Li}$  ion ( $\approx 175 \text{ keV} \cdot \mu\text{m}^{-1}$ ) (Figure 43a). These highly energetic particles, having a short path length of 5-9  $\mu\text{m}$ , tend to deposit their energy, and induce destructive effects within a confined diameter, presenting the size of a single cell. By extrapolating this notion into biological tissues, cells possessing  $^{10}\text{B}$  atoms will be destroyed in the presence of neutrons, while neighboring cells having no  $^{10}\text{B}$  will stay safe [115] (Figure 43b).

Thus, the BNCT tumor-targeted therapeutic efficacy depends both on the sufficient and selective  $^{10}\text{B}$  accumulation in tumor tissues (35-50  $\mu\text{g}$  of  $^{10}\text{B}/\text{g}$  of tumor or  $\sim 10^9$   $^{10}\text{B}$  atoms per cell), and the presence of adequate amounts of low energy thermal neutrons (fluence of  $10^{12}$ - $10^{13}$   $\text{n} \cdot \text{cm}^{-2}$ ) [115]. The co-existence of these two components is essential for triggering the neutron capture reaction and provoking specific damages in the infiltrating tumor cells. The absence of one component will hinder the BNCT curative effect.

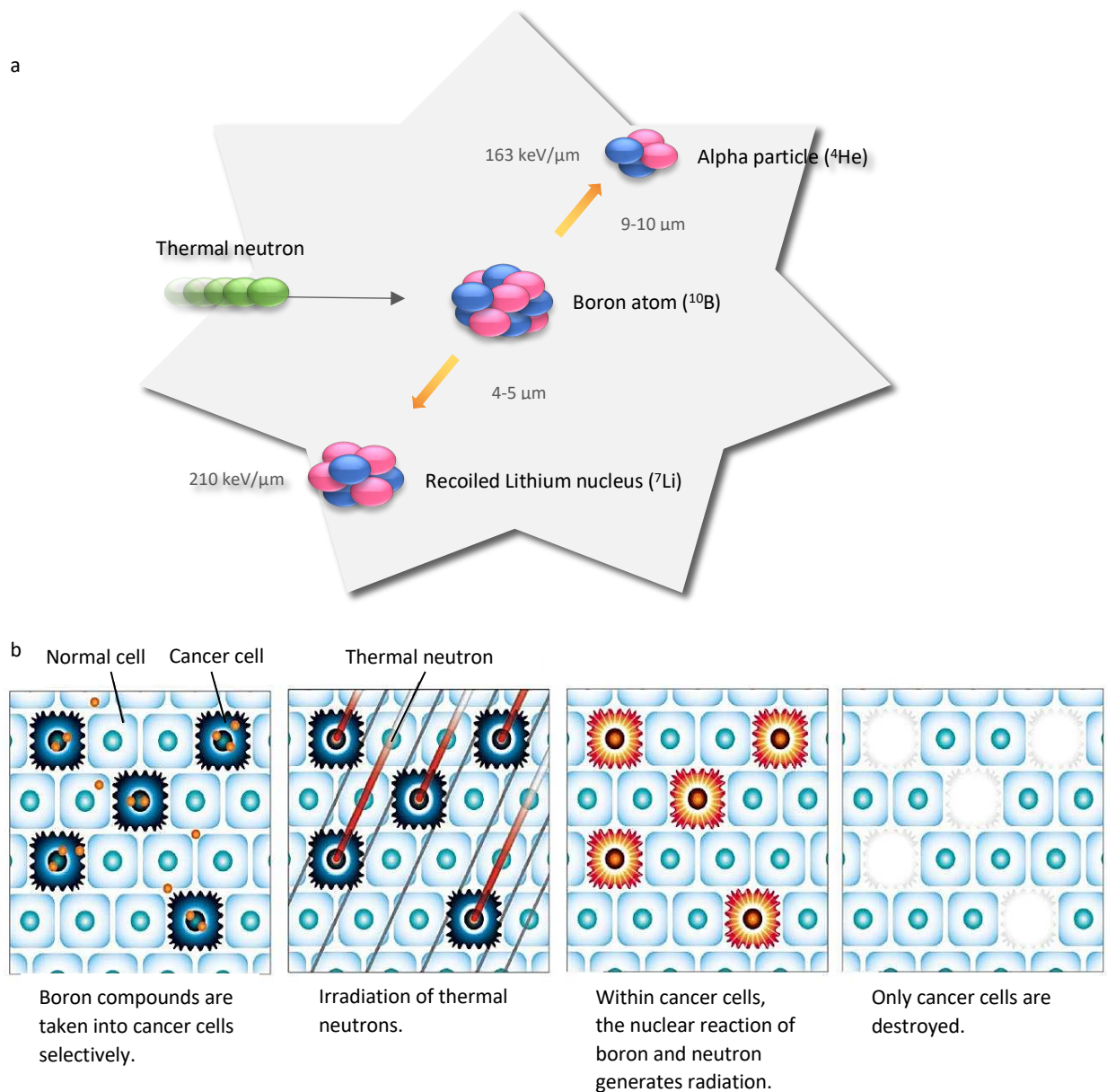


Figure 43: Scheme presenting the boron neutron capture reaction (a). (b) The detailed mechanism of BNCT selective tumor destruction [116].

## 4.2 BNCT: History

Four years following the neutron discovery in 1932, LOCHER was the first to describe the use of neutron capture reaction for cancer treatment [117]. Nonetheless, the first BNCT trial was performed in 1951. Until 1961, several glioma patients were treated at the Brookhaven Graphite Research Reactor and Massachusetts Institute of Technology reactor, using inorganic boron compounds and disodium decahydrodecaborate ( $\text{Na}_2\text{B}_{10}\text{H}_{10}$ ) respectively. The adverse side effects (untreatable radiodermatoses of the scalp, deep ulcerations, and appearance of brain necrosis) and the unsatisfactory survival times, led to the suppression of BNCT activities in the USA [118].

Clinical BNCT was then reevaluated (in 1968) thanks to the effort of Hatanaka who reported a 50% 5-year survival in grade 3 and 4 glioma patients, following their administration with a new boron compound called sodium borocaptate. Interesting data were also obtained by Mishima (1987) who treated superficial melanomas using a novel compound named Boronophenylalanine. These favorable reports drove the re-emergence of BNCT worldwide in the 1990s [119].

## 4.3 BNCT: Boron compounds

The first essential component of the binary therapy (BNCT), is the boron source. An ideal BNCT boron delivery agent should meet the following requirements: low toxicity, sufficient tumor uptake (35-50  $\mu\text{g}$  of  $^{10}\text{B}/\text{g}$  of tumor or  $\sim 10^9$   $^{10}\text{B}$  atoms per cell) [115], selective tumor accumulation, with a tumor to normal tissue and tumor to blood ratios  $>3$ , along with rapid clearance from normal tissues and tumor persistence during the neutron irradiation time [120].

### 4.3.1 Clinically available boron compounds

60 years ago, two boron-containing compounds were developed: Sodium borocaptate (BSH) [121, 122] and Boronophenylalanine (BPA) [123] (Figure 44). These two  $^{10}\text{B}$  sources have been and are still the only compounds used for clinical BNCT.

BPA or Boronophenylalanine or (L)-4-dihydroxy-borylphenylalanine, is a single-boron-containing amino acid (Figure 44). Being an analog for the melanin precursor “tyrosine”, BPA was first used for BNCT treatment of high melanin-synthesizing tumors like melanoma [124]. However, experimental data evidenced its selective delivery to other tumor types [125], through aromatic amino acid transporters; especially the L type [126-128]. A more soluble form of BPA, complexed with fructose (BPA-F) [129], has then entered clinical use to treat high-grade gliomas and recurrent head and neck tumors, providing significant therapeutic potential.

BSH or Sodium borocaptate or sodium mercaptoundecahydro-*clos*o-dodecaborate ( $\text{Na}_2\text{B}_{12}\text{H}_{11}\text{SH}$ ), is an icosahedron (polyhedron with 20 faces) borane anion possessing 12 boron atoms (Figure 44). Initially, BSH was used to treat high-grade glioma patients, with beneficial results. It was suggested to diffuse passively into tumor cells where the blood-brain barrier was damaged [130].

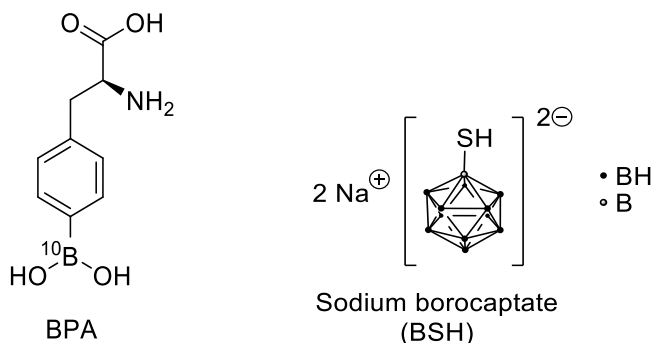


Figure 44: Structure of the two clinically used BNCT compounds: BPA and BSH

#### 4.3.1.1 Clinically available boron compounds: Limitations

Regardless of the favorable clinical data, both BPA and BSH possess several limitations. BPA accumulates hugely in tumors however measurable quantities were also observed in healthy tissues, leading to a low tumor to normal tissue ratio [131]. In addition, its ability to target actively dividing tumor cells [132] and cells overexpressing aromatic amino acid transporters, while avoiding quiescent ones [133], provides a clear explanation of its heterogeneous boron distribution between tumor regions and tumors of different patients [134]. On the other hand, BSH, even if it has a high tumor to normal tissue ratio (due to its low normal tissue uptake), tumor accumulation isn't always sufficient for an efficient BNCT [131]. Similarly, intratumoral and inter-tumor variabilities in boron distribution were observed following BSH administration [135].

#### 4.3.1.2 Clinically available boron compounds: possible solutions

To address the issues of BPA and BSH, the co-administration of both compounds was used to compensate for each other's faults [136]. An improved therapeutic outcome was elicited as compared to BPA or BSH alone [131, 137]. In addition, optimizing the dosing paradigm was beneficial, for example, a prolonged BPA infusion with higher doses increased the survival of glioma patients [138].

### 4.3.2 Theranostic boron compounds

The inability to quantify real  $^{10}\text{B}$  concentrations accumulating within tissues (cancerous and healthy ones), which is hugely variable between individuals, makes it difficult to estimate the required neutron radiation dose and the potential anti-tumor effect. In this context, the development of boron-containing compounds delivering an adequate amount of  $^{10}\text{B}$  atoms, and possessing imaging properties that allow their tracking and quantification, could optimize the treatment plan, leading to better efficacy. In other words, a theranostic compound, combining both therapy and diagnosis (through imaging) [139] is required for a more efficient, personalized BNCT.

#### 4.3.2.1 Clinical example: $^{18}\text{F}$ -BPA

$^{18}\text{F}$ -BPA or 4-borono-2- $^{18}\text{F}$ fluoro-D,L-phenylalanine (Figure 45) could be considered as the only theranostic compound used in clinical BNCT. The direct fluorination of BPA led to the development of  $^{18}\text{F}$ -BPA [140], a radiolabeled form of BPA that can be detected by PET imaging. The pharmacokinetics of  $^{18}\text{F}$ -BPA was assessed in glioma patients using a three-compartment model (*i.e.* with three rate constants). A correlation between the malignancy stage and the  $^{18}\text{F}$ -BPA tumor uptake was demonstrated [141], and a quantitative method for tumor  $^{10}\text{B}$  levels determination was established based on PET Imaging [142]. It provided an important tool for selecting BNCT patients and estimating the BPA dose required for therapy. Another quantitative method based on both PET data and plasma  $^{10}\text{B}$  concentrations, obtained from blood samples, was then described [143]. It allowed through a four-rate constant model to estimate more accurately the tumor  $^{10}\text{B}$  concentrations.

Using these two methods, a consistency between the estimated tumor  $^{10}\text{B}$  levels and those measured within the surgical specimens was observed.  $^{18}\text{F}$ -BPA PET imaging was then used to screen other tumor types and grades like malignant melanomas [144], head and neck malignancies [145], recurrent cancer of the oral cavity and cervical lymph node metastases [146], and recurrent malignant gliomas [147].

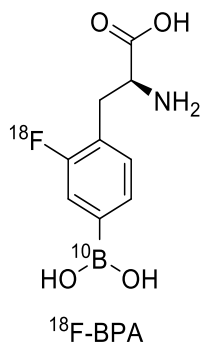


Figure 45: Structure of  $^{18}\text{F}$  radiolabeled BPA

Currently,  $^{18}\text{F}$ -BPA PET is applied in the clinical routine before BNCT. It provides information about the BPA uptake into tumors as compared to the healthy surrounding. Tumor-to-normal tissue (T/N) and tumor-to-blood (T/B) ratios obtained from PET imaging serve as a criterion to include/exclude patients for BNCT. Only patients with favorable tumor  $^{18}\text{F}$ -BPA accumulation and high  $\text{T/N} > 2.5$  will be selected, to avoid any BNCT failure due to low  $^{10}\text{B}$  tumor uptake. These PET data serve also as an input for neutron radiation treatment planning.

Although the development of  $^{18}\text{F}$ -BPA has revolutionized the BNCT treatment, it just served as a diagnostic molecule before BNCT, while BPA, a structurally distinct molecule was used for therapy.  $^{18}\text{F}$ -BPA was administrated at tracer (low) doses whereas BPA was infused in high therapeutic doses [148]. In addition, the short half-life of  $^{18}\text{F}$  (1.83 h) [149], the need for a reliable  $^{18}\text{F}$ -BPA radiosynthesis [150], and the possible detachment of boron from  $^{18}\text{F}$ -BPA (deboronation) made the estimation of boron distribution by  $^{18}\text{F}$ -BPA sometimes debatable [148]. Based on these reasons, there was always a need to synthesize a boron-containing compound that can be used both for imaging and therapy, allowing more accurate determination of  $^{10}\text{B}$  pharmacokinetics, distribution, and quantification within tissues.

#### 4.3.2.2 Preclinical examples

Accordingly, several BNCT theranostic compounds have been developed and investigated in preclinical animal models. Here, we present some examples of boron-containing amino acids, peptides, nanoparticles, micelles, and liposomes that were either radiolabeled or functionalized with contrast agents, allowing their tracking by PET, SPECT, MRI, or fluorescence imaging.

##### 4.3.2.2.1 Small boron-containing molecules:

Compared to  $^{18}\text{F}$ -BPA, a metabolically stable [ $^{18}\text{F}$ ] fluoroboronotyrosine ([ $^{18}\text{F}$ ] FBY) was synthesized with a high radiochemical yield (50%) and purity (98%) (Figure 46) [148]. The correlation between the  $^{18}\text{F}$ -FBY PET images and the boron distribution *in vivo*, in mice-bearing

subcutaneous B16-F10 melanomas, and the prolonged survival time obtained following neutron irradiation, demonstrated the potential of [ $^{18}\text{F}$ ] FBY as a theranostic agent for PET image-guided BNCT. Yet, the data were just slightly better than those of the BPA group.

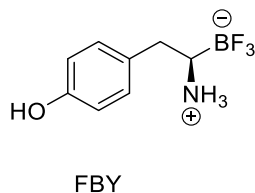


Figure 46: Structure of fluoroboronotyrosine FBY.

$^{19}\text{F}$  can replace  $^{18}\text{F}$  and can be detected by magnetic resonance imaging (MRI) or magnetic resonance spectroscopy (MRS). Several difluoro and trifluoro BPA derivatives were synthesized and assessed for  $^{19}\text{F}$  MR feasibility [151, 152] however only  $^{19}\text{F}$ -BPA was assessed *in vivo* (Figure 47).  $^{19}\text{F}$ -MRI provided a spatial mapping of  $^{19}\text{F}$ -BPA distribution within rat brains, and  $^{19}\text{F}$ -MRS provided information about  $^{19}\text{F}$ -BPA pharmacokinetics from blood samples. These findings demonstrated the utility of  $^{19}\text{F}$ -BPA for treatment planning in BNCT [153].

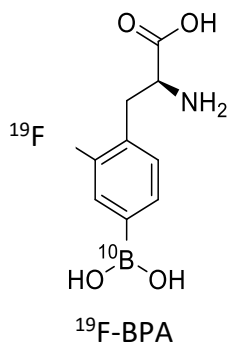


Figure 47: Structure of  $^{19}\text{F}$ -BPA.

Another BNCT theranostic agent containing 6 boron cages, for BNCT, a cyanine dye for fluorescent imaging, and an integrin ligand for tumor targeting, was reported (Figure 48) [154]. Its tumor accumulation was demonstrated *in vitro* and in mice-bearing subcutaneous WM115 melanomas. Further *in vivo* experiments are required to determine its therapeutic efficacy under neutron beam.

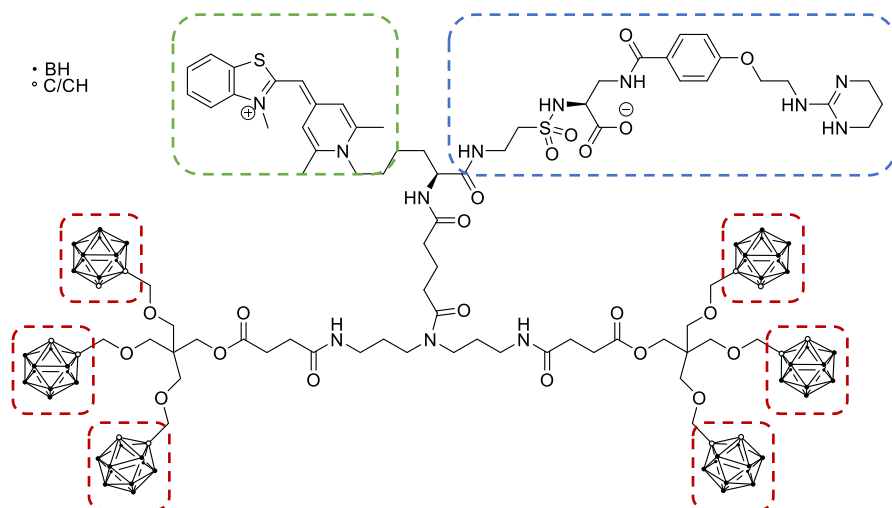


Figure 48: Structure of the dendritic wedge BNCT theranostic molecule, bearing 6 carborane cages (red boxes), a monomethine cyanine dye for fluorescent imaging (green box), and a nonpeptidic RGD - a ligand for  $\alpha_v\beta_3$  integrin - for tumor targeting (blue box) [155].

BSH fused with 3 arginine peptides (BSH-3R) was synthesized. It was able to penetrate tumor cell membranes *in vitro* and in mice bearing U87 $\Delta$ EGFR brain tumors. Coupling BSH-3R to  $^{64}\text{Cu}$ -DOTA allowed its pharmacokinetics monitoring using PET imaging (Figure 49) [156], and its high tumor accumulation demonstrated its potential for theranostic BNCT. It is worth noting that  $^{64}\text{Cu}$ -labeled BSH-3R-DOTA is the only BNCT theranostic compound based on cell-penetrating peptides (CPPs).

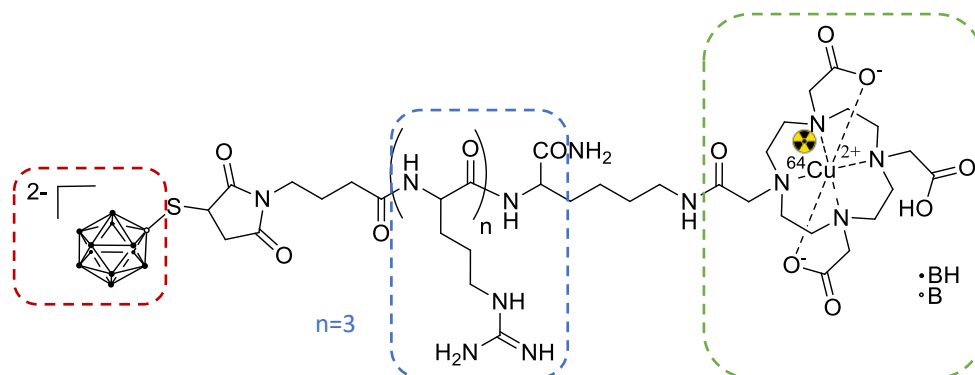


Figure 49: Structure of the BNCT theranostic cell-penetrating peptide,  $^{64}\text{Cu}$ -labeled BSH-3R-DOTA, made up of BSH (for BNCT, red box) coupled to a three arginine peptide for cell penetration (blue box) and  $^{64}\text{Cu}$ -DOTA for PET imaging (green box) [155].

#### 4.3.2.2.2 Large boron carriers:

Theranostic gold nanoparticles (AuNPs) functionalized with boron-rich anions and radiolabeled with  $^{124}\text{I}$ , were described and evaluated in a fibrosarcoma xenograft mouse model [157]. PET imaging confirmed their *in vivo* stability however their poor tumor accumulation required further size and shape adjustments.

Another theranostic AuNPs were developed and assessed in mice-bearing N87 gastric cancer xenografts [158]. They were functionalized with boron cages for BNCT therapy, anti-Her2

antibodies for tumor targeting, and radioactive iodine  $^{123}\text{I}$  for SPECT imaging (Figure 50). These nanoparticles allowed monitoring the pharmacokinetics and tumor accumulation *in vivo* and delivered sufficient  $^{10}\text{B}$  content into the tumors.

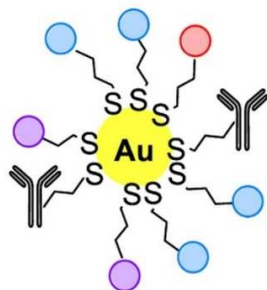


Figure 50: Schematic illustration of PEGylated (blue circles) gold nanoparticle (AuNP) functionalized with carborane cages (purple circles),  $^{123}\text{I}$  radioisotope (red circle), and anti-Her2 antibody [158].

To reduce the toxicity of free boronated porphyrins, micelles containing tetraboronated porphyrins chelated with  $^{64}\text{Cu}$  were reported for BNCT application (Figure 51) [159]. Bimodal fluorescence (through porphyrin) and PET (through  $^{64}\text{Cu}$ ) imaging demonstrated the favorable tumor accumulation in subcutaneous 4T1 breast cancer and B16-F10 melanoma bearing mice, respectively. However, due to the non-desired liver accumulation, modification of the treatment plan from a single to multiple injections of smaller doses was applied, and a reduction in tumor growth was achieved following neutron irradiation. Yet, will this treatment plan be acceptable in clinical practice? A one-day BNCT treatment is ideal, with a shorter hospital stay, lower health care cost, and higher patient satisfaction [156]. Though, some studies reported several BNCT sessions.

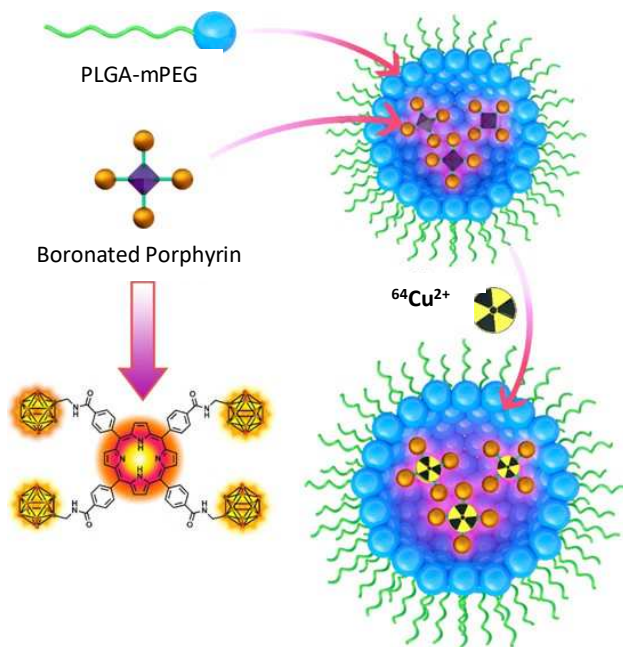


Figure 51: Schematic illustration of the  $^{64}\text{Cu}$ -tetraboronated porphyrin encapsulated within biocompatible PLGA-mPEG micelle [159].

A boron nitride nanoparticle (BNNPs) protected by phase-transitioned lysozyme (PTL) coat and radiolabeled with  $^{64}\text{Cu}$ , was developed as a theranostic BNCT agent (Figure 52) [160]. Thanks to PET imaging, a favorable tumor accumulation was observed in mice-bearing subcutaneous 4T1 breast tumors. Yet, the high liver uptake required a change in the treatment plan. The dose was administered in smaller fractions before neutron irradiation, and a delay in tumor growth was observed as compared to the controls. Following neutron irradiation, vitamin C was injected to destroy and release the remaining BNNPs, thus minimizing their side effect.

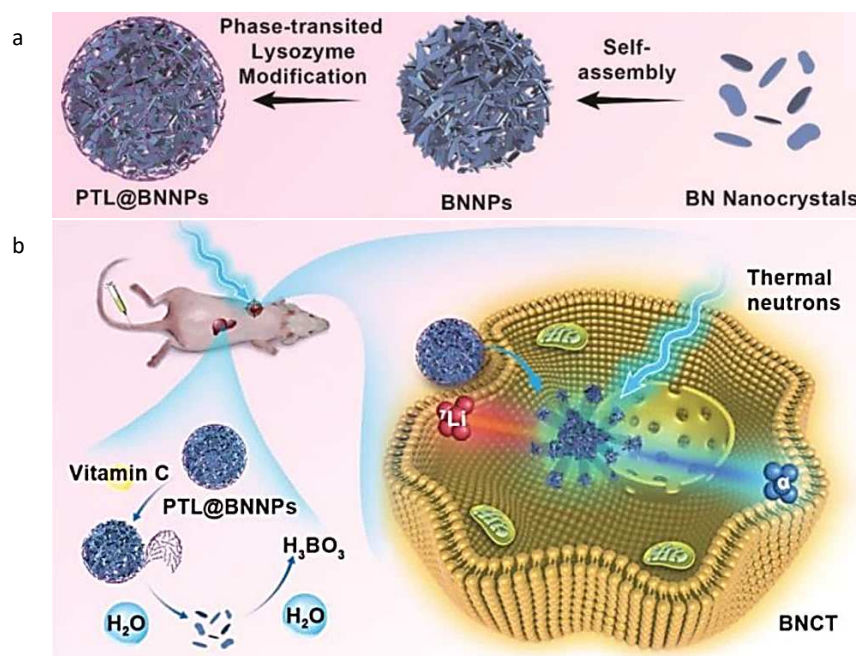


Figure 52: (a) Scheme illustrating the synthesis of boron nitride nanoparticles coated with phase-transitioned lysozyme, PTL@BNNPs. (b) Schematic illustration of the *in vivo* PTL@BNNP-based BNCT, and the on-demand vitamin C degradation of the nanoparticles [160].

Another BNCT theranostic formulation based on boron cage coupling to gadolinium, and encapsulation within low-density lipoproteins (LDLs), was reported to target tumor cells overexpressing LDL receptors (Figure 53) [161]. Thanks to T1-MRI, this formulation was monitored *in vivo*, in a lung metastases mouse model generated by intravenous injection of TUBO breast cancer cells. A reduction in lung tumor growth was observed following neutron irradiation. However, tumor re-growth was then detected, suggesting that the combination of BNCT with other therapies would be needed to avoid relapse.

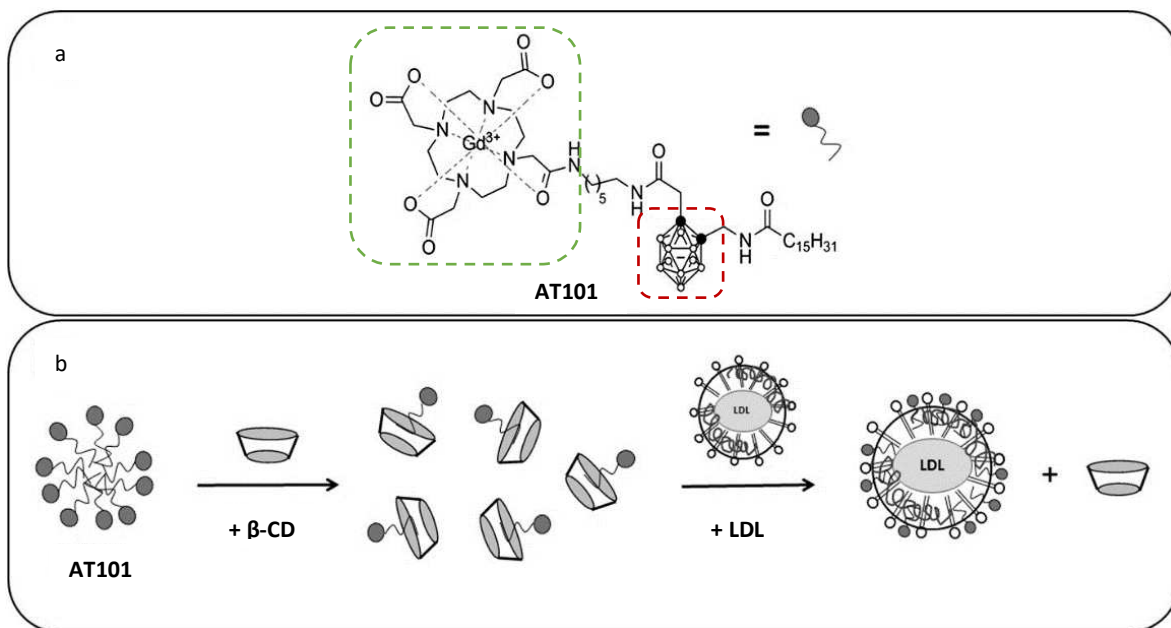


Figure 53: (a) Structure of the Gadolinium-carborane complex (green and red boxes respectively), AT101. (b) Scheme illustrating the synthesis of the Gadolinium-carborane-LDL formulation [161].

A 90 nm-sized  $^{10}\text{B}$  nanoparticle coated with silica for enhanced biocompatibility, functionalized with gadolinium for MRI imaging and FITC-labeled RGD peptide for tumor targeting, was synthesized (Figure 54) [162]. Thanks to MRI image-guided BNCT,  $^{10}\text{B}$ SGRF nanoparticles were able to selectively target brain tumors, providing them with high boron therapeutic doses, and suppressing their growth in a superior manner compared to BPA.

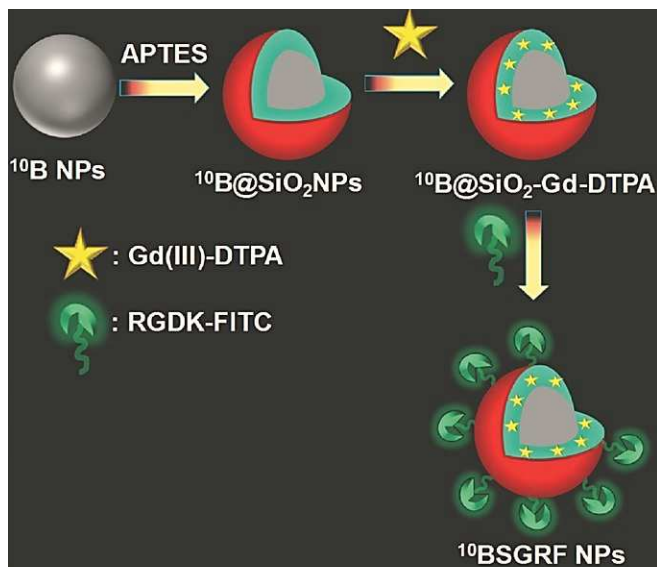


Figure 54: Schematic illustration of the three-step synthesis of  $^{10}\text{B}$ SGRF nanoparticles [162].

A next-generation theranostic compound made up of gadolinium borate and iron oxide bioconjugates was described [163]. *In vitro* experiments showed its potential for neutron capture therapy, magnetic targeted therapy, MRI, and fluorescence imaging. Yet further synthesis control and *in vivo* experiments are required to emphasize its importance.

A carborane (for BNCT) coupled to Gd complex (for MRI imaging) from one side and cholesterol unit from the other side, was synthesized (Figure 55) and assembled into liposomes. The liposomes were then functionalized with folic acid to target tumor cells overexpressing folate receptors [164]. *In vitro* liposome delivery into tumor cells was demonstrated, and the decline in surviving tumor cells following neutron irradiation confirmed its potential for dual MRI/BNCT application.

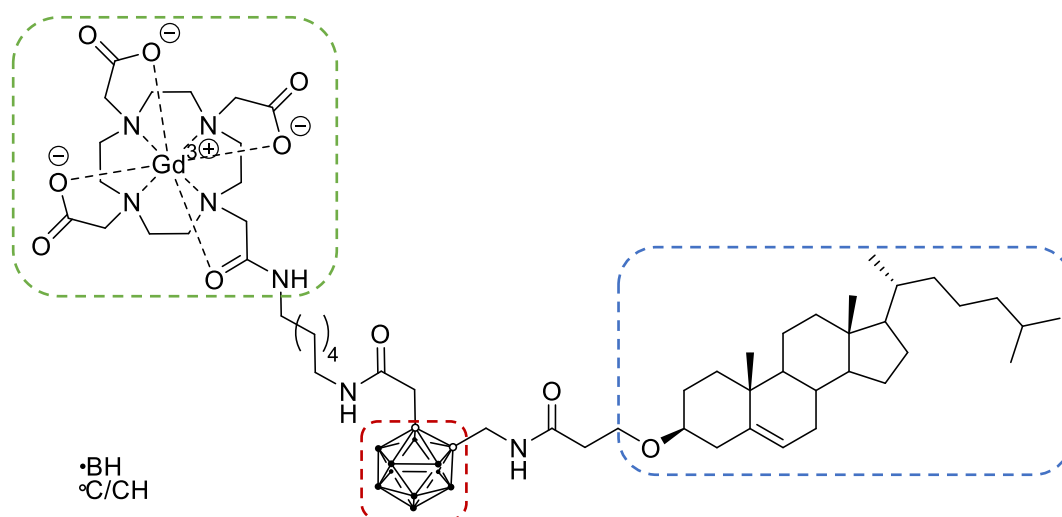


Figure 55: Structure of the  $Gd^{3+}$ -carborane-cholesterol derivative (green, red and blue boxes respectively), the precursor of the theranostic BNCT/MRI liposome [155].

Several reports described the detection of BSH and BPA even without labeling.  $^{10}B$  [165]/ $^{11}B$  [166] NMR were used to detect BSH borons, in *in vivo* tumors. However, due to the need for  $^{10}B$ / $^{11}B$ -enriched compounds and specific hardware [167] to perform the direct detection, these techniques are not used in the clinic. On the other hand,  $^1H$  NMR:  $^1H$  MRS/MRSI was reported to detect non-invasively and in real-time BPA accumulation *in vivo* [168, 169]. However, its low sensitivity and unsuitability for resected tumors, limit its use [167].

To date, none of these theranostic BNCT compounds have passed to clinical assessment, except  $^{18}F$ -BPA. Poor tumor uptake, toxicity, difficult synthesis, and the absence of impressive tumoricidal effect are the main reasons. Considering all these issues will enable the development of novel efficient theranostic boron compounds.

## 4.4 BNCT: Neutron source

The second essential component of the binary therapy (BNCT), is the neutron field. Neutrons of appropriate energies, high fluence rate ( $10^{12}$ - $10^{13}$  n.cm<sup>-2</sup>), and low contaminants are required for BNCT application. Thermal neutrons, of 0.025 eV energy, were first used. Due to their rapid attenuation in tissues, epithermal neutrons of 1-10 000 eV energy had replaced them. Epithermal neutrons have better penetration and are capable of producing thermal neutrons in deep tissues, making them suitable for deep-seated tumors [115].

Until 2012, nuclear research reactors have been the only source for neutron production. The closure of several reactors and the cease of BNCT activities in others have been a real threat to BNCT development. To address this issue, accelerator-based neutron sources (ABNS) have emerged. Different types were described, from low-energy electrostatic machines to higher energy cyclotrons and much higher energy Linacs or synchrotrons. Compared to nuclear reactors, these accelerators can be easily licensed and installed within hospitals, allowing better monitoring of patients' inclusion and clinical data gathering. In addition, being less expensive, compact, simple to install and repair (thanks to the experience of radiotherapy departments with accelerators), and easy to turn off following irradiation, highlights the advantages of ABNS over nuclear reactors [119].

It is important to note that the first cyclotron-based accelerator, developed by Sumitomo Heavy Industries (Figure 56), was approved by the Japanese Ministry of Health, Labor and Welfare (MHLW); in march 2020. This accelerator was used in phase 1 and 2 clinical trials for recurrent malignant glioma patients and was approved for clinical use for head and neck tumors. Other clinical trials have been also initiated [170]. This news presents a milestone towards establishing BNCT as a standard treatment for several cancer types.

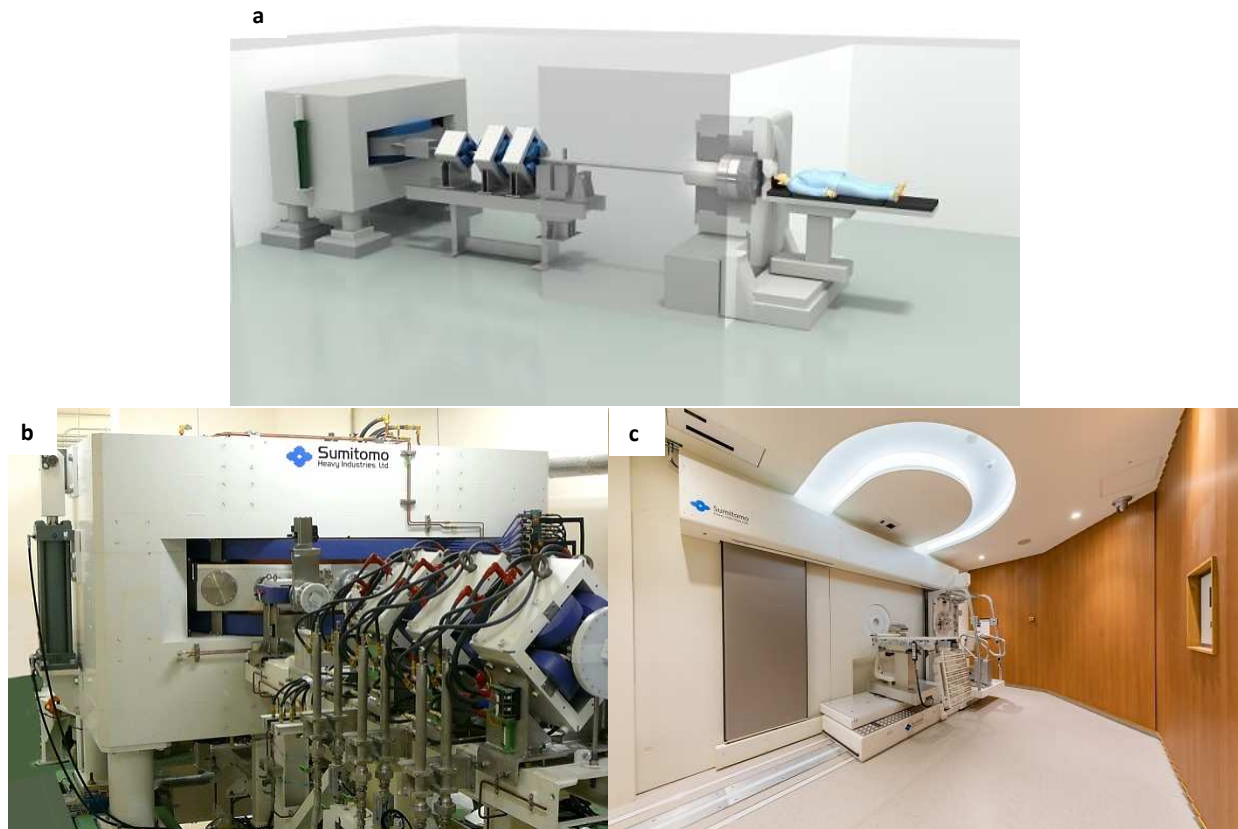


Figure 56: Schematic view (a) and photograph (b, c) of the approved accelerator-based neutron source developed by Sumitomo Heavy Industries. It includes the cyclotron (b) and the treatment room with the coach system (c) [171].

## 4.5 BNCT: Clinical evidence of efficacy

It is of great importance to shed light on the clinical advancement in BNCT. Here we present some of the promising BNCT clinical trials/ investigations applied to various tumor types.

### 4.5.1 Newly diagnosed Glioblastoma (NDGB)

One month following craniotomy, 21 patients with NDGB were subjected to BNCT. The patients received both BSH and BPA infusions. To prevent tumor recurrence, 11 patients were further subjected to X-ray radiation therapy (XRT) following BNCT. A significant prolongation in survival time was obtained (MST= 15.6 months) as compared to the institution's historical controls treated with surgery followed by XRT and chemotherapy (MST=10.3 months). These favorable results indicated the utility of this treatment protocol for NDGB patients, good and poor prognosis ones [172]. An impressive example is presented in Figure 57, where an 18-years old patient diagnosed with glioblastoma, had undergone re-craniotomy, BNCT followed by XRT. Two years following BNCT, the patient was neurologically safe and showed no tumor progression.

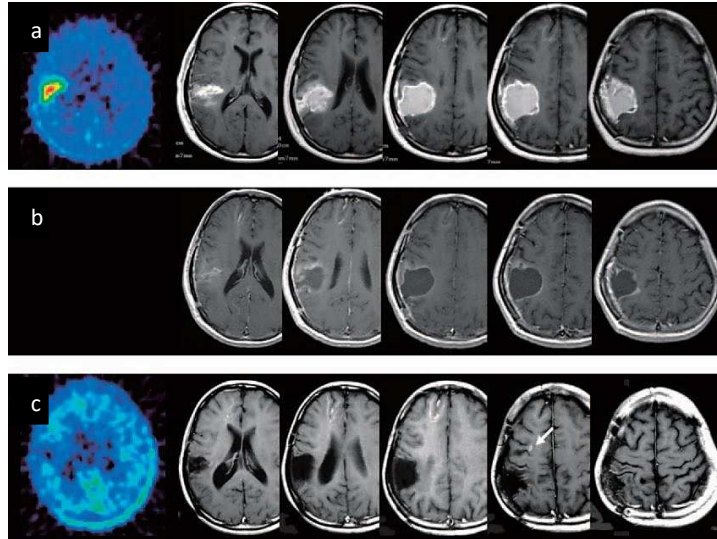


Figure 57: Brain MRI images of an 18-years-old patient following partial glioblastoma resection (a), re-craniotomy (b), and 2 years following BNCT treatment (c).  $^{18}\text{F}$ -BPA PET images are presented on the left panel in rows (a) and (c) [172].

#### 4.5.2 Recurrent Head and Neck malignancies (rHNM)

It is worth noting the first case report of 6 recurrent HNM patients treated with BNCT, following BSH and BPA administration. Remarkable reduction in tumor volumes (Figure 58) and improvement in life quality (pain relief, decreased bleeding, the disappearance of ulceration) were observed, indicating the potential of BNCT for treating huge, advanced, and inoperable HNM [173]. Similar results were obtained on a larger cohort of 26 rHNM patients, with a notable 6-years survival of 24% [174].



Figure 58: HNM patient before (A) and 22 months following BNCT treatment (B). A remarkable reduction in tumor size and an improvement in facial appearance were obtained [173].

#### 4.5.3 High-grade meningiomas

Twenty patients with high-grade meningiomas were included in a BNCT study, following several surgeries and radiation treatment failure. Nineteen patients showed favorable tumor-to-normal tissue ratios ( $>2.7$ ) following  $^{18}\text{F}$ -BPA PET. Two months following neutron exposure, a significant

shrinkage in tumor mass, with a 64.5% mean reduction, was observed. A median survival time of 14.1 months was obtained and a decrease in clinical symptoms was reported. Altogether these data demonstrated the success of BNCT in treating high-grade meningiomas [175]. Figure 59 provides a notable example of tumor shrinkage, obtained 2 years following BNCT treatment.

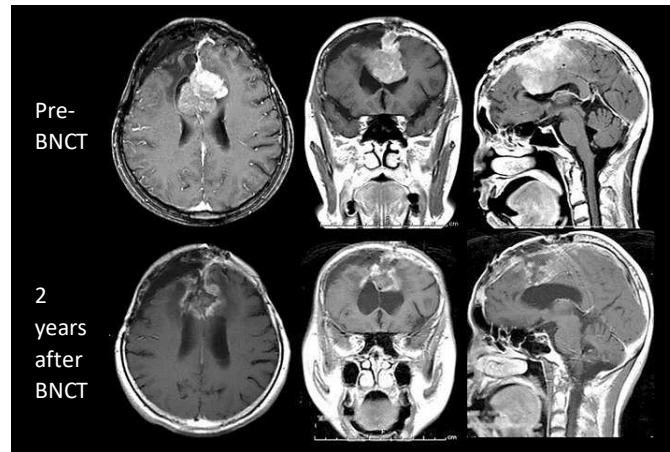


Figure 59: MRI images of a high-grade meningioma patient before and 2 years after BNCT treatment. A clear reduction in the tumor lesion was observed with no neurological deterioration. It is important to note that the BNCT treated lesion has reoccurred following several surgeries, stereotactic radiosurgery, and X-ray treatment [170].

#### 4.5.4 Recurrent Malignant gliomas

Twenty-two patients with recurrent malignant glioma were involved in a BNCT study. BPA and BSH were used simultaneously before neutron irradiation. A marked survival prolongation was observed in the high-risk group, with a median survival time (MST) of 9.1 months as compared to 4.4 months of the reference recursive partitioning analysis (RPA) classification [176]. Similar survival benefits and clinical symptoms improvement were achieved when BNCT was combined with anti-VEGF antibody bevacizumab [147] (Figure 60).

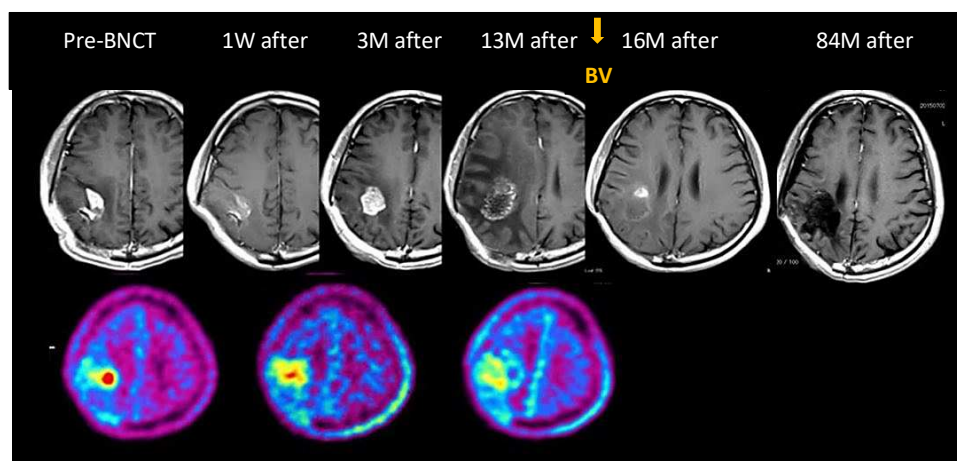


Figure 60: A representative case of recurrent glioblastoma treated with BNCT. The reduction in the  $^{18}\text{F}$ -BPA tracer signal in PET images (lower panel) indicates the efficacy of BNCT treatment. The radiation necrosis observed at months 13 by MRI images (upper panel), was treated by bevacizumab (BV). 84 months following BNCT and bevacizumab treatment, the patient is doing well with no tumor progression or radiation necrosis [170].

Altogether these impressive results evidence the efficacy of BNCT in treating multiple cancer types.

## 4.6 Conclusion

Along with the remarkable clinical data, the installation of hospital-based neutron accelerators is paving the way towards the implantation of BNCT as a standard cancer treatment. The main need now is the collaboration between the chemists and biologists to develop innovative boron compounds, combining all the needed requirements (safety, high tumor uptake, high T/N) and possessing imaging properties that allow their tracking, quantification, and optimization of the neutron radiation plan to achieve the best efficacy. The development of such theranostic compounds will be addressed in article 4 of the thesis work section.

To increase the number of patients included in clinical trials, and to further provide strong clinical data about BNCT efficacy, the hospitals should work together at the international level to homogenize both accelerator-based neutron sources, boron quantification, treatment planning, and clinical protocols. This step is the cornerstone to make BNCT a daily clinic weapon in the arsenal against cancer.

## 5 BODIPY fluorophores and their derivatives for cancer diagnosis and therapy

Following their synthesis in 1968 [177], BODIPY (4,4-difluoro-4-bora-3a,4a diaza-s-indacene) dyes have been implicated in a wide variety of fields including laser generators, photovoltaic cells, electroluminescent devices, light-emitting diodes (OLED), as well as biomedical applications (fluorescence imaging, photoacoustic imaging, photodynamic therapy...) [178].

### 5.1 BODIPY fluorophores and their derivatives for cancer fluorescence imaging

BODIPYs, considered as boron-bridged monomethine cyanine dyes (Figure 61a), their exclusive conformation restricts rotation and increases rigidity, resulting in higher fluorescence quantum yield and brightness compared to cyanine dyes [179]. Due to their unique photophysical properties including strong absorption (larger molar absorption coefficient), high fluorescence quantum yield, excellent chemical and photochemical stability within physiological conditions, and the multiple reactive sites available for functionalization, BODIPYs present a promising class of organic fluorophores for bioapplication [178].

However, as the absorption and emission bands of conventional BODIPYs are confined to the visible window, their use is limited to *in vitro* applications. To be suitable for *in vivo* fluorescence imaging, the photophysical properties of BODIPYs should be tuned and pushed towards the NIR-I biological transparency window, in which minimum light absorption, reduced autofluorescence and scattering can provide better light penetration and imaging quality *in vivo* [180].

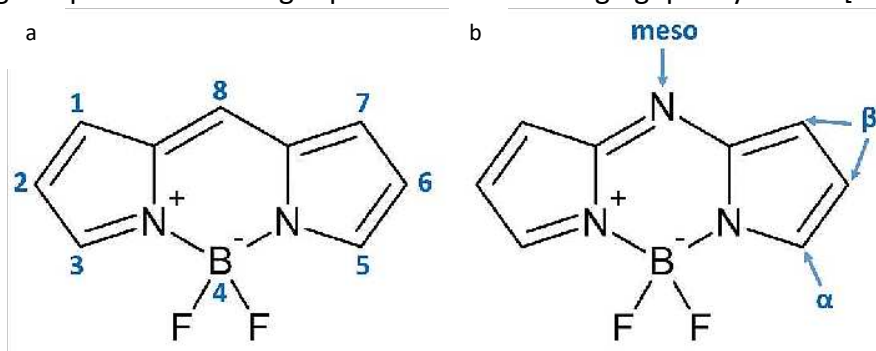


Figure 61: Conventional BODIPYs (a) and aza-BODIPYs (b) structures with IUPAC numbering and typical notation respectively [181].

#### 5.1.1 Aza-BODIPYs for NIR-I cancer fluorescence imaging

Several chemical modifications can induce the red-shifting of BODIPYs' fluorescence toward the NIR-I window, including the functionalization of the BODIPY core and the fusion with aromatic rings [180]. Here, we will focus on another strategy based on the replacement of the carbon atom present in the meso position of the BODIPYs with a nitrogen atom (N), resulting in a BODIPY derivative called the aza-BODIPY (Figure 61b) [180]. Aza-BODIPYs, in addition to retaining the excellent photophysical properties of conventional BODIPYs, their absorption and emission

bands are shifted into the NIR-I optical window, making them suitable for *in vivo* fluorescence imaging applications. Below are some examples of aza-BODIPYs used for NIR-I tumor fluorescence imaging.

O'Shea et al. reported the design of a lysosome-responsive NIR-emitting aza-BODIPY (Figure 62a) ( $\lambda_{\text{emission}}=707$  nm) that showed selectivity to the acidic environment of the lysosomes *in vitro* (within HeLa cell lines) (Figure 62b-e), and succeeded in tumor imaging *in vivo*, in MDA-MB-231 subcutaneous human breast adenocarcinoma bearing mice (Figure 62g) [182]. The same group also developed two new aza-BODIPYs with red-shifted emissions between 757 and 818 nm (Figure 63a2,3). They investigated their utility for endoscopic tattooing, a commonly used method for lesions identification during gastroenterology and colorectal surgery. The aza-BODIPYs positive fluorescent tattooing was observed on *ex vivo* human colonic tissue (Figure 63b), and their superior stability compared to ICG proved their clinical potential [183].

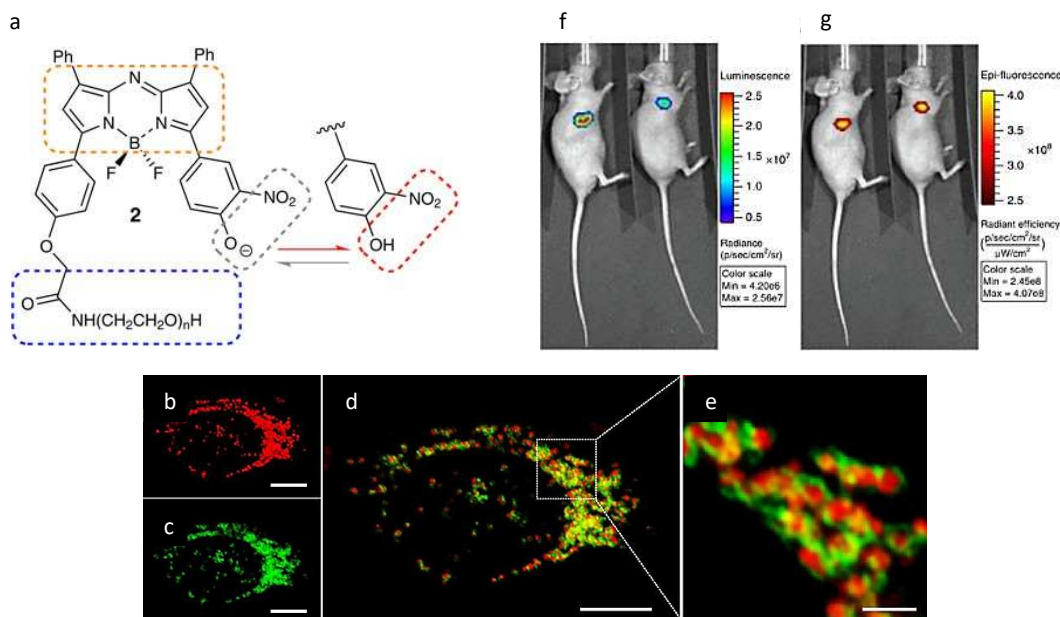


Figure 62: (a) Structure of the lysosome-responsive NIR-emitting aza-BODIPY, composed of aza-BODIPY core (orange box), pH-sensitive site (red box), and polyethylene glycol (PEG) polymer (blue box), for aqueous solubility and endocytosis promotion. Confocal images showing the localization of the lysosome-responsive NIR-emitting aza-BODIPY (b), and the lysosome-associated membrane protein 1 (LAMP1) (c), in HeLa cells. Images overlay (d) and zoom-in (e) showing circumferential staining of LAMP1 to the lysosome membrane, with the aza-BODIPY dye being within the lysosome acidic lumen. Scale bars represent 10  $\mu\text{m}$  (b-d) and 2  $\mu\text{m}$  (e). (f) Bioluminescence imaging localizes the MDA-MB-231-luc-D3H1 subcutaneous tumors in two representative mice. (g) NIR fluorescence imaging of the same mice 24 h post intravenous administration of the lysosome-responsive NIR-emitting aza-BODIPY (excitation 660–690 nm, emission 710–730 nm) [182].

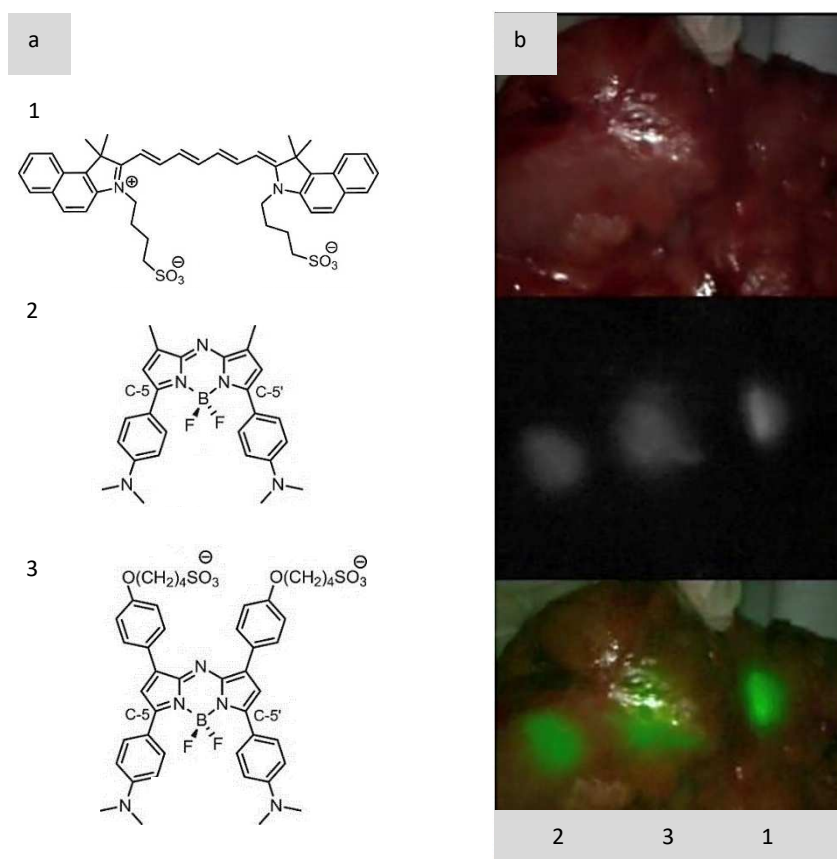


Figure 63: (a) Structure of ICG (1), and the two developed NIR-emitting aza-BODIPYs (2,3). (b) White light image (upper panel), NIR fluorescence image shown in grey-scale (middle panel), and an overly of both fluorescence, presented in green, and white light images (bottom panel) of an ex vivo colonic tissue, following 0.1 ml injection of 10  $\mu$ M solutions of 1, 2 and 3. Images were acquired using Novadaq PINPOINT Endoscopic instrument [183].

### 5.1.2 aza-BODIPYs for NIR-II cancer fluorescence imaging

Recently, NIR-II fluorescence imaging has emerged providing better penetration depth and resolution compared to NIR-I imaging. The need for new NIR-II fluorophores with easy synthesis, sufficient brightness, and stable/tunable photophysical properties drove the synthesis of NIR-II dyes based on the aza-BODIPY platform. By incorporating strong electron-donating groups at the 3, 5-positions, and 1, 2-positions of the aza-BODIPY core, large emission red-shifts from NIR-I to NIR-II window could be achieved.

Accordingly, three NIR-II emitting aza-BODIPYs (NJ960, NJ1030, NJ1060) were synthesized with variable  $\lambda_{\text{emission}} = 960, 1030, \text{ and } 1060 \text{ nm}$ , depending on the increasing electron-donating ability of the incorporated groups (Figure 64a). These fluorophores showed slightly higher quantum yields compared to other reported NIR-II fluorophores such as CH1055, superior photostability, and good brightness. For *in vivo* application, NJ1060 possessing the best photophysical properties was encapsulated within the Pluronic F-127 matrix, forming 90 nm-sized NJ1060 nanoparticles (NPs). Following intravenous injection of these NPs to mice bearing subcutaneous 4T1 tumors, a

weak tumor fluorescence staining was observed 3h post-administration, then it was enhanced until 24 h due to the EPR effect (Figure 64b). Strong fluorescence was also detected in the liver and spleen. This study provided the starting point for the development of aza-BODIPYs based NIR-II fluorophores for tumor NIR-II fluorescence imaging [184].

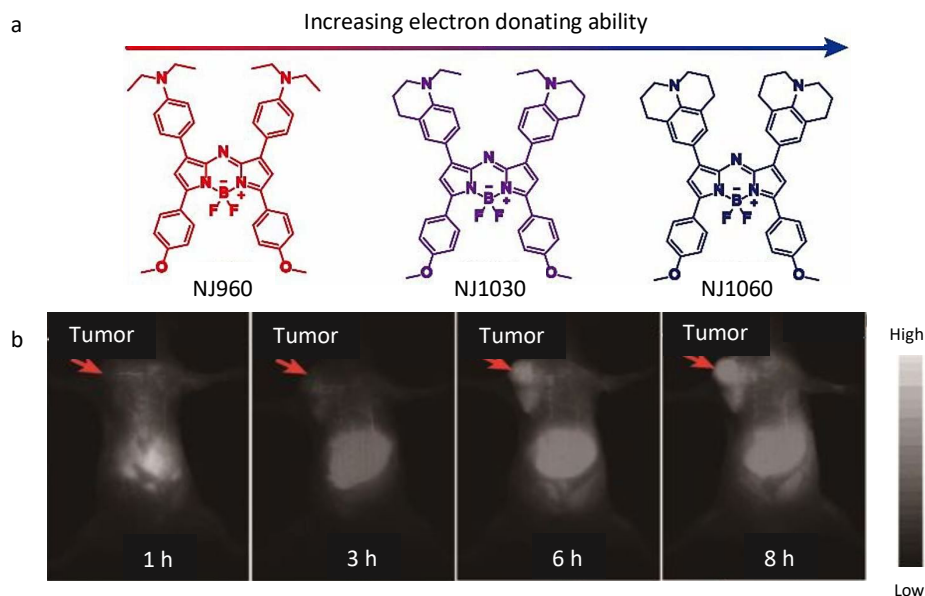


Figure 64: (a) Chemical structure of NJ960, NJ1030, and NJ1060 NIR-II emitting aza-BODIPYs. (b) NIR-II fluorescence images of a mouse bearing subcutaneous 4T1 tumor on the shoulder, 1, 3, 6, and 8 h following intravenous injection of NJ1060 nanoparticles. The tumor is indicated by red arrows [184].

More recently, another NIR-II aza-BODIPY was implicated in the design of a pH sensor for dynamic *in vivo* NIR-II tumor pH monitoring [185]. The aza-BODIPY ( $\lambda_{\text{emission}} = 949 \text{ nm}$ ) and a pH activable rhodamine ( $\lambda_{\text{emission}} = 1026 \text{ nm}$ ) were encapsulated within DSPE-PEG2000-OCH<sub>3</sub> micelles, for enhanced hydrophilicity and stability (Figure 65a). At low pH, rhodamine becomes protonated and activated, and a Förster resonance energy transfer (FRET) can occur between the aza-BODIPY (donor) and protonated rhodamine (acceptor), leading to a decrease in the aza-BODIPY 940 nm emission and an increase in the protonated rhodamine 1026 nm emission, respectively (Figure 65a). After the intravenous injection to tumor-bearing mice, the pH sensors rapidly accumulated within the tumors two hours following administration and were maintained for more than 24 h. The decrease and increase in tumor pH, induced by vascular inclusion and intratumoral administration of sodium bicarbonate respectively, were sensitively detected by a dual-channel (940/1026 nm) ratiometric fluorescence imaging in the NIR-II window (Figure 65b), and the data were in accordance with those recorded by the pH meter.

These two examples demonstrate the potential of aza-BODIPYs-based fluorophores for NIR-II tumor fluorescence imaging, further studies should focus on the construction of water-soluble aza-BODIPYs with higher quantum yields. Articles 1, 2, and 3 of the thesis work section address these issues, through the development of water-soluble aza-BODIPYs with enhanced quantum yield.

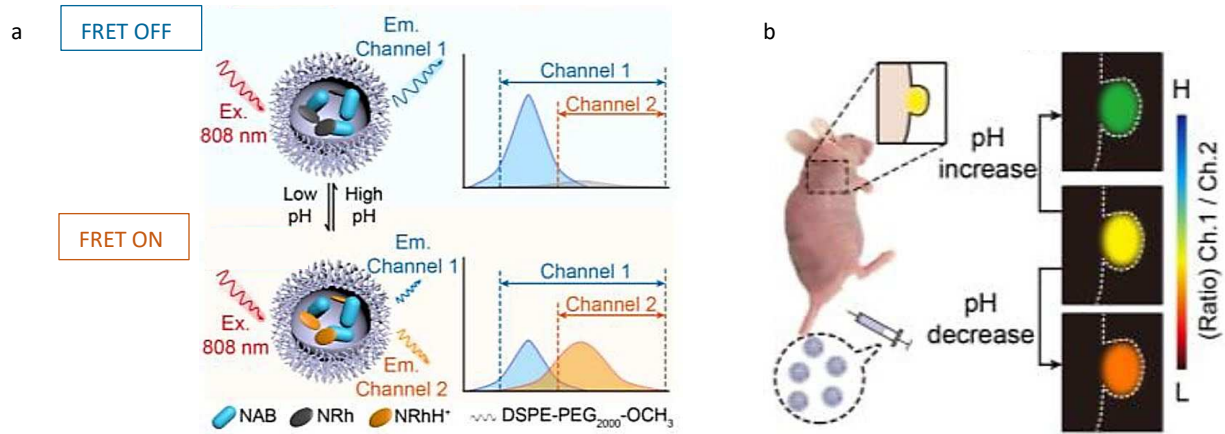


Figure 65: Schematic illustration of the pH sensor response to pH changes, in terms of NIR-II emitted signals. In acidic pH (low pH), the rhodamine (NRh) gets protonated (NRh<sup>+</sup>) and activated, leading to a FRET between the aza-BODIPY (NAB) and the NRh<sup>+</sup>. This activation induces the NRh<sup>+</sup>NIR-II emission within channel 2 while decreasing the NAB NIR-II emission in channel 1. (b) Schematic illustration of the in vivo dynamic tumor pH monitoring using ratiometric NIR-II fluorescence imaging (ratio of channel 1/ channel 2) [185].

## 5.2 BODIPYs fluorophores and their derivatives for cancer therapy: BNCT in particular

Although BODIPYs have been widely investigated for tumor Photodynamic Therapy and Photothermal Therapy, here we will focus on its implication in BNCT.

In an attempt to develop improved BNCT agents, Vicente et al. reported the synthesis of new low molecular weight theranostic BNCT agents, based on BODIPYs fluorophores linked to one or two carborane clusters (Figure 66) [186]. Spectroscopic analysis of these molecules revealed absorptions and emissions within the visible window. The molecules' blood-brain barrier (BBB) permeabilities were assessed using a human brain endothelial cell line hCMEC/D3 as BBB model. The different obtained permeabilities were explained by the molecules' variable molecular weights and hydrophobic character. One year later, the same group reported the synthesis of other BODIPYs-containing carboranes [187]. In addition to spectroscopic analysis and BBB permeability assessment, the molecules' cellular uptake and cytotoxicity were investigated *in vitro* in T98G human glioma cells. Among the synthesized series, molecules with the highest BBB permeability, tumor cell uptake, and minimal cytotoxicity presented the most promising BNCT agents.

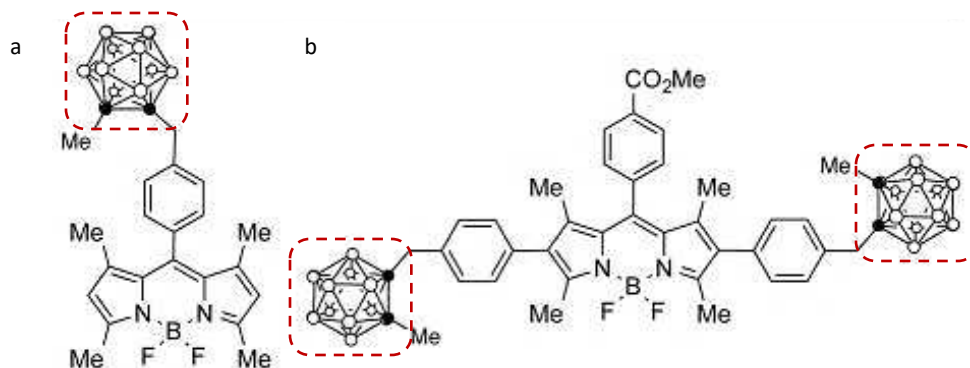


Figure 66: Representative examples of BODIPYs containing one (a) or two carborane clusters (b). Carboranes are indicated by dashed red boxes [186].

More recently, Núñez et al. reported the synthesis of BODIPYs attached to different carboranyl fragments (Figure 67) [188]. The variability in cellular uptake and subcellular localization within Hela cells was attributed to the molecules' variable static dipole moments and partition coefficients, that determine their lipophilicity and their ability to interact with cells' lipophilic microenvironment. The BODIPY-carboranyl derivatives possessing higher lipophilicity showed better cellular internalization, thus providing better boron carriers for BNCT.

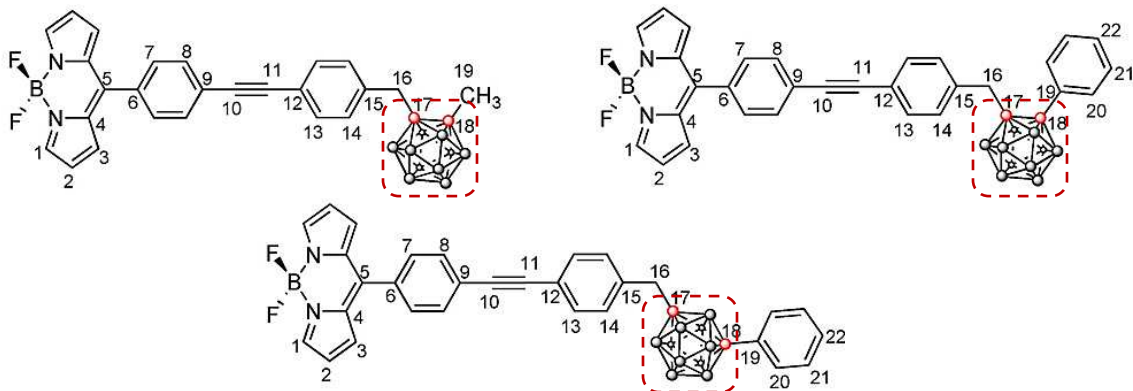


Figure 67: Representative examples of the BODIPYs-carboranyl molecules. Carboranyl molecules are indicated by dashed red boxes [188].

Although the development of BODIPY-based BNCT agents can benefit from the fluorescence properties of the BODIPY to track the boron compounds, this field is still in its primitive state. None of the BODIPY-based BNCT agents bypassed the *in vitro* assessment into *in vivo* investigations, and no evaluation under neutron beam was reported. This could be attributed to the BODIPYs' visible emission properties, hydrophobic characteristics, and low boron content that requires their coupling to molecules with high boron content (e.g. carborane). Future studies should focus on the development of BODIPY-based BNCT agents emitting within the NIR transparency window and possessing suitable solubilities. The development of aza-BODIPY-based BNCT agents meeting these requirements will be presented in article 4 of the thesis work section.

Most of the BODIPYs reported biological applications were investigated *in vitro*. However, considering the *in vivo* studies reported in the last five years confirms that BODIPYs and their derivatives could be considered as important as cyanine dyes for *in vivo* and even clinical applications.

## Thesis work

In this manuscript, I will present one part of my thesis work dedicated to the bioevaluation of aza-BODIPYs fluorophores (provided by our collaborators at ICMUB (Institut de Chimie Moléculaire de l'Université de Bourgogne, Dijon, France), for both NIR-II cancer imaging and BNCT application. The second part of my thesis devoted to the biological assessment of polymer-based nanogels (provided by our collaborators at the CERMAV, Grenoble, France), will not be discussed here.

My thesis objectives were the following:

- 1) To evaluate NIR-II emitting fluorophores possessing adequate biocompatibilities, high quantum yields, and selective tumor targeting capacities, in an attempt to be used for NIR-II tumor imaging *in vivo* and particularly for NIR-II FGS.
- 2) To evaluate theranostic boron compounds possessing adequate safety profiles, sufficient and selective boron delivery into tumors, and intrinsic imaging properties that allow boron quantification and subsequent adjustment of neutron radiation doses, in an attempt to achieve enhanced BNCT efficacy.

In an attempt to achieve these goals, the obtained research data were organized in a patent and four articles, of which two were published in peer-reviewed journals, and two are in preparation to be submitted. The research work was also presented in several national and international meetings, in which I was awarded three awards. Additionally, I was granted a GDR 2073 AIM mobility grant to perform a short internship in Dijon.

# Article 1: Water-Soluble Aza-BODIPYs: Biocompatible Organic Dyes for High Contrast *In vivo* NIR-II Imaging

As discussed in section 3.6 of the introduction, the progress of the NIR-II fluorescence imaging field is dependent both, on the development of affordable high-quality NIR-II cameras, and the design of biocompatible NIR-II fluorophores possessing high quantum yields. With the InGaAs NIR-II cameras becoming more and more commercially available, the development of NIR-II fluorophores possessing unique properties remains the main challenge. Several NIR-II dyes have been reported, yet none of them have bypassed the preclinical investigations due to their potential toxicities, poor water solubilities, or low quantum yields, in addition to the costly regularity investigations.

To address these issues, we worked in collaboration with the chemists at ICMUB (Institut de Chimie Moléculaire de l'Université de Bourgogne) on the development and the biological evaluation of NIR-II emitting fluorophores based on aza-BODIPY platform. We were the first to declare the use of aza-BODIPYs as contrast agents emitting in the NIR-II window, in the patent EP19315089.3 / PCT/EP2020/071865/ WO2021/023731: "UTILISATION DE COMPOSÉS FLUOROPHORES DE TYPE AZABODIPY COMME AGENTS DE CONTRASTE DANS L'INFRAROUGE TRÈS LOINTAIN" Sancey L, Goze C, Bodio E, Busser B, Pliquet J, Godard A, Kalot G, Josserand V, Le Guével X, Coll J-L, Denat F.

Following the patent filling, we published the article entitled "*Water-Soluble Aza-BODIPYs: Biocompatible Organic Dyes for High Contrast In vivo NIR-II Imaging*", in bioconjugate chemistry journal. In this paper, the first water-soluble aza-BODIPY emitting in the NIR-II window i.e SWIR-WAZABY-01 was described, and its potential for biological applications, in particular for *in vivo* NIR-II tumor imaging, was investigated.

After synthesis and chemical characterization, the photophysical properties of SWIR-WAZABY-01 were investigated and showed a significant NIR-II signal with an emission tail reaching 1200 nm, and Q.Y. of 2.5%. *In vitro*, the fluorophore was quickly internalized into U-87 MG tumor cells cultured both in 2D and 3D. *In vivo*, SWIR-WAZABY-01 rapidly accumulated in rodents bearing U-87 MG subcutaneous tumors with long-lasting retention (up to one week), and favorable tumor to healthy tissues ratios (>10 after 72 h). Additionally, a primary toxicity study revealed no adverse events in the main organs of non-desired accumulation (i.e. liver, kidney, and spleen). These data demonstrated the great potential and biocompatibility of SWIR-WAZABY-01 for NIR-II tumor imaging *in vivo*. To assess the aza-BODIPY utility for NIR-II fluorescence-guided surgery, further investigations were performed, and this will be the subject of article 2.

To note, I was responsible for the biological investigations applied in article 1. The chemical synthesis and the photophysical studies were performed by the chemists and the physicists at ICMUB and BAM (Federal Institute for Materials Research and Testing), respectively. I presented this work as a poster-pitch at the "Clara Cancéropôle 2021".

# Water-Soluble Aza-BODIPYs: Biocompatible Organic Dyes for High Contrast *In Vivo* NIR-II Imaging

Amélie Godard,<sup>⊥</sup> Ghadir Kalot,<sup>⊥</sup> Jacques Pliquett, Benoit Busser, Xavier Le Guével, K. David Wegner, Ute Resch-Genger, Yoann Rousselin, Jean-Luc Coll, Franck Denat, Ewen Bodio,\* Christine Goze,\*<sup>⊥</sup> and Lucie Sancey\*<sup>⊥</sup>



Cite This: *Bioconjugate Chem.* 2020, 31, 1088–1092



Read Online

ACCESS |



Metrics & More

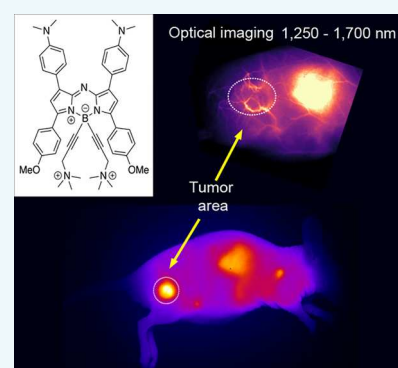


Article Recommendations



Supporting Information

**ABSTRACT:** A simple NIR-II emitting water-soluble system has been developed and applied *in vitro* and *in vivo*. *In vitro*, the fluorophore quickly accumulated in 2D and 3D cell cultures and rapidly reached the tumor in rodents, showing high NIR-II contrast for up to 1 week. This very efficient probe possesses all the qualities necessary for translation to the clinic as well as for the development of NIR-II emitting materials.



Among the different molecular imaging techniques, optical imaging presents unique advantages, such as being nonionizing and inexpensive, presenting high sensitivity and resolution, and offering multiscale capability from *in vitro* subcellular to *in vivo* investigations. More recently, this technique has been shown to be very promising in the clinic for fluorescence-guided surgery (FGS)<sup>1</sup> thanks to the development of fluorophores emitting in the NIR-I region (700–900 nm), which provide deeper penetration in the tissues and images with improved quality relative to those obtained with fluorophores emitting in the visible region.<sup>2</sup> Accordingly, there is a need to develop fluorophores that emit in another region of the light spectrum: the NIR-II region (1000–1700 nm, also called shortwave infrared region or SWIR). In this optical region, despite the strong absorption of water at 1400 nm, both scattering and autofluorescence phenomena are reduced, resulting in clearer tissue images compared to those obtained in the NIR-I.<sup>1,3–5</sup> The pioneering reports showed that NIR-II fluorophores were nanomaterials (single wall carbon nanotubes, SWCNTs),<sup>6</sup> Ag<sub>2</sub>S<sup>7</sup> and PbS quantum dots,<sup>8</sup> and rare-earth-doped nanoparticles,<sup>9–11</sup> highlighting the potential of NIR-II imaging at the preclinical stage. Unfortunately, their clinical application is hampered because of their potential toxicity.<sup>12</sup> To date, only two types of organic NIR-II fluorophores emitting over 1000 nm have been reported: (i) polymethines with extended conjugation, including cyanine dyes, and (ii) donor–acceptor–donor (D–A–D′) type compounds based on a benzobisthiadiazole core, such as CH1055,<sup>13–17</sup> presenting better fluorescence properties and

bimodal NIR II/photoacoustic properties.<sup>18</sup> Some of these NIR-II fluorophores have also been incorporated in multifunctional nanostructure systems.<sup>19</sup> However, these compounds often require a tedious synthesis and are difficult to functionalize or they display poor water solubility and limited stability, which limit their use for biomedical applications. Therefore, designing NIR-II-emitting fluorophores that avoid these pitfalls and are suitable for biological applications is challenging.

Aza-BODIPY (aza-dipyrrromethene boron difluoride) fluorophores are a very promising class of BODIPY fluorophores, which present remarkable NIR-I fluorescence properties, high quantum yields (QYs), and excellent chemical and photophysical stabilities, making them a very promising class of fluorophores for preclinical optical imaging studies.<sup>20</sup> Very recently, we noticed and reported the potential of aza-BODIPYs as NIR-II fluorophores.<sup>21</sup> In parallel, Bai *et al.* reported a complete photophysical study of similar derivatives based on D–A–D′ structures, but their poor water solubility limits their usefulness for *in vivo* studies.<sup>22</sup> We, on the other hand, developed aza-SWIR-01 (Figure 1), an aza-BODIPY

Received: March 28, 2020

Revised: March 30, 2020

Published: March 31, 2020



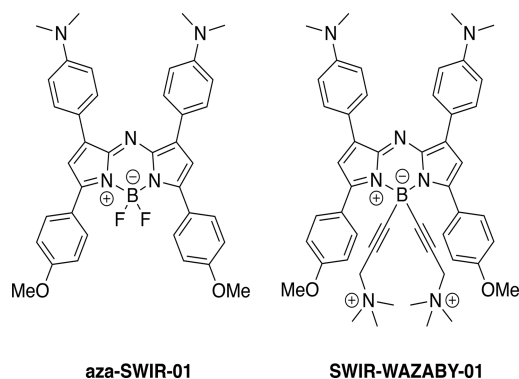


**Figure 1.** Structure of the NIR-II aza-BODIPY dyes.

with an NIR-II emission maximum at approximately 980 nm in DMSO (QY = 0.8%; Figure 2A, Table S2). To address the poor water solubility of aza-BODIPYs, we previously reported

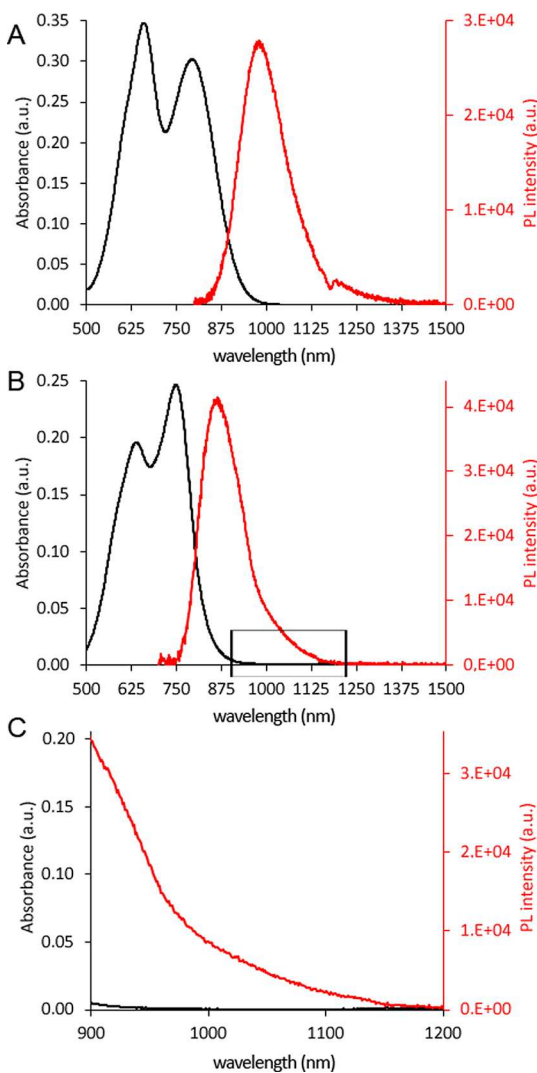


**Figure 2.** (A) Absorption (black line) and fluorescence emission spectra (red line) for aza-SWIR-01 in DMSO ( $\lambda_{exc} = 707$  nm, emission between 800 and 1500 nm). (B) Absorption spectra and photoluminescence (PL) emission range for SWIR-WAZABY-01 ( $\lambda_{exc} = 638$  nm, emission between 720 and 1200 nm in mouse plasma). (C) Expansion of the spectra shown in (B).

a strategy based on the introduction of ammonium groups onto the boron atom, which enabled us to prepare the first class of water-soluble aza-BODIPYs, named WAZABYs.<sup>23</sup> Here, we used this strategy to make aza-SWIR-01 water-soluble, thus obtaining SWIR-WAZABY-01 (Figure 1), and we will demonstrate its potential as an NIR-II fluorophore *in vitro* and *in vivo* for NIR-II tumor targeting without any vectorization strategy. SWIR-WAZABY-01 enriches the library of available organic small fluorescent dye agents and represents a valuable candidate for future translation to the clinic.

Aza-SWIR-01 was synthesized by adapting a previously reported procedure<sup>24,25</sup> (see the Supporting Information (SI) for the synthesis details). We then water-solubilized aza-SWIR-01 in two steps: (1) substitution of the fluorine atoms on the boron center using the Grignard reagent of *N,N*-dimethylpropargylamine and (2) quaternization of the amino groups, giving SWIR-WAZABY-01 (see the SI). The photophysical properties of the water-insoluble dye aza-SWIR-01 in DMSO revealed a sharp emission in the NIR-II region (Figure 2A) and a QY of 0.8% (see the SI), which is due to its D-A-D' character. The photophysical properties of the SWIR-WAZABY-01 were evaluated in plasma (see the SI). Interestingly, we observed an ~60 fold-enhancement of the fluorescence signal in 10% plasma as compared to PBS (see Figure S14) with prolonged emission up to 1200 nm and a QY of 2.5% (see Figure 2B and C; SI Table S2 and Figure S15). Such an increase in fluorescence intensity in the presence of plasma has already been reported for indocyanine green.<sup>1,26–30</sup> It is postulated that the confinement of the probe in a hydrophobic pocket of plasma components may minimize the torsional rotations of the probe, leading to an increase in the fluorophore's quantum yield.<sup>31,32</sup>

Before the *in vivo* investigations, SWIR-WAZABY-01 was first studied *in vitro* to evaluate its toxicity and distribution in 2D and 3D cell cultures (Figure 3). SWIR-WAZABY-01

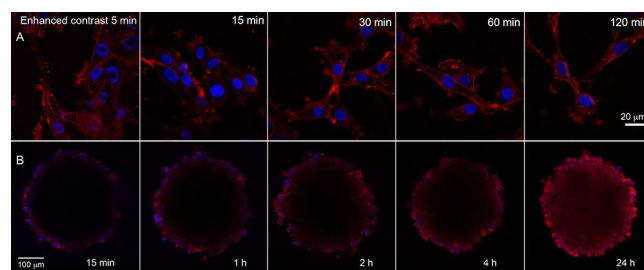


**Figure 3.** Human glioblastoma U87MG cells cultured in (A) 2D and (B) 3D incubated with SWIR-WAZABY-01 (red signal). Nuclei were labeled with Hoechst (blue signal).

showed no toxicity to healthy human cells (*i.e.*, MRC5 fibroblasts and HEK293 kidney cells) up to 20  $\mu$ M (see the SI). When incubated with human glioblastoma cells, SWIR-WAZABY-01 rapidly stained the cell membrane and was internalized by small cytoplasmic vesicles within a few minutes (Figure 3A). In 3D cell cultures, SWIR-WAZABY-01 was detected by fluorescence confocal microscopy on the outer cell layers within 15 min. After 24 h of incubation, fluorescence was present even in the core of the spheroid, demonstrating the capacity of this compound to diffuse within the cell layers (Figure 3B).

To further evaluate the potential of SWIR-WAZABY-01 *in vivo*, the compound was then administered intravenously to

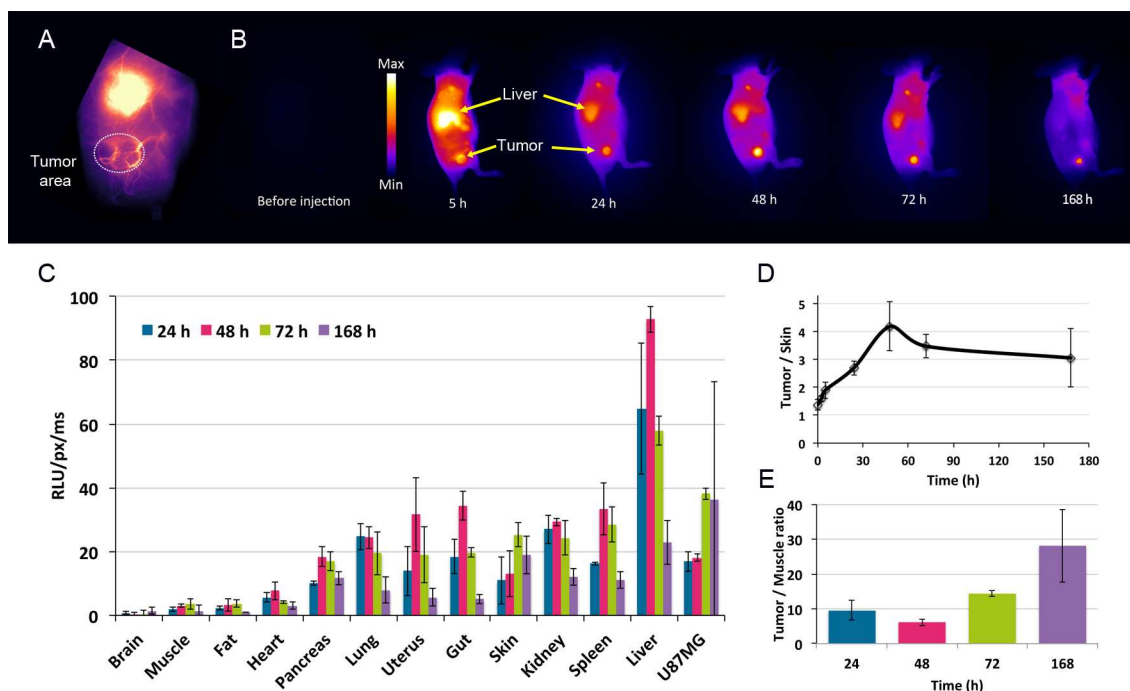


**Figure 4.** *In vivo* distribution and behavior of SWIR-WAZABY-01 in mice bearing U87MG (A) at 1 min and (B) until 7 days, collected from 1250 to 1700 nm during 250 ms. Distributions were observed from 24 to 168 h post injection (C). (D) Tumor/skin and (E) tumor/muscle ratios from *in vivo* and *ex vivo* analyses.

mice bearing subcutaneous U87MG tumor cells (Figure 4,  $n = 3/\text{condition}$ ). The animals were imaged in the NIR-II window before and after injection until day 7. SWIR-WAZABY-01 (200  $\mu\text{L}$  at 300 or 600  $\mu\text{M}$ ) is well tolerated (i.e., no obvious side effects were observed, see Figure S17) and distributed very well in the animals presenting two half-lives (see Figure S18), namely, 1.2 min for free circulating SWIR-WAZABY-01 and 55.5 min for SWIR-WAZABY-01 linked to plasma components, and the compound was mainly eliminated by the liver with a maximum accumulation at early time points. Interestingly, it also rapidly accumulated in subcutaneous tumors, even if not vectorized, reaching its maximum tumor uptake at 72 h after administration and enabling very clear localization of the tumor site by NIR-II fluorescence imaging. More precisely, the NIR-II fluorescence measurements revealed that a maximum tumor-to-skin ratio (approximately 4) was reached 48 h after injection. Moreover, the *ex vivo* analysis indicated important residual staining of the tumor even 1 week after injection (tumor-to-muscle ratio of  $\sim 30$ , at day 7). Indeed, at day 7, SWIR-WAZABY-01 was mainly present in the tumor with a maintained uptake, while it had begun to be eliminated from other organs. Such fast and long-term retention has never been reported previously for NIR-II fluorophores, highlighting the great potential of SWIR-WAZABY-01. For comparison, tumor-to-normal tissue ratios were reported following CH1055-PEG injection; these ratios reached a maximum of 5.5 at 72 h postinjection for brain tumors, and 15 for subcutaneous tumors.<sup>33</sup>

Altogether, we designed, synthesized, and evaluated a novel, water-soluble organic fluorophore emitting in the NIR-II region, SWIR-WAZABY-01, which shows photoluminescence emission with an extended tail reaching 1200 nm in biocompatible solutions and can be easily observed *in vivo* within the NIR-II window. The enhanced water solubility

induced by boron functionalization enables the intravenous injection of SWIR-WAZABY-01 in mice bearing tumors. SWIR-WAZABY-01 rapidly reached and accumulated in the tumor. We observed a long-lasting tumor retention of SWIR-WAZABY-01, with favorable tumor-to-skin and tumor-to-muscle ratios. SWIR-WAZABY-01 offers new perspectives for NIR-II optical imaging applications and cancer sciences; further *in vivo* toxicity experiments will be performed to confirm the potential of this valuable dye for biomedical use. This communication presents the first water-soluble NIR-II aza-BODIPY fluorophore suitable for *in vivo* NIR-II imaging of tumors without vectorization.

## ■ ASSOCIATED CONTENT

### Supporting Information

The Supporting Information is available free of charge at <https://pubs.acs.org/doi/10.1021/acs.bioconjchem.0c00175>.

Experimental and synthesis details;  $^1\text{H}$  NMR spectra; HPLC data; absorption and emission spectra; tissue analysis (PDF)

Crystallographic data for aza-SWIR-01 (PDF)

## ■ AUTHOR INFORMATION

### Corresponding Authors

**Lucie Sancey** – *Institute for Advanced Biosciences, UGA INSERM U1209 CNRS UMR5309, 38000 Grenoble, France;* [orcid.org/0000-0002-0084-3775](https://orcid.org/0000-0002-0084-3775); Email: [Lucie.Sancey@univ-grenoble-alpes.fr](mailto:Lucie.Sancey@univ-grenoble-alpes.fr)

**Christine Goze** – *Institut de Chimie Moléculaire de l'Université de Bourgogne, UMR 6302, CNRS, Université Bourgogne Franche-Comté, 21078 Dijon, France;* [orcid.org/0000-0002-3484-3837](https://orcid.org/0000-0002-3484-3837); Email: [Christine.Goze@u-bourgogne.fr](mailto:Christine.Goze@u-bourgogne.fr)

Ewen Bodio – Institut de Chimie Moléculaire de l'Université de Bourgogne, UMR 6302, CNRS, Université Bourgogne Franche-Comté, 21078 Dijon, France; [orcid.org/0000-0003-2896-113X](https://orcid.org/0000-0003-2896-113X); Email: Ewen.Bodio@u-bourgogne.fr

## Authors

Amélie Godard – Institut de Chimie Moléculaire de l'Université de Bourgogne, UMR 6302, CNRS, Université Bourgogne Franche-Comté, 21078 Dijon, France

Ghadir Kalot – Institute for Advanced Biosciences, UGA INSERM U1209 CNRS UMR5309, 38000 Grenoble, France

Jacques Pliquett – Institut de Chimie Moléculaire de l'Université de Bourgogne, UMR 6302, CNRS, Université Bourgogne Franche-Comté, 21078 Dijon, France

Benoit Busser – Institute for Advanced Biosciences, UGA INSERM U1209 CNRS UMR5309, 38000 Grenoble, France; Grenoble Alpes University Hospital, 38043 Grenoble, France; [orcid.org/0000-0002-9425-1577](https://orcid.org/0000-0002-9425-1577)

Xavier Le Guével – Institute for Advanced Biosciences, UGA INSERM U1209 CNRS UMR5309, 38000 Grenoble, France; [orcid.org/0000-0003-3634-7762](https://orcid.org/0000-0003-3634-7762)

K. David Wegner – BAM Federal Institute for Materials Research and Testing, 12489 Berlin, Germany

Ute Resch-Genger – BAM Federal Institute for Materials Research and Testing, 12489 Berlin, Germany; [orcid.org/0000-0002-0944-1115](https://orcid.org/0000-0002-0944-1115)

Yoann Rousselin – Institut de Chimie Moléculaire de l'Université de Bourgogne, UMR 6302, CNRS, Université Bourgogne Franche-Comté, 21078 Dijon, France

Jean-Luc Coll – Institute for Advanced Biosciences, UGA INSERM U1209 CNRS UMR5309, 38000 Grenoble, France; [orcid.org/0000-0002-2453-3552](https://orcid.org/0000-0002-2453-3552)

Franck Denat – Institut de Chimie Moléculaire de l'Université de Bourgogne, UMR 6302, CNRS, Université Bourgogne Franche-Comté, 21078 Dijon, France

Complete contact information is available at:

<https://pubs.acs.org/10.1021/acs.bioconjchem.0c00175>

## Author Contributions

<sup>†</sup>A.G., G.K., C.G., and L.S. contributed equally.

## Funding

The research in this paper has been funded by the Ministère de l'Enseignement Supérieur et de la Recherche, the Centre National de la Recherche Scientifique (CNRS), the Conseil Régional de Bourgogne (PhD JCE Grant # 2015-9205AAO033S04139/BG0003203), and the French Research National Agency (ANR) via project JCJC "SPID" ANR-16-CE07-0020 and project JCJC "WazaBY" ANR-18-CE18-0012. This work was also supported by the GEFLUC Grenoble Dauphiné Savoie, and the French funding agencies: FLI (France Life Imaging) for the project Thera-BODIPY, the CNRS Mission for Transversal and Interdisciplinary Initiatives for the project BREVET-ISOTOP, the Fondation pour la Recherche Médicale (FRM) for the specific support of G.K. (FRM ECO201806006861) and Plan Cancer funding (C18038CS). This work is part of the projects "Pharmacoi-magerie et agents théranostiques" et "Chimie durable, environnement et agroalimentaire" supported by the Université de Bourgogne and the Conseil Régional de Bourgogne through the Plan d'Actions Régional pour l'Innovation (PARI) and the European Union through the PO FEDER-FSE Bourgogne 2014/2020 programs. It was performed within the Dijon's pharmaco-imaging consortium, a regional center of

excellence in pharmacoi-maging. U.R.-G. gratefully acknowledges support by the German Research Council (DFG; Grant 1203/12-3).

## Notes

The authors declare no competing financial interest.

## ACKNOWLEDGMENTS

The authors want to thank M. Dakir and B. Musnier for technical contribution, and the GDR CNRS AIM (Agent d'imagerie Moléculaire).

## REFERENCES

- (1) Zhu, S., Tian, R., Antaris, A. L., Chen, X., and Dai, H. (2019) Near-Infrared-II Molecular Dyes for Cancer Imaging and Surgery. *Adv. Mater.* 31, 1900321.
- (2) Zhu, S., Yung, B. C., Chandra, S., Niu, G., Antaris, A. L., and Chen, X. (2018) Near-Infrared-II (NIR-II) Bioimaging via Off-Peak NIR-I Fluorescence Emission. *Theranostics* 8, 4141–4151.
- (3) Byrd, B. K., Folaron, M. R., Leonor, J. P., Strawbridge, R. R., Cao, X., Bruza, P., and Davis, S. C. (2019) Characterizing short-wave infrared fluorescence of conventional near-infrared fluorophores. *J. Biomed. Opt.* 24, 035004.
- (4) Jin, T. (2019) Critical Review—Recent Progress in NIR Fluorophores Emitting over 1000 nm for Bioimaging. *ECS J. Solid State Sci. Technol.* 8, R9–R13.
- (5) Musnier, B., Wegner, K. D., Comby-Zerbino, C., Trouillet, V., Jourdan, M., Hausler, I., Antoine, R., Coll, J. L., Resch-Genger, U., and Le Guevel, X. (2019) High photoluminescence of shortwave infrared-emitting anisotropic surface charged gold nanoclusters. *Nanoscale* 11, 12092–12096.
- (6) Takeuchi, T., Iizumi, Y., Yudasaka, M., Kizaka-Kondoh, S., and Okazaki, T. (2019) Characterization and Biodistribution Analysis of Oxygen-Doped Single-Walled Carbon Nanotubes Used as in Vivo Fluorescence Imaging Probes. *Bioconjugate Chem.* 30, 1323–1330.
- (7) Shen, Y., Lifante, J., Ximendes, E., Santos, H. D. A., Ruiz, D., Juarez, B. H., Zabala Gutierrez, I., Torres Vera, V., Rubio Retama, J., Martin Rodriguez, E., et al. (2019) Perspectives for Ag<sub>2</sub>S NIR-II nanoparticles in biomedicine: from imaging to multifunctionality. *Nanoscale* 11, 19251–19264.
- (8) Jeong, S., Song, J., Lee, W., Ryu, Y. M., Jung, Y., Kim, S. Y., Kim, K., Hong, S. C., Myung, S. J., and Kim, S. (2017) Cancer-Microenvironment-Sensitive Activatable Quantum Dot Probe in the Second Near-Infrared Window. *Nano Lett.* 17, 1378–1386.
- (9) Cai, Y., Wei, Z., Song, C., Tang, C., Han, W., and Dong, X. (2019) Optical nano-agents in the second near-infrared window for biomedical applications. *Chem. Soc. Rev.* 48, 22–37.
- (10) He, S., Chen, S., Li, D., Wu, Y., Zhang, X., Liu, J., Song, J., Liu, L., Qu, J., and Cheng, Z. (2019) High Affinity to Skeleton Rare Earth Doped Nanoparticles for Near-Infrared II Imaging. *Nano Lett.* 19, 2985–2992.
- (11) Naczynski, D. J., Stafford, J. H., Turkcan, S., Jenkins, C., Koh, A. L., Sun, C., and Xing, L. (2018) Rare-Earth-Doped Nanoparticles for Short-Wave Infrared Fluorescence Bioimaging and Molecular Targeting of alphaVbeta3-Expressing Tumors. *Mol. Imaging* 17, 1536012118799131.
- (12) Kim, J. H., Kim, H. R., Lee, B. R., Choi, E. S., In, S. I., and Kim, E. (2015) Carcinogenic activity of PbS quantum dots screened using exosomal biomarkers secreted from HEK293 cells. *Int. J. Nanomed.* 10, 5513–27.
- (13) Lei, Z., Sun, C., Pei, P., Wang, S., Li, D., Zhang, X., and Zhang, F. (2019) Stable, Wavelength-Tunable Fluorescent Dyes in the NIR-II Region for In Vivo High-Contrast Bioimaging and Multiplexed Biosensing. *Angew. Chem., Int. Ed.* 58, 8166–8171.
- (14) Shi, Y., Yuan, W., Liu, Q., Kong, M., Li, Z., Feng, W., Hu, K., and Li, F. (2019) Development of Polyene-Bridged Hybrid Rhodamine Fluorophores for High-Resolution NIR-II Imaging. *ACS Materials Lett.* 1, 418–424.

- (15) Yang, Q., Ma, Z., Wang, H., Zhou, B., Zhu, S., Zhong, Y., Wang, J., Wan, H., Antaris, A., Ma, R., et al. (2017) Rational Design of Molecular Fluorophores for Biological Imaging in the NIR-II Window. *Adv. Mater.* 29, 1605497.
- (16) Zhu, S., Hu, Z., Tian, R., Yung, B. C., Yang, Q., Zhao, S., Kieseewetter, D. O., Niu, G., Sun, H., Antaris, A. L., et al. (2018) Repurposing Cyanine NIR-I Dyes Accelerates Clinical Translation of Near-Infrared-II (NIR-II) Bioimaging. *Adv. Mater.* 30, 1802546.
- (17) Tu, L., Xu, Y., Ouyang, Q., Li, X., and Sun, Y. (2019) Recent advances on small-molecule fluorophores with emission beyond 1000 nm for better molecular imaging in vivo. *Chin. Chem. Lett.* 30, 1731.
- (18) Ding, F., Chen, Z., Kim, W. Y., Sharma, A., Li, C., Ouyang, Q., Zhu, H., Yang, G., Sun, Y., and Kim, J. S. (2019) A nano-cocktail of an NIR-II emissive fluorophore and organoplatinum(ii) metallacycle for efficient cancer imaging and therapy. *Chem. Sci.* 10, 7023–7028.
- (19) Sun, Y., Ding, F., Chen, Z., Zhang, R., Li, C., Xu, Y., Zhang, Y., Ni, R., Li, X., Yang, G., et al. (2019) Melanin-dot-mediated delivery of metallacycle for NIR-II/photoacoustic dual-modal imaging-guided chemo-photothermal synergistic therapy. *Proc. Natl. Acad. Sci. U. S. A.* 116, 16729–16735.
- (20) Ge, Y., and O'Shea, D. F. (2016) Azadipyrrromethenes: from traditional dye chemistry to leading edge applications. *Chem. Soc. Rev.* 45, 3846–64.
- (21) Sancey, L., Goze, C., Bodio, E., Pliquett, J., Godard, A., Kalot, G., Josserand, V., Le Guével, X., Coll, J., and Denat, F. (2019) Université Grenoble Alpes, CNRS, INSERM, Univ. de Bourgogne, Patent No. 19315089.3-1110.
- (22) Bai, L., Sun, P., Liu, Y., Zhang, H., Hu, W., Zhang, W., Liu, Z., Fan, Q., Li, L., and Huang, W. (2019) Novel aza-BODIPY based small molecular NIR-II fluorophores for in vivo imaging. *Chem. Commun. (Cambridge, U. K.)* 55, 10920–10923.
- (23) Pliquett, J., Dubois, A., Racœur, C., Mabrouk, N., Amor, S., Lescure, R., Bettaieb, A., Collin, B., Bernhard, C., Denat, F., et al. (2019) A Promising Family of Fluorescent Water-Soluble aza-BODIPY Dyes for in Vivo Molecular Imaging. *Bioconjugate Chem.* 30, 1061–1066.
- (24) Jiao, L., Wu, Y., Wang, S., Hu, X., Zhang, P., Yu, C., Cong, K., Meng, Q., Hao, E., and Vicente, M. G. (2014) Accessing near-infrared-absorbing BF2-azadipyrrromethenes via a push-pull effect. *J. Org. Chem.* 79, 1830–5.
- (25) Swamy, C. A., Prinyanka, R. N., Mukherjee, S., and Thilagar, P. (2015) Panchromatic Borane-aza-BODIPY Conjugate: Synthesis, Intriguing Optical Properties, and Selective Fluorescent Sensing of Fluoride Anions. *Eur. J. Inorg. Chem.* 2015, 2338–2344.
- (26) Desmettre, T., Devoisselle, J. M., and Mordon, S. (2000) Fluorescence properties and metabolic features of indocyanine green (ICG) as related to angiography. *Surv. Ophthalmol.* 45, 15–27.
- (27) Starosolski, Z., Bhavane, R., Ghaghada, K. B., Vasudevan, S. A., Kaay, A., and Annapragada, A. (2017) Indocyanine green fluorescence in second near-infrared (NIR-II) window. *PLoS One* 12, No. e0187563.
- (28) Tian, R., Zeng, Q., Zhu, S., Lau, J., Chandra, S., Ertsey, R., Hettie, K. S., Teraphongphom, T., Hu, Z., Niu, G., et al. (2019) Albumin-chaperoned cyanine dye yields superbright NIR-II fluorophore with enhanced pharmacokinetics. *Sci. Adv.* 5, No. eaaw0672.
- (29) Carr, J. A., Franke, D., Caram, J. R., Perkinson, C. F., Saif, M., Askoxylakis, V., Datta, M., Fukumura, D., Jain, R. K., Bawendi, M. G., et al. (2018) Shortwave infrared fluorescence imaging with the clinically approved near-infrared dye indocyanine green. *Proc. Natl. Acad. Sci. U. S. A.* 115, 4465–4470.
- (30) Philip, R., Penzkofer, A., Bäuml, W., Szeimies, R., and Abels, C. (1996) Absorption and fluorescence spectroscopic investigation of indocyanine green. *J. Photochem. Photobiol., A* 96, 137–148.
- (31) Antaris, A. L., Chen, H., Diao, S., Ma, Z., Zhang, Z., Zhu, S., Wang, J., Lozano, A. X., Fan, Q., Chew, L., et al. (2017) A high quantum yield molecule-protein complex fluorophore for near-infrared II imaging. *Nat. Commun.* 8, 15269.
- (32) Hof, M., Hutterer, R., and Fidler, V. (2005) *Fluorescence Spectroscopy in Biology: advanced Methods and Their Applications to Membranes, Proteins, DNA, and Cells*, Springer.
- (33) Antaris, A. L., Chen, H., Cheng, K., Sun, Y., Hong, G., Qu, C., Diao, S., Deng, Z., Hu, X., Zhang, B., et al. (2016) A small-molecule dye for NIR-II imaging. *Nat. Mater.* 15, 235–42.

# Water-Soluble Aza-BODIPYs: biocompatible organic dyes for high contrast *in vivo* NIR-II imaging

Amélie Godard<sup>a‡</sup>, Ghadir Kalot<sup>b‡</sup>, Jacques Pliquett<sup>a</sup>, Benoit Busser<sup>b-c</sup>, Xavier Le Guével<sup>b</sup>, K. David Wegner<sup>d</sup>, Ute Resch-Genger<sup>d</sup>, Yoann Rousselin<sup>a</sup>, Jean-Luc Coll<sup>b</sup>, Franck Denat<sup>a</sup>, Ewen Bodio<sup>a\*</sup>, Christine Goze<sup>a‡\*</sup>, Lucie Sancey<sup>b‡\*</sup>.

(a) Institut de Chimie Moléculaire de l'Université de Bourgogne, UMR 6302, CNRS, Université Bourgogne Franche-Comté, 21000 Dijon, France. (b) Institute for Advanced Biosciences, UGA INSERM U1209 CNRS UMR5309, 38000 Grenoble, France. (c) Grenoble Alpes University Hospital, 38042 Grenoble, France. (d) BAM Federal Institute for Materials Research and Testing, Richard-Willstaetter-Str. 11, 12489 Berlin, Germany.

## ESI Part

### Experimental Part

Complete ESI is available online at <https://pubs.acs.org/doi/10.1021/acs.bioconjchem.0c00175>.

### Photophysical characterization

Absorbance measurements were recorded on a UV-Vis-NIR spectrophotometer Cary5000 between 300 and 1,200 nm. Steady-state photoluminescence spectra were measured from 700 to 1,500 nm with a calibrated FSP 920 (Edinburgh Instruments, Edinburgh, United Kingdom) spectrofluorometer equipped with a nitrogen-cooled PMT R5509P.

Relative measurements of photoluminescence QYs ( $\Phi_{f,x}$ ) were performed using the dye IR125 dissolved in dimethylsulfoxide (DMSO) as reference. The QY of this dye was previously determined absolutely to  $\Phi_{f,st} = 0.23$ . The relative QY were calculated according to the formula of Demas and Crosby, see equation below.

$$\Phi_{f,x} = \Phi_{f,st} \frac{F_x}{F_{st}} \frac{f_{st}(\lambda_{ex,st})}{f_x(\lambda_{ex,x})} \frac{n_x^2(\lambda_{ex,x})}{n_{st}^2(\lambda_{ex,st})}$$

The subscripts x, st, and ex denote sample, standard, and excitation respectively.  $f(\lambda_{ex})$  is the absorption factor, F the integrated spectral fluorescence photon flux, and n the refractive index of the solvents used (DMSO for IR125 and **aza-SWIR-01**; 10% mouse plasma for **SWIRWAZABY-01**).

All spectroscopic measurements were done in a 1 cm quartz cuvettes from Hellma GmbH at room temperature using air-saturated solutions.

**Table S2:** Photophysical characterization of **aza-SWIR-01** in DMSO and **SWIR-WAZABY-01** in 10% plasma.

Compound	Emission (723-1,300 nm)	n (refractive index)	Quantum Yield (%)
IR125	32,800,000	1.48	23
aza-SWIR-01	1,183,000	1.48	0.83
SWIR-WAZABY-01	4,450,000	1.335	2.54

## Fluorescence calibration

Serial dilutions of **SWIR-WAZABY-01** were performed in various aqueous media (PBS, NaCl 0.9%, Glucose 5%), BSA 40 g/L or mouse plasma, and the fluorescence was recorded from 1,250 to 1,700 nm (100 ms acquisition signal). Analyses were performed using FIJI software.

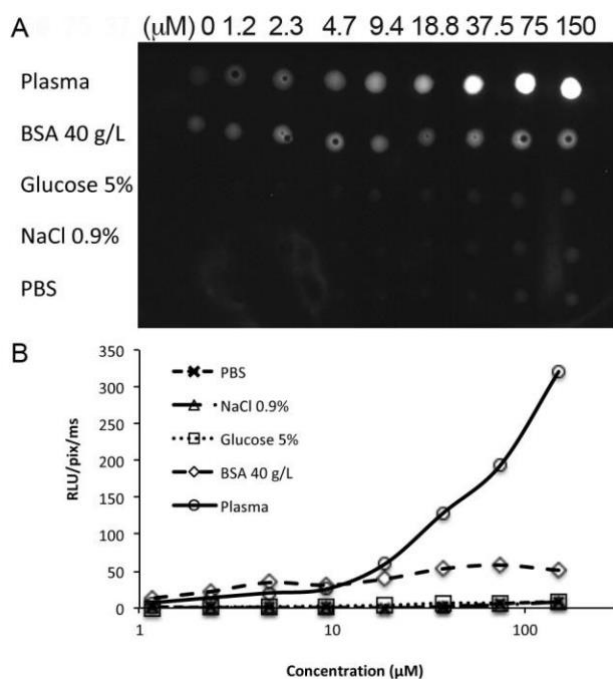


**Figure S14:** Representative fluorescence of **SWIR-WAZABY-01** in various media: (A) SWIR imaging of the drops, and (B) their quantifications. **SWIR-WAZABY-01** was moderately fluorescent in BSA 40 g/L and highly fluorescent in plasma.

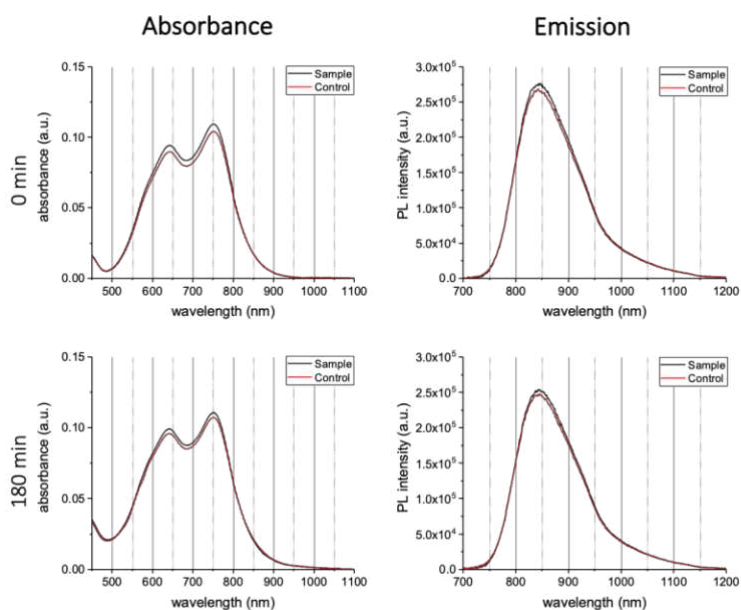


**Figure S15:** Absorbance and emission spectra of **SWIR-WAZABY-01** kept in the dark at room temperature (control) or continuously illuminated (sample) over a period of 180 min with light of 638 nm (1.13 mW). **SWIR-WAZABY-01** does not show any signs of significant photobleaching after 180 minutes of illumination under these exemplarily chosen conditions.

## Evaluation of cell toxicity

Human healthy cells (renal HEK293 and fibroblast MRC5) and glioblastoma U87MG cells were cultured in appropriated medium enriched with fetal bovine serum before incubation for 72 hours with the indicated concentration of **SWIR-WAZABY-01**. Cell viability was assessed using MTS assay following the company's instructions (Abcam) and signal was measured at 490 nm, ensuring to avoid any overlap with the SWIR compounds.

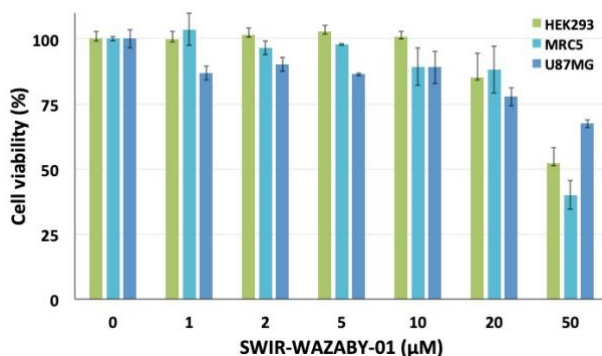


**Figure S16:** Cell viability of healthy kidney HEK293 and fibroblasts MRC5 cells, and glioblastoma U87MG cells after 72 h exposure with **SWIR-WAZABY-01**. The cell viability was assessed by MTS assay.

## Mice experiments and pharmacokinetics

This experimental part was ethically approved by local and national ethics committee following the European Guidelines (APAFIS #8782-201732813328550 v1). Mice were sub-cutaneously injected with 3M U87MG cells, 3 weeks before imaging. The animals (n=3/time) were imaged before and at different times after IV administration of 200 µL of **SWIR-WAZABY-01** (600 µM). NIR-II imaging was performed using a Princeton camera 640ST (900-1.700 nm) coupled with a laser excitation source at  $\lambda = 830$  nm (50 mW/cm<sup>2</sup>). A short-pass excitation filter at 1.000 nm (Thorlabs) was used, in addition of long-pass filters on the SWIR camera from Semrock (LP1.064 nm) and Thorlabs (LP1.250 nm). A 25 mm lens with 1.4 aperture (Navitar) was used to focus on the samples or mice. After *in vivo* imaging, organs were sampled for *ex vivo* analysis. Briefly, the organs were frozen and sections of 7 µm were cut and stained with hematoxylin and eosin. Representative histological sections are reported in Figure S16. They indicated the absence of any microscopic change in the liver, kidney and spleen of the animals after a bolus administration of the probe.

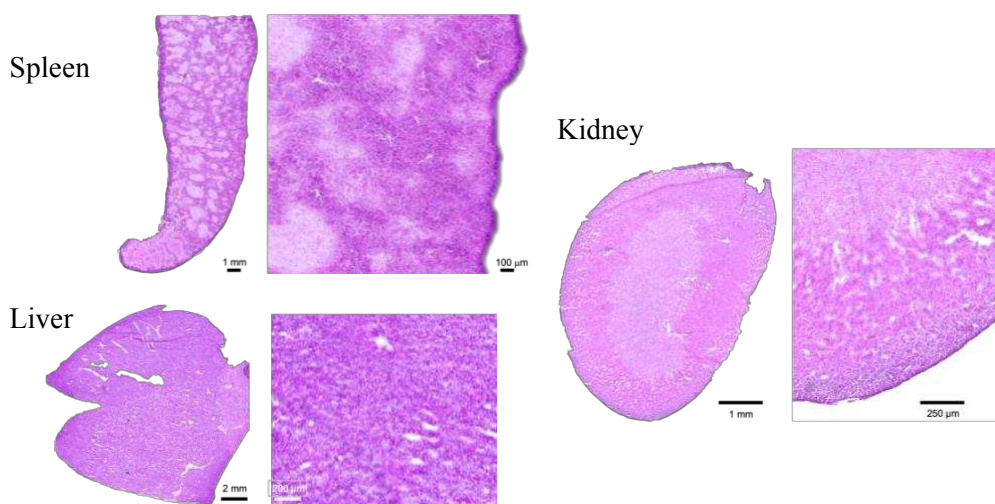


**Figure S17:** Tissue analysis of spleen, liver and kidney sections, 24 h after bolus injection of **SWIR-WAZABY-01**, showed the absence of histological toxicity at the microscopic level.

Mice (n=3) were injected intravenously with 200  $\mu\text{L}$  of **SWIR-WAZABY-01** (300  $\mu\text{M}$ ) and blood was collected just after injection and at the following times: 5, 10, 15, 30, 60, 120 and 300 minutes. Blood was centrifuged to sample and quantify the fluorescence in the plasma using the 50 mm lens and LP1.064 nm. The pharmacokinetic was calculated using Prism software, and fitted with two-phase decay equation.

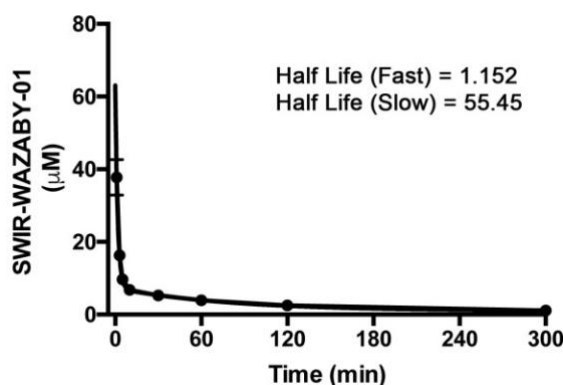


**Figure S18:** Plasma half-life of **SWIR-WAZABY-01** in mice, fitted with two-phase decay equation.

## References

- Jiao, L., Wu, Y., Wang, S., Hu, X., Zhang, P., Yu, C., Cong, K., Meng, Q., Hao, E., Vicente, M. G. (2014) Accessing near-infrared-absorbing BF2-azadipyromethenes via a push-pull effect. *J. Org. Chem.* 79, 1830-1835.
- Pliquett, J., Dubois, A., Racoeur, C., Mabrouk, N., Amor, S., Lescure, R., Bettaieb, A., Collin, B., Bernhard, C., Denat, F., et al. (2019) A Promising Family of Fluorescent Water-Soluble aza-BODIPY Dyes for in Vivo Molecular Imaging. *Bioconjug. Chem.* 30, 1061-1066.
- Dolomanov, O.V., Bourhis, L.J., Gildea, R.J., Howard, J.A.K., Puschmann, H. (2009) Olex2: A complete structure solution, refinement and analysis program. *J. Appl. Cryst.* 42, 339-341.
- Sheldrick, G.M. (2015) ShelXT-Integrated space-group and crystal-structure determination. *Acta Cryst.* A71, 38.
- Bruker, A.X.S., Madison, W.I. Software for the Integration of CCD Detector System Bruker Analytical X-ray Systems, after 2013.
- Sheldrick, G.M. (2015) Crystal structure refinement with ShelXL, *Acta Cryst.* C71, 3-8.

## Article 2: Lipoproteins interaction with water-soluble NIR-II emitting aza-BODIPYs boosts the fluorescence signal and favors selective tumor targeting

In the perspective of using the NIR-II emitting aza-BODIPY (*i.e.* SWIR-WAZABY-01) described in article 1 for NIR-II fluorescence-guided surgery, it was necessary first to explore how this aza-BODIPY is transported in the blood circulation, how it is taken up by tumor cells, and will it be suitable for a wide range of tumors. To address these questions, several *in vitro* and *in vivo* investigations were performed and the results are presented in article 2, in preparation, entitled “*Lipoproteins interaction with water-soluble NIR-II emitting aza-BODIPYs boosts the fluorescence signal and favors selective tumor targeting*”.

Compared to other contrast agents or drugs that interact mainly with plasma proteins in the circulation, SWIR-WAZABY-01 was shown to interact with plasma lipoproteins resulting in its fluorescence enhancement. Lipoprotein gel electrophoresis and lipoprotein ultracentrifugation assays confirmed this interaction. To observe if SWIR-WAZABY-01 interaction with lipoproteins influences its tumor uptake, SWIR-WAZABY-01 was administrated to mice bearing tumors with variable expression of lipoprotein receptors. Accordingly, variable accumulation profiles were observed. Comparing SWIR-WAZABY-01 accumulation profiles to the lipoprotein receptors expression in those tumors, a positive correlation was observed. In other words, SWIR-WAZABY-01 tended to accumulate in tumors with high lipoprotein receptors expression.

To conclude, this dye interacts with lipoproteins in the bloodstream, and can specifically identify and delineate tumors with high lipoprotein receptors expression like brain tumors (glioma and glioblastomas). In perspective to target a wider range of tumors regardless of their lipoprotein receptors expression, coupling SWIR-WAZABY-01 to biological targeting moieties such as antibodies or peptides could be performed, and this will be the subject of article 3.

To note, I was responsible for the biological investigations applied in article 2. The lipoprotein studies were performed at the “Lipids Nutrition Cancer laboratory” in Dijon, under the supervision of Dr. Thomas Gautier. Thanks to the GDR 2073 AIM mobility grant (2000 €) that I was granted, this two-week internship was possible. Another short stay is planned to finalize the results. This study was presented as a poster at the “16<sup>th</sup> European Molecular Imaging Meeting (EMIM 2021)”, in which I was awarded the “EMIM 2021 Poster Award”.

An overview of plasma lipoproteins structure, types, physiological role, and role as delivery vehicles in cancer, is discussed in the following section before article 2.

# Lipoproteins

## 1. Lipoproteins: General Overview

Lipoproteins are natural nanostructures present within biological fluids [189, 190]. They consist of a central hydrophobic core of cholesterol esters and triglycerides, surrounded by a hydrophilic monolayer of phospholipids, free cholesterol, and apolipoproteins (a specific type of proteins associated with lipoproteins) (Figure 68). The major role of lipoproteins is to carry the water-insoluble lipids, cholesterol, and triglycerides, within the circulation. The lipoproteins ensure the transport of the dietary lipids from the intestine into the liver and peripheral tissues (through exogenous lipoprotein pathway), the transport of the lipids from the liver into peripheral tissues (through endogenous lipoprotein pathway), and the transport of the lipids from peripheral tissues into the liver (through reverse cholesterol transport). These pathways will be discussed in detail in the next section.

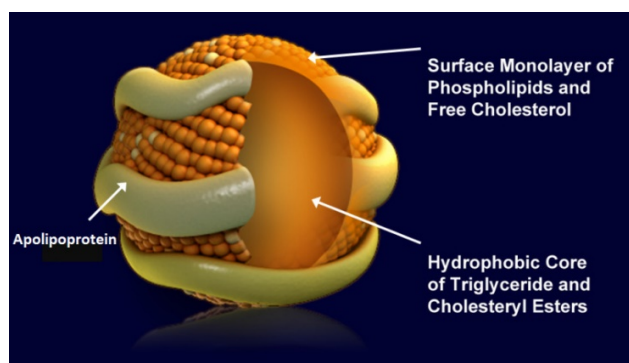


Figure 68: Schematic representation of lipoprotein structure [190].

According to their density, size, lipid, and apolipoprotein composition, seven classes of lipoproteins can be defined: chylomicrons, chylomicron remnants, Very Low-Density Lipoproteins (VLDL), Intermediate-Density Lipoproteins (IDL), Low-Density Lipoproteins (LDL), High-Density Lipoproteins (HDL), and Lipoprotein (a) Lp (a) (Table 5, Figure 69). Chylomicrons, VLDL, LDL, and HDL present the major classes. Apolipoproteins play an important role in lipoproteins formation and structure, interaction with lipoprotein receptors, and enzymes involved in lipoprotein metabolism.

Table 5: The seven lipoprotein classes and their corresponding densities, sizes, major lipids, and apolipoproteins composition [190].

Lipoprotein	Density (g/ml)	Size (nm)	Major Lipids	Major Apolipoproteins
<b>Chylomicrons</b>	< 0.930	75-1200	Triglycerides	Apo B-48, Apo C, Apo E, Apo A-I, A-II, A-IV
<b>Chylomicron Remnants</b>	0.930-1.006	30-80	Triglycerides Cholesterol	Apo B-48, Apo E
<b>VLDL</b>	0.930-1.006	30-80	Triglycerides	Apo B-100, Apo E, Apo C
<b>IDL</b>	1.006-1.019	25-35	Triglycerides Cholesterol	Apo B-100, Apo E, Apo C
<b>LDL</b>	1.019-1.063	18-25	Cholesterol	Apo B-100
<b>HDL</b>	1.063-1.210	5-12	Cholesterol Phospholipids	Apo A-I, Apo A-II, Apo C, Apo E
<b>Lp (a)</b>	1.055-1.085	~30	Cholesterol	Apo B-100, Apo (a)

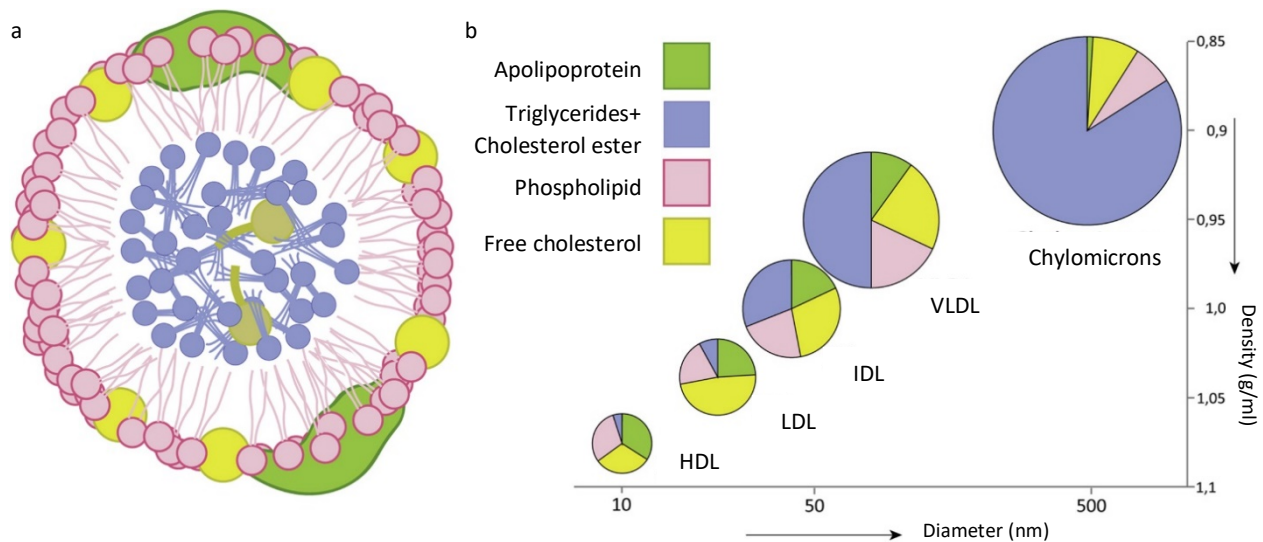


Figure 69: (a) Cross-section of a lipoprotein. (b) Composition and physicochemical characteristics of major lipoprotein classes [191].

## 2. Lipoprotein pathways

**The exogenous lipoprotein pathway** starts following ingestion of a fatty diet. In the intestine, dietary lipids (triglycerides and cholesterol) are incorporated into chylomicrons, the largest lipoproteins possessing Apo B-48 as the structural apolipoprotein and other apolipoproteins (Apo C-II, Apo A-V...). Following chylomicron release into the circulation (Figure 70, step 1), the chylomicrons triglycerides (TG) are hydrolyzed by muscle and adipose tissues Lipoprotein Lipases (LPL) releasing fatty acids (FA) that can be taken up by the cells. Apo C-II, present on the surface of the chylomicrons, serves as a co-factor for LPL activation. The catabolism of triglycerides results in the conversion of chylomicrons into chylomicron remnants (Figure 70, step 2). These later are smaller in size and enriched with cholesterol. Upon the loss of Apo C-II, the chylomicron remnants are cleared from the circulation by liver LDL receptor (LDLR) and LDL receptor-related protein (LRP), recognizing the chylomicron remnants Apo E (Figure 70, step 3).

Thus, the exogenous lipoprotein pathway mediates the transfer of dietary triglycerides (fatty acids) into muscle and adipose tissues for energy use and storage, and dietary cholesterol into the liver for VLDL and bile acids formation or secretion into the bile.

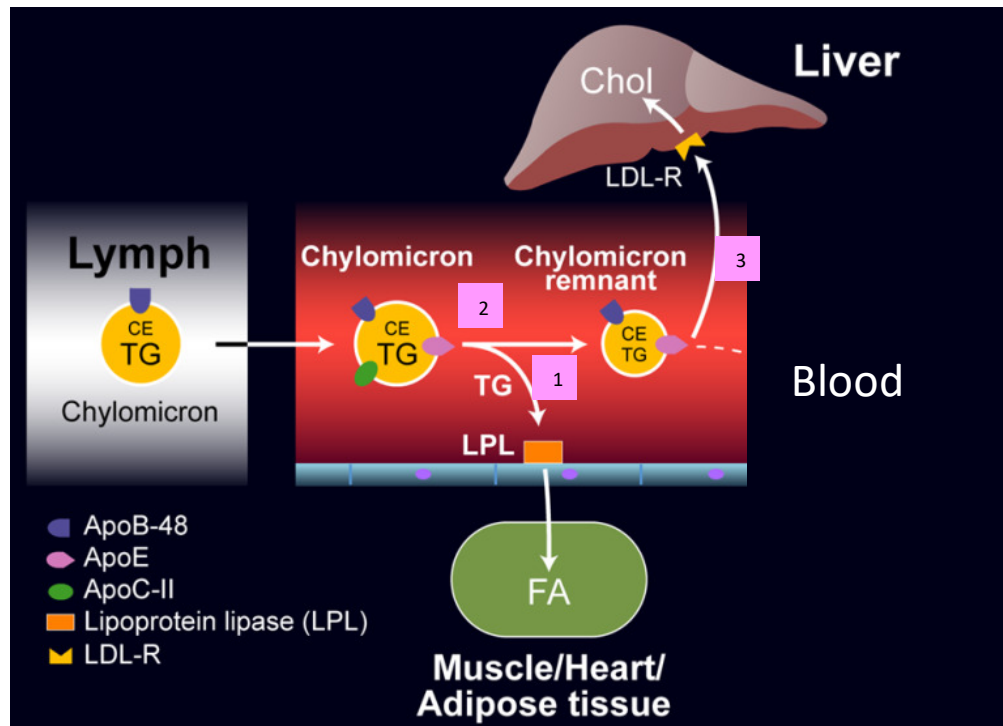


Figure 70: Schematic representation of the "Exogenous lipoprotein pathway" [190].

**The endogenous lipoprotein pathway** consists of VLDL formation in the liver. VLDL are triglyceride-rich lipoproteins, possessing Apo B-100 as the structural apolipoprotein and other apolipoproteins (Apo E, Apo C-II...). Following VLDL release into the circulation (Figure 71, step 1), VLDL triglycerides are hydrolyzed by muscle and adipose tissues LPL releasing fatty acids that can be taken up by the cells. Apo C-II, present on the surface of the VLDL, serves as a co-factor for LPL activation. The catabolism of VLDL triglycerides results in the formation of smaller, cholesterol-enriched transitory lipoprotein called IDL (Figure 71, step 2). Maintaining Apo B-100 and Apo E on its surface, part of the IDL is cleared from the circulation by liver LDLR and LRP, recognizing the IDL Apo E (Figure 71, step 3). However, the majority of the IDL (IDL triglycerides) are hydrolyzed by lipases, converting IDL into a lipoprotein with further enhanced cholesterol content, which is the LDL (Figure 71, step 4). LDL is the major cholesterol carrier in the circulation, possessing Apo B-100 as the only apolipoprotein. LDL is cleared by the liver (70%) or taken up by extrahepatic tissues through LDL receptor-mediated endocytosis by LDLR (Figure 71, step 5). LDLR recognizes the Apo B-100 present on the surface of LDL particles. Thus, the endogenous lipoprotein pathway mediates the transfer of triglycerides synthesized in the liver into muscle and adipose tissues, and cholesterol into the liver and peripheral tissues.



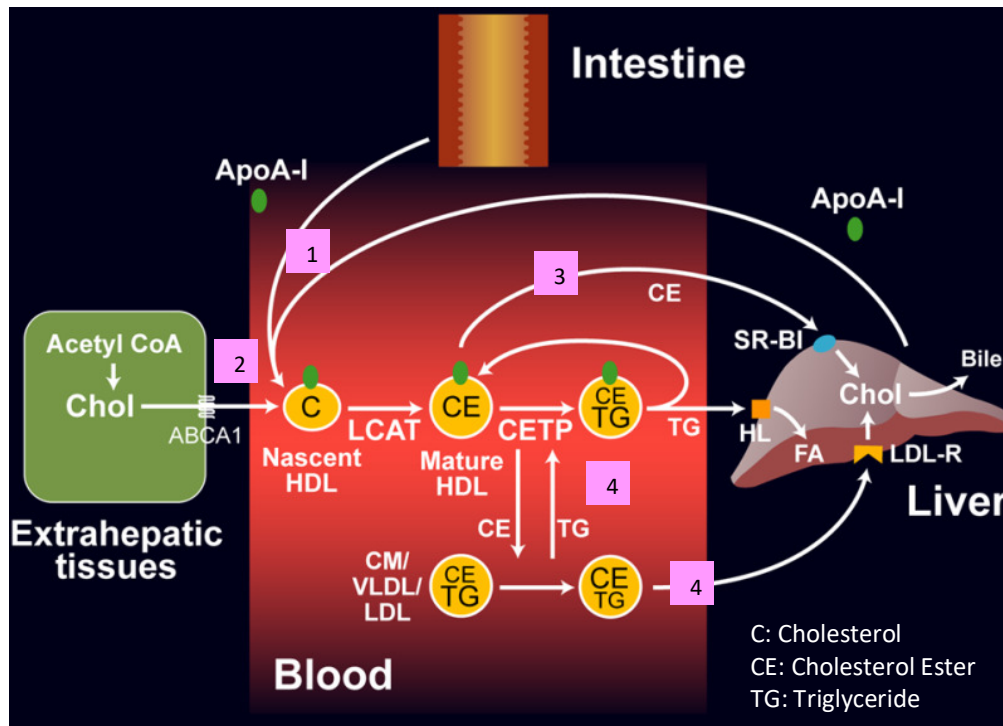


Figure 72: Schematic representation of the HDL metabolism and the “reverse cholesterol transport” [190].

Lipoprotein (a) (Lp (a)) is an LDL particle having an apolipoprotein (a) linked to its Apo B-100. Its function is not yet known.

### 3. Lipoprotein receptors

#### 3.1. LDL receptor (LDLR)

LDLR [190, 192] is present on the liver and other tissues, it recognizes Apo B-100 and Apo E containing lipoproteins thus allowing the uptake of LDL, IDL, and chylomicron remnants via receptor-mediated endocytosis.

Following lipoprotein binding to LDLR, the LDLR cluster into clathrin-coated pits that fold inward and pinch, forming endocytic vesicles. These vesicles fuse with endosomes and upon pH decrease, the LDL receptor can either dissociate from the lipoproteins and be recycled back to the cell surface, or sorted towards the lysosomes where they get digested/degraded, releasing the cholesterol content and amino acids (Figure 73).

The LDLR trip into and out of the cells requires around 10 minutes, thus providing an efficient way for cholesterol delivery into the cells.

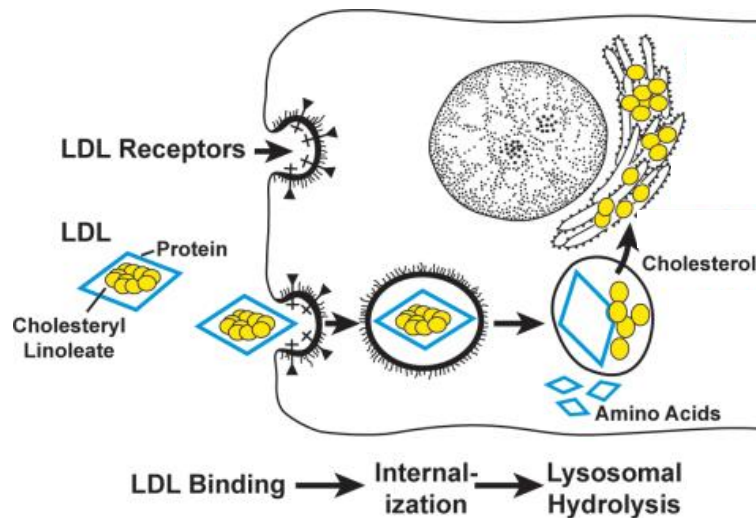


Figure 73: Schematic representation of the LDLR mediated endocytosis of lipoproteins, in mammalian cells [192].

### 3.2. LDL receptor-related protein (LRP)

LRP is a member of the LDL receptor family, it is present on the liver and other tissues. It recognizes Apo E-containing lipoproteins, thus mediating the uptake of chylomicron remnants and IDL (which are the VLDL remnants) [193].

### 3.3. Class B, type I scavenger receptor (SR-BI)

SR-BI [190, 194] is present on the liver, adrenal glands, ovaries, testes, macrophages, and other cells.

Following HDL binding to SR-BI, selective uptake of cholesterol into the liver and steroid-producing cells occurs through a hydrophobic channel made up of SR-BI extracellular domains (Figure 74). The cholesterol moves into the cells down a concentration gradient, without internalizing the entire HDL particle. The cholesterol-depleted HDL particles return into the circulation. It is worth noting that Apo A-I facilitates the interaction between HDL and SR-BI.

On the other hand, SR-BI mediates the efflux of cholesterol from macrophages and other cells into the HDL particles. Accordingly, the physiological function of SR-BI as an HDL receptor was validated.

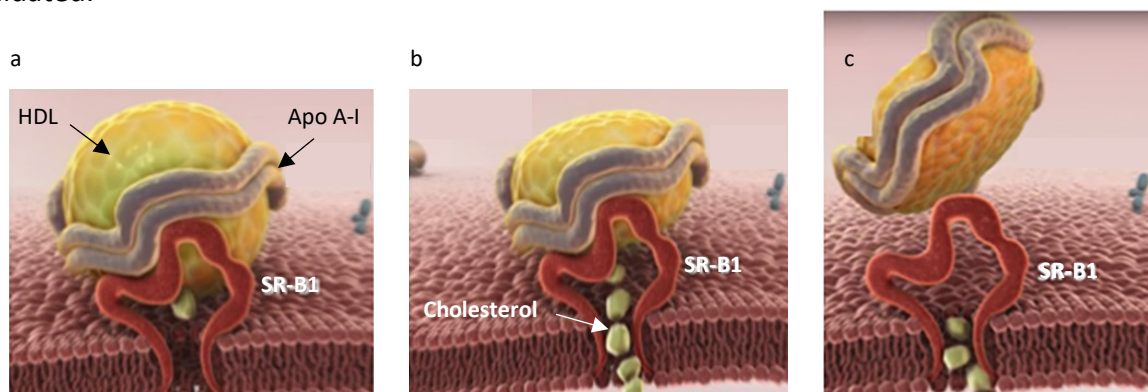


Figure 74: Schematic illustration of cholesterol transfer into liver cells via SR-BI. (a) Cholesterol-rich HDL binds to SR-BI present on liver cells via Apo A-I. (b) HDL delivers its cholesterol content through SR-BI. (c) Cholesterol-depleted HDL is released into the circulation [195].

### 3.4. ATP-Binding Cassette Transporter A1 (ABCA1)

ABCA1 is expressed in many cells including hepatocytes, enterocytes, and macrophages. It mediates the transport of cellular cholesterol and phospholipids into Apo A-I to form nascent HDL particles [190, 196].

### 3.5. ATP-Binding Cassette Transporter G1 (ABCG1)

ABCG1 is expressed in many different cell types and mediates the efflux of cellular cholesterol into mature HDL particles [190, 197].

## 4. Lipoproteins in cancer targeting

Considering the altered metabolism and the high demand for cholesterol in cancer cells, abnormal high expression of LDLR [198-200] and SR-BI [201, 202], receptors involved in cholesterol transfer into cells, has been widely observed in various tumor types including breast [198, 200, 202], prostate [201] and brain cancers [203, 204]. In this context, long-circulating lipoproteins (LDL and HDL) have been proposed and investigated for delivery of contrast/imaging agents [205, 206] and therapeutic drugs [207, 208] to tumors overexpressing these receptors. Biocompatibility, biodegradability, lack of immunogenicity, ability to carry hydrophobic and hydrophilic payloads, and the possession of natural molecular targets (i.e. LDLR, SR-BI), provided the main advantages of the LDL and HDL nanocarriers. VLDL and chylomicrons were rarely studied due to their short half-lives [209].

Both natural and synthetic lipoproteins were utilized [209, 210]. Natural lipoproteins were isolated from biological fluids mainly blood plasma, coupled to the imaging or therapeutic cargo then administered. However, challenges of lipoprotein isolation, possible disease transmission, and batch-to-batch inconsistency have led to the emergence of semi or fully synthetic lipoproteins. Lipoproteins were synthesized by mixing protein subunits (natural, recombinant, or synthetic apolipoproteins) with commercial lipids or other hydrophobic compounds in solution, generating nanoparticles mimicking the natural ones, in which cargos can be loaded. Yet, there is still a need for less-expensive, scalable, and commercially viable synthesis protocols to favor the clinical translation of these tumor-targeting vehicles. Regardless of these challenges, LDL and HDL delivery systems showed promising therapeutic potential and imaging capabilities in the cancer field.

# Lipoproteins interaction with water-soluble NIR-II emitting aza-BODIPYs boosts the fluorescence signal and favors selective tumor targeting

Ghadir Kalot<sup>1</sup>, Amélie Godard<sup>2</sup>, Benoit Busser<sup>1,3,4</sup>, Fabien Dalonneau<sup>1</sup>, Karl David Wegner<sup>5</sup>, Jean Luc Coll<sup>1</sup>, Franck Denat<sup>2</sup>, Ewen Bodio<sup>2</sup>, Christine Goze<sup>2</sup>, Thomas Gautier<sup>6</sup>, Lucie Sancey<sup>1</sup>

<sup>1</sup> Institute for Advanced Biosciences, Grenoble Alpes University, INSERM U1209, CNRS UMR 5309, Grenoble, France.

<sup>2</sup> Institut de Chimie Moléculaire de l'Université de Bourgogne, Université Bourgogne Franche-Comté, CNRS UMR 6302, Dijon, France.

<sup>3</sup> Institut Universitaire de France (IUF)

<sup>4</sup> Grenoble Alpes University Hospital (CHUGA), Grenoble, France.

<sup>5</sup> BAM Federal Institute for Materials Research and Testing, Richard-Willstaetter-Str. 11, 12489 Berlin, Germany.

<sup>6</sup> INSERM UMR1231, UFR Sciences de santé, Université Bourgogne Franche-Comté, Dijon, France.

## Abstract

Following intravenous administration, the interaction of exogenous molecules with circulating endogenous transporters can influence their photophysical properties as well as their fate, and especially their recognition by different cell types. This type of interaction can be used to target tissues of interest for drug delivery or imaging. In this study, we investigated the behavior of SWIR-WAZABY-01 fluorophore, a water-soluble aza-BODIPY dye emitting in the NIR-II region, both *in vitro* and *in vivo*. While the fluorescence emission of SWIR-WAZABY-01 was weak in aqueous solutions, it was dramatically magnified in the presence of plasma. Further analyses using lipoprotein gel electrophoresis and ultracentrifugation revealed interactions between SWIR-WAZABY-01 and plasma lipoproteins *in vitro*, in particular with LDL. Western blotting and immunohistology analysis revealed that tumors possessing high lipoprotein receptor expression are the ones with significant *in vivo* SWIR-WAZABY-01 tumor accumulation. Overall, we could conclude that SWIR-WAZABY-01 interacts with human lipoproteins enabling their NIR-II fluorescence properties and targeting capacity toward tumors expressing high levels of lipoprotein receptors. Accordingly, SWIR-WAZABY-01, by exploiting endogenous lipoproteins, arises as a new, relevant tool to efficiently label tumors.

## 1. Introduction

Twenty years ago, fluorescence imaging in the NIR-II window (1000-1700 nm) has emerged [1]. Providing less photon scattering and reduced autofluorescence, NIR-II imaging has surpassed imaging in the NIR-I region (700-900 nm), resulting in clearer images with an enhanced signal-to-noise ratio [2]. Pioneering NIR-II fluorophores were inorganic dyes including single-walled carbon nanotubes (SWCNTs) [3], quantum dots [4], and rare-earth-doped nanoparticles [5]. Organic NIR-II fluorophores were also developed based on donor-acceptor-donor systems [6] and cyanine dyes [7]. Despite promising tumor imaging capacities in preclinical tumor models, these NIR-II fluorophores presented long-term toxicities [8, 9], low quantum yields [4, 6], and poor water solubilities that hindered their clinical application.

To address these issues, we recently developed a water-soluble organic fluorophore based on the aza-BODIPY platform [10] with unique fluorescence properties in the NIR-II window and showing a favorable tumor-targeting capacity even in the absence of any vectorization. With no systematic toxicities observed, this aza-BODIPY named SWIR-WAZABY-01 presented great potential for clinical translation as compared to previously reported dyes. In the perspective of using SWIR-WAZABY-01 for NIR-II fluorescence-guided surgery, it is important to understand how the SWIR-WAZABY-01 accumulates in tumors and to validate its effectiveness for various tumor types.

Once introduced into the organism, exogenous molecules may interact with endogenous biomolecules, acquiring a unique biological identity that will influence their biodistribution, pharmacokinetics, and fate *in vivo* [11]. Among the endogenous molecules, interactions with plasma proteins, especially albumin, have been widely studied [12, 13]. However, limited studies have addressed the interaction of exogenous molecules with less abundant species such as plasma lipids [14] or lipoproteins [15].

Lipoproteins are naturally occurring macromolecular complexes composed of lipids and apolipoproteins [16]. They are responsible for transporting water-insoluble lipids (cholesterol, triglycerides...) in the circulation. According to their size, density, type of apolipoproteins and lipid composition, several classes of lipoproteins can be identified, with chylomicrons, very-low-density lipoproteins (VLDL), low-density lipoproteins (LDL), and high-density lipoproteins (HDL), being the major ones.

Cancer-related metabolic alterations are associated with higher demand for cholesterol that is required for cell proliferation and buildup of new cell membranes [17]. LDL and HDL provide a major source of cholesterol for tumor cells, evidenced by the elevated expression of LDL and HDL lipoprotein receptors: LDL receptor (LDLR) [18, 19] and Class B Scavenger receptor BI (SR-BI) [20, 21], observed in multiple cancer types. In this context, LDL and HDL lipoproteins have been

proposed as an appealing platform to deliver imaging [22, 23] and therapeutic molecules into tumors [24, 25], taking advantage of their biocompatibility, biodegradability, long-circulation time, and selective targeting toward cells overexpressing LDL and HDL lipoprotein receptors. Both isolated lipoproteins (from blood plasma) and synthetic ones were applied for tumor targeting.

To evaluate the potential of the SWIR-WAZABY-01 for fluorescence-guided surgery, the dye was administered intravenously to mice-bearing brain tumors (U-87 MG), pancreatic carcinoma (PANC-1), and Head and Neck carcinoma (CAL-33). We observed a huge difference in SWIR-WAZABY-01 tumor uptake between the different tumor types. To identify the rules driving the tumor accumulation, we investigated the possible interactions of the fluorophore with plasma content, in particular the interaction with lipoproteins. We observed that interactions between SWIR-WAZABY-01 and lipoproteins increased the fluorescence properties of the dye, and allowed a specific tumor accumulation toward cancer cells displaying a high expression of lipoprotein receptors (LDLR, SR-BI).

## 2. Materials and Methods

### **NIR-II imaging**

NIR-II fluorescence imaging was performed using a Princeton camera 640ST (900–1700 nm) coupled to a laser excitation source of  $\lambda = 830$  nm (50 mW/cm<sup>2</sup>). A short-pass excitation filter at 1000 nm (Thorlabs), and long-pass filters LP1064 nm (Semrock) and LP1250 nm (Thorlabs) were added to the NIR-II camera. A 25 mm lens with a 1.4 aperture (Navitar) was used to focus on the mice and drops.

### ***In vivo* NIR-II imaging**

All the animal experiments were approved by the Animal Ethics Committee of the French Ministry, under the agreement number APAFIS#8782-2017032813328550, and were performed according to the Institutional Animal Care and Use Committee of Grenoble Alpes University. These experiments were carried out within the *Small Animal Imaging Platform* (Drs X. Le Guével/V. Josserand), IAB Grenoble.

Female NMRI nude mice (6-week-old) (Janvier Labs, Le Genest-Saint Isle, France) were subcutaneously injected on their right flank with either 5 million of human glioblastoma astrocytoma U-87 MG cancer cells or 8 million of human pancreatic carcinoma of ductal cell origin PANC-1 cancer cells, or 5 million of human tongue squamous cell carcinoma CAL-33 cancer cells, or 10 million of human ovarian adenocarcinoma SKOV-3 cancer cells, or 8 million of human ovarian adenocarcinoma OVCAR-3 cancer cells (n=3/condition). The used cell lines were obtained from the European Collection of Authenticated Cell Cultures (ECACC, French authorization CODECOH DC-2020-4226). They were cultured in a 37°C humidified environment containing 5%

CO<sub>2</sub>, and in DMEM media supplemented with 10% heat-inactivated fetal bovine serum. For U-87 MG cell cultures 1% non-essential amino acids were added.

Following tumor growth, the mice were intravenously injected in their tail vein with 200  $\mu$ L of 600  $\mu$ M SWIR-WAZABY-01 solution diluted in PBS. Whole-body NIR-II fluorescence imaging was performed before and after administration at 5, 24, and 48 h. At 48 h, the mice were euthanized and their organs were sampled for *ex-vivo* fluorescence imaging. Acquired images were analyzed using Fiji software, and semi-quantitative fluorescence data were obtained by drawing regions of interest (ROI) around the organs.

### NIR-II imaging of drops

150  $\mu$ M SWIR-WAZABY-01 solution was serially diluted in blood plasma, bovine serum albumin (BSA) 40 g/L, glucose 5%, sodium chloride (NaCl) 0.9%, and phosphate buffered saline (PBS) solution. 10  $\mu$ L of the diluted samples were dropped on a paraffin paper and imaged by a NIR-II camera. Similarly, NIR-II images of SWIR-WAZABY-01 diluted in normal and fat-enriched plasma obtained from healthy and dyslipidemic donors were acquired.

### Experimental conditions

The following conditions were used for incubation prior to analyses using lipoprotein gel electrophoresis and lipoprotein ultracentrifugation. 150  $\mu$ L of each condition were prepared. A 100  $\mu$ M SWIR-WAZABY-01 solution was selected to obtain a good fluorescence signal without quenching. LDL, HDL, and VLDL, isolated from blood plasma by density-gradient ultracentrifugation were used at their physiological concentrations indicated by “[ ]p” in Table 1.

**Table 1:** Experimental conditions assessed using lipoprotein gel electrophoresis and lipoprotein ultracentrifugation.

Experimental condition	Final volume, 150 $\mu$ L (100 $\mu$ M SWIR-WAZABY-01)	
PBS + Plasma	15 $\mu$ L PBS	135 $\mu$ L Plasma
SWIR-WAZABY-01 + PBS	15 $\mu$ L SWIR-WAZABY-01	135 $\mu$ L PBS
SWIR-WAZABY-01 + Plasma	15 $\mu$ L SWIR-WAZABY-01	135 $\mu$ L Plasma
SWIR-WAZABY-01 + LDLp	15 $\mu$ L SWIR-WAZABY-01	135 $\mu$ L [LDL]p= 1.5 g/L
SWIR-WAZABY-01 + HDLp	15 $\mu$ L SWIR-WAZABY-01	135 $\mu$ L [HDL]p= 0.45 g/L
SWIR-WAZABY-01 + VLDLp	15 $\mu$ L SWIR-WAZABY-01	135 $\mu$ L [VLDL]p= 0.5 g/L

### Lipoprotein electrophoresis on agarose gel

Lipoprotein gel electrophoresis (BIOTEC-FISCHER Agarose Gel Kit LPE) separates plasma lipoproteins (LDL, VLDL, and HDL) according to their electrostatic charges.

Five (5)  $\mu$ L of each experimental condition were loaded onto the agarose gel. Following 30 min of migration, the gel was fixed and dried. Fluorescence imaging of the gel was performed to localize the SWIR-WAZABY-01 (ChemiDoc MP imaging system with  $\lambda_{\text{Ex.}} = 835$  nm and  $\lambda_{\text{Em.}} = 850$  nm), then Sudan Black staining allowed to localize the different lipoproteins. Superimposing the

fluorescence and the black/white images allowed the determination of possible SWIR-WAZABY-01-lipoprotein interactions.

### **Lipoprotein ultracentrifugation**

Three-step sequential ultracentrifugation, in TLA100 rotor (Beckman, Palo Alto, CA), was used to fractionate plasma into its three lipoprotein components (VLDL, LDL, and HDL) and free proteins according to their densities: VLDL fraction ( $d < 1.006$ ), LDL fraction ( $1.006 < d < 1.063$ ), HDL fraction ( $1.063 < d < 1.21$ ) and protein fraction ( $d > 1.21$ ). Densities were adjusted by mixing the samples with PBS or KBr solutions ([KBr]) with the appropriate density.

The sequential ultracentrifugation was done as follows:

First run: 50  $\mu$ L of plasma gently mixed with 150  $\mu$ L of PBS, in a thick wall polycarbonate tube (230  $\mu$ L, 7 x 20 mm – 4 000Pk, Beckman Coulter), was subjected to an ultracentrifugation run of 100 000 turns/min for 2 h, leading to the separation of VLDL (at top). Second run: the non-separated components of the 1<sup>st</sup> run (at the bottom, 50  $\mu$ L) were collected, mixed with 50  $\mu$ L of [KBr] = 1.125 and 100  $\mu$ L of [KBr] = 1.063, and subjected to a second ultracentrifugation run of 100 000 turns/min for 3 h. By the end of the second run, LDL was collected at the top. Third run, the non-separated components of the 2<sup>nd</sup> run (at the bottom, 50  $\mu$ L) were collected, mixed with 50  $\mu$ L of [KBr] = 1.357 and 100  $\mu$ L of [KBr] = 1.21, and subjected to a third ultracentrifugation run of 100 000 turns/min for 5.5 h. This final step separated the HDL (at top) from free proteins being at the bottom of the tube.

Overall, 50  $\mu$ L of each experimental condition was subjected to sequential ultracentrifugation, resulting in four fractions (VLDL, LDL, HDL, and free proteins). These fractions (50  $\mu$ L each) were transferred into a black bottom 96-well-plate, and the SWIR-WAZABY-01 fluorescence was collected at 850 nm following its excitation at 638 nm (TECAN plate reader).

### **Western blot**

U-87 MG, PANC-1, and CAL-33 tumor cells cultured in 2D were harvested, washed with PBS, lysed and their protein content was quantified using Micro BCA™ Protein Assay Kit (Thermo Fisher Scientific). Forty micrograms of protein/cell line were loaded into a 12% polyacrylamide gel. Following migration/electrophoresis, the proteins were transferred onto an activated PVDF (polyvinylidene difluoride) membrane (#10600023, Amersham). The membrane was then blocked with 5% milk for 1 h at RT, and incubated with primary antibodies overnight at 4°C: anti-LDL receptor antibody (1/1000, Abcam [EP1553Y] (ab52818)), anti-scavenging receptor SR-BI antibody (1/2000, Abcam [EPR20190] (ab217318)), and anti-GAPDH antibody (1/1000, SC-365062, Santa Cruz Biotechnology) serving as loading and transfer control. The membrane was then incubated with the secondary antibodies, anti-mouse/rabbit-horseradish peroxidase HRP (1/2000, #7076S, Cell Signaling Technology) for 1h at RT. The proteins (LDLR/SR-B1/GAPDH) were finally revealed using Clarity Western ECL Substrate (Bio-Rad), and western blot imaging was performed using Fusion FX (Vilber). LDLR/SR-BI bands intensities were quantified and normalized to GAPDH bands in each cell line, using ImageJ software.

### Immunohistochemical analyses

Excised tumor tissues (U-87 MG, PANC-1, CAL-33) were frozen in OCT-embedding medium (VWR international, Fontenay-sous-Bois, France), cut into 7  $\mu\text{m}$  thick sections using a cryomicrotome and mounted onto SuperFrost Ultra Plus slides (Thermo Fisher Scientific). The sections were then fixed with 4% formalin, subjected to heat-mediated antigen retrieval, blocked with BLOXALL (SP600, Vector laboratories) and 2.5% horse serum (MP 7401, Vector laboratories), incubated with 1<sup>st</sup> antibodies (anti-LDLR antibody [EP1553Y] (ab52818) or SR-BI antibody [EPR20190] (ab217318)) overnight at 4°C, incubated with 2<sup>nd</sup> antibody ImmPRESS™ HRP Polymer Anti-Rabbit IgG for 30 min at RT, and revealed using ImmPACT™NovaRED™Diluent (SK 4805, Vector laboratories). To localize the nucleus, the slides were counterstained with Hematoxylin. Finally, the slides were dehydrated using ethanol and xylene, mounted with merckoglass and coverslips. The sections were imaged using Zeiss AxioImager M2 microscope.

### 3. Results

Recently, we developed the first water-soluble aza-BODIPY dye (**Figure 1a**) emitting in the NIR-II window (named SWIR-WAZABY-01), with an emission peak at 960 nm and an emission tail reaching 1'200 nm (**Figure 1b,c**), and evaluated its capability for tumor imaging *in vivo*. Without any specific targeting moiety, SWIR-WAZABY-01 clearly stained subcutaneous U-87 MG tumors, with prolonged retention up to one week (**Figure 1d**), and favorable tumor to healthy tissue ratios (**Figure 1e,f**). It was mainly eliminated by the hepatic route (**Figure 1g**) and no systemic toxicities were observed. Altogether these data present SWIR-WAZABY-01 as a promising candidate for biomedical applications, in particular, NIR-II fluorescence-guided surgery [10].

Considering that SWIR-WAZABY-01 has unique NIR-II fluorescence properties and significant tumor-targeting capacity for U-87 MG tumors, we investigated the biological behavior of the fluorophore and its tumor accumulation properties in different tumor types. The fluorophore was administered to mice bearing subcutaneous tumors of different origins: U-87 MG (human glioblastoma astrocytoma), PANC-1 (human pancreatic carcinoma of ductal cell origin), CAL-33 (human tongue squamous cell carcinoma), SKOV-3, and OVCAR-3 (human ovarian adenocarcinomas) (see Supplementary Information for SKOV-3 and OVACR-3, Figure S1). Similar to previously reported data, the SWIR-WAZABY-01 rapidly reached and accumulated in U-87 MG and PANC-1 tumors (**Figure 2a**), and the tumors were clearly evidenced at both 24 and 48 h post-administration. On the contrary, CAL-33, SKOV-3, and OVCAR-3 tumors were difficult to visualize at the different imaging time points (**Figure 2a, Figure S1a**). Furthermore, *ex-vivo* U-87 MG and PANC-1 tumors possessed favorable Tumor/Muscle ratio (~7) and Tumor/Skin ratio (~1), which were twice those achieved for CAL-33, SKOV-3, and OVCAR-3 tumors (**Figure 2b, Figure S1b**). This inconsistency in the SWIR-WAZABY-01 tumor uptake could be attributed to the enhanced permeability and retention effect (EPR effect) and/or could reveal a specificity in tumor accumulation induced by a selective tumor targeting mechanism.

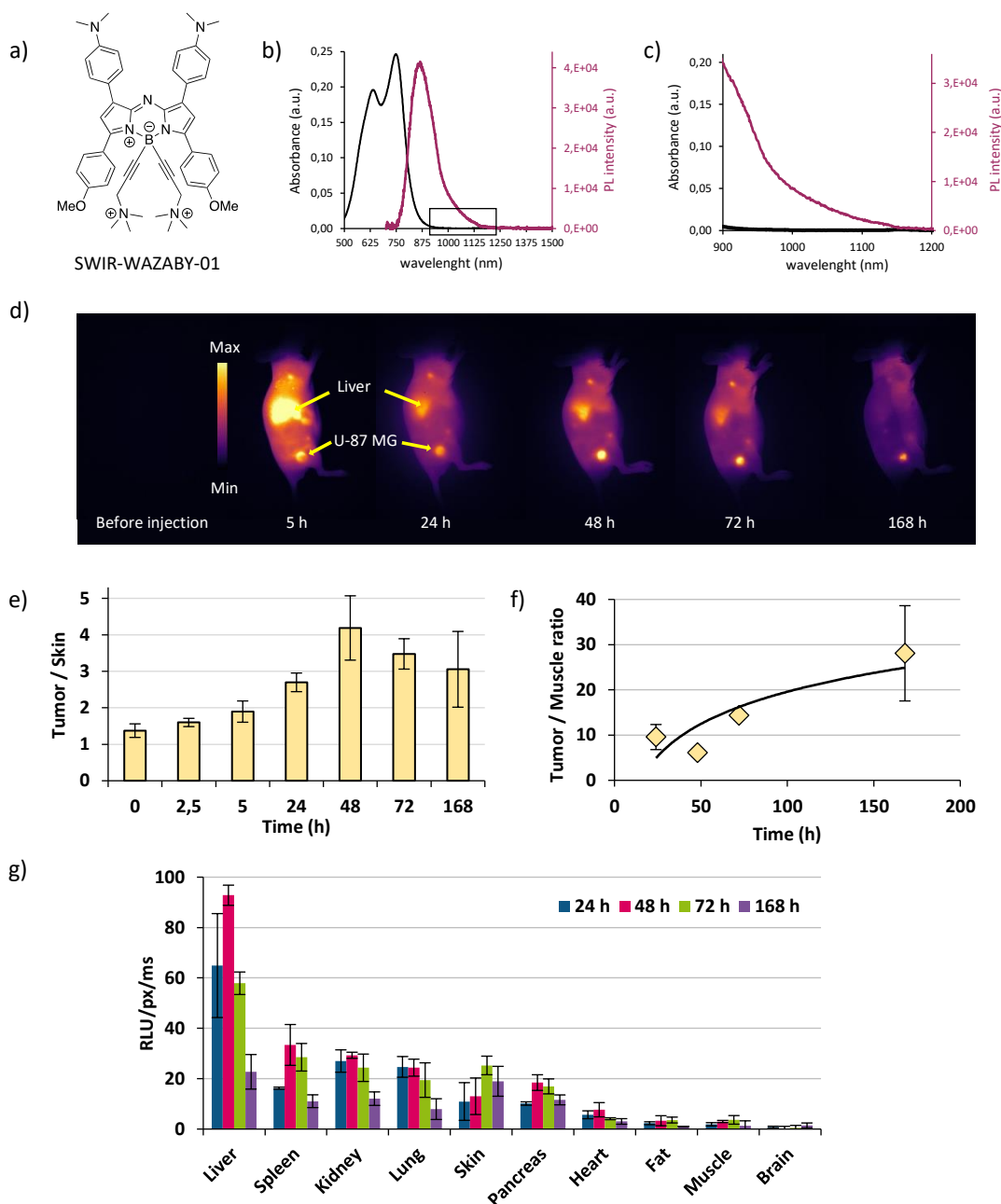


**Figure 1: SWIR-WAZABY-01 NIR-II fluorescence properties and tumor-targeting capacity.** (a) Structure of the water-soluble NIR-II emitting SWIR-WAZABY-01. (b) Absorption (black line) and fluorescence emission spectra (purple line) of SWIR-WAZABY-01 in mouse plasma. (c) Expansion of the spectra shown in (b). (d) NIR-II fluorescence imaging of a mouse bearing subcutaneous U-87 MG tumor, before and up to 7 days post SWIR-WAZABY-01 administration (200  $\mu$ L at 600  $\mu$ M). Tumor/skin ratios (e) and tumor/muscle ratios (f) obtained from *in-vivo* and *ex-vivo* analyses respectively. (g) SWIR-WAZABY-01 biodistribution at different time points. The results are expressed as the mean  $\pm$  standard deviation (S.D.) (n=12) (Adapted with permission from KALOT et al. Bioconjugate Chem 2020, copyright © 2020, American Chemical Society).

To address these hypotheses and to understand the mechanism of tumor accumulation, it was essential first to decipher how this NIR-II emitting fluorophore is carried in the blood stream. Is

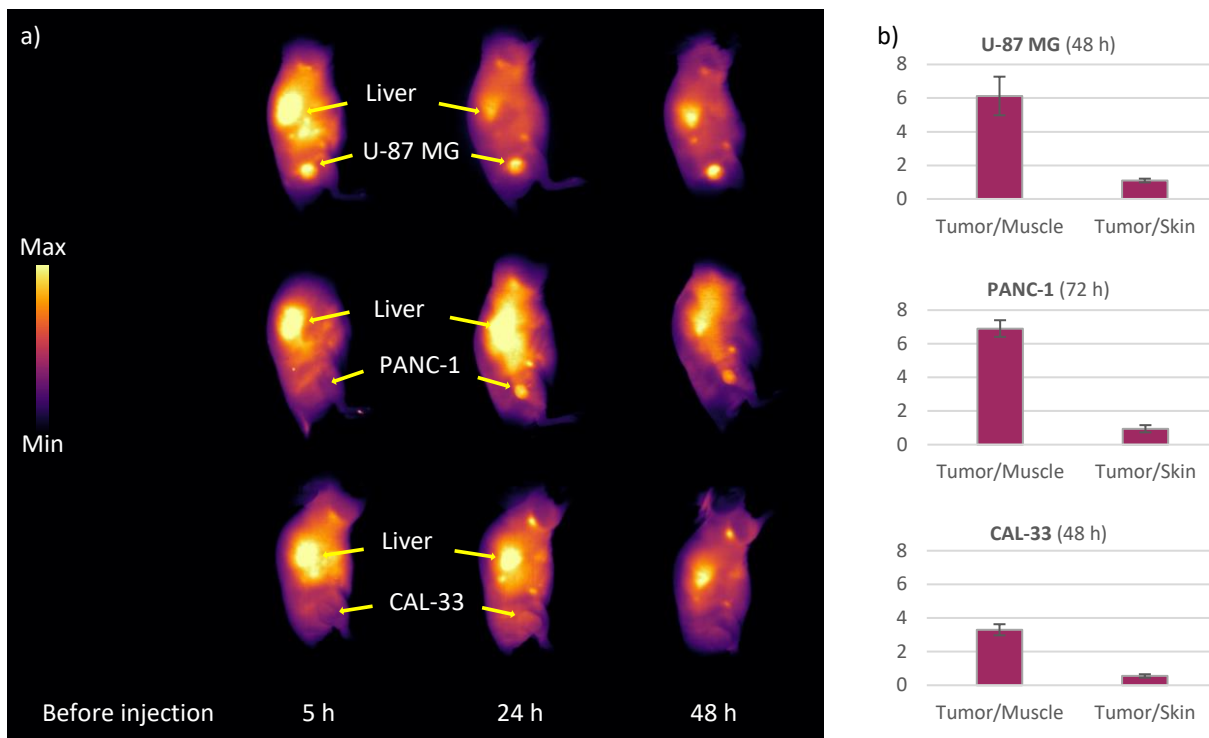


**Figure 2: SWIR-WAZABY-01 tumor-dependent accumulation and staining.** (a) NIR-II fluorescence imaging of mice bearing subcutaneous U-87 MG, PANC-1, and CAL-33 tumors before and at 5, 24 and 48 h post intravenous administration of SWIR-WAZABY-01 (200  $\mu$ L at 600  $\mu$ M). Tumors and livers are indicated by yellow arrows. Note: mice bearing PANC-1 tumors were imaged at 1 h post administration instead of 5 h. (b) *Ex-vivo* tumor/muscle and tumor/skin ratios calculated from excised organs. The results are expressed as the mean  $\pm$  S.D. (n=3/condition).

it freely transported, linked to protein corona, or coupled to other plasma components? To this end, the fluorophore was serially diluted in several media and assessed for its fluorescence signal. As indicated in **Figure 3a,c**, and **Figure S2d**, the SWIR-WAZABY-01 fluorescence was quenched in PBS, NaCl 0.9%, and glucose 5%. When diluted in the presence of 40 g/L of albumin, the fluorescence was faintly restored. However, the fluorophore diluted in blood plasma was strongly fluorescent, as indicated by the recovery of the drops' fluorescent signal. The fluorescence signal was almost similar in DMSO and blood plasma (See ESI **Figure S2a**). Therefore, we postulated that some interactions with plasma components, other than albumin, drive the SWIR-WAZABY-01 distribution and optical properties. Additionally, mixing the SWIR-WAZABY-01 with dyslipidemic (fat-rich) plasma further enhanced its fluorescence compared to normal plasma (**Figure 3b**, **Figure S2b,c**). The fluorescence enhancement suggested that plasma lipids or lipoproteins may play a role in the SWIR-WAZABY-01 fluorescence, and may interact directly with the dye.

To investigate this assumption, two lipoprotein separation techniques were performed: lipoprotein gel electrophoresis and sequential ultracentrifugation. Lipoprotein gel electrophoresis allows the separation of the main human plasma lipoproteins, i.e. LDL, VLDL,

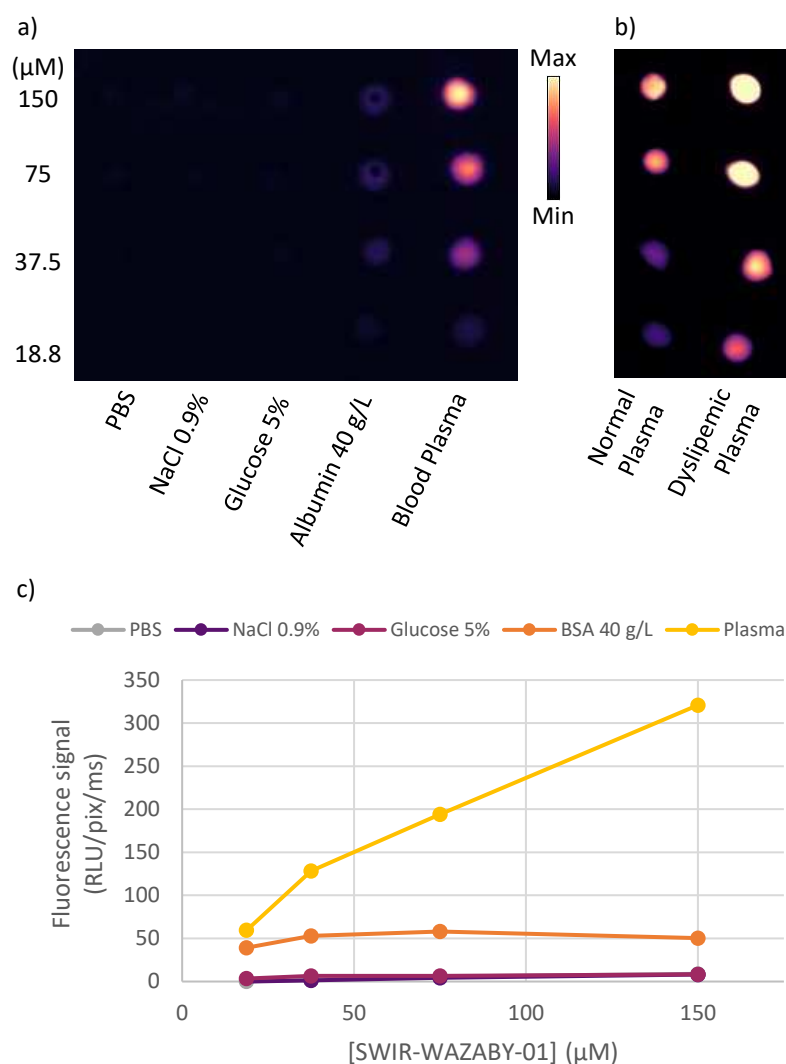


**Figure 3: SWIR-WAZABY-01 solvent-dependent fluorescence.** (a) NIR-II fluorescence image of SWIR-WAZABY-01 (150 μM) serial dilution in phosphate buffered saline (PBS), sodium chloride (NaCl) 0.9%, glucose 5%, bovine serum albumin (BSA) 40 g/L, and blood plasma. (b) NIR-II fluorescence image of SWIR-WAZABY-01 serial dilution in normal and dyslipemic (fat-enriched) blood plasma, obtained from healthy and dyslipidemic donors respectively. (c) Quantification of the drops fluorescence in (a).

and HDL (**Figure 4a**), according to their electrostatic charges. The lipoproteins were then stained by Sudan black staining to be visualized on the gel (**Figure 4b**, lane 1). In absence of fluorophore, no fluorescence signal was evidenced in the plasma. In absence of plasma, the SWIR-WAZABY-01 fluorescence signal migrated in direction of the anode (lane 2) in a faint and diffuse band. Colocalization between the SWIR-WAZABY-01 fluorescence signal and the lipoprotein bands was observed in the mix of SWIR-WAZABY-01 and plasma (lane 3). The main interaction matched with the LDL band. This strong colocalization pattern was also detected in lane 4 containing the SWIR-WAZABY-01 mixed with a single lipoprotein fraction of LDLp (“p” for used at physiological concentration). On the contrary, weak colocalizations were observed in presence

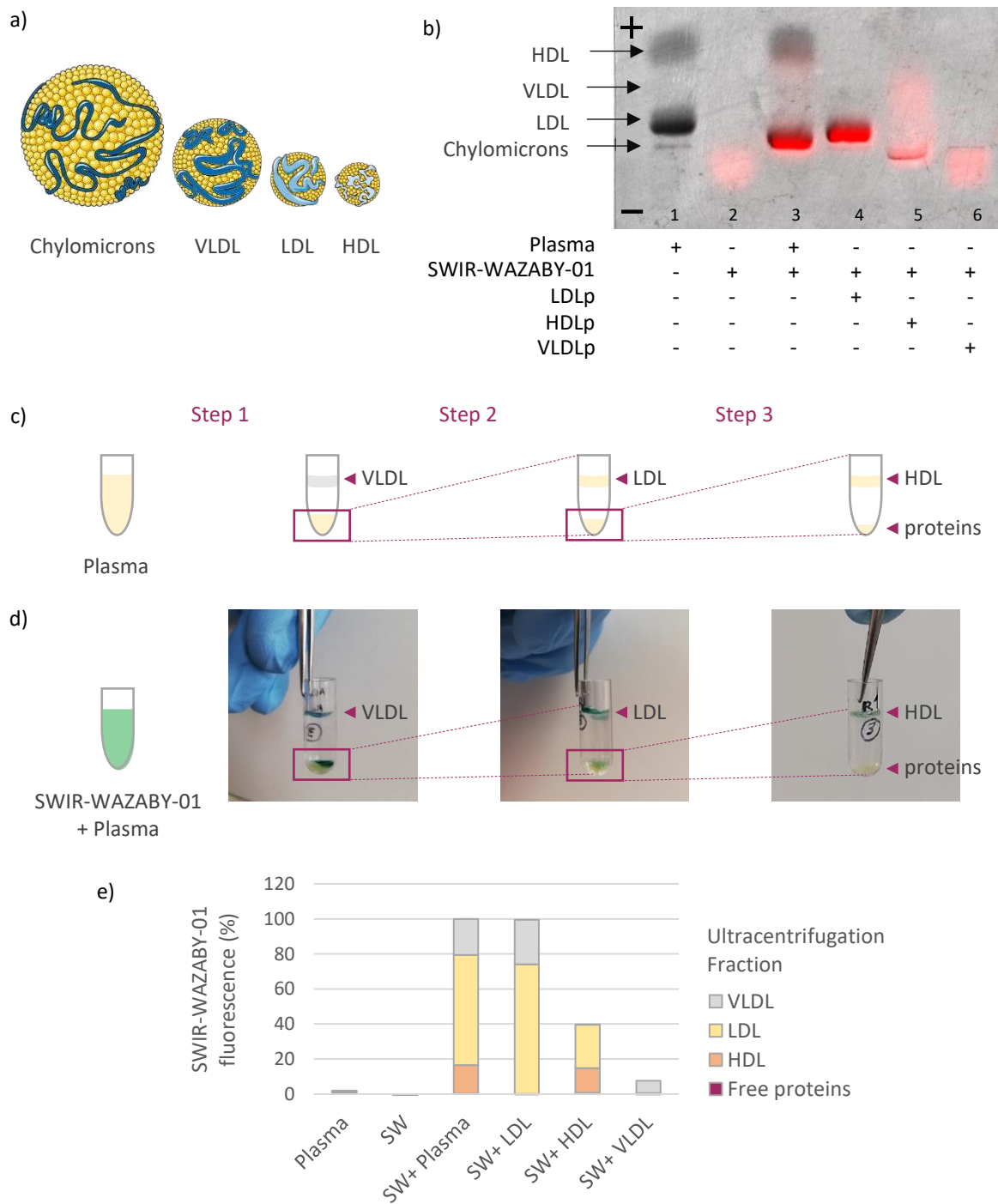


**Figure 4: Aza-BODPIY interaction with plasma lipoproteins revealed by lipoprotein gel electrophoresis and ultracentrifugation.** (a) Illustration of the lipoproteins (chylomicrons, VLDL, LDL and HDL) (smart.servier.com). (b) Overlay of SWIR-WAZABY-01 fluorescence image and black/white image of the lipoprotein electrophoresis gel. SWIR-WAZABY-01 fluorescence is designated by red color while the lipoprotein bands (LDL, VLDL, HDL) are detected in gray, thanks to Sudan Black staining. (c) Illustration of the three-step ultracentrifugation assay of blood plasma, resulting in the separation of plasma lipoproteins (VLDL, LDL and HDL) and proteins, according to their densities. (d) Photos illustrating the SWIR-WAZABY-01 (blue-green color) co-localization with plasma lipoproteins (VLDL/ LDL/ HDL) after each ultracentrifugation step, in the SWIR-WAZABY-01 + plasma condition. (e) Quantification of SWIR-WAZABY-01 (SW) fluorescence in the 4 ultracentrifugation fractions (VLDL, LDL, HDL and free proteins) of each experimental condition.

of SWIR-WAZABY-01 mixed with HDLp, or VLDLp (lane 5, and 6 respectively). Altogether these

data demonstrate that the SWIR-WAZABY-01 fluorophore interacts with plasma lipoproteins, mainly the LDL and to a lesser extent HDL and VLDL.

To further confirm the SWIR-WAZABY-01-lipoprotein interactions, lipoproteins were also isolated from human plasma using ultracentrifugation assay. Following 3-step sequential ultracentrifugation of plasma, 4 fractions were separated according to their densities, corresponding respectively to VLDL, LDL, HDL, and free proteins (**Figure 4c**). The SWIR-WAZABY-01 solution, which color is blue-greenish, allowed the identification of the fluorophore within the fractions before its quantification. A co-localization between the SWIR-WAZABY-01 and the three lipoproteins fractions (VLDL, LDL, HDL) was observed after each ultracentrifugation run of the mix SWIR-WAZABY-01 and human plasma solution, while no co-localization was observed with the protein fraction (**Figure 4d**). Furthermore, the fluorescence of the 4 fractions (VLDL, LDL, HDL, and free proteins) of each experimental condition was quantified (**Figure 4e**). The results evidenced that within the mix SWIR-WAZABY-01 and plasma, the LDL fraction contained the major fluorescence signal (62.7 % of total), followed by VLDL (20.6 %) and HDL (16.3 %) fractions, whereas no substantial fluorescence was detected in the free protein fraction. Interestingly, while the mix of SWIR-WAZABY-01 and a single fraction of LDLp evidenced a major interaction of the dye with the LDL, some fluorescence signal was surprisingly observed within the fraction corresponding to the VLDL. Therefore, we can hypothesize that the interaction of the low molecular weight fluorophore with the LDL, partially affects the density of the lipid moiety allowing the total LDL fraction to be spared into the LDL and VLDL fractions. Such results were also observed when mixing SWIR-WAZABY-01 and HDLp: a moderate fraction of the SWIR-WAZABY-01 fluorophore was quantified within the HDL condition (40%), and the density of the HDL was modified as evidenced by a large part of the fluorescence signal detected in the fraction corresponding to the LDL. The mix SWIR-WAZABY-01 with VLDLp confirmed the slight interaction of the 2 entities. No fluorescence was detected in the mix of SWIR-WAZABY-01 and PBS, or within the free protein fractions. Altogether, these results supported the hypothesis that the SWIR-WAZABY-01 interacts with plasma lipoproteins, predominantly with the LDL. LDL may therefore play a major role in SWIR-WAZABY-01 transport *in vivo*.

Bearing in mind that *in vivo* SWIR-WAZABY-01 could be distributed in the bloodstream coupled to lipoproteins and that several tumors overexpress lipoprotein receptors, we evaluated the influence of lipoprotein receptors expression in tumors on the SWIR-WAZABY-01 accumulation. The expression of LDLR and SR-B1 (i.e. the main receptors for LDL and HDL, respectively) were studied using western blotting of tumor cell extracts (**Figure 5a,b**) and immunohistochemical analysis of excised tumor sections (**Figure 5c**). The western blot analysis indicated a strong expression of the LDLR in the U-87 MG cell line while its expression was very faint or absent in PANC-1, CAL-33, SKOV-3, and OVCR-3 (see **Figure S3**). SR-B1 was overexpressed in PANC-1, and weakly expressed or not detected in U-87 MG, CAL-33, SKOV-3, and OVACR-3. These results were confirmed by immunohistology investigations on different tumor sections: U-87 MG

overexpressed the LDLR, PANC-1 overexpressed SR-B1, while both receptors were not or poorly expressed in the other cell lines. Comparing those lipoprotein receptors expression patterns to the SWIR-WAZABY-01 tumor accumulation *in vivo* (Figure 2 and Figure S1), lead to identifying a strong correlation between the SWIR-WAZABY-01 tumor accumulation and the tumor lipoprotein receptors expression. We can conclude that the expression of lipoprotein receptors by tumors, and more particularly LDLR and SR-BI expression, influences the SWIR-WAZABY-01 accumulation *in vivo*, additionally to the EPR effect.

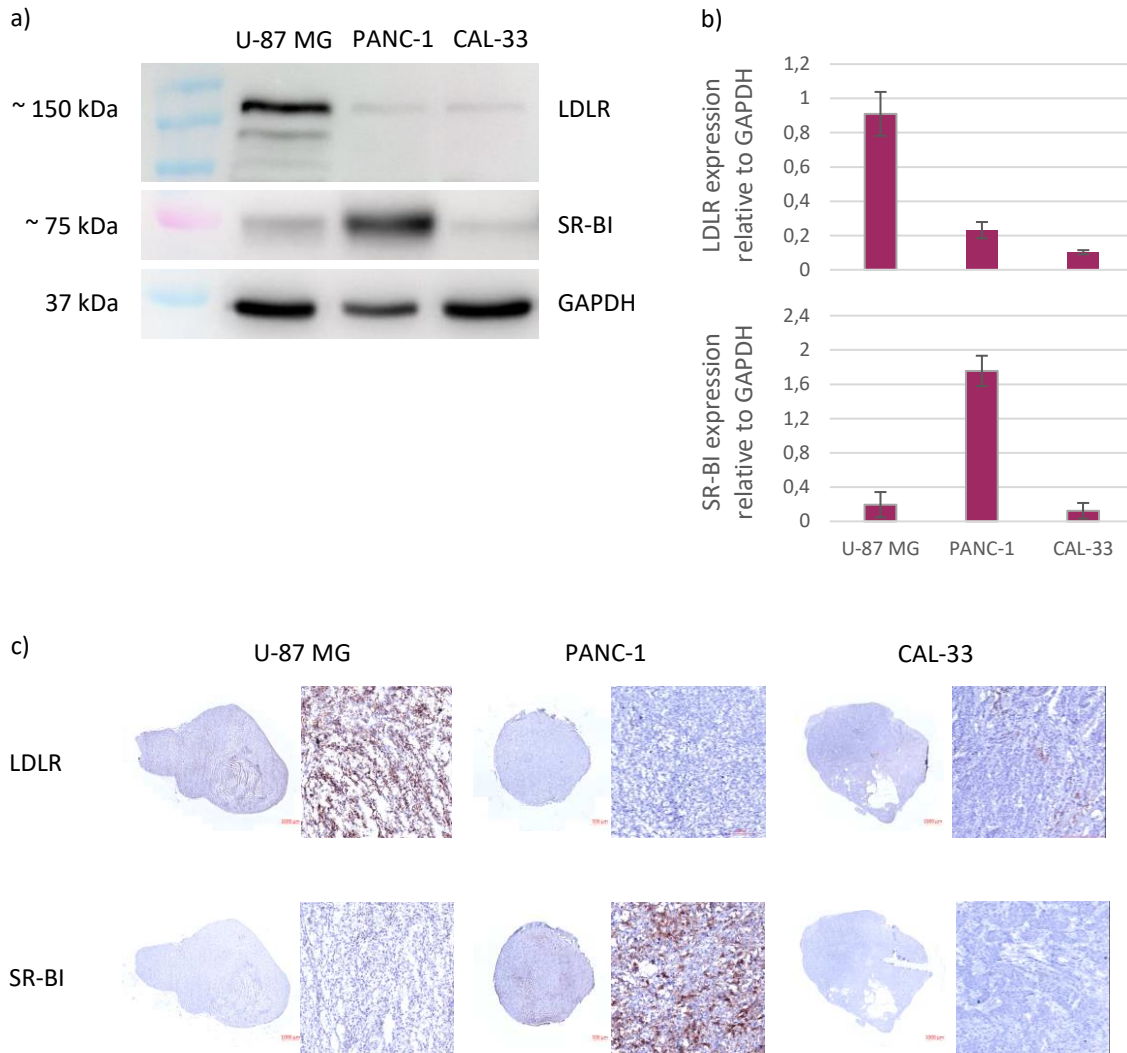


**Figure 5: Lipoprotein receptors expression profile in tumor cells (a) and resected tumors (b).** (a) Lipoprotein receptors (LDLR, SR-BI) expression in U-87 MG, PANC-1 and CAL-33 cells, assessed by western blotting of whole cell extracts. GAPDH served as a loading control. (b) Quantification of LDLR and SR-BI expression relative to GAPDH. The results are represented as the mean of 3 independent experiments  $\pm$  S.D. (c) Lipoprotein receptors (LDLR, SR-BI) expression in U-87 MG, PANC-1 and CAL-33 excised tumors, detected by immunohistochemical staining.

#### 4. Discussion

The development of NIR-II emitting fluorophores for image-guided surgery, aiming at discovering molecules with performant optical properties, favorable biological behavior in terms of water-solubility, enhanced pharmacokinetics, long-term retention, and selective uptake in the tumor area, is a real challenge. The pharmacokinetics properties are partly driven by potential interactions of the molecule of interest with plasma content. Albumin is the most abundant protein in plasma, and a remarkable carrier for many dyes [26], or chemical drugs [27, 28]. As any molecule administrated in the bloodstream, fluorophores can also interact with blood components. Previously reported studies investigated interactions of some BODIPYs with serum albumin [29] and blood plasma proteins [30]. Here, we investigated the interaction of a water-soluble NIR-II emitting aza-BODIPY derivative with plasma lipoproteins.

We investigated the possible interactions of the SWIR-WAZABY-01 with albumin and lipoproteins and discovered that SWIR-WAZABY-01 fluorophore mainly interacts with LDL lipoproteins, and to a lesser extent with HDL and VLDL lipoproteins, in human plasma *ex vivo* (**Figure 4b,e**). This finding could be explained by the quantitative and qualitative properties of the human lipoprotein system, with the LDL being the most abundant lipoprotein and the one possessing the highest amount of cholesterol [16].

Despite the functionalization of SWIR-WAZABY-01 on the boron atom that eases its water-solubility [31], SWIR-WAZABY-01 possesses a large aromatic structure that may facilitate its interactions with lipophilic structures similar to those present in lipoproteins [32]. Similar studies have reported the interaction of the fluorescent indocyanine green (ICG) with the hydrophobic pocket of the albumin [33]. In our case, we can postulate that the association of SWIR-WAZABY-01 with lipoproteins could also help to isolate the fluorophore and/or minimize its vibration, participating in the increase of fluorescence [33].

The interaction of SWIR-WAZABY-01 with the lipoproteins slightly modified both the global charge and density of these lipidic moieties. As the fluorophore is positively charged in solution, it increased the positive charge of the lipoproteins, as observed by the migration shift of lipoprotein bands towards the negative end of the membrane when mixed with the aza-BODIPY (**Figure 4b**). Similarly, the overall density of the lipidic vectors was decreased in presence of the dye (**Figure 4e**). These modifications constitute further proof of the tight interaction between the probe and the lipoproteins.

Since the LDL endocytic pathway and the HDL cholesterol delivery were proven to be highly active in malignant cancer cells, the use of LDL and HDL as endogenous drug carriers to target cancer cells has been proposed. Such vectorization has been reported for the delivery of siRNA [34]/ genes [35], chemotherapies [25, 36]/ anticancer drugs [37], and fluorescent probes [22, 23].

However, the complexity of LDL and HDL isolation, storage, and drug incorporation strategies, hindered its industrial development. Similarly, the development of synthetic LDL and HDL-like particles was highly complicated. In the present case, the interaction between SWIR-WAZABY-01 and endogenous LDL and HDL occurs spontaneously after SWIR-WAZABY-01 administration. Therefore, lipoproteins act as natural carriers vectorizing SWIR-WAZABY-01 towards cells overexpressing LDLR and SR-BI, respectively. Similar spontaneous *in vivo* loading of squalenoylated anti-cancer drugs into lipoproteins and cancer targeting have been reported [38, 39].

The selective targeting of SWIR-WAZABY-01 could help to specifically identify and delineate tumor lesions characterized with high LDLR expression such as gliomas and glioblastomas [37], and high SR-BI expression such as breast [21] and prostate cancers [20]. This specific vectorization was evidenced in LDLR-positive U-87 MG subcutaneous tumors and SR-BI-positive Panc-1 subcutaneous tumors (**Figure 2**). Additionally, SWIR-WAZABY-01 was able to cross the blood-brain barrier and accumulate in orthotopic glioblastoma tumors with a tumor/healthy brain ratio of ~5 (**Figure S4**).

However, the NIR-II emitting fluorophore could also be modified for chemical ligation to a biological ligand as a small molecule or antibody for wide use in fluorescence-guided surgery.

## 5. Conclusion

In conclusion, we demonstrated the preferential interaction of the NIR-II emitting SWIR-WAZABY-01 with LDL which favors specific targeting of tumors-expressing the LDL receptor *in vivo*. Such natural carriers will be of particular interest for future fluorescence-guided surgery investigations.

## Funding

The research in this paper is funded by FRM ECO201806006861, GDR CNRS AIM mobility grant, Oncostarter project of the cancerôpole CLARA (Agnostic project), France Life Imaging (Thera-BODIPY), GEFLUC Grenoble Dauphiné Savoie, ANR (JCJC ANR-18-CE18-0012).

## Acknowledgments

The authors would like to thank Dr. Olivier Lamotte (Agroécologie – AgroSup, CNRS, INRAE, University of Burgundy, Dijon) for using the TECAN plate reader, and the research engineer Maxime Henry for technical help in orthotopic glioblastoma tumor implantation. The authors are grateful to V. Jossierand from the OPTIMAL platform (platform responsible) and X. Le Guével for technical access and optical experiments.

## References

1. Welsher, K., et al., *A route to brightly fluorescent carbon nanotubes for near-infrared imaging in mice*. *Nat Nanotechnol*, 2009. **4**(11): p. 773-80.
2. Hong, G., A.L. Antaris, and H. Dai, *Near-infrared fluorophores for biomedical imaging*. *Nature Biomedical Engineering*, 2017. **1**(1): p. 0010.
3. Ghosh, D., et al., *Deep, noninvasive imaging and surgical guidance of submillimeter tumors using targeted M13-stabilized single-walled carbon nanotubes*. *Proc Natl Acad Sci U S A*, 2014. **111**(38): p. 13948-53.
4. Hong, G., et al., *In vivo fluorescence imaging with Ag2S quantum dots in the second near-infrared region*. *Angew Chem Int Ed Engl*, 2012. **51**(39): p. 9818-21.
5. Naczynski, D.J., et al., *Rare-earth-doped biological composites as in vivo shortwave infrared reporters*. *Nat Commun*, 2013. **4**: p. 2199.
6. Antaris, A.L., et al., *A small-molecule dye for NIR-II imaging*. *Nat Mater*, 2016. **15**(2): p. 235-42.
7. Meng, X., et al., *Hypoxia-triggered single molecule probe for high-contrast NIR II/PA tumor imaging and robust photothermal therapy*. *Theranostics*, 2018. **8**(21): p. 6025-6034.
8. Liu, Z., et al., *Circulation and long-term fate of functionalized, biocompatible single-walled carbon nanotubes in mice probed by Raman spectroscopy*. *Proc Natl Acad Sci U S A*, 2008. **105**(5): p. 1410-5.
9. Zhang, Y., et al., *Biodistribution, pharmacokinetics and toxicology of Ag2S near-infrared quantum dots in mice*. *Biomaterials*, 2013. **34**(14): p. 3639-46.
10. Godard, A., et al., *Water-Soluble Aza-BODIPYs: Biocompatible Organic Dyes for High Contrast In Vivo NIR-II Imaging*. *Bioconjug Chem*, 2020. **31**(4): p. 1088-1092.
11. Monopoli, M.P., et al., *Biomolecular coronas provide the biological identity of nanosized materials*. *Nat Nanotechnol*, 2012. **7**(12): p. 779-86.
12. Tiwari, A., P. Bhatia, and J.K. Randhawa, *Systematic spectroscopic investigation of structural changes and corona formation of bovine serum albumin over magneto-fluorescent nanoparticles*. *Dalton Trans*, 2020. **49**(35): p. 12380-12389.
13. Wang, Q., et al., *Thermodynamic Implications and Time Evolution of the Interactions of Near-Infrared PbS Quantum Dots with Human Serum Albumin*. *ACS Omega*, 2021. **6**(8): p. 5569-5581.
14. Kapralov, A.A., et al., *Adsorption of surfactant lipids by single-walled carbon nanotubes in mouse lung upon pharyngeal aspiration*. *ACS Nano*, 2012. **6**(5): p. 4147-56.
15. Hellstrand, E., et al., *Complete high-density lipoproteins in nanoparticle corona*. *Febs j*, 2009. **276**(12): p. 3372-81.
16. Feingold, K.R., *Introduction to Lipids and Lipoproteins*, in *Endotext*, K.R. Feingold, et al., Editors. 2000, MDText.com, Inc. Copyright © 2000-2021, MDText.com, Inc.: South Dartmouth (MA). South Dartmouth (MA).
17. Ho, Y.K., et al., *Low-density lipoprotein (LDL) receptor activity in human acute myelogenous leukemia cells*. *Blood*, 1978. **52**(6): p. 1099-114.
18. Rudling, M.J., et al., *Content of low density lipoprotein receptors in breast cancer tissue related to survival of patients*. *Br Med J (Clin Res Ed)*, 1986. **292**(6520): p. 580-2.
19. Versluis, A.J., et al., *Receptor-mediated uptake of low-density lipoprotein by B16 melanoma cells in vitro and in vivo in mice*. *Br J Cancer*, 1996. **74**(4): p. 525-32.
20. Gutierrez-Pajares, J.L., et al., *SR-BI: Linking Cholesterol and Lipoprotein Metabolism with Breast and Prostate Cancer*. *Front Pharmacol*, 2016. **7**: p. 338.
21. Yuan, B., et al., *High scavenger receptor class B type I expression is related to tumor aggressiveness and poor prognosis in breast cancer*. *Tumour Biol*, 2016. **37**(3): p. 3581-8.
22. Li, H., et al., *Carbocyanine labeled LDL for optical imaging of tumors*. *Acad Radiol*, 2004. **11**(6): p. 669-77.
23. Cao, W., et al., *Synthesis and evaluation of a stable bacteriochlorophyll-analog and its incorporation into high-density lipoprotein nanoparticles for tumor imaging*. *Bioconjug Chem*, 2009. **20**(11): p. 2023-31.
24. Gal, D., et al., *Low-density lipoprotein as a potential vehicle for chemotherapeutic agents and radionucleotides in the management of gynecologic neoplasms*. *Am J Obstet Gynecol*, 1981. **139**(8): p. 877-85.
25. Mooberry, L.K., et al., *Receptor mediated uptake of paclitaxel from a synthetic high density lipoprotein nanocarrier*. *J Drug Target*, 2010. **18**(1): p. 53-8.
26. Tian, R., et al., *Albumin-chaperoned cyanine dye yields superbright NIR-II fluorophore with enhanced pharmacokinetics*. *Sci Adv*, 2019. **5**(9): p. eaaw0672.

27. Hartung, G., et al., *Phase I trial of methotrexate-albumin in a weekly intravenous bolus regimen in cancer patients. Phase I Study Group of the Association for Medical Oncology of the German Cancer Society.* Clin Cancer Res, 1999. **5**(4): p. 753-9.
28. Schmid, P., et al., *Atezolizumab and Nab-Paclitaxel in Advanced Triple-Negative Breast Cancer.* N Engl J Med, 2018. **379**(22): p. 2108-2121.
29. Solomonov, A.V., et al., *The Interaction of BODIPY with bovine serum albumin and its bilirubin complex.* Biophysics, 2014. **59**(1): p. 35-42.
30. Marfin, Y.S., et al., *Interaction of BODIPY Dyes with the Blood Plasma Proteins.* J Fluoresc, 2016. **26**(1): p. 255-61.
31. Pliquett, J., et al., *A Promising Family of Fluorescent Water-Soluble aza-BODIPY Dyes for in Vivo Molecular Imaging.* Bioconjug Chem, 2019. **30**(4): p. 1061-1066.
32. Deckelbaum, R.J., G.G. Shipley, and D.M. Small, *Structure and interactions of lipids in human plasma low density lipoproteins.* J Biol Chem, 1977. **252**(2): p. 744-54.
33. Kuzmin, V.A., et al., *Complex formation of albumin with tricarbo-cyanine dyes containing phosphonate groups.* Photochem Photobiol Sci, 2016. **15**(11): p. 1377-1384.
34. Kim, S.I., et al., *Systemic and specific delivery of small interfering RNAs to the liver mediated by apolipoprotein A-I.* Mol Ther, 2007. **15**(6): p. 1145-52.
35. Varshosaz, J., H. Vakilzadeh, and E. Ghassami, *Lipoprotein Like Nanoparticles Used in Drug and Gene Delivery.* Curr Pharm Des, 2016. **22**(22): p. 3466-85.
36. Masquelier, M., et al., *Low density lipoprotein as a carrier of cytostatics in cancer chemotherapy: study of stability of drug-carrier complexes in blood.* J Drug Target, 2000. **8**(3): p. 155-64.
37. Nikanjam, M., et al., *Synthetic nano-low density lipoprotein as targeted drug delivery vehicle for glioblastoma multiforme.* Int J Pharm, 2007. **328**(1): p. 86-94.
38. Sobot, D., et al., *Conjugation of squalene to gemcitabine as unique approach exploiting endogenous lipoproteins for drug delivery.* Nat Commun, 2017. **8**: p. 15678.
39. Sobot, D., et al., *Circulating Lipoproteins: A Trojan Horse Guiding Squalenoylated Drugs to LDL-Accumulating Cancer Cells.* Mol Ther, 2017. **25**(7): p. 1596-1605.

## Supplementary Information

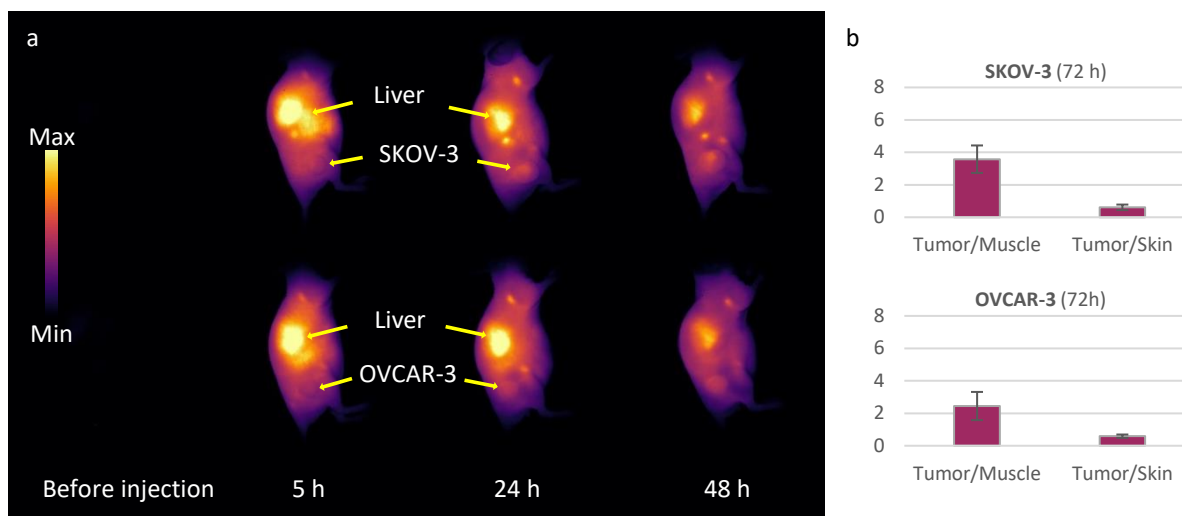


**Figure S1: SWIR-WAZABY-01 tumor-dependent accumulation and staining.** (a) NIR-II fluorescence imaging of mice bearing subcutaneous SKOV-3, OVCAR-3 tumors before and at 5, 24 and 48 h post intravenous administration of SWIR-WAZABY-01 (200  $\mu$ L at 600  $\mu$ M). Tumors and livers are indicated by yellow arrows. (b) *Ex-vivo* tumor/muscle and tumor/skin ratios calculated from excised organs. The results are expressed as the mean  $\pm$  S.D. (n=3/condition).

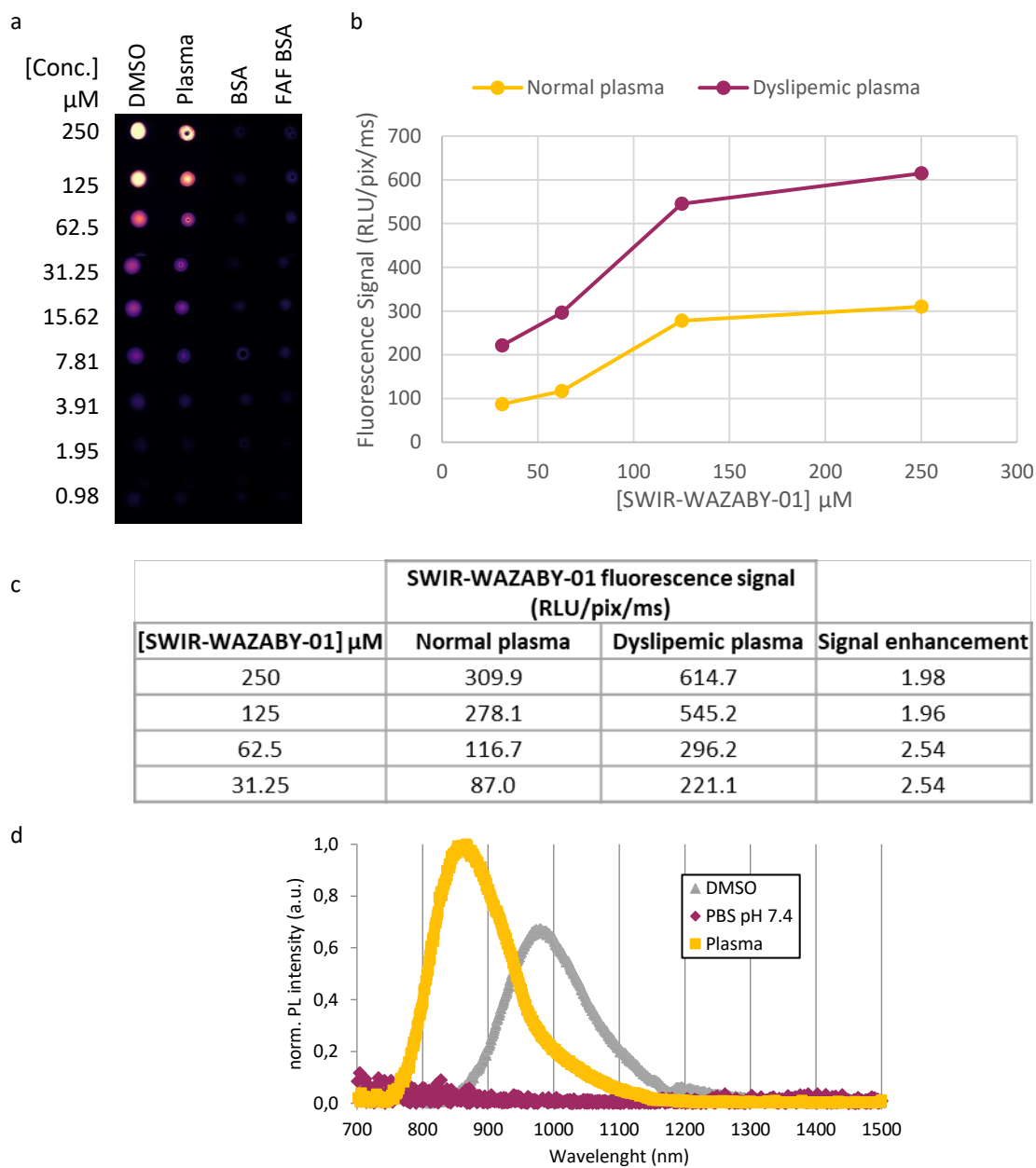


**Figure S2:** (a) Serial dilution of the SWIR-WAZABY-01 in DMSO, plasma, BSA 40 g/L, and fatty acid free (FAF)-BSA 40 g/L, showing high fluorescence signals observed in the presence of DMSO and plasma ( $\lambda_{em} = 1250$  nm). (b) Graphical representation and (c) quantification of the SWIR-WAZABY-01 fluorescence signal obtained following serial dilution in normal and dyslipemic plasma (from Figure 3(b)). (d) Normalized photoluminescence intensity of the SWIR-WAZABY-01 in DMSO (grey), PBS (purple) and plasma (yellow), recorded after excitation at  $\lambda_{ex} = 806$  nm.

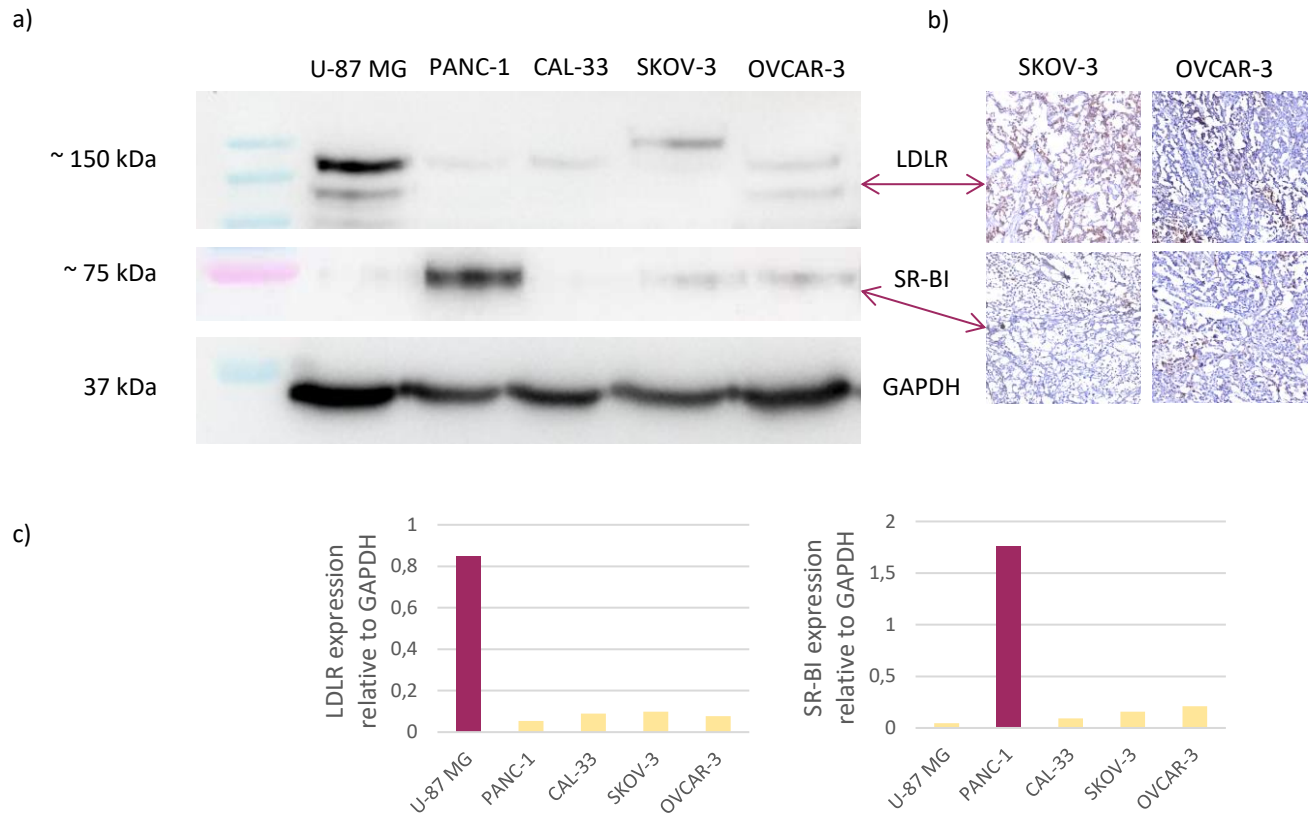


**Figure S3:** (a) Lipoprotein receptors (LDLR, SR-BI) expression in U-87 MG, PANC-1, CAL-33 cells, SKOV-3 and OVCAR-3 cells assessed by western blotting of whole cell extracts. GAPDH served as a loading control. (b) Histological sections of SKOV-3 and OVCAR-3 tumors and their immunolabelling for LDLR and SB-BI. (c) Quantification of LDLR and SR-BI expression relative to GAPDH, from (a) data.

## Materials and Methods:

6 mice were implanted with U-87 MG cells orthotopically in their brains, according to the approved ethical guidelines and the following procedure: anesthetized mice (isoflurane/air 4% for induction and 1.5% thereafter) were placed on a stereotaxic frame and 50  $\mu\text{L}$  of bupivacaine (5 mg/mL) were administered subcutaneously before scalp opening. The skull was revealed by gently removing the membranes (connective tissues) located on its external side. The point of needle injection was determined on the cranium surface (bregma 0, mediolateral 2 mm, dorsoventral 3 mm), and a hole was drilled allowing the Hamilton syringe to be inserted (3 mm into the striatum). U-87 MG cells suspension ( $1.0 \times 10^5$  cells in 5  $\mu\text{L}$ ) was slowly pumped in (5  $\mu\text{L}/\text{min}$ ) using the needle, after which it was slowly removed (0.5 mm/30 sec). Finally, the opening was stoppered with Horsley wax and the skin was sutured. Following tumor growth, the mice were intravenously injected in their tail vein with 200  $\mu\text{L}$  of 600  $\mu\text{M}$  SWIR-WAZABY-01 solution diluted in PBS. *In vivo*, NIR-II fluorescence imaging of the head was performed before and after SWIR-WAZABY-01 administration at 5, 24, and 48 h. Three mice were euthanized (at 24 and 48 h), and their brains were sampled for *ex-vivo* fluorescence imaging. Acquired images were analyzed using Fiji software, and semi-quantitative fluorescence data were obtained by drawing regions of interest (ROI).

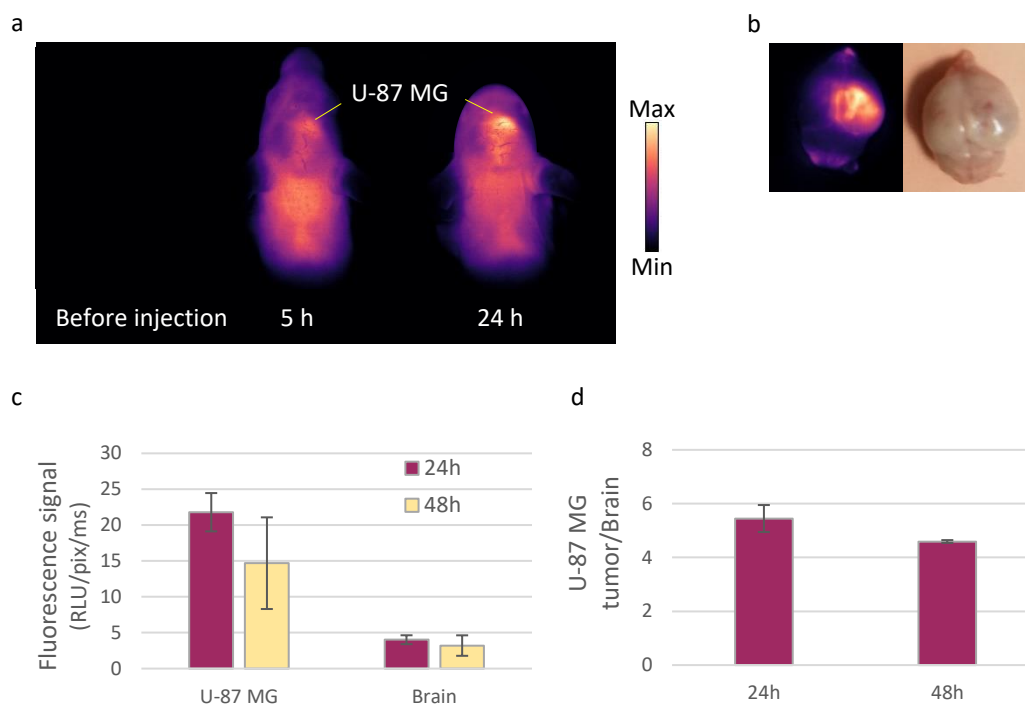


**Figure S4: SWIR-WAZABY-01 accumulation in U-87 MG intracranial orthotopic tumors.** (a) Example of *in vivo* NIR-II fluorescence imaging of mouse head, before and at 5 and 24 h post intravenous administration of SWIR-WAZABY-01 (200  $\mu\text{L}$  at 600  $\mu\text{M}$ ). The mouse brain bears an intracranial U-87 MG tumor in the right hemisphere. (b) *Ex-vivo* NIR-II fluorescence image and bright field image of the excised brain. (c) Quantification of U-87 MG tumor and brain fluorescence signal obtained from the NIR-II fluorescence images of dissected brains, collected at 24 and 48 h. (d) U-87 MG tumor/Brain fluorescence ratio calculated from (c) data. The results are expressed as the mean  $\pm$  S.D. (n=3).

## Article 3: Bioconjugated aza-BODIPYs NIR-II probes for selective imaging of HER2-positive ovarian cancer

Taking advantage of SWIR-WAZABY-01 (aza-BODIPY described in both articles 1 and 2) water-solubility, biocompatibility, and unique NIR-II fluorescence properties, to target tumors possessing unique receptor profiles, regardless of their lipoprotein receptors expression, we aimed to couple SWIR-WAZABY-01 to antibodies specific to the tumor expressed receptors. As a proof of concept, two ovarian cancer cell lines expressing (SKOV-3) or not (OVCAR-3) HER2 receptor, with limited or no lipoprotein receptors expression, were selected. Accordingly, SWIR-WAZABY-01 was coupled to a HER2-specific antibody i.e. Trastuzumab. The resulting NIR-II bioconjugated probe named aza-SWIR-Trastuzumab-01 was characterized and its targeting capacity for HER2 was assessed *in vitro* and *in vivo*. In the same context, a brighter water-soluble NIR-II fluorophore was then developed named SWIR-WAZABY-04. This latter was also bioconjugated to Trastuzumab, resulting in aza-SWIR-Trastuzumab-02. The *in vivo* tumor targeting potential of both NIR-II bioconjugated probes was compared. This study is presented in paper 3, in preparation, entitled “*Bioconjugated aza-BODIPYs NIR-II probes for selective imaging of HER2-positive ovarian cancer*”.

SWIR-WAZABY-01 was specifically conjugated to the heavy chain of Trastuzumab, with a ratio of 1.9 dye per antibody. The resulting NIR-II bioconjugated probe, aza-SWIR-Trastuzumab-01, showed a preserved fluorescence stability in sera (for 72 h at 37 °C) and a maintained affinity to HER2, both in solution and *in vitro*. Additionally, aza-SWIR-Trastuzumab-01 demonstrated selectivity to HER2 positive tumors *in vivo*, which was not the case for HER2 negative tumors or mice injected with the non-bioconjugated fluorophore (SWIR-WAZABY-01). These findings provided a proof of concept of our vectorization strategy. Aza-SWIR-Trastuzumab-02 was then synthesized under the same conditions as aza-SWIR-Trastuzumab-01. Aza-SWIR-Trastuzumab-02 presented enhanced fluorescence signal and superior tumor/muscle ratio, signifying its distinction over aza-SWIR-Trastuzumab-01, and opening a new perspective for its potential use in NIR-II FGS (discussed following the paper).

To note, I was responsible for the *in vitro* and *in vivo* biological investigations applied in article 3. The chemical synthesis, bioconjugation process, stability, and affinity tests in solution were performed by the chemists and the biologists at ICMUB and LIIC (Laboratoire Immunologie et Immunothérapie des Cancers), respectively. I presented this work as a poster at the “16th European Molecular Imaging Meeting (EMIM 2021)”. In the thesis manuscript, all the preceding data were organized in one article (article 3). However, acquiring additional data, article 3 will be divided into two papers focused on aza-SWIR-Trastuzumab-01, and comparing both aza-SWIR-Trastuzumab-01/02 respectively.

# Bioconjugated aza-BODIPYs NIR-II probes for selective imaging of HER2-positive ovarian cancer

**Authors (order to be adjusted):** Ghadir Kalot<sup>1</sup> & Amélie Godard<sup>2</sup> & Malorie Privat<sup>3,4</sup>, Benoit Busser<sup>1,5,6</sup>, Franck Denat<sup>2</sup>, Jean Luc Coll<sup>1</sup>, Ewen Bodio<sup>2</sup>, Catherine Paul<sup>3,4</sup>, Christine Goze<sup>2</sup>, Lucie Sancey<sup>1</sup>

<sup>1</sup> Institute for Advanced Biosciences, Grenoble Alpes University, INSERM U1209, CNRS UMR 5309, Grenoble, France.

<sup>2</sup> Institut de Chimie Moléculaire de l'Université de Bourgogne, Université Bourgogne Franche-Comté, CNRS UMR 6302, Dijon, France.

<sup>3</sup> Laboratoire d'Immunologie et Immunothérapie des Cancers, EPHE, PSL Research University, 75000 Paris, France.

<sup>4</sup> LIIC, EA7269, Université de Bourgogne, Dijon 21000, France.

<sup>5</sup> Grenoble Alpes University Hospital (CHUGA), Grenoble, France.

<sup>6</sup> Institut Universitaire de France (IUF).

## Abstract

Applying fluorescence-guided surgery (FGS) to cytoreductive surgery presents a cornerstone in achieving complete resection of microscopic ovarian tumors. The use of visible and NIR-I fluorophores has led to beneficial results in clinical trials; however, involving NIR-II dyes seems to outperform those benefits, due to the deeper tissue imaging and higher signal/noise ratios attained within the NIR-II optical window. In this context, we developed NIR-II emitting probes targeting HER2 positive ovarian tumors, by coupling water-soluble NIR-II aza-BODIPYs dyes to Trastuzumab antibody. Prolonged stability of the bioconjugated probes in sera, and maintained affinity towards HER2 receptors *in vitro*, were demonstrated. Selective targeting of HER2 positive tumors (SKOV-3) was also proved *in vivo*, with a favorable tumor/muscle ratio. In conclusion, we demonstrated the maintained fluorescence properties and the preserved affinity of the bioconjugated dyes to HER2 *in vivo*, thus their potential for NIR-II FGS.

## 1. Introduction

Ovarian cancer presents the most lethal gynecologic cancer, with 75% of patients being diagnosed at advanced or late stages, and 5-years relative survival being less than 50% [1]. The typical standard of care consists of performing cytoreductive surgery followed by platinum-based chemotherapy. Depending on the surgeon's visual inspection and palpation during surgery, cytoreductive surgery allows the resection of large easily visible tumors. However, the identification of microscopic lesions and metastatic ones remains challenging, even for skilled surgical practitioners. Those residual tumors are considered as an important predictor of survival, with a 5.5% increase in the median survival achieved for each 10% increase in optimal cytoreduction [2], and with patients undergoing complete or optimal cytoreduction (resected tumor size = 1-10 mm) showing improved overall survival as compared to patients undergoing suboptimal cytoreduction (resected tumor size > 10 mm) [3]. Thus, to reduce mortality, the ultimate goal is to optimize surgical debulking procedures to approach complete resection.

To this end, fluorescence-guided surgery, a safe (non-ionizing), cheap, sensitive, and real-time intraoperative molecular imaging technique, was introduced into the clinical practice [4, 5]. This latter is based on the use of a fluorophore, alone or coupled to a targeting moiety, that can label cancer cells improving their visibility, thus enhancing the complete resection rate. The first-in-human FGS clinical trial in ovarian cancer patients was performed using a visible region (400-700 nm) emitting fluorophore named fluorescein iso-thiocyanate (FITC). This latter was coupled to folate to target folate receptor alpha (FR $\alpha$ ) overexpressed in ovarian tumors [6]. Advancements in the fluorescent probes field have led to the development of fluorophores emitting in the NIR-I region (700-900 nm). Providing less photon absorption and scattering, and low tissue autofluorescence, the NIR-I region have enhanced the light penetration depth and provided optimal contrast as compared to the visible window [7]. Subsequently, OTL38, a molecule made up of a NIR-I probe conjugated to folic acid, was developed and has already reached phase III clinical trials in ovarian cancer patients [8, 9], demonstrating improved cytoreduction.

In the last couple of years, the NIR-II optical window (1000-1700 nm) has caught increasing attention due to its further reduced tissues autofluorescence and diminished photon scattering, resulting in even better light penetration depths, signal to noise ratios, and images of high resolution [10]. In this context, we recently developed a NIR-II emitting fluorophore based on the aza-BODIPY platform named SWIR-WAZABY-01. Its unique NIR-II emission properties and water-solubility favored its use for biological applications, in particular for *in vivo* tumor imaging [11]. Following intravenous administration, SWIR-WAZABY-01 was carried in the bloodstream via lipoproteins, favoring the specific labeling of tumors overexpressing lipoprotein receptors, LDLR and SR-BI. The NIR-II emitting dye accumulated significantly in the tumor area in the absence of any targeting moiety (Kalot et al. article 2). To benefit from SWIR-WAZABY-01 unique NIR-II photophysical properties and be able to target ovarian tumors regardless of their

lipoprotein receptors expression profiles, we thought of coupling SWIR-WAZABY-01 to Trastuzumab, an antibody specific to HER2 (human epidermal growth factor receptor 2) receptor overexpressed in several tumor types including ovarian tumors [12].

In this study, the synthesis of a HER2-positive ovarian cancer targeting NIR-II dye (i.e. aza-SWIR-Trastuzumab-01), based on the water-soluble aza-BODIPY dye SWIR-WAZABY-01 conjugated to Trastuzumab antibody, was reported. A specific bioconjugation process was applied resulting in a stable dual/bi-labeled trastuzumab antibody, with a maintained affinity to HER2, both in solution and *in vitro*. *In vivo*, aza-SWIR-Trastuzumab-01 showed selectivity to ovarian cancer expressing HER2 receptor which was not the case for non-targeted fluorophore SWIR-WAZABY-01. Another bioconjugate i.e. aza-SWIR-Trastuzumab-02 based on a brighter water-soluble aza-BODIPY dye i.e. SWIR-WAZABY-04 conjugated to Trastuzumab antibody, was synthesized. Comparing aza-SWIR-Trastuzumab-01 to aza-SWIR-Trastuzumab-02, aza-SWIR-Trastuzumab-02 showed an impressive tumor/muscle ratio superior to those reported in the literature.

## 2. Results and discussion

To couple SWIR-WAZABY-01 to Trastuzumab antibody, a specific bioconjugation process on the Fc region/heavy chain of the antibody was applied (**Scheme 1**). Both, the SWIR-WAZABY-01 precursor (i.e. compound 4) and the trastuzumab antibody were modified to allow the bioconjugation. The first set of experiments permitted the grafting of a TOTA-Boc group on aza-SWIR-05, resulting in the formation of SWIR-WAZABY-05. An alkyne group was then introduced resulting in the formation of aza-SWIR-08. On the other hand, an azide function was introduced onto the oligosaccharide chain of the antibody Fc part using GlycClick® technology, resulting in Trastuzumab-N3. Trastuzumab-N3 was then able to interact with the alkyne group of aza-SWIR-08 through a click chemistry reaction, Huisgen-like reaction, leading to the development of the bioconjugated species (i.e. aza-SWIR-Trastuzumab-01). This bioconjugation pathway allows obtaining a degree of labeling (DOL) close to 2, in a homogenous manner, to preserve the antibody's affinity towards HER-2 receptors.

The purified aza-SWIR-Trastuzumab-01 was concentrated and the Trastuzumab degree of labeling (DOL) was determined using MALDI-TOF mass spectrometry analyses. A DOL of 1.9 probes per antibody was obtained (**Figure S 1a**). To assess the fluorescence stability of the bioconjugated probe, aza-SWIR-Trastuzumab-01 was incubated in murine serum for several time durations (0, 24, 48, and 72 h) at 37 °C, to mimic the *in vivo* situation (**Figure 1**). The incubated mixtures were then separated on a polyacrylamide gel in native and reductive conditions (in presence of DTT and heating at 95 °C), followed by fluorescence analysis/imaging (according to previously reported procedure [13]). As expected, no fluorescence was detected in the non-labeled Trastuzumab condition. Concerning aza-SWIR-Trastuzumab-01, under native conditions, a single fluorescent band was observed at the position ~ 150 kDa, which is the size of Trastuzumab antibody [14], in all the incubation time points. No evolution or decline in the fluorescence signal was observed after 72 h of incubation indicating the fluorescence stability of the bioconjugated probe under physiological conditions. Under reductive conditions, in which the disulfide bridges connecting the heavy and light chains of the antibody are broken, the fluorescence bands were observed at a lower position (~ 50 kDa), resembling the size of the antibody heavy chain [14], while no fluorescence was observed at the light chain position (~ 25 kDa) [14]. These data confirm that the probe was specifically grafted on the antibody heavy (Fc) chain. Similar data were also obtained using human serum (**Figure S 2**).

To assess if the fluorophore grafting modified Trastuzumab affinity towards its target i.e. HER2 receptor, a bilayer interferometry experiment was performed [15]. This latter allowed the determination of the association/dissociation of aza-SWIR-Trastuzumab-01 to/from HER2 protein (**Figure 2b**). Accordingly, the affinity of aza-SWIR-Trastuzumab-01 for HER2 ( $K_D$ ) was calculated (**Figure 2c**). Using similar experimental conditions, the affinity of Trastuzumab to HER2 ( $K_D$ ) was calculated and served as a control (**Figure 2a,c**). The  $K_D$  of aza-SWIR-Trastuzumab-01 ( $K_D = 9.5$

nM  $\pm$  2.5 nM) was just slightly altered compared to that of native Trastuzumab ( $K_D = 4.8 \text{ nM} \pm 1.8 \text{ nM}$ ), indicating that the applied bioconjugation process conserved the affinity of the Trastuzumab antibody present within aza-SWIR-Trastuzumab-01.

The targeting capacity of the aza-SWIR-Trastuzumab-01 toward the Her2 receptor was also investigated *in vitro*. Two ovarian tumor cell lines were selected, a HER2-positive cell line (SKOV-3) and a HER2-negative cell line (OVCAR-3) (**Figure 2d**). The cells were incubated with aza-SWIR-Trastuzumab-01, and their fluorescence signal was assessed using flow cytometry technique (**Figure 2e,f**). After incubation, 60.15% of SKOV-3 cells were fluorescent compared to 5.85% of OVCAR-3 cells, demonstrating a higher specificity of aza-SWIR-Trastuzumab-01 towards cells expressing HER2 receptor (i.e. SKOV-3 cells). Additionally, a confocal microscopy experiment showed aza-SWIR-Trastuzumab-01 fluorescence signal within SKOV-3 cells, while the OVCAR-3 cells didn't accumulate the labeled antibody (**Figure 2g,h**). This experiment confirmed the previous results and, suggested that aza-SWIR-Trastuzumab-01 is able to internalize into cells expressing HER2 receptors.

Following the favorable *in vitro* assessment, aza-SWIR-Trastuzumab-01 targeting potential was investigated *in vivo* (**Figure 3a**). As a control, mice bearing subcutaneous SKOV-3 and OVCAR-3 were administered with the non-vectorized fluorophore SWIR-WAZABY-01. Similar to previously reported data, no significant tumor accumulation was observed, in both SKOV-3 and OVCAR-3 tumors, at any time point. As previously reported, SWIR-WAZABY-01 is carried in the bloodstream via lipoproteins, allowing a massive tumor uptake through the lipoprotein receptors, LDLR and SR-B1. Therefore, the weak tumor accumulation in SKOV-3 and OVCAR-3 models could be explained by the low or absent lipoproteins receptors expression in those tumors (**Figure 2d**), which prevent the accumulation of SWIR-WAZABY-01 fluorophore carried by lipoproteins. On the contrary, administering aza-SWIR-Trastuzumab-01 to mice bearing HER2 positive SKOV-3 tumors lead to a clear identification of the tumors and a high tumor/skin ratio that was enhanced with time reaching 5.5, 72 h after administration (**Figure 3b**). As expected, OVCAR-3 HER2 negative tumors did not accumulate the aza-SWIR-Trastuzumab-01 and the tumor/skin ratio was close to 1.5 (**Figure 3b**). These findings demonstrate that the trastuzumab antibody within aza-SWIR-Trastuzumab-01 maintained its high affinity towards HER2 positive tumors *in vivo*, and possessed the ability to vectorize the SWIR-WAZABY-01 fluorophore into tumors having a low expression of lipoprotein receptors. It is worth noting that the injected dose of SWIR-WAZABY-01 fluorophore was 10 times higher compared to the amount of fluorophore grafted onto the antibodies (20 nmol versus 2.5 nmol, respectively). Therefore, a superior visualization of HER2 expressing tumors could be attained using aza-SWIR-Trastuzumab-01, using a low dose of the injected fluorophore.

Another NIR-II emitting aza-BODIPY fluorophore was also synthesized, named SWIR-WAZABY-04 (**Scheme S 1**). It is structurally similar to SWIR-WAZABY-01 except that it contains

4 ammonium groups. SWIR-WAZABY-04 possessed a higher quantum yield compared to SWIR-WAZABY-01, both in DMSO and blood plasma (**Table 1**). Even though its fluorescence emission peak, in plasma, is narrower and more blue-shifted compared to SWIR-WAZABY-01 (**Figure 4a,b**), SWIR-WAZABY-04 owned a unique emission peak at 1200 nm that we suggested being responsible for a brighter emission in the NIR-II window, as demonstrated in **Figure 4c**.

Similar to SWIR-WAZABY-01, SWIR-WAZABY-04 was investigated *in vivo*. *In vitro* assessment was not possible due to its specific excitation wavelength (> 800 nm). SWIR-WAZABY-04 was injected into mice bearing SKOV-3 and OVCAR-3 tumors either alone without targeting moiety, or as a trastuzumab bioconjugate, i.e. aza-SWIR-Trastuzumab-02 (**Scheme 1**). Aza-SWIR-Trastuzumab-02 was synthesized using the same experimental conditions as Aza-SWIR-Trastuzumab-01 and a DOL of 1.4 was obtained (**Figure S 1b**). *In vivo*, SWIR-WAZABY-04 wasn't able to identify both SKOV-3 and OVCAR-3 tumors similar to SWIR-WAZABY-01 (**Figure S 3**). Whereas aza-SWIR-Trastuzumab-02 labeled pretty well HER2 positive SKOV-3 tumors and not HER2 negative OVCAR-3 tumors, in a similar manner to aza-SWIR-Trastuzumab-01 (**Figure S 3**).

Comparing aza-SWIR-Trastuzumab-01 to aza-SWIR-Trastuzumab-02, similar tumor accumulation kinetic was observed (**Figure 5a**), however, aza-SWIR-Trastuzumab-02 showed a brighter signal for similar exposure time and reduced injection dose of fluorophore (1 nmol *versus* 2.5 nmol, respectively). Similar biodistribution profiles were also observed, with aza-SWIR-Trastuzumab-02 possessing higher accumulation in the tumor and liver, and less accumulation in the other organs (**Figure 5b**). Accordingly, higher tumor/muscle (23.3 vs. 6.9, respectively) and tumor/skin (7.6 vs 3, respectively) ratios were obtained using aza-SWIR-Trastuzumab-02 (**Figure 5c**), presenting its superior potential over aza-SWIR-Trastuzumab-01.

### 3. Conclusion

To conclude, we reported and demonstrated a specific bioconjugation technique to couple water-soluble NIR-II emitting aza-BODIPYs dyes to Trastuzumab antibody. We showed that the bioconjugated dyes maintained prolonged fluorescence stability and affinity towards HER2 receptors both in solution and *in vitro*. *In vivo*, the bioconjugated probes sustained their fluorescence properties and allowed specific labeling of HER2 positive ovarian tumors that wasn't possible using the fluorophore itself, even with 10- and 20-times higher doses. The superior tumor/muscle ratios demonstrated the potential of the NIR-II bioconjugated probes for NIR-II fluorescence-guided surgery. This bioconjugation process could be valid for other aza-BODIPYs and antibodies allowing the targeting of an unlimited range of tumors with unique fluorescence properties.

## 4. Materials and Methods

The chemical synthesis will be described in the supplementary information.

### Reagents and chemicals for synthesis

Reactions were carried out in analytical reagent grade solvents from Carlo Erba under normal atmosphere. Non-stabilized dry solvents were purchased from Carlo Erba and dried using a MB-SPS-800 (MBraun) or PureSolv-MD-5 (Inert®). All reagents purchased from SigmaAldrich™, Thermo Fisher Scientific™, or ACROS Organics™ were used as received without further purification. Reactions were monitored by thin-phase chromatography and RP-HPLC-MS. Analytical thin-phase chromatography was performed using Merck 60 F254 silica gel (pre-coated sheets, 0.2 mm thick). Column chromatography was carried out using silica gel (SigmaAldrich; 40-63 μm 230-400 mesh 60Å).

### Photophysical studies

Absorbance measurements were recorded on a UV-Vis-NIR spectrophotometer Cary5000 between 300 and 1200 nm. Steady-state photoluminescence spectra were measured from 700 to 1500 nm with a calibrated FSP 920 (Edinburgh Instruments, Edinburgh, United Kingdom) spectrofluorometer equipped with a nitrogen-cooled PMT R5509P. Relative measurements of photoluminescence QYs ( $\Phi_{f,x}$ ) were performed using the dye IR125 dissolved in dimethylsulfoxide (DMSO) as reference. The QY of this dye was previously determined absolutely to  $\Phi_{f, st} = 0.23$ . The relative QY was calculated according to the formula of Demas and Crosby, see equation below.

$$\Phi_{f,x} = \Phi_{f,st} \frac{F_x f_{st}(\lambda_{ex,st}) n_x^2(\lambda_{ex,x})}{F_{st} f_x(\lambda_{ex,x}) n_{st}^2(\lambda_{ex,st})}$$

The subscripts x, st, and ex denote sample, standard, and excitation respectively.  $f(\lambda_{ex})$  is the absorption factor, F the integrated spectral fluorescence photon flux, and n the refractive index of the solvents used. All spectroscopic measurements were done in 1 cm quartz cuvettes from Hellma GmbH at room temperature using air-saturated solutions.

Photophysical analyses for these compounds were performed at the Federal Institute for Materials Research and Testing (BAM) Division Biophotonics in Berlin (Germany).

### Trastuzumab modification

Trastuzumab modification was carried out using the GlycClick® technology marketed by Génovis®. It consists of two steps. Step one involves the hydrolysis of the bonds between the two N-acetylglucosamines using EndoS, an enzyme belonging to the endoglycosidase family. This reaction was carried out for one hour, at room temperature, in TBS, and at pH = 7.5, resulting in a deglycosylated antibody. The second step involves a second enzyme, GalT, which belongs to the nucleotidyltransferase (galactosyltransferase) family. GalT allows the transfer of an azide-

bound galactose from UDP-GalNaz onto the deglycosylated antibody. This reaction was carried out overnight, at 25 °C., in THB and at pH = 7.5. The modified antibody can now be engaged in a Huygens-like reaction to the aza-SWIR-08/ aza-SWIR-09 probe.

### **Bioconjugation**

14 aza-SWIR-08 probe equivalents were incubated with 1 mg of Trastuzumab-N3 in PBS, at pH = 7.4, at 25 °C, for 16 h. The reaction is then purified by FPLC and the solution was concentrated to determine the DOL by MALDI-TOF. 20 aza-SWIR-09 probe equivalents were incubated per Trastuzumab-N3 antibody. The reaction was performed in PBS overnight, at pH = 7.4 and 25 °C. A PD-10 column size exclusion column was used to purify the bioconjugate. PD-10 allows the separation of high molecular weight compounds, the bioconjugated antibody, from low molecular weight compounds, the free probe. Two columns were used to ensure that all the free probes had been removed. The recovered sample was then concentrated on Amicon® and was analyzed using MALDI-TOF to determine the DOL.

### **Antibody Stability**

The stability of Aza-SWIR-Trastuzumab-01 was determined using the following procedure. Aza-SWIR-Trastuzumab-02 was diluted in PBS at 1 mg/mL, then it was incubated in murine or human sera for 24 h, 48 h, or 72 h, at 0.5 mg/mL. Incubations were carried out at 37°C, in the dark and under gentle agitation. Trastuzumab incubated in sera for 72 h served as a control. Each antibody sample was then diluted to 0.125 mg/mL in Laemmli buffer under either reducing (in the presence of dithiothreitol (DTT) and heating at 95°C for 5 minutes) or non-reducing (without DTT) conditions, after which they were separated on a sodium dodecyl sulfate polyacrylamide gel electrophoresis (SDS-PAGE). For each experimental condition, the equivalent of 1.5 µg of antibody was deposited on a 10% acrylamide gel, and migration for 1 hour and a half at 100 V was performed. Following the migration, the fluorescence of the gel was monitored using a ChemiDoc © MP imaging device (BioRad®) with an IRdye800CW filter. Finally, the gels were stained with Coomassie blue for 1 h, and visualized on a Chemidoc XRS + analyzer (Bio-Rad), to detect the proteins.

### **Biolayer Interferometry**

The affinity of Aza-SWIR-Trastuzumab-01 or native trastuzumab antibodies to HER-2 was determined using biolayer interferometry (BLI), on an OctetRed96e instrument (FortéBio). HER-2 was first biotinylated with 5 equiv of biotin (biotin-PEG4-NHS EZkit, Pierce) according to the manufacturer's instructions. The streptavidin-coated biosensor was then dipped into the wells containing biotinylated HER-2 resulting in a functionalized biosensor. To study the trastuzumab-HER-2 interaction, association and dissociation phases were determined by dipping the functionalized biosensor (Accrobiosystem) into wells containing different concentrations of trastuzumab or Aza-SWIR-Trastuzumab-01 (1.6 to 100 nM), followed by wells

containing PBS. Finally, KD was determined using the Octet software (version 3.1, FortéBio, Menlo Park, CA, USA) with a 1:1 stoichiometry model.

### **Cell Lines and Culture**

Human ovarian adenocarcinoma cell lines, SKOV-3 and OVCAR-3, were obtained from the European Collection of Authenticated Cell Cultures (ECACC, French authorization CODECOH DC-2020-4226). The cell lines were cultured in a 37 °C humidified environment containing 5% CO<sub>2</sub>, and in DMEM media supplemented with 10% heat-inactivated fetal bovine serum.

### **Flow Cytometry**

SKOV-3 and OVCAR-3 cells were harvested, washed, and incubated with aza-SWIR-Trastuzumab-01 for 2 h at 37°C. The cells were then rinsed, fixed with PFA 4%, and analyzed using LSRII (BD-Biosciences). At least, 10000 events were recorded and APC-Cy7 excitation settings were used, without a passband filter for optimal collection (LP 755 nm). Data analysis was performed using FCS Express Flow (V7- Pro RUO) software.

### **Confocal Microscopy**

SKOV-3/OVCAR-3 cells (n = 50 000) were plated on LabTek chamber I and kept at 37 °C in 5% CO<sub>2</sub>. After 24 h of adhesion, the cells were washed and incubated with 36 mg/L of Aza-SWIR-Trastuzumab-01 compound solution (i.e. 0.5 µM of fluorophore) diluted in cell culture medium, for 2 h. The cells were then washed and counterstained with Hoechst 33342 (1 µM). Fluorescence microscopy images were acquired using a confocal laser-scanning microscope (LSM 710 Carl Zeiss, Jena, Germany) in live mode. Plan x63 objective was used. Fluorescent signal of Aza-SWIR-Trastuzumab-01 was obtained with a 25% 633 nm excitation laser, and a collection wavelength > 650 nm (confocal section 1.5 µm). Images were processed using Fiji software. The experiments were performed at the MicroCell (Optical Microscopy-Cell Imaging) platform, IAB Grenoble.

### **Western blot**

SKOV-3 and OVCAR-3 tumor cells cultured in 2D were harvested, washed with PBS, lysed and their protein content was quantified using Micro BCA™ Protein Assay Kit (Thermo Fisher Scientific). 40 µg of protein/cell line was loaded into a 12% polyacrylamide gel. Following migration/electrophoresis, the proteins were transferred into an activated PVDF (polyvinylidene difluoride) membrane (#10600023, Amersham). The membrane was then blocked in 5% milk for 1 h at RT, and incubated with primary antibodies overnight at 4°C: anti-LDL receptor antibody (1/1000, Abcam [EP1553Y] (ab52818)), anti-scavenging receptor SR-BI antibody (1/2000, Abcam [EPR20190] (ab217318)), anti-HER2 antibody (1/1000, cell signaling #4290) and anti-GAPDH antibody (1/1000, SC-365062, Santa Cruz Biotechnology) serving as loading and transfer control. The membrane was then incubated with the secondary antibodies, anti-mouse/rabbit-horseradish peroxidase HRP (1/2000, #7076S, Cell Signaling Technology) for 1 h at RT. The proteins

(LDLR/SR-B1/HER2/GAPDH) were finally revealed using Clarity Western ECL Substrate (Bio-Rad), and western blot imaging was performed using Fusion FX (Vilber).

### ***In vivo* NIR-II imaging**

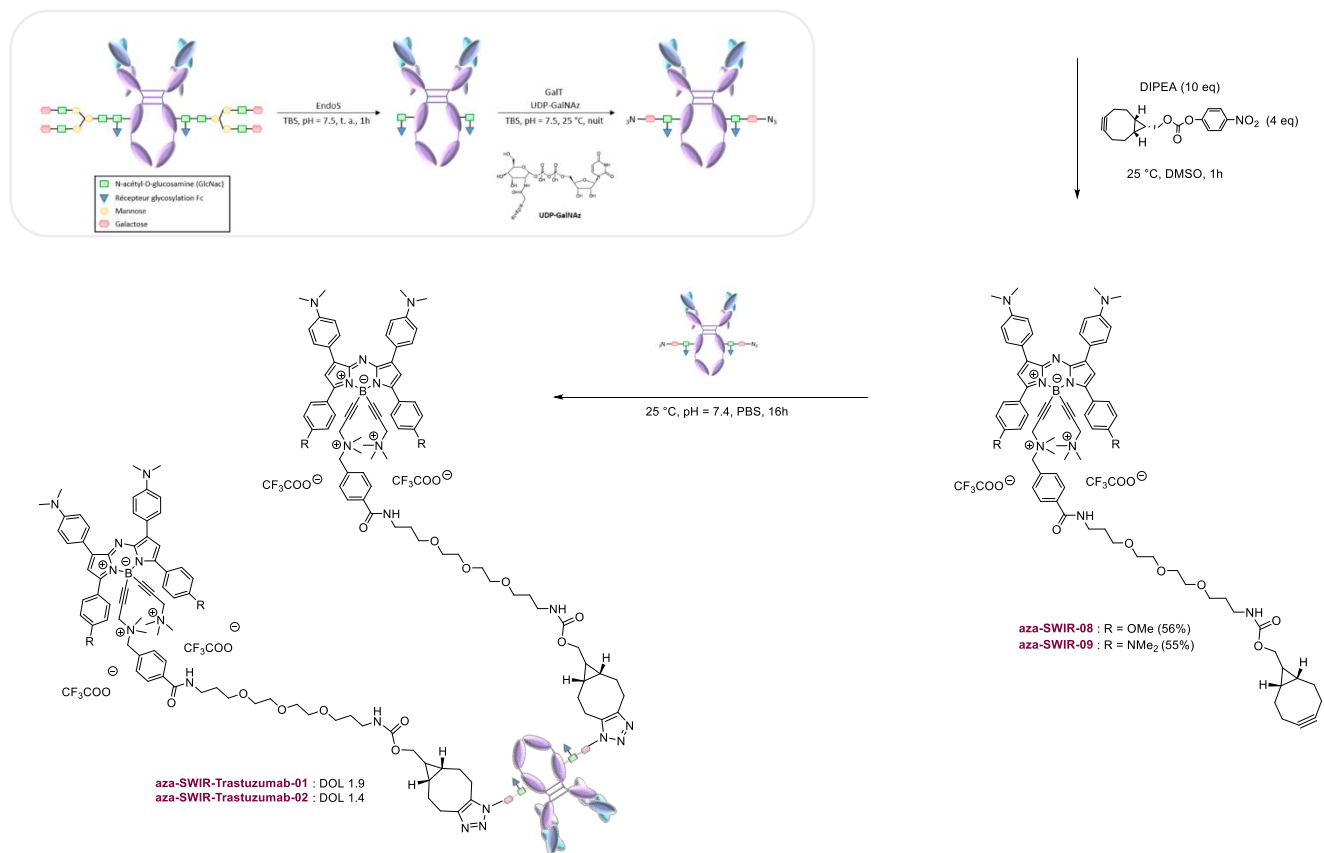
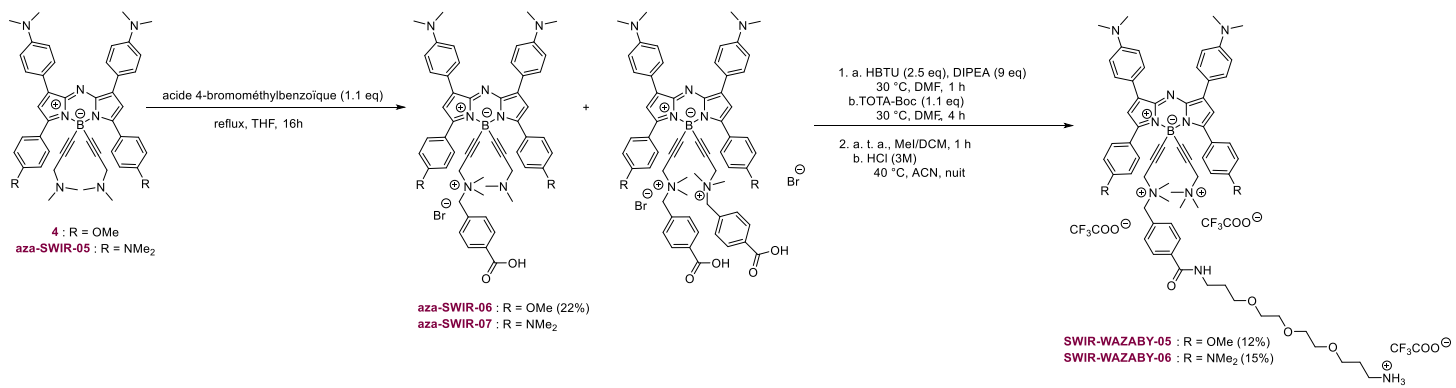
All animal experiments were performed in accordance with national legislation, and with the approval of the institutional and national (Ministère de l'Enseignement Supérieure et de la Recherche) animal ethics committees (APAFIS#8782-2017032813328550), and were performed according to the Institutional Animal Care and Use Committee of Grenoble Alpes University and the Federation of European Animal Science Associations. These experiments were carried out within the small animal imaging platform *Optimal* (V. Jossierand), IAB Grenoble. Female NMRI nude mice (6-week-old) (Janvier Labs, Le Genest-Saint Isle, France) were subcutaneously injected on their right flank with either 10 million human ovarian adenocarcinoma SKOV-3 cancer cells or 8 million human ovarian adenocarcinoma OVCAR-3 cancer cells. Following tumor growth, SKOV-3 and OVCAR-3 bearing mice were intravenously injected in their tail vein with either 100  $\mu$ L of 200  $\mu$ M SWIR-WAZABY-01 or SWIR-WAZABY-04 solution diluted in PBS, or with 100  $\mu$ L of 200  $\mu$ g aza-SWIR-Trastuzumab-01 or 100  $\mu$ g of aza-SWIR-Trastuzumab-02 (n=3/condition). Whole-body NIR-II fluorescence imaging was performed before and after administration at 5, 24, 48, and 72 h. At 72 h, the mice were euthanized and their organs were sampled for *ex-vivo* fluorescence imaging. Acquired images were analyzed using Fiji software, and semi-quantitative fluorescence data were obtained by drawing regions of interest (ROI) around the organs. NIR-II fluorescence imaging was performed using a Princeton camera 640ST (900–1700 nm) coupled to a laser excitation source of  $\lambda = 830$  nm (50 mW/cm<sup>2</sup>). A short-pass excitation filter at 1000 nm (Thorlabs), and a long-pass filter LP1064 nm (Semrock) were added to the NIR-II camera. A 25 mm lens with a 1.4 aperture (Navitar) was used to focus on the mice.

### **NIR-II imaging of drops**

60  $\mu$ M of SWIR-WAZABY-01 and SWIR-WAZABY-04 solutions were serially diluted in blood plasma. 10  $\mu$ L of the diluted samples were dropped on a paraffin paper and imaged by the NIR-II imaging system (setup described above).

## References

1. Randall, L.M., et al., *A phase II, multicenter, open-label trial of OTL38 injection for the intra-operative imaging of folate receptor-alpha positive ovarian cancer*. *Gynecol Oncol*, 2019. **155**(1): p. 63-68.
2. Bristow, R.E., et al., *Survival effect of maximal cytoreductive surgery for advanced ovarian carcinoma during the platinum era: a meta-analysis*. *J Clin Oncol*, 2002. **20**(5): p. 1248-59.
3. du Bois, A., et al., *Role of surgical outcome as prognostic factor in advanced epithelial ovarian cancer: a combined exploratory analysis of 3 prospectively randomized phase 3 multicenter trials: by the Arbeitsgemeinschaft Gynaekologische Onkologie Studiengruppe Ovarialkarzinom (AGO-OVAR) and the Groupe d'Investigateurs Nationaux Pour les Etudes des Cancers de l'Ovaire (GINECO)*. *Cancer*, 2009. **115**(6): p. 1234-44.
4. Vahrmeijer, A.L., et al., *Image-guided cancer surgery using near-infrared fluorescence*. *Nat Rev Clin Oncol*, 2013. **10**(9): p. 507-18.
5. Tipirneni, K.E., et al., *Oncologic Procedures Amenable to Fluorescence-guided Surgery*. *Ann Surg*, 2017. **266**(1): p. 36-47.
6. van Dam, G.M., et al., *Intraoperative tumor-specific fluorescence imaging in ovarian cancer by folate receptor- $\alpha$  targeting: first in-human results*. *Nat Med*, 2011. **17**(10): p. 1315-9.
7. Weissleder, R. and V. Ntziachristos, *Shedding light onto live molecular targets*. *Nat Med*, 2003. **9**(1): p. 123-8.
8. Clinicaltrials.gov, *ELUCIDATE: Enabling LUng Cancer IDentification Using folATE Receptor Targeting*. 2020.
9. Hoogstins, C.E., et al., *A Novel Tumor-Specific Agent for Intraoperative Near-Infrared Fluorescence Imaging: A Translational Study in Healthy Volunteers and Patients with Ovarian Cancer*. *Clin Cancer Res*, 2016. **22**(12): p. 2929-38.
10. Hong, G., A.L. Antaris, and H. Dai, *Near-infrared fluorophores for biomedical imaging*. *Nature Biomedical Engineering*, 2017. **1**(1): p. 0010.
11. Godard, A., et al., *Water-Soluble Aza-BODIPYs: Biocompatible Organic Dyes for High Contrast In Vivo NIR-II Imaging*. *Bioconjug Chem*, 2020. **31**(4): p. 1088-1092.
12. Verri, E., et al., *HER2/neu oncoprotein overexpression in epithelial ovarian cancer: evaluation of its prevalence and prognostic significance. Clinical study*. *Oncology*, 2005. **68**(2-3): p. 154-61.
13. Pliquett, J., et al., *A Promising Family of Fluorescent Water-Soluble aza-BODIPY Dyes for in Vivo Molecular Imaging*. *Bioconjug Chem*, 2019. **30**(4): p. 1061-1066.
14. Shibui, T., K. Bando, and S. Misawa, *High-level secretory expression, purification, and characterization of an anti-human Her II monoclonal antibody, trastuzumab, in the methylotrophic yeast *Pichia pastoris**. *Advances in Bioscience and Biotechnology*, 2013. **04**: p. 640-646.
15. Abdiche, Y., et al., *Determining kinetics and affinities of protein interactions using a parallel real-time label-free biosensor, the Octet*. *Anal Biochem*, 2008. **377**(2): p. 209-17.



**Scheme 1: Synthetic pathway of the Trastuzumab-conjugated NIR-II emitting aza-BODIPYs: aza-SWIR-Trastuzumab-01 and aza-SWIR-Trastuzumab-02**

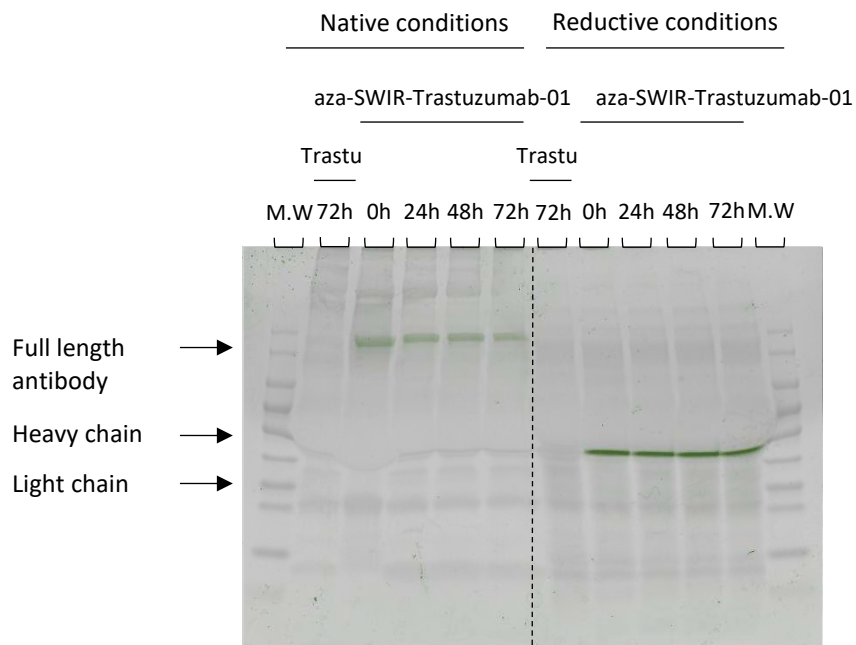


**Figure 1: Assessment of aza-SWIR-Trastuzumab-01 stability in plasma solution.** Superimposed fluorescence image (in green) and bright field image of aza-SWIR-Trastuzumab-01 + plasma mixture migration on SDS-PAGE gel, under native and reducing conditions (DTT + heating), acquired using ChemiDoc © MP imaging device (BioRad®) with an IRdye800CW filter. Aza-SWIR-Trastuzumab-01 was incubated in murine sera for 0, 24, 48 and 72 h. Free Trastuzumab (non-fluorescent) incubated with serum for 72 h, served as a control.

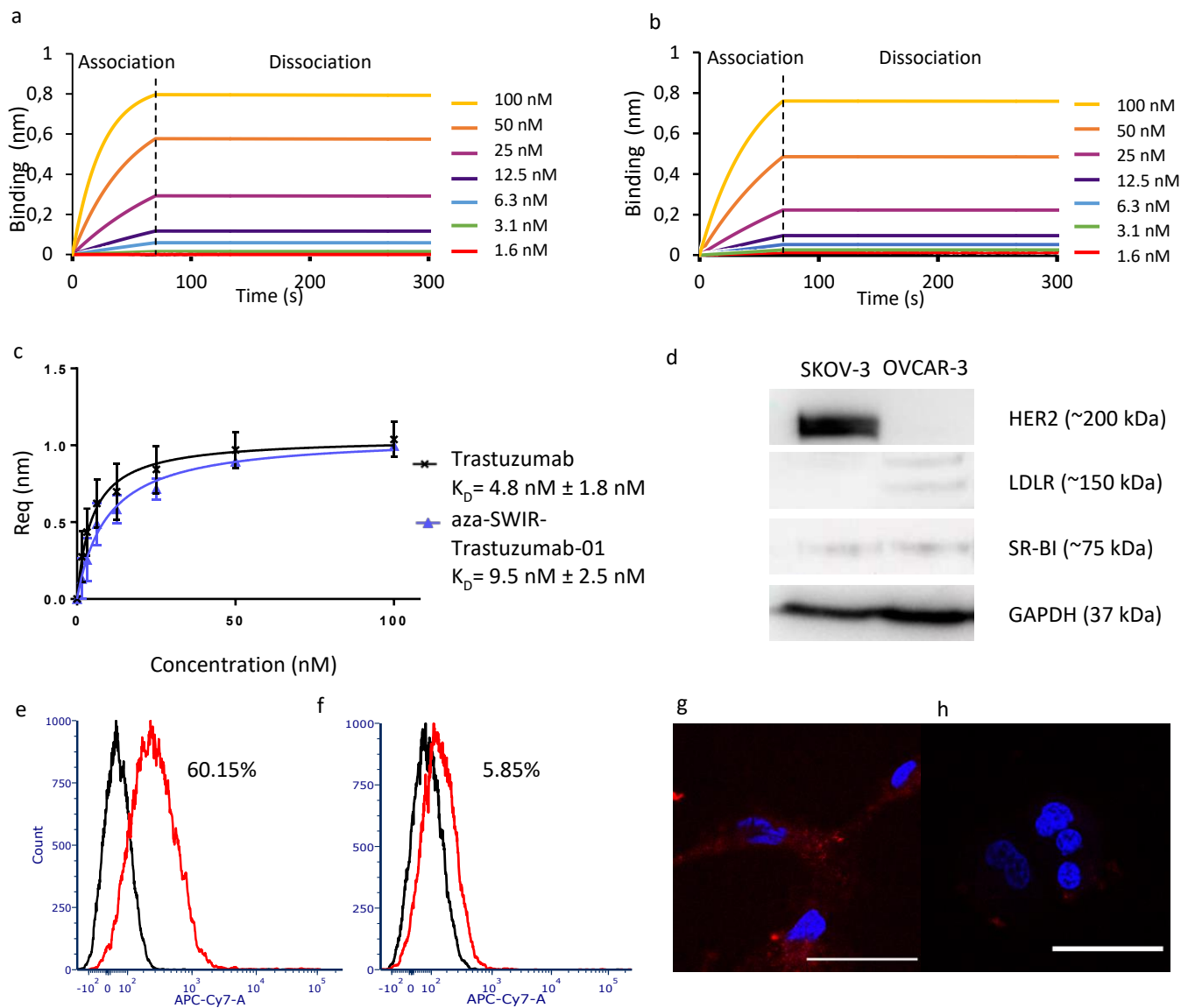


**Figure 2: Assessment of aza-SWIR-Trastuzumab-01 affinity to HER2 in solution (a-c) and *in vitro* (e-h).** (a) Association/dissociation curves representing the interaction between trastuzumab (different concentrations: 1.6 to 100 nM in wells) and HER2 proteins (coated on the biosensor), obtained using biolayer interferometry on an Octet Red96 system. (b) Association/dissociation curves representing the interaction between aza-SWIR-Trastuzumab-01 (different concentrations: 1.6 to 100 nM in wells) and HER2 proteins (coated on the biosensor), obtained using biolayer interferometry on an Octet Red96 system. (c)  $K_D$  determination from standard curve of free trastuzumab ( $K_D = 4.8 \text{ nM} \pm 1.8 \text{ nM}$ ) and aza-SWIR-Trastuzumab-01 ( $K_D = 9.5 \text{ nM} \pm 2.5 \text{ nM}$ ). (d) HER2 and lipoprotein receptors (LDLR, SR-BI) expression in SKOV-3 and OVCAR-3 cells, assessed by western blotting of whole cell extracts. GAPDH served as a loading and transfer control. Flow cytometry histograms of SKOV-3 (e) and OVCAR-3 cells (f) incubated (red lines) or not (black lines) with aza-SWIR-Trastuzumab-01, with the percentage of fluorescently labeled cells indicated. Aza-SWIR-Trastuzumab-01 fluorescence is recorded using the APC-Cy7 channel. Confocal images of SKOV-3 (g) and OVCAR-3 (h) cells incubated with aza-SWIR-Trastuzumab-01 for 2h. Aza-SWIR-Trastuzumab-01 fluorescence signal is indicated in red and the nucleus is counterstained in blue. Scale bars represent  $20 \mu\text{m}$ .

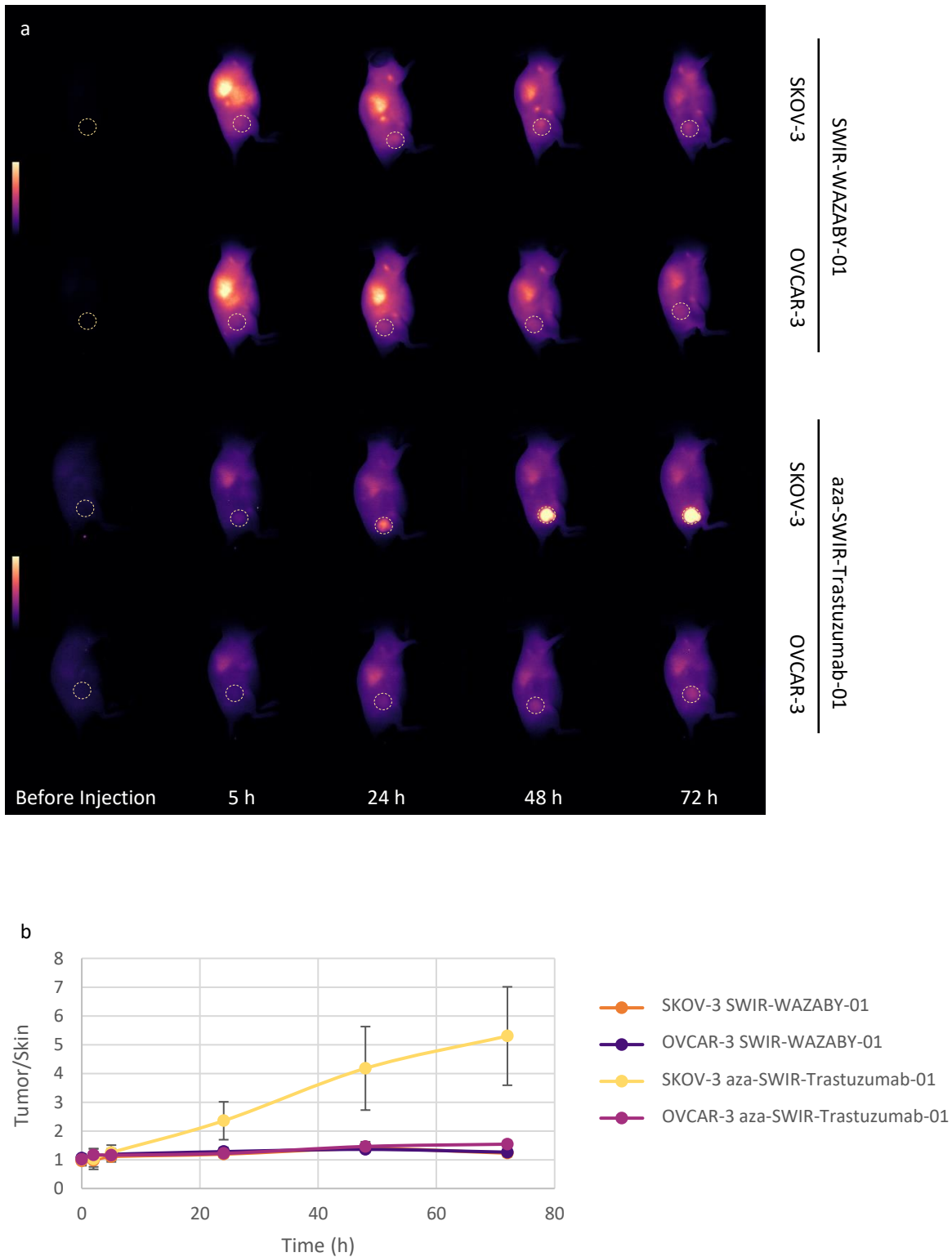


**Figure 3: Assessment of aza-SWIR-Trastuzumab-01 affinity to HER2 *in vivo*.** (a) NIR-II fluorescence images of mice bearing subcutaneous SKOV-3 or OVCAR-3 tumors, before and at 5, 24, 48 and 72 h post intravenous administration of SWIR-WAZABY-01 or aza-SWIR-Trastuzumab-01. Tumors are indicated by dashed circles. Images were acquired using 100 ms of laser exposure. (b) Tumor/Skin ratios calculated from the *in vivo* NIR-II fluorescence images of the mice in (a). The results are represented as the mean  $\pm$  standard deviation (S.D.) (n=3/condition).

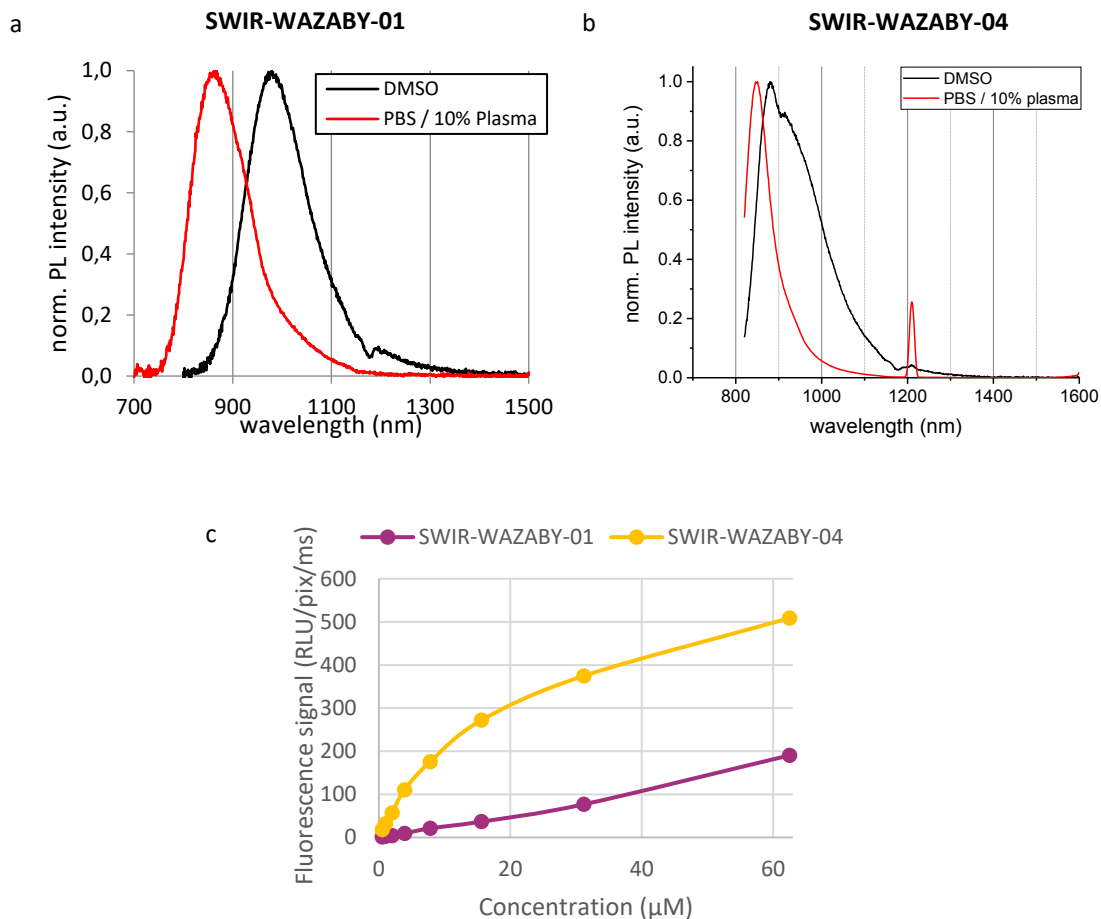


**Figure 4:** Emission spectra of SWIR-WAZABY-01 (a) and SWIR-WAZABY-04 (b), in DMSO (black line) and 10% plasma (red line), obtained using a UV-Vis-NIR spectrophotometer.  $\lambda_{excitation}$  = 638 nm for SWIR-WAZABY-01 and 808 nm for SWIR-WAZABY-04. (c) Quantification of SWIR-WAZABY-01 and SWIR-WAZABY-04 NIR-II fluorescence signal following serial dilution in blood plasma and imaging using the NIR-II imaging system ( $\lambda_{excitation}$  = 830 nm).

Compound	In DMSO					In 10% Plasma		
	$\epsilon$ ( $M^{-1}cm^{-1}$ )	Stokes Shift ( $cm^{-1}$ )	$\lambda_{max,abs}$ (nm)	$\lambda_{max,em}$ (nm)	$\Phi$ (%)	$\lambda_{max,abs}$ (nm)	$\lambda_{max,em}$ (nm)	$\Phi$ (%)
SWIR-WAZABY-01	37948	2739	780	992	0.3	746	867	2.5
SWIR-WAZABY-04	72886	831	820	880	1.1	802	846	2.5

**Table 1:** Photophysical properties of the non-conjugated SWIR-WAZABY-01 and SWIR-WAZABY-04 probes/fluorophores.

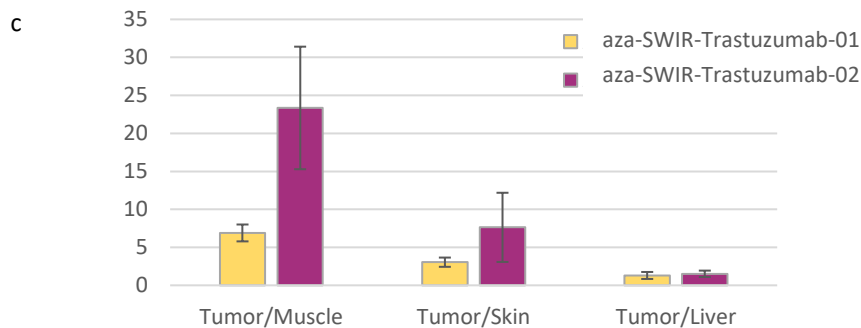
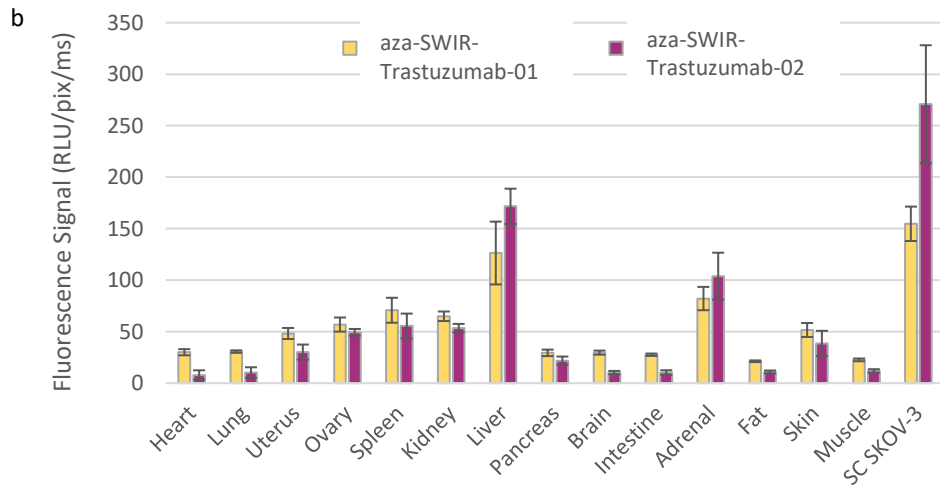
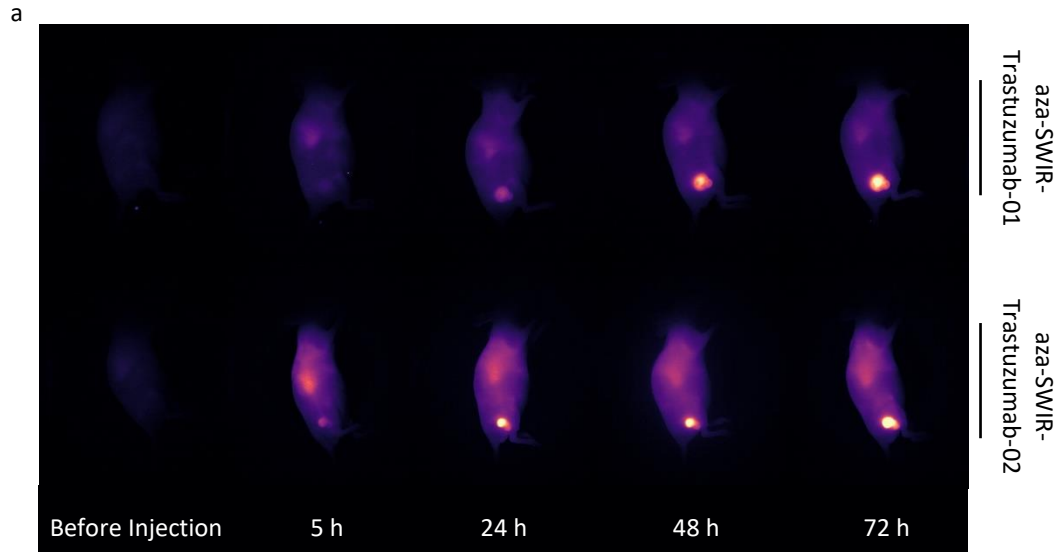


**Figure 5: Comparison between aza-SWIR-Trastuzumab-01 and aza-SWIR-Trastuzumab-02.** (a) NIR-II fluorescence images of mice bearing subcutaneous SKOV-3 before and at 5, 24, 48 and 72 h post intravenous administration of aza-SWIR-Trastuzumab-01 or aza-SWIR-Trastuzumab-02. Images were acquired at 100 ms of laser exposure. (b) *Ex-vivo* biodistribution of aza-SWIR-Trastuzumab-01 and aza-SWIR-Trastuzumab-02 in mice bearing subcutaneous SKOV-3 tumors. (c) Tumor/Muscle, Tumor/Skin and Tumor/Liver ratios calculated from the organs fluorescence in (b). The results are represented as the mean  $\pm$  S.D. (n=3/condition).

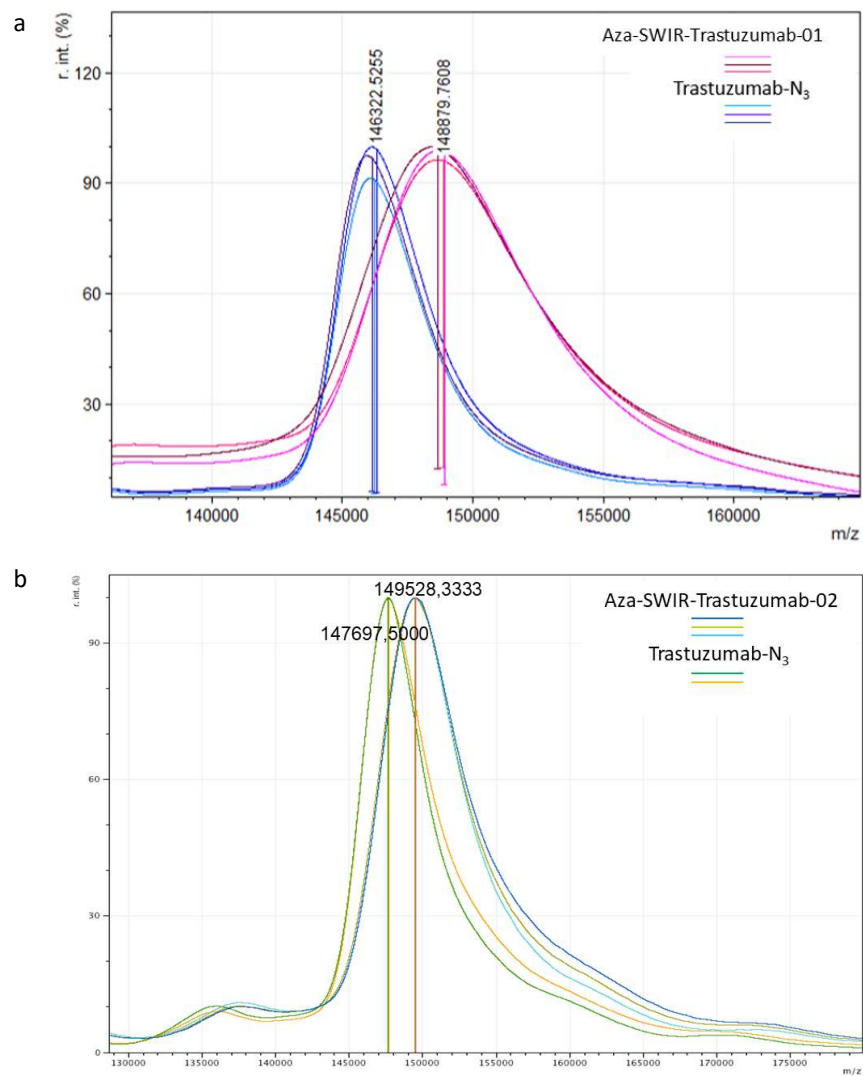


**Figure S 1:** Determining Trastuzumab degree of labeling (DOL) in aza-SWIR-Trastuzumab-01 (a) and aza-SWIR-Trastuzumab-02 (b), using MALDI-TOF spectrum (mass differences). The DOL are 1.9 and 1.4 respectively.

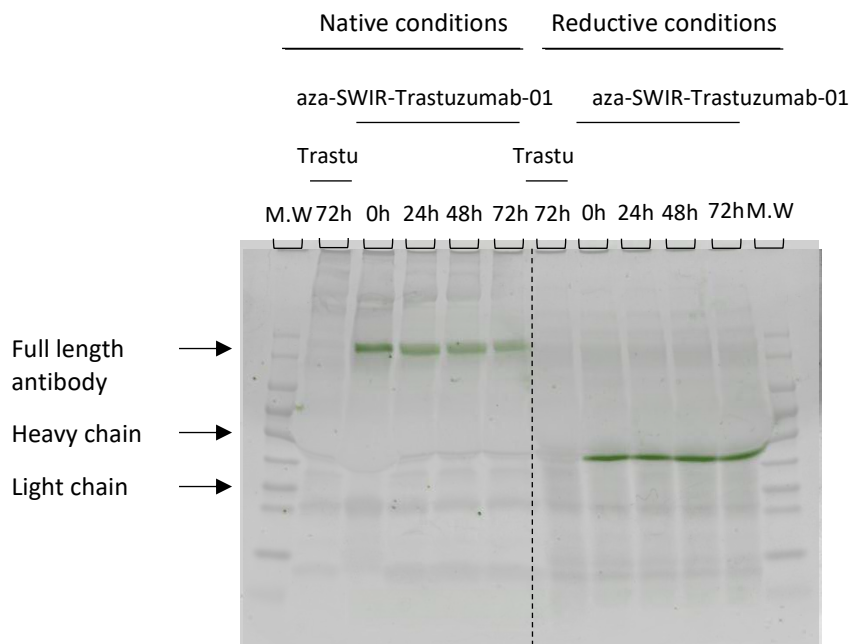
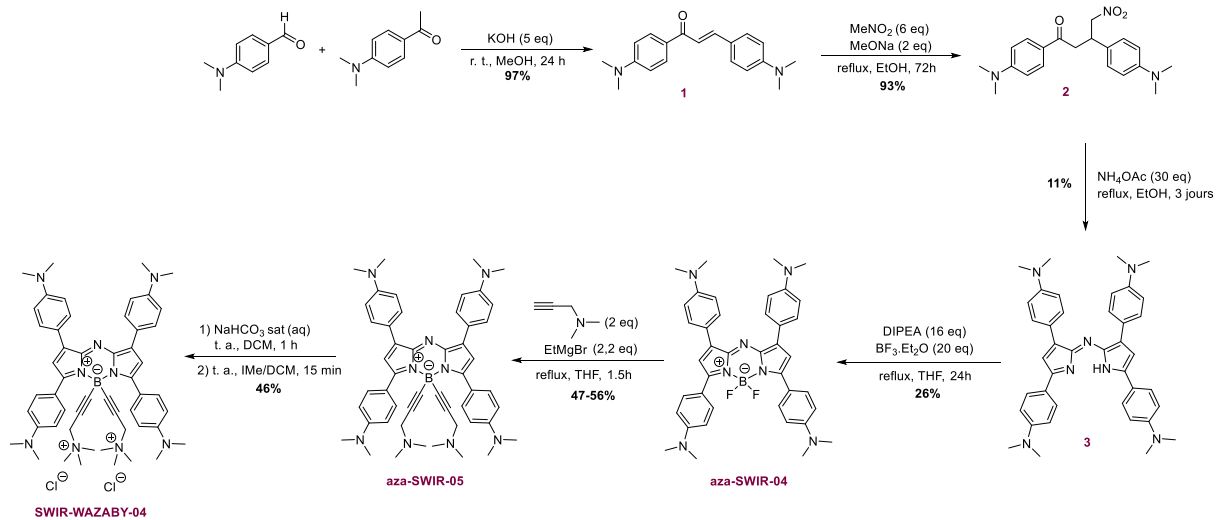


**Figure S 2: Assessment of aza-SWIR-Trastuzumab-01 stability in plasma solution.** Superimposed fluorescence image (in green) and bright field image of aza-SWIR-Trastuzumab-01 + plasma mixture migration on SDS-PAGE gel, under native and reducing conditions (DTT + heating). Aza-SWIR-Trastuzumab-01 was incubated in human sera for 0, 24, 48 and 72 h. Free Trastuzumab (non-fluorescent) incubated with serum for 72 h, served as a control.



**Scheme S 1:** Synthetic pathway of the NIR-II emitting aza-BODIPYs: SWIR-WAZABY-04.

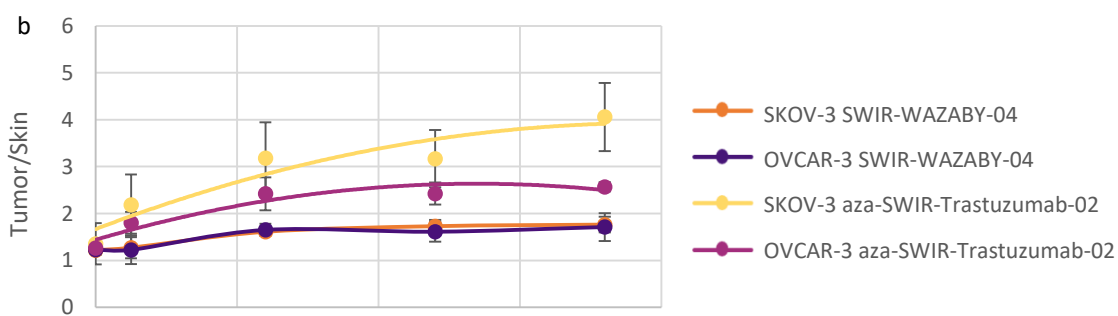
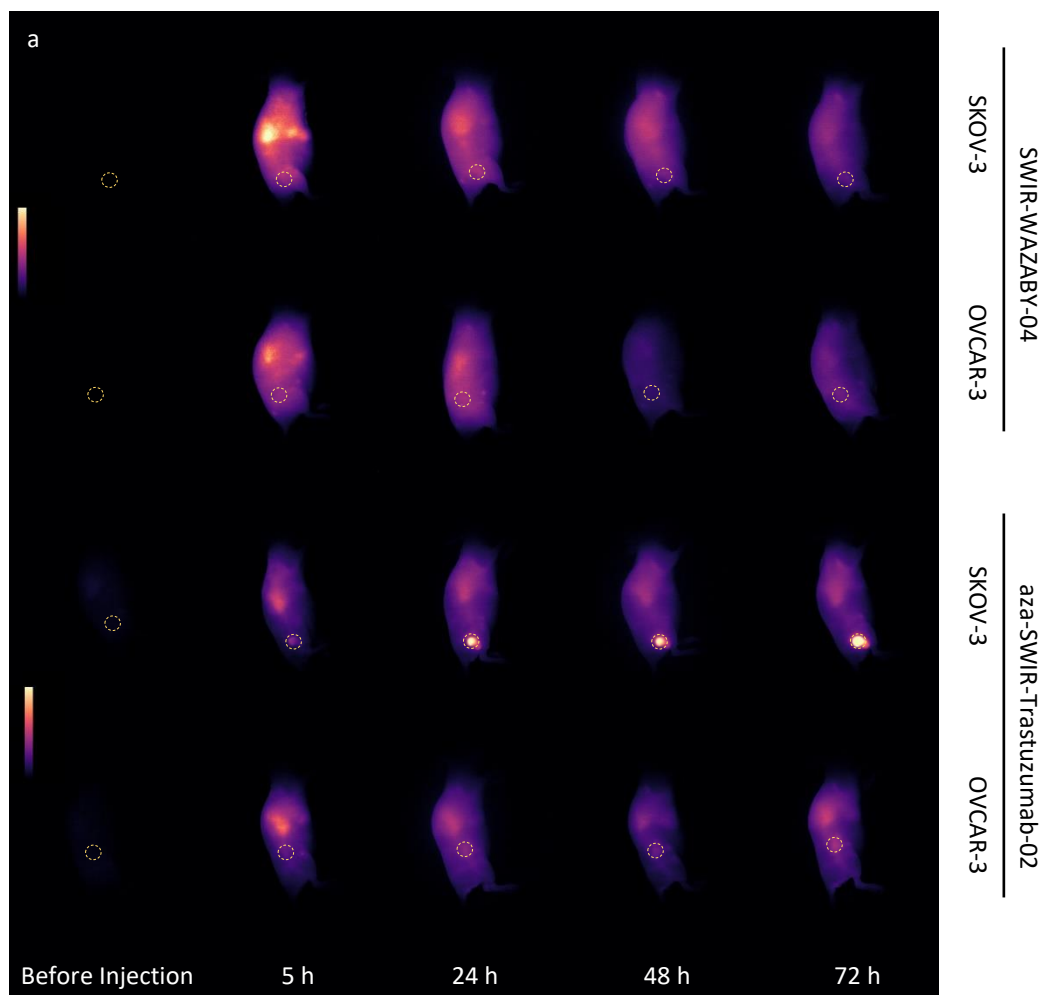


**Figure S 3: Assessment of aza-SWIR-Trastuzumab-02 affinity to HER2 *in vivo*.** (a) NIR-II fluorescence images of mice bearing subcutaneous SKOV-3 or OVCAR-3 tumors, before and at 5, 24, 48 and 72 h post intravenous administration of SWIR-WAZABY-04 or aza-SWIR-Trastuzumab-02. Tumors are indicated by dashed circles. Images of mice injected with SWIR-WAZABY-04 and aza-SWIR-Trastuzumab-02 were acquired using 10 ms and 100 ms of laser exposure respectively. (b) Tumor/Skin ratios calculated from the *in vivo* NIR-II fluorescence images of the mice in (a) . The results are represented as the mean  $\pm$  S.D. (n=3/condition).

## Supplementary information

### NMR Spectroscopy:

(<sup>1</sup>H, <sup>13</sup>C, <sup>11</sup>B, <sup>19</sup>F) were recorded at 298 K or 343K on Bruker spectrometers Avance Neo 500 MHz equipped with a 5 mm BBOF iProbe and Avance III HD 600 MHz equipped with a 5 mm BBOF N<sub>2</sub> cryoprobe. NMR spectroscopy chemical shifts are quoted in parts per million (δ) relative to TMS (for <sup>1</sup>H, <sup>13</sup>C), BF<sub>3</sub>·Et<sub>2</sub>O (for <sup>11</sup>B), CFC<sub>3</sub> (<sup>19</sup>F), calibration was made by using residual signals of the partially deuterated solvent. For all other nuclei, SR value obtained after zero-calibration of the corresponding reference was applied.

### Mass Spectrometry:

High-resolution mass spectrometry analyses were recorded on a LTQ Orbitrap XL mass spectrometer (Thermo Scientific) equipped with an electrospray ionization source (HESI 2) . The following source parameters were used if no further specification is mentioned:

Heater Temperature: 50°C

Gas Flow: Sheath 15 / Aux 10 / Sweep 0

Spray Voltage: 4 kV

Capillary Temperature: 275°C

Capillary Voltage: 22 V

Resolution (m/z = 400): 60 000

Typical conditioning: A stock solution of the analyte was prepared by dissolving 1 mg of the analyte in 1 mL of a HPLC-grade solvent chosen from the following list: CH<sub>2</sub>Cl<sub>2</sub>, MeOH, CH<sub>3</sub>CN, H<sub>2</sub>O, or in RPE-grade DMSO. For small molecules (MW < 1000 Da) a 1/100 dilution was performed using 10.0 μL of the stock solution completed to 1.0 mL by a HPLC-grade solvent of the following list sorted by order of preference: MeOH, H<sub>2</sub>O, CH<sub>3</sub>CN, CH<sub>2</sub>Cl<sub>2</sub>. For high-weight molecules (MW > 1000 Da) a 1/10 dilution was performed using 100.0 μL of the stock solution completed to 1.0 mL by a HPLC-grade solvent of the following list sorted by order of preference: MeOH, H<sub>2</sub>O, CH<sub>3</sub>CN, CH<sub>2</sub>Cl<sub>2</sub>.

The 10<sup>-5</sup> M resulting solution of the analyte was then directly infused into the spectrometer using a 500 μL syringe. The system was rinsed three times between two consecutive analyses with 500 μL of HPLC grade water and/or MeOH. Mass calibration in the 100-2000 Da mass range was operated using the commercially available Pierce LTQ ESI Positive/Negative ion Calibration solutions (ThermoFisher Scientific ref 88322/88324).

NMR, mass-analyses and elemental analysis were performed at the "Plateforme d'Analyse Chimique et de Synthèse Moléculaire de l'Université de Bourgogne" (PACSMUB).

### Analytical HPLC:

HPLC-MS analyses were obtained on a Thermo-Dionex Ultimate 3000 instrument (pump + autosampler at 20 °C + column oven at 25 °C) equipped with a diode array detector (Thermo-Dionex DAD 3000-RS) and a Thermo Scientific MSQ Plus single quadrupole mass spectrometer equipped with Phenomenex Kinetex® column (2.6 μm C18 100 Å, LC Column 50 x 2.1 mm). The corresponding low-resolution mass spectra (LRMS) were recorded with this latter mass spectrometer, with an electrospray (ESI) source (HPLC-MS coupling mode).

The employed gradient for analyses is the following:

Time [min]	% H <sub>2</sub> O + 0.1% formic acid	% ACN + 0.1% formic acid	Flow [mL/min]
0	95	5	0.5
5	0	100	0.5
6.5	0	100	0.5
6.6	95	5	0.5
8.5	95	5	0.5
8.51	95	5	0.05

### Semi-preparative HPLC:

Semi-preparative separations were executed on a HPLC-system from Shimadzu that is equipped with 2 LC-20AT pumps, a SPD-20A UV/Vis detector, a FRC-10A fraction collector, a SIL-10AP sampler, and a CBM-20A control unit. The column was a Shim-Pack GIST 5  $\mu$ m C18 10x250 mm column obtained from Shimadzu. The gradient using a mixture of ACN and water with 0.1% TFA with a flow rate of 5 mL/min is the following:

Gradient A				Gradient B			
Time [min]	% H <sub>2</sub> O + 0,1 %TFA	% ACN + 0,1 %TFA	Flow [mL/min]	Time [min]	% H <sub>2</sub> O + 0,1 %TFA	% ACN + 0,1 %TFA	Flow [mL/min]
0	75	25	5	0	70	30	5
5	75	25	5	5	70	30	5
25	0	100	5	27	0	100	5
28	0	100	5	30	0	100	5
30	75	25	5	31	70	30	5

### MALDI-TOF:

Mass spectra were recorded with a Bruker Daltonics Microflex LRF spectrometer equipped with a N<sub>2</sub> beam (337 nm) used in the MALDI-TOF reflectron mode (50-3500 Da mass range) for small molecules. Samples were prepared by using sinapic acid ([530-59-6], purchased from Sigma-Aldrich) as the matrix and spotted on a MSP 96 MALDI plate.

MALDI samples conditioning: A saturated solution of the matrix was prepared daily in a mixture of ACN/water (3/2). A 1:1 ratio of analyte/matrix was then spotted on the plate by using 2.5  $\mu$ L of the matrix solution mixed with 2.5  $\mu$ L of the analyte solution. The MALDI plate was then transferred to the MALDI chamber after complete drying of the plate. Accurate calibration was achieved by using an appropriate Trastuzumab or Trastuzumab-N<sub>3</sub> as reference (same mass range as the analyte).

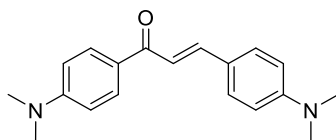
### Ion Chromatography:

Chromatographic analysis was performed using an ion chromatograph Thermo Scientific Dionex ICS 5000 with a conductivity detector CD (Thermo Scientific Dionex) and a conductivity suppressor ASRS-ultra II 4 mm (Thermo Scientific Dionex). TFA was separated using an Ion Pac AS11-HC analytical column (4  $\mu$ m, 4x250 mm, Thermo Scientific Dionex) and an Ion Pac AS11-HC guard column (4  $\mu$ m, 4x250 mm, Thermo Scientific Dionex). Chromatographic analysis was recorded with Chromeleon software, 7.2 version. The elution of TFA and Cl<sup>-</sup> was conducted in the following conditions: flow rate: 1.5 mL/min; column temperature: 30 °C; injection volume: 10  $\mu$ L. Elution: isocratic during 15 min, 90 % eluent A (NaOH 30 mM) / 10 % eluent B (H<sub>2</sub>O, ultra-pure 18.2 M $\Omega$ .cm<sup>-1</sup>).

All solutions were prepared in 18.2 mΩ.cm<sup>-1</sup> water. Sodium hydroxide (50 %, w/w, certified grade) and TFA (≥ 99.5 %, optima® LC/MS grade) were obtained from Fisher Scientific. A 1000 mg/L TFA standard solution was prepared by weighing. Commercial standard solutions at 1000 mg/L were used for chlorine ions. The mother liquor was diluted to the standard solutions of 1, 2.5, 5, and 10 mg/L before injection. A precisely weighed amount of each compound was diluted in ultra-pure water so that the concentration of TFA fits with the calibration curve. Two different dilutions were performed for each sample. The resulting concentrations of TFA allowed calculating the mass percentage of TFA contained in each sample. Measurements were performed at the “Plateforme d’Analyse Chimique et de Synthèse Moléculaire de l’Université de Bourgogne” (PACSMUB).

### Synthesis of SWIR-WAZABY-04:

#### Compound 1:

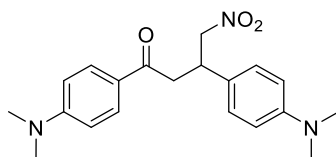


C<sub>18</sub>H<sub>19</sub>N<sub>2</sub>O  
294.398 g.mol<sup>-1</sup>  
Yellow powder  
97% Yield

KOH (2.75 g, 56.1 mmol, 4.6 eq) was dissolved in 30 mL of MeOH in a 100 mL round bottom flask. 4-dimethylaminoacetophenone (2.00 g, 12.3 mmol, 1 eq) and 4-dimethylaminobenzaldehyde (2.11 g, 14.1 mmol, 1.1 eq) were added successively and the resulting solution was stirred at room temperature. After 24 h, the reaction was stopped and the solvent was evaporated to dryness. The crude was solubilized in 80 mL of DCM and 80 mL of water was added. The two phases were separated and the aqueous phase was extracted with DCM (3 × 60 mL). The organic phases were combined, washed with brine (1 × 60 mL) and dried over sodium sulfate, and evaporated to dryness. The crude obtained was then purified by column chromatography on silica gel eluted with pentane/AcOEt (9:1 to 1:1) to isolate pure **1** as a yellow solid (3.51 g, 97 % yield).

<sup>1</sup>H NMR (500 MHz, 298 K, CDCl<sub>3</sub>) δ (ppm) = 3.03 (s, 6H), 3.07 (s, 3H), 6.69 (m, 4H), 7.41 (d, *J* = 15.4 Hz, 1H), 7.55 (d, *J* = 8.8 Hz, 2H), 7.77 (d, *J* = 15.4 Hz, 1H), 8.01 (m, 2H) <sup>13</sup>C NMR (150 MHz, 298 K, CDCl<sub>3</sub>) δ (ppm) = 40.2, 40.3, 110.9, 112.0, 117.3, 123.5, 126.9, 130.1, 130.7, 143.6, 151.8, 153.2, 188.2 HR-MS (ESI) (Da): *m/z* calculated for C<sub>19</sub>H<sub>24</sub>N<sub>3</sub>O<sub>2</sub><sup>+</sup> [M+H]<sup>+</sup> 482.18630 Da, found 482.18711 Da

#### Compound 2:



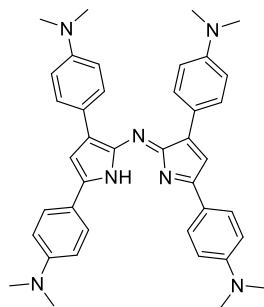
C<sub>20</sub>H<sub>25</sub>N<sub>3</sub>O<sub>3</sub>  
355.438 g.mol<sup>-1</sup>  
Brown solid  
93% Yield

The chalcone **1** (3 g, 10.2 mmol, 1 eq) was suspended in 150 mL of absolute EtOH in a 500 mL round bottom flask, and nitromethane (7.48 mL, 122.2 mmol, 12 eq) was added. Sodium methanolate (1.10 g, 20.6 mmol; 2 eq) was dissolved in 50 mL of absolute EtOH before being added to the reaction and the mixture was refluxed overnight. Upon completion, the reaction mixture was evaporated to dryness. The product was solubilized with 100 mL of DCM and 100 mL of water was added. The two phases were separated and the

aqueous phase was extracted with DCM (3 × 100 mL). The organic phases were combined, washed with brine (1 × 100 mL), and dried over sodium sulfate. The solvent was removed and the crude product purified by column chromatography on silica gel eluted with pentane/AcOEt (8/2) to obtain the corresponding pure product **2** as a brown solid (3.36 g, 93 % yield)

$^1\text{H NMR}$  (500 MHz, 298 K,  $\text{CDCl}_3$ )  $\delta$  (ppm) = 2.91 (s, 6H), 3.04 (s, 3H), 3.28 (qd,  $J$  = 16.9, 7.0 Hz, 2H), 4.10 (p,  $J$  = 7.0 Hz, 1H), 4.61 (dd,  $J$  = 12.2, 8.5 Hz, 1H), 4.81 (dd,  $J$  = 12.2, 6.2 Hz, 1H), 6.63 (d,  $J$  = 8.6 Hz, 2H), 6.67 (d,  $J$  = 8.6 Hz, 2H), 7.14 (d,  $J$  = 8.6 Hz, 2H), 7.84 (d,  $J$  = 8.6 Hz, 2H)  $^{13}\text{C NMR}$  (150 MHz, 298 K,  $\text{CDCl}_3$ )  $\delta$  (ppm) = 39.1, 40.1, 40.6, 41.2, 80.3, 110.8, 112.9, 124.6, 127.2, 128.2, 130.4, 150.1, 153.7, 195.3 **HR-MS** (ESI) (Da):  $m/z$  calculated for  $\text{C}_{20}\text{H}_{26}\text{N}_3\text{O}_3^+$   $[\text{M}+\text{H}]^+$  356.19687 Da, found 356.19707 Da.

### Compound 3:

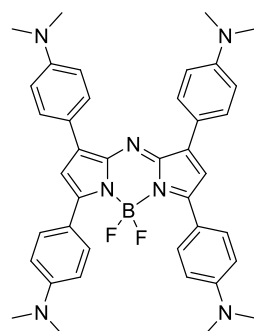


$\text{C}_{40}\text{H}_{43}\text{N}_7$   
621.833  $\text{g}\cdot\text{mol}^{-1}$   
dark powder  
11% yield

Compound **2** (0.98 g; 2.8 mmol; 1 eq) was dissolved in 30 mL of BuOH in a 100 mL round bottom flask.  $\text{NH}_4\text{OAc}$  (3.83 g, 49.6 mmol, 17.7 eq) was added and the suspension was refluxed overnight. Upon completion, the solvents were evaporated to 1/4<sup>th</sup> of the initial volume and transferred into Falcon centrifugation tubes. The mixture was centrifuged, the supernatant was discarded and the base was resuspended in EtOH. The process was repeated until the discarded supernatant came blue and the solid residue exhibits a clean, glossy surface. The solid was transferred into a round bottom flask and dried under vacuum to isolate the corresponding aza-dipyrrromethene **3** (191.5 mg, 11% yield).

$^1\text{H NMR}$  (500 MHz, 298 K,  $\text{CDCl}_3$ )  $\delta$  (ppm) = 3.03 (s, 12H), 3.09 (s, 12H), 6.79 (d,  $J$  = 8.6 Hz, 4H), 6.82 (d,  $J$  = 8.8 Hz, 4H), 6.99 (s, 2H), 7.85 (d,  $J$  = 8.6 Hz, 4H), 8.07 (d,  $J$  = 8.6 Hz, 4H)

### Compound Aza-SWIR-04:



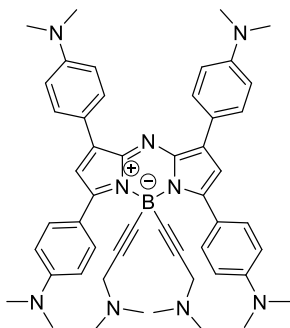
$\text{C}_{40}\text{H}_{42}\text{BF}_2\text{N}_7$   
669.632  $\text{g}\cdot\text{mol}^{-1}$   
crystaline purple/dark powder  
26% yield

Azadipyrrromethene **3** (80 mg, 0.13 mmol, 1 eq) were dissolved in 10 mL of dry THF in a 50 mL round bottom flask under argon. DIPEA (0.3 mL, 1.76 mmol, 13.5 eq) was added and the reaction was stirred for 15 min at room temperature.  $\text{BF}_3\cdot\text{Et}_2\text{O}$  (0.32 mL, 2.59 mmol, 19.9 eq) were added and the mixture was heated to reflux for 24 h. Upon completion, the reaction mixture was evaporated to dryness. The product was

solubilized with 50 mL of DCM, 50 mL of water was added and the mixture was transferred into a separating funnel. The two phases were separated and the aqueous phase was extracted with DCM (3 × 100 mL). The organic phases were combined, washed with brine (1 × 100 mL), and dried over sodium sulfate. The product was evaporated to dryness and solubilized with 50 mL of DCM and 20 mL of MeOH. DCM was gradually evaporated to replace by full MeOH. The solid was then decanted and the supernatant was removed. The obtained precipitate was resuspended in MeOH and the operation was repeated until the initially green supernatant took a blue color. The crude product was washed with Et<sub>2</sub>O (2 × 20 mL) and pentane (2 × 20 mL) and dried to obtain the corresponding **aza-SWIR-04** as a dark/purple powder (21.7 mg; 26% yield).

<sup>1</sup>H NMR (600 MHz, 298 K, CDCl<sub>3</sub>) δ (ppm) = 3.06 (s, 12H), 3.06 (s, 12H), 6.76 (d, *J* = 9.0 Hz, 4H), 6.78 (d, *J* = 9.0 Hz, 4H), 6.90 (s, 2H), 8.07 (d, *J* = 9.0 Hz, 4H), 8.09 (d, *J* = 9.0 Hz, 4H) <sup>13</sup>C NMR (150 MHz, 298 K, CDCl<sub>3</sub>) δ (ppm) = 40.3, 40.5, 111.8, 112.1, 114.9, 120.1, 122.0, 130.6, 131.3, 141.4, 145.1, 150.7, 151.5, 156.1 <sup>11</sup>B NMR (160 MHz, 298 K, CDCl<sub>3</sub>) δ (ppm) = 1.37 (t, *J* = 33.1 Hz) <sup>19</sup>F NMR (470 MHz, 298 K, CDCl<sub>3</sub>) δ (ppm) = -131.19 (q, *J* = 32.9 Hz) **HR-MS** (ESI) (Da): *m/z* calculated for C<sub>40</sub>H<sub>43</sub>BF<sub>2</sub>N<sub>7</sub><sup>+</sup> [M+H]<sup>+</sup> 670.36356 Da, found 670.36080 Da

#### Compound **aza-SWIR-05**:

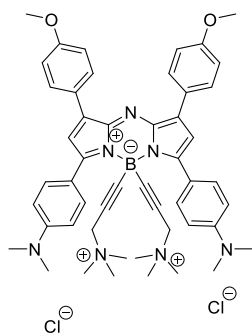


C<sub>50</sub>H<sub>58</sub>BN<sub>9</sub>  
795.887 g.mol<sup>-1</sup>  
crystalline purple powder  
47% yield

*N,N*-dimethylpropargylamine (17.2 μL, 0.15 mmol, 2 eq) was dissolved in dry THF (2 mL) in a schlenk flask under argon. Ethylmagnesium bromide (0.17 mL, 0.17 mmol, 2.3 eq) was added and the mixture was heated to reflux for 45 min. In parallel, compound **aza-SWIR-04** (50 mg, 0.075 mmol, 1 eq) was dissolved in dry THF (2 mL) in a second schlenk flask under argon. The first schlenk was then cannulated in the second one and the resulting mixture was heated to reflux for 45 min. Upon completion, the reaction was quenched with 2 mL of EtOH and evaporated to dryness. The crude product was then purified by column chromatography on silica gel eluted with 100 % ethyl acetate followed by DCM/MeOH (98/2) to obtain the corresponding pure product **aza-SWIR-05** as a fine crystalline purple powder (27.8 mg, 47 % yield).

<sup>1</sup>H NMR (600 MHz, 298 K, CDCl<sub>3</sub>) δ (ppm) = 2.25 (s, 12H), 3.06 (s, 24H), 3.29 (s, 4H), 6.72 (d, *J* = 8.8 Hz, 4H), 6.77 (d, *J* = 8.6 Hz, 4H), 6.83 (s, 2H), 8.05 (d, *J* = 8.6 Hz, 4H), 8.23 (d, *J* = 8.6 Hz, 4H) <sup>13</sup>C NMR (150 MHz, 298 K, CDCl<sub>3</sub>) δ (ppm) = 40.3, 40.4, 43.0, 48.5, 89.4, 111.0, 112.1, 115.7, 120.8, 121.8, 130.5, 132.4, 140.9, 143.0, 150.6, 151.1, 156.0 <sup>11</sup>B NMR (160 MHz, 298 K, CDCl<sub>3</sub>) δ (ppm) = -13.06 (bs) **HR-MS** (ESI) (Da): *m/z* calculated for C<sub>50</sub>H<sub>59</sub>BN<sub>9</sub><sup>+</sup> [M+H]<sup>+</sup> 796.49810 Da, found 796.49822 Da **Analytical HPLC**: Tr = 4.46 min.

### Compound SWIR-WAZABY-04:



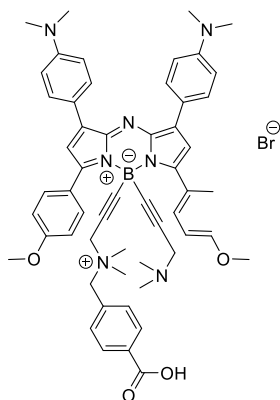
$C_{50}H_{58}BCl_2N_7O_2$   
870.771 g.mol<sup>-1</sup>  
purple solid  
46%

### Synthesis of aza-SWIR-Trastuzumab-01/ aza-SWIR-Trastuzumab-02

Compound **aza-SWIR-05** (50 mg, 0.06 mmol, 1 eq) was dissolved in 4 mL of DCM in a 10 mL round bottom flask, and 3 mL of a saturated aqueous solution of NaHCO<sub>3</sub> were added. The reaction was stirred for 1 h at room temperature. The two phases were separated and the aqueous phase was extracted with DCM (3 × 5 mL). The organic phases were combined, washed with brine (2 × 10 mL) and dried over sodium sulfate, and evaporated to dryness. The crude obtained was dissolved in 3 mL of DCM in a 10 mL round bottom flask. Iodomethane (1.5 mL, 24.1 mmol, 402 eq) was added and the mixture was stirred for 15 min at room temperature. The crude was evaporated to dryness and then purified by semi-preparative HPLC using gradient A. Product fractions were collected, evaporated to dryness, and ion exchange was performed. The product was lyophilized to obtain **SWIR-WAZABY-04** product as a blue solid (29.7 mg, 46 % yield).

<sup>1</sup>H NMR (500 MHz, DMSO-d<sub>6</sub>) δ (ppm) = 2.78 (s, 18H), 3.06 (d, J = 16 Hz, 24H), 4.02 (s, 4H), 6.83 (m, 8H), 7.31 (s, 2H), 8.08 (d, J = 8.2 Hz, 4H), 8.32-8.33 (m, 2H) <sup>13</sup>C NMR (125 MHz, 298 K, DMSO-d<sub>6</sub>) δ (ppm) = 40.1, 40.6, 51.6, 56.2, 86.1, 111.8, 113.3, 116.2, 118.2, 121.8, 130.1, 132.4, 139.1, 141.9, 149.8, 151.2 <sup>11</sup>B NMR (160 MHz, 298 K, DMSO-d<sub>6</sub>) δ (ppm) = -13.31 (bs) HR-MS (ESI) (Da): *m/z* calculated for C<sub>52</sub>H<sub>64</sub>BN<sub>9</sub><sup>2+</sup> [M]<sup>2+</sup> 412.76834 Th, found 412.76700 Th **Analytical HPLC**: Tr = 4,56 min

### Compound aza-SWIR-06:



$C_{56}H_{59}BBrN_7O_4$   
984.847 g.mol<sup>-1</sup>  
crystalline dark powder  
13% yield

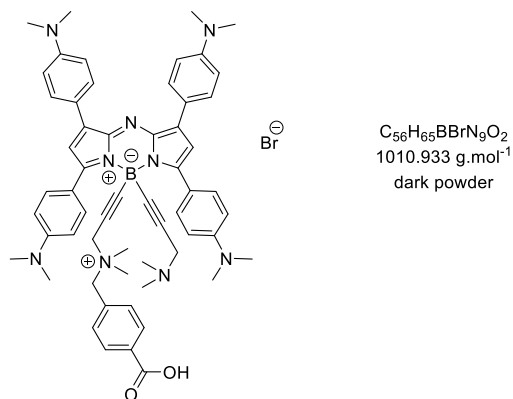
aza-SWIR-06

Under argon, compound **4** (75 mg, 97 μmol, 1 eq) was dissolved in 60 mL of dry THF in a 250 mL round bottom flask. 4-(bromomethyl)benzoic acid (22.9 mg; 106 μmol; 1.1 eq) was added and the reaction refluxed overnight. The reaction was decanted and the supernatant containing starting material removed. The

precipitate was washed with THF (3 × 15 mL) and evaporated to dryness. The crude was then purified by column chromatography on silica gel. The starting material was removed eluted with toluene/MeOH (1/0 → 8/2) followed by full MeOH to elute **aza-SWIR-06**. The fractions containing the compound were evaporated to dryness to isolate **aza-SWIR-06** as a crystalline dark powder (20.6 mg, 13% yield).

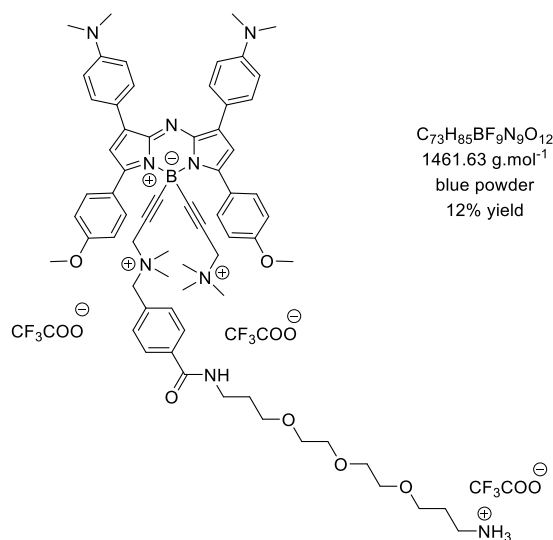
$^1\text{H NMR}$  (600 MHz, 298 K, MeOD- $d_4$ )  $\delta$  (ppm) = 2.66 (s, 6H), 2.67 (s, 6H), 3.05 (s, 12H), 3.57 (s, 2H), 3.79 (s, 6H), 3.87 (s, 2H), 3.98 (s, 2H), 6.80 (d,  $J$  = 9.0 Hz, 4H), 6.97 (s, 2H), 7.05 (d,  $J$  = 9.0 Hz, 4H), 7.32 (d,  $J$  = 8.2 Hz, 2H), 8.00 (d,  $J$  = 8.2 Hz, 2H), 8.06 (d,  $J$  = 9.0 Hz, 4H), 8.26 (d,  $J$  = 9.0 Hz, 4H)  $^{13}\text{C NMR}$  (150 MHz, 298 K, MeOD- $d_4$ )  $\delta$  (ppm) = 40.4, 42.7, 50.6, 55.2, 56.1, 66.4, 87.4, 88.6, 113.2, 114.8, 116.8, 121.9, 126.5, 131.3, 131.8, 133.3, 133.3, 133.6, 136.9, 144.1, 144.1, 152.8, 157.9, 162.8, 170.5  $^{11}\text{B NMR}$  (160 MHz, 298 K, MeOD- $d_4$ )  $\delta$  (ppm) = -12.4 (bs) **HR-MS** (ESI) (Da):  $m/z$  calculated for  $\text{C}_{56}\text{H}_{59}\text{BN}_7\text{O}_4^+$   $[\text{M}]^+$  904.47161 Th, found 904.47158 Th **Analytical HPLC**: Tr = 4.48 min.

#### Compound aza-SWIR-07:



Under argon, **aza-SWIR-05** (50 mg, 63  $\mu\text{mol}$ , 1 eq) was dissolved in 40 mL of dry THF. 4-(bromomethyl)benzoic acid (15 mg; 69  $\mu\text{mol}$ ; 1.1 eq) was added and the reaction refluxed overnight. The reaction was decanted and the precipitated was washed with 45 °C THF (3 × 15 mL) and evaporated to dryness. The supernatants were combined, evaporated to dryness, and purified by column chromatography on silica gel eluted with Toluene/MeOH (1/1 → 8/2) to remove the starting material followed by full MeOH to isolate **aza-SWIR-07** as a dark powder (8 mg). The product was also in the precipitate but with 30% impurities. Pure **aza-SWIR-07** was used for the characterization and the one with impurities was used without any further purifications for the **aza-SWIR-07** synthesis.

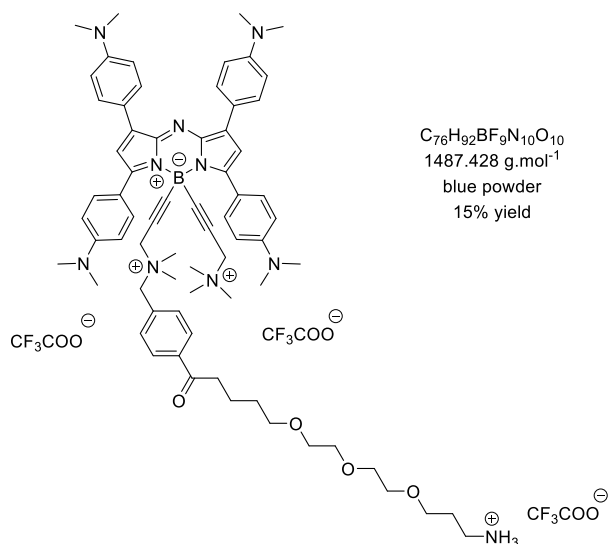
$^1\text{H NMR}$  (600 MHz, 298 K, MeOD- $d_4$ )  $\delta$  (ppm) = 2.29 (s, 6H), 2.60 (s, 6H), 2.97 (s, 12H), 3.07 (s, 12H), 3.22 (s, 2H), 3.43 (s, 2H), 3.84 (s, 2H), 6.80 (d,  $J$  = 9.0 Hz, 4H), 6.84 (d,  $J$  = 9.0 Hz, 4H), 7.03 (s, 2H), 7.28 (d,  $J$  = 8.2 Hz, 2H), 8.00 (d,  $J$  = 8.2 Hz, 2H), 8.08 (d,  $J$  = 9.0 Hz, 4H), 8.43 (d,  $J$  = 9.0 Hz, 4H)  $^{13}\text{C NMR}$  (150 MHz, 298 K, MeOD- $d_4$ )  $\delta$  (ppm) = 38.8, 39.1, 42.9, 48.1, 49.1, 53.7, 65.0, 110.8, 111.8, 115.0, 119.9, 121.2, 128.4, 129.6, 130.0, 131.8, 132.2, 135.5, 140.8, 142.4, 151.0, 151.4, 155.7 **HR-MS** (ESI) (Da):  $m/z$  calculated for  $\text{C}_{58}\text{H}_{65}\text{BN}_9\text{O}_2^+$   $[\text{M}]^+$  930.53488 Th, found 930.53471 Th **Analytical HPLC**: Tr = 4.51 min.

**Compound SWIR-WAZABY-05:**

Compound **aza-SWIR-06** (21 mg, 0.02 mmol, 1 eq) was dissolved in 2 mL of dry DMF in a round bottom flask. HBTU (20 mg, 0.05 mmol, 2.5 eq) was dissolved in dry DMF (2 mL) before being added to the solution followed by DIPEA (32  $\mu$ L, 0.16 mmol, 8 eq). The mixture was stirred at room temperature for 30 min at 30 °C and TOTA-Boc (10 mg, 0.02 mmol, 1 eq) was added. The solution was stirred at 30 °C for 1 h 30. Solvents were evaporated and the crude purified by column chromatography on silica gel eluted with DCM/MeOH (10/0  $\rightarrow$  1/1) to isolate the Boc-intermediate as a dark solid. This intermediate was immediately dissolved in dry DCM (4 mL). Iodomethane (1 mL, 16.1 mmol, 805 eq) was added and the reaction stirred at room temperature for one hour. The solvents were evaporated and the crude solubilized in 20 mL of ACN. 10 mL of HCl (3M) was added and the solution was stirred at 40 °C for 2 h. The crude was evaporated to dryness and purified by semi-preparative HPLC. **SWIR-WAZABY-05** was lyophilized and isolated as a blue solid (3.5 mg, 12% yield).

**RMN  $^1H$**  (600 MHz, 343 K, ACN- $d_3/D_2O$ )  $\delta$  (ppm) = 1.84 (h,  $J$  = 7.2 Hz, 2H), 1.99 (p,  $J$  = 6.9 Hz, 2H), 2.76-2.77 (m, 3H), 2.78 (s, 3H), 2.83 (s, 3H), 2.96 (s, 3H), 3.11 (s, 12H), 3.17 (t,  $J$  = 6.9 Hz, 2H), 3.57-3.60 (m, 2H), 3.63 (s, 3H), 3.64 (s, 9H), 3.76 (s, 1H), 3.88-3.91 (m, 6H), 3.92 (s, 1H), 4.03 (s, 1H), 4.06 (s, 1H), 4.11 (s, 1H), 7.02-7.03 (m, 2H), 7.10 (dd,  $J$  = 8.2 ; 2.0 Hz, 4H), 7.17 (d,  $J$  = 8.2 Hz, 4H), 7.34-7.35 (m, 1H), 7.36-7.38 (m, 1H), 7.70-7.72 (m, 2H), 8.01-8.03 (m, 4H), 8.14 (d,  $J$  = 8.2 Hz, 4H) **RMN  $^{13}C$**  (150 MHz, 343 K, ACN- $d_3/D_2O$ )  $\delta$  (ppm) = 27.0, 28.8, 28.9, 37.8, 38.3, 38.4, 42.3, 42.8, 43.4, 43.6, 48.1, 50.9, 50.9, 53.0, 54.4, 54.6, 54.7, 56.3, 56.3, 57.8, 67.1, 68.7, 68.8, 69.2, 69.3, 69.8, 69.9 ; 69.9, 70.0, 70.1, 86.7, 87.1, 114.5, 114.6, 116.9, 117.1, 118.6, 125.1, 127.9, 128.0, 128.3, 130.4, 130.7, 131.2, 131.3, 132.6, 132.6, 133.1, 133.6, 136.5, 136.5, 136.9, 141.1, 141.2, 143.3, 158.1, 161.7, 168.9, 170.1 **RMN  $^{11}B$**  (193 MHz, 343 K, ACN- $d_3/D_2O$ )  $\delta$  (ppm) = -12.38 (bs) **HR-MS** (ESI) (Da):  $m/z$  calculated for  $C_{66}H_{83}BN_9O_6^{3+}$  [M] $^{3+}$  374.22331 Th, found 374.22292 Th **Analytical HPLC**: Tr = 4.18 min

### Compound SWIR-WAZABY-06:



A mixture of **aza-SWIR-07** containing 30% of impurities (30.5 mg, 28  $\mu$ mol mmol, 1 eq) was dissolved in 3 mL of dry DMF in a round bottom flask. HBTU (42.5 mg, 112  $\mu$ mol, 4 eq) was dissolved in dry DMF (2 mL) before being added to the solution with DIPEA (43.8  $\mu$ L, 252  $\mu$ mol, 8 eq). The mixture was stirred at room temperature for 30 min at 30 °C. A solution of TOTA-Boc (16.1 mg, 38  $\mu$ mol, 1.1 eq) in 3 mL DMF was added. The solution was stirred at 30 °C for 1 h 30. The solvents were evaporated to dryness. The crude was solubilized with 20 mL of DCM/water (1/1) and transferred into a separating funnel. The two phases were separated. The aqueous phase was extracted with DCM (3  $\times$  15 mL). The organic phases were combined, washed with brine (1  $\times$  20 mL) and with a saturated solution of NaHCO<sub>3</sub> (1  $\times$  20 mL), and dried over sodium sulfate. The crude was evaporated to dryness and solubilized with 2 mL of DCM. Iodomethane (1 mL, 16.1 mmol, 805 eq) was added and the reaction stirred at room temperature for one hour. The solvents were evaporated and the crude solubilized in 20 mL of ACN. 10 mL of HCl (3M) was added and the solution was stirred at 40 °C for 2 h. The crude was evaporated to dryness and purified by semi-preparative HPLC. The resulting compound was lyophilized to isolate pure **SWIR-WAZABY-06** as a green solid (4.7 mg, 15% yield).

**RMN <sup>1</sup>H** (600 MHz, 343 K, DMSO-d<sub>6</sub>)  $\delta$  (ppm) = 1.75 (dp,  $J$  = 13.3, 6.5 Hz, 4H), 2.59 (s, 2H), 2.64 (s, 2H), 2.83 (s, 9H), 2.71 (s, 6H), 2.83 (s, 3H), 2.96-2.99 (m, 12H), 3.04 (s, 12H), 3.30-3.32 (m, 4H), 3.51-3.53 (m, 8H), 3.85 (s, 2H), 3.93 (s, 1H), 3.799 (s, 1H), 4.09 (s, 2H), 6.77-6.80 (m, 4H), 6.83 (d,  $J$  = 8.7 Hz, 4H), 7.32 (s, 2H), 7.34 (d,  $J$  = 8.1 Hz, 2H), 7.67 (bs, 3H), 7.84-7.87 (m, 2H), 8.08 (d,  $J$  = 9.0 Hz, 4H), 8.34-8.37 (m, 4H), 8.58 (t,  $J$  = 5.5 Hz, 1H) **RMN <sup>13</sup>C** (150 MHz, 343 K, DMSO-d<sub>6</sub>)  $\delta$  (ppm) = 27.20 (C<sub>z</sub>), 29.4 (C<sub>ad</sub>), 36.8 (C<sub>y</sub>), 36.9 (C<sub>ae</sub>), 40.1 (C<sub>a</sub>), 41.1 (C<sub>n</sub>), 49.4 (C<sub>p'</sub>), 51.6 (C<sub>q</sub>), 56.3 (C<sub>p</sub>), 67.4 (C<sub>t</sub>), 68.7 (C<sub>ab</sub>), 68.3 (C<sub>aa</sub>), 69.5 (C<sub>ab</sub>), 69.6 (C<sub>ab</sub>), 69.7 (C<sub>aa</sub>), 69.8 (C<sub>aa</sub>), 86.1 (C<sub>o</sub>), 111.2 (C<sub>c</sub>), 111.3 (C<sub>c</sub>), 112.0 (C<sub>i</sub>), 115.6 (C<sub>h</sub>), 115.9 (C<sub>h</sub>), 118.5 (C<sub>e</sub>), 120.1 (C<sub>j</sub>), 127.7 (C<sub>i</sub>), 130.1 (C<sub>v</sub>), 130.1 (C<sub>d</sub>), 132.3 (C<sub>k</sub>), 132.5 (C<sub>u</sub>), 136.2 (C<sub>s</sub>), 139.6 (C<sub>f</sub>), 141.7 (C<sub>g</sub>), 151.3 (C<sub>b</sub>), 154.6 (C<sub>m</sub>), 158.0 (C<sub>i</sub>), 158.2 (C<sub>i</sub>), 165.3 (C<sub>w</sub>) **RMN <sup>11</sup>B** (193 MHz, 343 K, DMSO-d<sub>6</sub>)  $\delta$  (ppm) = -12.30 (bs) **HR-MS** (ESI) (Da):  $m/z$  calculated for C<sub>69</sub>H<sub>90</sub>BN<sub>11</sub>O<sub>4</sub><sup>2+</sup> [M]<sup>2+</sup> 573.86297 Th, found 573.86482 Th **Analytical HPLC**: Tr = 4.06 min

## Discussion and perspectives

Two water-soluble NIR-II Trastuzumab-bioconjugated probes (i.e. aza-SWIR-Trastuzumab-01 and aza-SWIR-Trastuzumab-02) were successfully developed. Both probes were stable with time and showed high specificity in detecting ovarian tumors expressing HER2 receptor *in vivo* (i.e. SKOV-3 tumors), which wasn't achieved using their non-bioconjugated fluorophore counterparts i.e. SWIR-WAZABY-01 and SWIR-WAZABY-04, respectively. Considering the superior NIR-II fluorescence properties and the improved tumor/muscle ratio (~23) attained by aza-SWIR-Trastuzumab-02 compared to aza-SWIR-Trastuzumab-01 (~7), aza-SWIR-Trastuzumab-02 presents the ideal NIR-II bioconjugated probe model for NIR-II FGS application.

In the perspective of applying the latter probe model (SWIR-WAZABY-04 coupled to an antibody) to NIR-II FGS, we aim at targeting head and neck tumors to facilitate the surgery and to precisely delineate and resect those tumors with negative margins. To this end, our next step will consist of coupling SWIR-WAZABY-04 precursor to relevant antibodies in the context of Head and Neck tumors, as anti-PDL1 antibodies, since 80 % of head and neck tumors express PDL1. This work presents an important step in the valorization of the patent and it has been recently supported by the Linksiem (SATT Transfert de Technologies & Création de Startup).

Several head and neck tumor cell lines were characterized and the corresponding *in vivo* orthotopic tumor models have been well established in the laboratory. Following aza-SWIR-anti-PDL1 antibody synthesis, the optimal concentration/dose, and the time interval between the probe injection and imaging will be determined. The Ph.D. student Dr. Christole FABRE, MD, a surgeon at CHU Grenoble Alpes, will then perform NIR-II fluorescence-guided surgery for head and neck tumors using the aza-SWIR-anti-PDL1 antibody, and compare its tumor-free survival with those obtained following ICG, IRDye800, and IRDye800-anti-PDL1 antibody "Gold standard fluorophores" FGS. We hope that the obtained data will provide a proof of concept of our NIR-II bioconjugated probe superiority over dyes assessed in the clinic.

To have a chance to be evaluated in a clinical trial, the bioconjugated aza-BODIPY probe should have better optical properties *in vivo* as compared to the 2 gold-standard dyes, better or prolonged tumor accumulation, and no toxicity. In addition, chemical and economic considerations are necessary. The dye should be easy to produce at a large scale, very cheap, and chemically and photochemically stable. All these considerations will be evaluated in the next studies of the team.

Further perspectives include the introduction of a chelator (for PET/SPECT imaging) into the NIR-II bioconjugated probe. The resulting probe will allow both, a preoperative PET/SPECT imaging to localize different tumor lesions and an intraoperative NIR-II FGS to assist surgeons during lesions resection. In fact, the development of SPECT/NIR-I bimodal imaging bioconjugated probe has been recently reported by our collaborators at ICMUB [211], suggesting that the synthesis of SPECT/NIR-II bimodal imaging bioconjugated probe seems feasible.

To avoid liver accumulation, and facilitate the regulatory validation of our NIR-II bioconjugated probes, applying it topically to superficial tumors would be a solution. For instance, spraying bevacizumab-IRDye800CW topically on the esophagus lumen of patients possessing esophageal adenocarcinoma, allowed the visualization of all dysplastic and neoplastic lesions, and provided a slightly higher tumor-to-background ratio (TBR) compared to systemic administration [212]. This probe has already completed phase I clinical trial and started phase II trials.

## Article 4: Aza-BODIPY: A New Vector for Enhanced Theranostic Boron Neutron Capture Therapy Applications

As discussed in section 4 of the introduction, the implantation of BNCT in daily clinical practice requires both, the installation of hospital-based neutron sources, and the development of novel boron-10 rich compounds possessing adequate safety profiles, selective and high tumor uptake, and intrinsic imaging properties that allow their tracking and quantification. With more accelerator-based neutron sources being approved, the development of theranostic boron compounds remains a main requisite. Since the development of BSH and (<sup>18</sup>F)-BPA, several theranostic BNCT compounds have been reported. However none of them have passed to clinical assessment due to either their poor tumor uptake, toxicity, difficult synthesis, or absence of an impressive anti-tumor effect.

To address this challenge, we developed with our collaborators at ICMUB a theranostic BNCT compound based on the previously reported aza-BODIPY fluorophore i.e. SWIR-WAZABY-01 (article 1) coupled to the clinically used boron compound i.e. BSH. The resulting compound i.e. aza-SWIR-BSH-01 takes advantage of SWIR-WAZABY-01 significant tumor-targeting capacity and unique fluorescence properties, to enable enhanced BSH vectorization into tumors and real-time imaging respectively. Aza-SWIR-BSH-01 synthesis, tumor accumulation, and therapeutic potential following neutron irradiation were investigated in the following article entitled “*Aza-BODIPY: A New Vector for Enhanced Theranostic Boron Neutron Capture Therapy Applications*”, published in *Cells*.

Aza-SWIR-BSH-01 showed strong uptake in tumor cells *in vitro* and in mice tumors *in vivo*, as demonstrated by fluorescence optical imaging and boron quantification data. Following neutron field irradiation, a reduction in tumor growth was observed in tumor cells *in vitro* and in *in ovo* glioblastoma tumor model, as compared to BSH alone. These experiments demonstrated the potential and the efficacy of aza-SWIR-BSH-01 as a theranostic BNCT compound in preclinical tumor models.

To note, I was responsible for the biological investigations applied in article 4. The neutron irradiation experiments were performed at the ILL (Institut Laue-Langevin) within our dedicated beam time. In this context, I have developed an *in ovo* glioblastoma tumor model to substitute the use of *in vivo* rodents at the ILL. It is worth noting that this model wasn't established in our laboratory previously. The chemical synthesis and the laser-induced breakdown spectroscopy studies were performed by the chemists and the physicists at ICMUB and ILM (Institut Lumière Matière) respectively.

The use of aza-SWIR-BSH-01 as a theranostic BNCT compound was presented as an oral communication at the “SFNano-C’Nano joint meeting 2019” and as a poster pitch at the “15th

European Molecular Imaging Meeting (vEMIM 2020)". Accordingly, I was awarded the "Best flash presentation prize" and "Best of vEMIM Poster-Pitches award".

Article

# Aza-BODIPY: A New Vector for Enhanced Theranostic Boron Neutron Capture Therapy Applications

Ghadir Kalot <sup>1,†</sup>, Amélie Godard <sup>2,†</sup>, Benoît Busser <sup>1,3</sup>, Jacques Pliquett <sup>2</sup>, Mans Broekgaarden <sup>1</sup>, Vincent Motto-Ros <sup>4</sup>, Karl David Wegner <sup>5</sup>, Ute Resch-Genger <sup>5</sup>, Ulli Köster <sup>6</sup>, Franck Denat <sup>2</sup>, Jean-Luc Coll <sup>1</sup>, Ewen Bodio <sup>2,\*</sup>, Christine Goze <sup>2,\*</sup> and Lucie Sancey <sup>1,\*</sup>

<sup>1</sup> Institute for Advanced Biosciences, UGA INSERM U1209 CNRS UMR5309, 38700 La Tronche, France; Ghadir.kalot@univ-grenoble-alpes.fr (G.K.); bbusser@chu-grenoble.fr (B.B.); mans.broekgaarden@univ-grenoble-alpes.fr (M.B.); jean-luc.coll@univ-grenoble-alpes.fr (J.-L.C.)

<sup>2</sup> Institut de Chimie Moléculaire de l'Université de Bourgogne, ICMUB CNRS, UMR 6302, Université Bourgogne Franche-Comté, 21078 Dijon, France; amelie\_godard@etu.u-bourgogne.fr (A.G.); jacques.pliquett@googlemail.com (J.P.); franck.denat@u-bourgogne.fr (F.D.)

<sup>3</sup> Grenoble Alpes University Hospital, 38043 Grenoble, France

<sup>4</sup> Institut Lumière Matière UMR 5306, Université Lyon 1-CNRS, Université de Lyon, 69622 Villeurbanne, France; vincent.motto-ros@univ-lyon1.fr

<sup>5</sup> Division Biophotonics, Federal Institute for Materials Research and Testing (BAM), Richard-Willstaetter-Str. 11, 12489 Berlin, Germany; karl-david.wegner@bam.de (K.D.W.); ute.resch@bam.de (U.R.-G.)

<sup>6</sup> Institut Laue Langevin, 38042 Grenoble, France; koester@ill.fr

\* Correspondence: Ewen.bodio@u-bourgogne.fr (E.B.); Christine.goze@u-bourgogne.fr (C.G.); lucie.sancey@univ-grenoble-alpes.fr (L.S.); Tel.: +33-380-396-076 (E.B.); +33-380-399-043 (C.G.); +33-476-549-410 (L.S.)

† G.K. and A.G. contributed equally to this work.

Received: 29 July 2020; Accepted: 20 August 2020; Published: 25 August 2020



**Abstract:** Boron neutron capture therapy (BNCT) is a radiotherapeutic modality based on the nuclear capture of slow neutrons by stable <sup>10</sup>B atoms followed by charged particle emission that inducing extensive damage on a very localized level (<10 μm). To be efficient, a sufficient amount of <sup>10</sup>B should accumulate in the tumor area while being almost cleared from the normal surroundings. A water-soluble aza-boron-dipyrromethene dyes (BODIPY) fluorophore was reported to strongly accumulate in the tumor area with high and BNCT compatible Tumor/Healthy Tissue ratios. The clinically used <sup>10</sup>B-BSH (sodium borocaptate) was coupled to the water-soluble aza-BODIPY platform for enhanced <sup>10</sup>B-BSH tumor vectorization. We demonstrated a strong uptake of the compound in tumor cells and determined its biodistribution in mice-bearing tumors. A model of chorioallantoic membrane-bearing glioblastoma xenograft was developed to evidence the BNCT potential of such compound, by subjecting it to slow neutrons. We demonstrated the tumor accumulation of the compound in real-time using optical imaging and ex vivo using elemental imaging based on laser-induced breakdown spectroscopy. The tumor growth was significantly reduced as compared to BNCT with <sup>10</sup>B-BSH. Altogether, the fluorescent aza-BODIPY/<sup>10</sup>B-BSH compound is able to vectorize and image the <sup>10</sup>B-BSH in the tumor area, increasing its theranostic potential for efficient approach of BNCT.

**Keywords:** aza-BODIPY; BNCT; in ovo model; theranostic; boron compound; <sup>10</sup>B-BSH; optical imaging; NIR-I; SWIR

## 1. Introduction

Boron neutron capture therapy (BNCT) is a cancer treatment modality based on the vectorization of  $^{10}\text{B}$ -rich compounds in tumor tissues before neutron exposure to selectively destroy cancer cells. Under low-energy neutron irradiation, the stable  $^{10}\text{B}$  atoms may capture neutrons producing energetic alpha and  $^7\text{Li}$  particles. The generated high-linear energy transfer (LET) particles have a cell killing effect within a 10  $\mu\text{m}$ -range [1,2]. Such type of cancer treatment may not only spare the surrounding healthy tissues but may be efficient to treat recurrent, or radioresistant to conventional X-ray photon therapy tumors [3–6].

BNCT has obtained promising clinical results for several pathologies as head and neck tumors including recurrent pathologies [3,5,7], malignant brain tumors [8,9], and malignant melanoma [10,11]. Regardless of these reports, there are still several limitations. The first limitation of this treatment modality meanwhile overcome was the lack of hospital neutron sources that limited the clinical practice to research nuclear reactor sites. Recent developments have permitted the installation of accelerator-based neutron sources [12,13], opening new perspectives to BNCT. In the last 4 decades, only two compounds have been used as  $^{10}\text{B}$ -sources for BNCT in patients: sodium mercaptoundecahydrododecaborate (also called sodium borocaptate,  $\text{Na}_2^{10}\text{B}_{12}\text{H}_{11}\text{SH}$ ;  $\text{Na}_2^{10}\text{BSH}$ ; or BSH) and L-*p*-boronophenylalanine (L- $^{10}\text{BPA}$ ). While not used in clinical trials, GB-10 ( $[\text{closo-B}_{10}\text{H}_{10}]^{2-}$ , dodecahydrododecaborate) is also an FDA approved molecule [14]. Despite their clinical use, both compounds do not fulfill all the required criteria. In particular, to be successful, 20 to 50  $\mu\text{g}$  of  $^{10}\text{B}$  per gram of tumor is necessary, with a tumor-to-normal tissue and tumor-to-blood ratio > 3:1 [15].

To deliver boron-containing compounds in tumors, various low molecular weight molecules have been developed for preclinical research including boron clusters [16,17], amino acid derivatives [18], RGD-BSH conjugates for integrin  $\alpha_v\beta_3$  targeting [19], and several other specific targeted systems [20–22]. The clinical application of BNCT requires the tracking of the compound in vivo to predict the  $^{10}\text{B}$  concentration in the tumor and surrounding non-tumor tissues. Blood samples are required for indirect  $^{10}\text{B}$  tumor amount estimation [23,24] and adjustment of the treatment planning system that permits to deliver the optimal neutron exposure time and to determine the dose delivered to the patient. Positron emission tomography (PET) or single-photon emission computed tomography (SPECT), which are highly sensitive nuclear imaging techniques, are non-invasive quantification procedures used to track and quantify boron carriers in vivo, for personalized treatment protocols.

For preclinical studies, optical imaging (OI) can be also used [25,26]. Among the different optical probes, boron-dipyrromethene dyes (BODIPYs, Figure 1a) are very versatile organic fluorophores with tunable optical properties from the visible to the NIR-I (Near Infrared) and SWIR (Short Wave Infrared) optical windows [27–29], which display excellent photophysical properties controlled by substitution pattern conferring a strong interest for these compounds as theranostic tools [30,31]. Moreover, the fluorine atoms on the boron could be substituted by acetylides bearing ammonium groups for engrafting functional groups to increase the water-solubility and to conjugate them with chelates for OI/PET, OI/SPECT bimodal imaging [32–35], and therapeutic moieties [31,36,37]. BODIPY fluorophores are also interesting for BNCT, as they possess a boron atom. However, the presence of only a single boron atom in the BODIPY core and the limited number of commercially available  $^{10}\text{B}$ -boron reagents make it difficult to synthesize enriched  $^{10}\text{B}$ -BODIPYs. For this reason, BODIPY derivatives reported for a BNCT use implied their conjugation to a  $^{10}\text{B}$ -boron cluster [38–41]. Up-to-now, none of these studies described either in vivo BNCT investigations or OI distribution studies due to the fact that BODIPYs emit in the visible region of the light spectrum while preclinical OI studies require fluorescence emission in the NIR-I and, if possible, in the NIR-II/SWIR optical window. To bridge this gap, we decided to tether a  $^{10}\text{B}$ -BSH on a NIR-emitting BODIPY derivative named aza-BODIPY (Figure 1b), thereby creating a theranostic system gathering the advantages of both aza-BODIPY and  $^{10}\text{B}$ -BSH components.

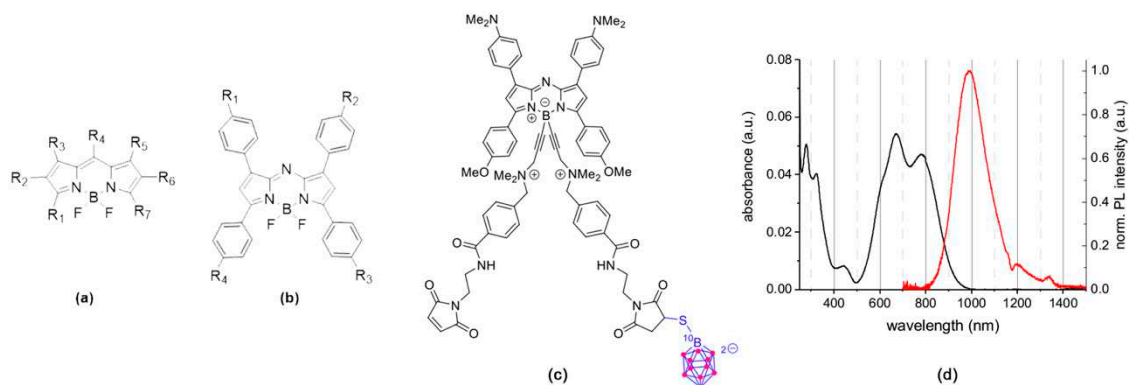


**Figure 1.** (a) General structure of boron-dipyromethene dyes (BODIPY), (b) aza-BODIPY, and (c) aza-SWIR-BSH-01, (d) absorption and emission spectra of aza-SWIR-BSH-01 in DMSO [29].

We recently reported the use of a *B*-functionalized aza-BODIPY emitting in the SWIR region and accumulating in tumors via EPR effect (Enhanced permeability and retention effect) with high and prolonged Tumor/Healthy Muscle ratio (between 5 and 30, from 24 to 168 h post-injection) without the need of tethering vector [29]. SWIR fluorophores enable to reach a penetration depth of 1 to 10 mm with increased resolution of the images as compared to those obtained with NIR-I probes [42,43]. Here, such aza-BODIPY was used to vectorize the small  $^{10}\text{B}$ -BSH molecule at the tumor site while benefitting from the imaging properties of the fluorophore for theranostic applications. First, the tumor cell loading capacity of the compound was demonstrated using original microscopy settings and its *in vitro* BNCT efficacy. Then, its distribution and behavior in tumor-bearing mice were described. For BNCT experiments performed on animals, the chorioallantoic membrane (CAM) model in fertilized chicken eggs was used to establish vascularized glioblastoma *in vivo* and evaluated the aza-BODIPY/ $^{10}\text{B}$ -BSH conjugate tumor uptake with optical imaging and laser-induced breakdown spectroscopy [44–47]. Finally, a neutron beam was used to evaluate the expected toxicity of the neutron-exposed aza-BODIPY/ $^{10}\text{B}$ -BSH compounds and demonstrated their strong potential as efficient theranostic boron-vectors for promising BNCT applications.

## 2. Materials and Methods

### 2.1. Synthesis and Characterization of Compounds

Detailed syntheses and analyses—NMR, mass-analyses (the calculations are based on the mass of the most abundant isotopologue, unless otherwise specified), and HPLC-MS—can be found in ESI and previously reported studies [29,48]. ( $^1\text{H}$ ,  $^{11}\text{B}$ ,  $^{13}\text{C}$ ,  $^{19}\text{F}$ )-NMR spectra were recorded at 300 K on Bruker 500 Avance III or 600 Avance III spectrometers. Chemical shifts are given relative to TMS (tetramethylsilane) ( $^1\text{H}$ ,  $^{13}\text{C}$ ),  $\text{BF}_3 \cdot \text{Et}_2\text{O}$  ( $^{11}\text{B}$ ),  $\text{CFCl}_3$  ( $^{19}\text{F}$ ), and were referenced to the residual solvent signal. High-resolution mass spectra (HR-MS) were recorded on a Thermo LTQ Orbitrap XL ESIMS spectrometer. NMR and mass-analyses were performed at the “Plateforme d’Analyse Chimique et de Synthèse Moléculaire de l’Université de Bourgogne” (PACSMUB). The photophysical characterization has been performed as described previously [29] using UV-Vis-NIR spectrophotometer Cary5000 between 300 and 1200 nm. Steady-state photoluminescence spectra were measured from 700 to 1500 nm with a calibrated FSP 920 (Edinburgh Instruments, Edinburgh, UK) spectrofluorometer equipped with a nitrogen-cooled PMT R5509P.

### 2.2. Cell Lines and Culture

Human glioblastoma astrocytoma cell lines, U-87 MG and U-251 MG, were obtained from the European Collection of Authenticated Cell Cultures (ECACC).

U-87 MG and U-251 MG cell lines were cultured in a 37 °C humidified environment containing 5%  $\text{CO}_2$  in DMEM media supplemented with 10% heat-inactivated fetal bovine serum, and for U-87 MG

cell cultures 1% non-essential amino acids. A total of 10,000 cells were plated into 4-well chambered cover glass Nunc™ Lab-Tek™ II (Roskilde, Denmark) for 48 h to be used for fluorescence microscopy.

### 2.3. Fluorescence Microscopy

Previously prepared 2D cell cultures were kept at 37 °C, 5% CO<sub>2</sub> and incubated with 10 μM aza-SWIR-BSH-01 compound solution diluted in cell culture medium. Fluorescence microscopy images were acquired using a confocal laser-scanning microscope (LSM 710 Carl Zeiss, Jena, Germany) in combi mode. Plan apochromat 63× in oil objective was used. Hoechst 33,342 was used to counterstain the cell nuclei (1 μM). Optimal fluorescent signal would be obtained with a 680 nm excitation laser, and a collection wavelength between 800–1200 nm would be required. However, such settings are not available in our current microscopy system. Therefore, the fluorescent signal of the water-soluble aza-BODIPY was collected after excitation with 1.5% 633 nm laser (pinhole aperture 200 μm, gain 1000) using a LP736 filter, in APD (avalanche photodiode) mode.

Images were processed using ImageJ software. The experiments were performed at the MicroCell (Optical Microscopy-Cell Imaging) platform, IAB Grenoble.

### 2.4. In Vivo Imaging Experiments

All animal experiments were performed in accordance with the Institutional Animal Care and Use Committee at Grenoble Alpes University. These experiments were also approved by the Animal Ethics Committee of the French Ministry, under the agreement number APAFIS #8782. The experiments were performed at the Optimal (Small Animal Imaging Platform) platform, IAB Grenoble.

U-87 MG cancer cells (5 million cells per 100 μL PBS) were injected subcutaneously on the right flank of female NMRI nude mice (6-8-week-old) (Janvier Labs, Le Genest-Saint Isle, France). After tumor growth (~two weeks), 6 mice were anesthetized (air/isoflurane 4% for induction and 2% thereafter) and injected intravenously in the tail vein with 200 μL of aza-SWIR-BSH-01 (600 μM in PBS). Whole-body NIR fluorescence images were acquired before and 2, 5, 24, and 48 h post-administration. Three mice were euthanized at 24 and 48 h, respectively, and their organs were sampled for ex vivo fluorescence imaging. Acquired images were analyzed using ImageJ software. Semi-quantitative data were obtained by drawing regions of interest (ROI) around the organs. The fluorescence imaging was performed using a Pear Trilogy LI-COR system with a laser excitation source of 785 nm and a CCD (charge couple device) collecting fluorescence > 820 nm.

### 2.5. Neutron Exposure at the Institut Laue-Langevin

#### 2.5.1. Neutron Beam Characteristics

Neutron irradiation experiments were performed at the Institut Laue-Langevin (ILL) (Grenoble, France). The beam line PF1b [49] provides cold neutrons that were collimated through a 3 m long system to obtain a final circular beam of 2 cm diameter. Before the experiment, the thermal neutron capture equivalent flux was measured by activation of thin Au foils, at  $2.85 \times 10^9 \text{ cm}^{-2} \text{ s}^{-1}$ . For cell irradiations, this cold neutron beam provides results equivalent to a thermal neutron irradiation as explained in detail in Pedrosa-Riviera et al. [50], but for egg irradiations, a significant attenuation towards deeper layers has to be considered.

#### 2.5.2. BNCT Experiment on Cells

Exponentially growing glioblastoma cancer cells (U251 MG/U87 MG cells) were incubated with media alone, media containing BSH, or media containing aza-SWIR-BSH-01, at a <sup>10</sup>B concentration of 40 μg/mL. Cells incubated with media alone were used as a control. After 2 h, the cells (in each incubation condition) were washed, collected, and divided into 4 quartz cuvettes (Hellma, 110-QS, 1-mm layer thickness). These cuvettes were kept as control or exposed to the neutron beam for 1, 5, and 10 min, respectively. Following the neutron irradiation, cells were counted, diluted, and re-plated

in T25 flasks in triplicates (500 cells/flask) for the colony formation assay. When 128-cell-colonies were formed in the control condition, the flasks were washed with PBS, fixed with 4% formol (U-87 MG) (for 15 min) or with 4% glutaraldehyde (U-251 MG) (for 5 min), stained with methylene blue (for 15–30 min), and dried. Finally, the colonies were counted and the results were normalized to the control condition in each cell line and treatment condition.

### 2.5.3. In Ovo BNCT Experiment

According to the French and European regulations, no ethical approval is needed for the scientific experimentations using oviparous embryos. This model was developed to restrict the use of animals and to facilitate BNCT experiments, according to the following procedure: fertilized white leghorn chicken eggs (Couvair de Cerveloup, Vourey, France) were incubated at 38 °C with 60% relative humidity. At day-3 of chicken embryo development, 3 mL albumin was removed from the eggs and a small window was made into the eggshell above the chorioallantoic membrane (CAM). At day 7, the CAM was gently lacerated and  $5 \times 10^6$  pelleted glioma cells mixed with 30  $\mu$ L of matrigel (Growth Factor Reduced (GFR) Basement Membrane Matrix 354,230, Corning® Matrigel® (Wiesbaden, Germany)) were deposited on the lacerated region. At day 10, 100  $\mu$ L of  $^{10}\text{B}$ -containing formulations ( $^{10}\text{B}$ -BSH or aza-SWIR-BSH-01) were added on top of the grown tumors (1.35  $\mu\text{g}$  of  $^{10}\text{B}$ /egg) 1 h prior to irradiation, untreated eggs served as a control. The eggs were then exposed to neutron beam for 1 h, split in 2 sessions of 30 min to expose each tumor on both sides ( $n \leq 3$ /condition). Following neutron exposure, the eggs were re-incubated for additional 6 days after which they were terminated and the tumors were carefully collected, weighed, and analyzed.

### 2.5.4. Statistical Analysis

In vitro data passed the Shapiro-Wilk normality test and were analyzed using a One-way ANOVA and a Sidak's test for multiple comparisons (Graphpad Prism 7.0 (La Jolla, CA, USA)). CAM data passed the Shapiro-Wilk normality test and the indicated treatment groups were compared using a student's *t*-test.

### 2.6. Elemental Imaging Using Laser-Induced Breakdown Spectroscopy (LIBS)

Frozen tumor samples were cut into 7  $\mu\text{m}$ -thick sections before mounting onto plastic slides. The samples were analyzed with a LIBS system to determine their elemental composition, i.e., boron (B (I) 208.8 nm) and phosphorus (P (I) 214.9 nm) elements in our case. The homemade LIBS setup was based on an optical microscope that combined a LIBS laser injection line, a standard optical-imaging apparatus, and a three-dimensional motorized platform for sample positioning [45]. In brief, the ablation was created using a quadruple Nd:YAG laser pulses of 1064 nm. The pulse duration was 8 ns, the pulse energy 1 mJ, and the repetition rate 100 Hz. During the sample scan, the objective to sample distance was carefully controlled to compensate for any flatness anomalies. The light emitted by the plasma was collected and connected by an optical fiber to a Czerny-Turner spectrometer equipped with an intensified charge-coupled device camera (Shamrock 303 and iStar, Andor Technology, Belfast, UK). The experiments were performed by Ablatom S.A.S.

### 2.7. In Ovo Fluorescence Imaging

The experiments were performed at the OPTIMAL (Small animal optical imaging) platform, IAB Grenoble. In order to determine the in ovo tumoral accumulation kinetics, in ovo glioma models were prepared. Eggs bearing well-developed and vascularized glioma xenografted tumors were incubated with 20  $\mu\text{L}$  of aza-SWIR-BSH-01 compound. Fluorescence images of the eggs were acquired before and at specific time intervals following the incubation. Obtained images were analyzed using ImageJ software. Semi-quantitative data regarding the tumoral accumulation were obtained by drawing regions of interest (ROI) around the tumors. NIR-I 2D-fluorescence reflectance imaging device (Fluobeam 800®, Fluoptics, France) was used to image the eggs incubated with aza-SWIR-BSH-01

compound. Fluobeam 800 was provided by a class 1 expanded laser source at 780 nm delivering 10 mW/cm<sup>2</sup> on the imaging field. The resulting fluorescence signals were collected by a CCD through a high pass filter > 830 nm.

### 2.8. Quantification of B Content by Inductively Coupled Plasma—Atomic Emission Spectrometry (ICP-AES)

Mice bearing U-87 MG tumors were injected with 40 µg of <sup>10</sup>B equivalent from aza-SWIR-BSH-01 or <sup>10</sup>B-BSH condition (*n* = 3/group). Determination of the boron content in the samples was performed by ICP-AES analyses (Agilent 720 ES) with a detection limit of 0.1 mg/L. The samples were mineralized using 1 mL of aqua regia (mixture of acids: nitric and hydrochloric). After complete mineralization, the samples were diluted with HNO<sub>3</sub> (5%, *w/w*) to reach a 3 mL volume and finally filtered at 0.2 µm for the measurements. The results were expressed as µg of <sup>10</sup>B/g of tumor. The experiments were performed at the ISTerre platform, Grenoble.

## 3. Results

### 3.1. Rationale, Design, and Characterization of the Compounds

To design an efficient theranostic boron vector, we used a fluorescent reporter platform based on the versatile BODIPY family (Figure 1a) displaying (i) a strong tumor accumulation and (ii) a biocompatible water-solubility, (iii) which can be easily functionalized. In particular, we used *B*-functionalized aza-BODIPYs (Figure 1b,c), as they have numerous advantages, such as a very high chemical and photochemical photostability, and excellent photophysical properties, rendering them suitable fluorophore for the NIR-I to the SWIR region (Figure 1d). Previously, we developed a strategy, which favored their solubilization and limited their aggregation in biologically relevant media (i.e., water, PBS, or serum), by substituting the fluorine atoms on the boron by alkyne ammonium groups [34,35,48]. Very recently, we used this strategy on a particular Donor-Acceptor-Donor' aza-BODIPY structure, which emits in the SWIR region, yielding a water-soluble derivative SWIR-WAZABY-01 (See the ESI and Reference [29]; WAZABY for Water-Soluble aza-BODIPY). SWIR-WAZABY-01 could accumulate *in vivo* very efficiently at the tumor site, without any vectorization, showing high SWIR contrast for up to one week [29].

In this study, we took advantage of the SWIR-WAZABY-01 structure to deliver the <sup>10</sup>B-BSH at the tumor site, while enabling the tracking of the molecule *in vivo* by optical imaging. In order to tether the <sup>10</sup>B-BSH on the SWIR-WAZABY-01, we slightly modified its structure and adapted the synthetic method previously reported by us in order to synthesize aza-SWIR-BSH-01. It is functionalized with one <sup>10</sup>B BSH unit and emits in the near-infrared region (Figure 1c and see ESI section for the synthetic pathway of aza-SWIR-BSH-01).

### 3.2. *In Vitro* Distribution and BNCT Efficacy

To investigate the tumor cell accumulation capacity of aza-SWIR-BSH-01 compounds, the first set of experiments was conducted on brain tumor cells U-251 MG and U-87 MG using SWIR-WAZABY-01, a SWIR emitting aza-BODIPY structurally close to aza-SWIR-BSH-01 but without BSH (see Godard et al. [29]). While the fluorescent signal of SWIR-WAZABY-01 was more compatible with *in vivo* experiments, due to its emission in the SWIR optical region, it was still detectable by conventional fluorescence microscopy for *in vitro* investigations. SWIR-WAZABY-01 was incubated with human brain tumor cells U-251 MG and U-87 MG cultured in 2D, but also in 3D spheroids mimicking small tumors. This compound displayed a very fast tumor cell internalization in both 2D and 3D cultures.

Therefore, similar experiments were conducted using the new compound aza-SWIR-BSH-01 on U-87 MG cells. As displayed in Figure 2 after 3 h of incubation, aza-SWIR-BSH-01 accumulated massively in tumor cells, into small cytoplasmic vesicles. The main challenge of this compound was its fluorescence emission properties that can mostly be measured after 800 nm. A dedicated confocal

setting was used to collect with a high sensitivity to the photon of the compound. In the first hours of incubation, the signal of the internalized aza-SWIR-BSH-01 was weak and diffuse, but it was clearly visible at around 3 h of incubation as demonstrated in Figure 2a. Under the same experimental conditions, the control cells presented a very weak and homogenous signal (Figure 2b).

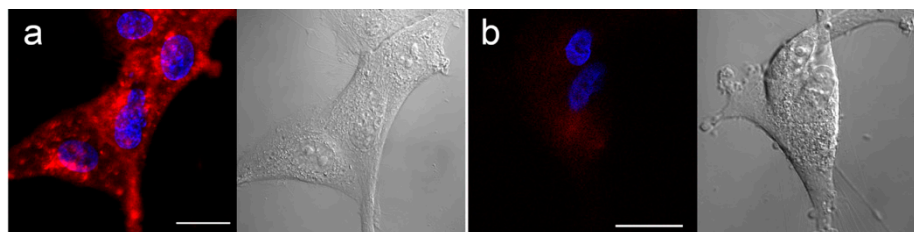


**Figure 2.** Human glioblastoma U-87 MG cells cultured in 2D incubated with aza-SWIR-BSH-01 (red signal) for 3 h (a), and control cells (b). Nuclei were labeled with Hoechst (blue signal). Corresponding phase-contrast pictures are depicted in black and white color. Scale bars represent 20  $\mu\text{m}$ .

To confirm cellular uptake and to further evaluate the compound's therapeutic potential *in vitro*, the cells were incubated with aza-SWIR-BSH-01 or  $^{10}\text{B}$ -BSH for 2 h, placed in quartz cuvettes, and exposed to the neutron beam for 1 to 10 min, or kept as control. The cells were then harvested and seeded for colony assay. After incubation with  $^{10}\text{B}$ -BSH and short neutron exposure (5 and 10 min), only the growth of U-87 MG cells was reduced as compared to the neutron exposure alone (Figure 3a). Similarly, aza-SWIR-BSH-01 with neutron irradiation was able to strongly reduce the number of colonies as compared to neutron alone (Figure 3a). Regarding U-251 MG cells (Figure 3b), aza-SWIR-BSH-01 strongly decreased the number of colonies as compared to both the  $^{10}\text{B}$ -BSH and neutron condition after 5 and 10 min neutron exposure (see also ESI Figure S9 (Supplementary Materials)). These results confirmed the therapeutic potential of aza-SWIR-BSH-01 *in vitro*, which is slightly better than  $^{10}\text{B}$ -BSH alone.

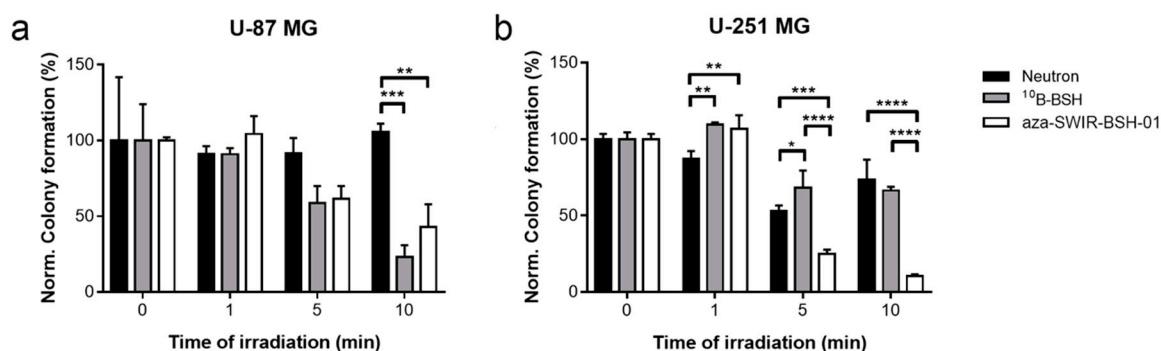


**Figure 3.** Boron neutron capture therapy (BNCT) experiment *in vitro*. U-87 MG (a) and U-251 MG (b) cells were incubated with  $^{10}\text{B}$ -BSH (grey) or aza-SWIR-BSH-01 (white) during 2 h before neutron exposure, and re-seeding for colony assay. Control condition (neutron alone) is indicated in black. The results are represented as the mean of 3 independent experiments  $\pm$  standard deviation (S.D.).

### 3.3. *In Vivo* Distribution and Behavior

Before studying the therapeutic potential of aza-SWIR-BSH-01 compound as a boron-vector, *in vivo* experiments were performed to determine the distribution profile of the compounds, and more importantly the tumor and tumor environment's uptake. The animals were imaged before and until 48 h post-intravenous administration of the compound using optical imaging, and the organs were collected at 24 and 48 h post-injection. As indicated in Figure 4a,b, the compound was largely distributed in the animal's body without any unexpected accumulation and was mainly eliminated by the kidneys. Aza-SWIR-BSH-01 accumulated very weakly in muscles, fat, and healthy brain tissues.

Contrariwise, aza-SWIR-BSH-01 accumulated strongly in U-87 MG tumors and was retained for a prolonged time. The remoted tumors revealed a homogenous distribution of aza-SWIR-BSH-01 at 24 and 48 h post-injection (Figure 4c). In parallel, dedicated quantitative experiments were performed in mice-bearing U-87 MG injected with aza-SWIR-BSH-01 and  $^{10}\text{B}$ -BSH to determine the boron tumor uptake at 24 h. Mice were injected intravenously with either 200  $\mu\text{L}$  of aza-SWIR-BSH-01 at 2 mM or  $^{10}\text{B}$ -BSH equivalent, i.e., 40  $\mu\text{g}$  of  $^{10}\text{B}$  equivalent per injection (i.e., >3-fold the dose administered for imaging purpose). Such a concentration of aza-SWIR-BSH-01 is sub-optimal for BNCT experiment, but still allows the optical tracking of the compound. Indeed, the fluorescent compound becomes partially quenched at high dose, which limits its detection. The ICP-AES revealed a tumor uptake of  $9.3 \pm 4.7 \mu\text{g}$  of  $^{10}\text{B}/\text{g}$  of tissue and  $6.3 \pm 4.7 \mu\text{g}$  of  $^{10}\text{B}/\text{g}$  of tissue, respectively. However, this difference was not significant ( $n = 3/\text{condition}$ ). The Tumor/Skin ratios were determined ex vivo; they reached  $1.9 \pm 0.5$  at 24 h, and then decreased at 48 h at  $1.5 \pm 0.7$  (Figure 4d). In Figure 4e, the ex vivo Tumor/Muscle ratios measured at 24 and 48 h were  $7.3 \pm 0.9$  and  $12.3 \pm 4.4$ , respectively. Such Tumor/Muscle ratios were in accordance with the required values for BNCT purpose (i.e., T/M ratio > 3–5) [4,7,51]. Furthermore, the investigations also revealed the absence of acute toxicity after intravenous administration of aza-SWIR-BSH-01 [29].

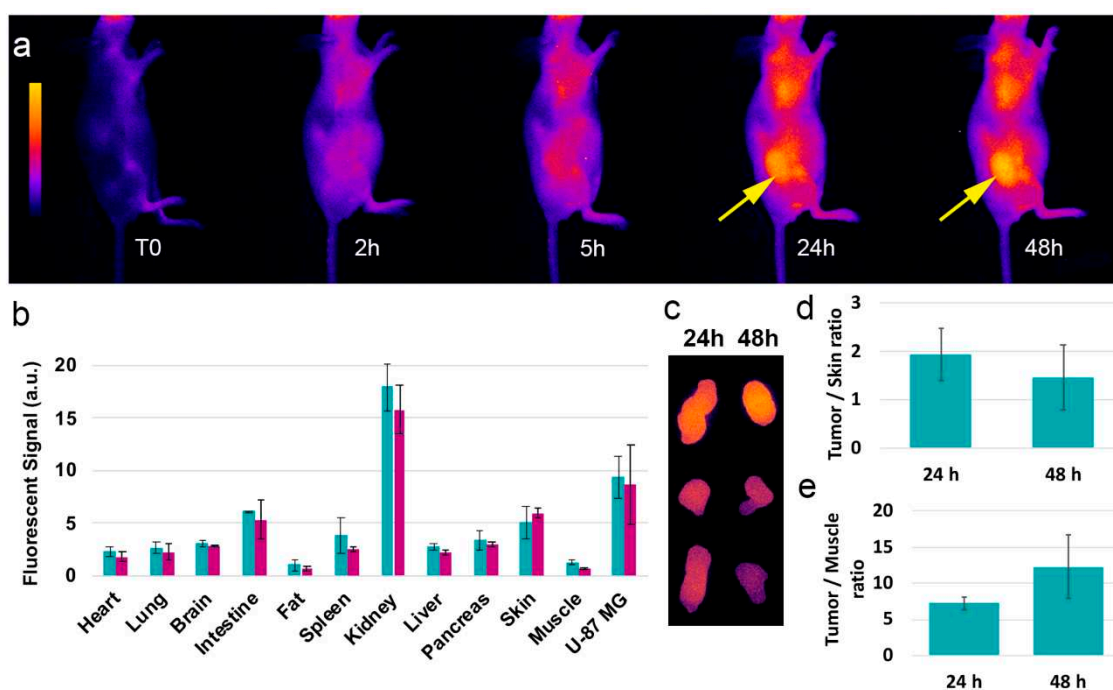


**Figure 4.** In vivo distribution and behavior of aza-SWIR-BSH-01 in mice-bearing subcutaneous U-87 MG tumors. The non-invasive images were taken from T0 until 48 h (a). Tumors are indicated with an arrow. (b) The distributions were observed at 24 h (green) and 48 h (blue) post-injection. (c) Remoted tumor observed at 24 h and 48 h post-injection revealed a higher tumor accumulation at 24 h. (d) Tumor/Skin and (e) Tumor/Muscle ratios from ex vivo analysis.

### 3.4. In Ovo BNCT Assay and Distribution

A specific model of tumor growth was used to perform the evaluation of the BNCT efficacy of aza-SWIR-BSH-01 compound. We worked with CAM into which U-251 MG or U-87 MG tumor cells were implanted (Figure 5a). To perform the BNCT experiment, aza-SWIR-BSH-01 and  $^{10}\text{B}$ -BSH (1.35  $\mu\text{g}$   $^{10}\text{B}/\text{egg}$ ) were added on the top of the U-251 MG tumors 1 h before neutron exposure (Figure 5b). The tumors were collected at day-16, i.e., few days before hatching. The tumor growth was significantly lower in the condition aza-SWIR-BSH-01 + neutron exposure as compared to neutron exposure

alone, or  $^{10}\text{B}$ -BSH + neutron exposure, with  $58.4 \pm 16.2\%$  versus  $100 \pm 37.6\%$ , and  $101.1 \pm 16.0\%$ , respectively (Figure 5c).

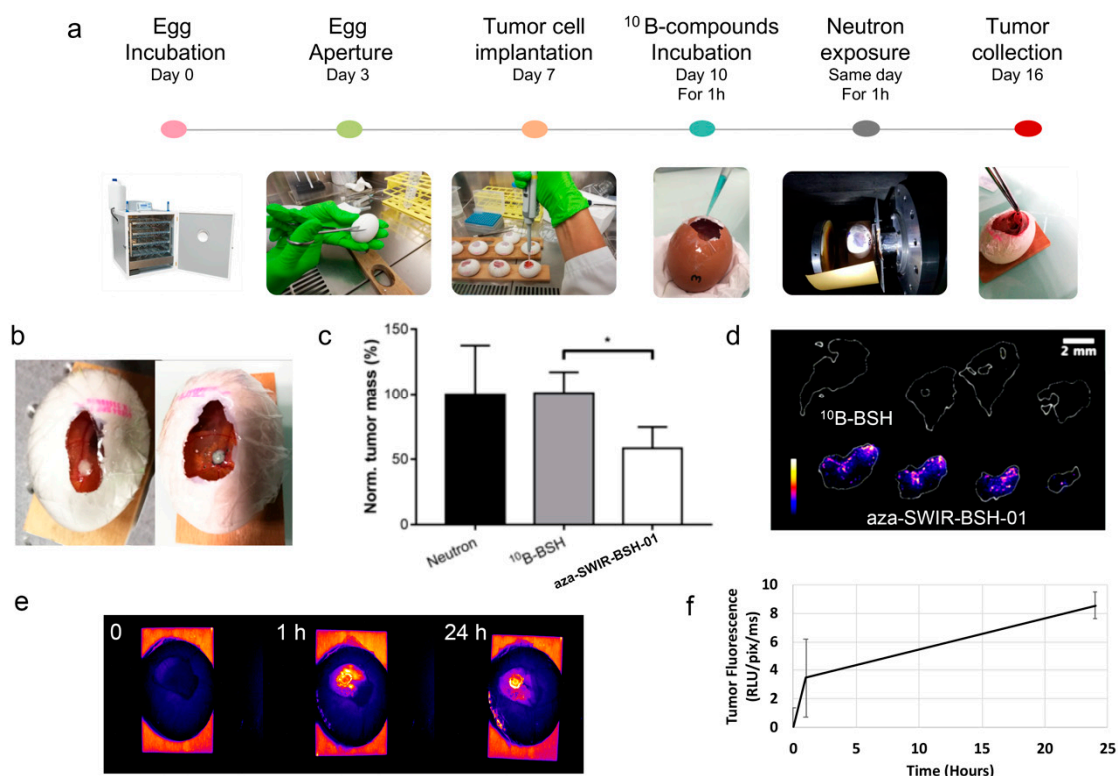


**Figure 5.** In ovo model of tumor for evaluation of theranostic aza-SWIR-BSH-01 compound. (a) Presentation of the in ovo tumor model for BNCT application. (b) Color images of tumor before and after administration of aza-SWIR-BSH-01 (pale blue color), indicating the presence of the compound at the tumor site. (c) Tumor development measured at day 16, i.e., 6 days after the addition of  $^{10}\text{B}$ -BSH and aza-SWIR-BSH-01 for 1 h followed by neutron exposure. (d) Laser-induced breakdown spectroscopy (LIBS) elemental imaging of boron from tumor sections collected at day 16 showing the presence of remaining boron in tumors treated with aza-SWIR-BSH-01. (e) 2D fluorescence imaging of aza-SWIR-BSH-01 distribution before and until 24 h post-administration onto glioma tumors implanted on chorioallantoic membrane (CAM). (f) Non-invasive measurement of aza-SWIR-BSH-01 fluorescence in tumors with time. Results are expressed as the tumor fluorescence mean  $\pm$  S.D ( $n = 4$ ).

We verified the presence of boron at the tumor site for boron-containing conditions to better understand the obtained results. Thus, the excised tumors collected at day 16 were sliced and analyzed by LIBS imaging for elemental analysis [44] and examine phosphorus (P) and boron (B) content and distribution. P was selected as it is present in every cell and its distribution reflects the area of the tissue itself [47,52]. P was used to delineate the tissue sections (in white in Figure 5d). As indicated in Figure 5d, B was observed in tumors treated with aza-SWIR-BSH-01, in all the different sections, while it was not observed for the  $^{10}\text{B}$ -BSH condition. In this case,  $^{10}\text{B}$ -BSH may accumulate at the tumor site, but presumably to a lower extent, and/or might be released from the tumor site after such a long time, being below the limits of detection of the LIBS system. Contrariwise, aza-SWIR-BSH-01 accumulated at very high levels in the tumor region (Figure 5d) and was retained in the tissues during 6 days after administration.

From the elemental images obtained with LIBS, we found that the distribution of boron atoms was not homogenous within tumors. A detailed fluorescence distribution study was then conducted in eggs bearing tumors to further understand the compound's tumor uptake in ovo. The results are presented in Figure 5e,f. Aza-SWIR-BSH-01 accumulated very well in the tumor at early time points

(1 h), evidencing some diffusion into vessels at time points with prolonged exposure, suggesting a long-lasting circulation in the blood vessels. The fluorescence signal increased with time, reaching a massive uptake peak at 24 h. As compared to the fluorescence signal obtained after 1 h, the fluorescent signal at 24 h was enhanced by a factor of  $\sim 2.5$ , confirming that the optimal and minimal time required for optimal aza-SWIR-BSH-01 tumor uptake was 24 h. These results also suggest that 24 h post-treatment could be the ideal delay for starting neutron irradiation for a more effective BNCT.

#### 4. Discussion

BODIPY derivatives have already been developed for BNCT application [38–41], but none of them, to our best knowledge, have been tested for BNCT anti-tumor development *in vitro* and *in vivo*. This study is the first to report the use and evaluation of aza-BODIPY-based compounds as theranostic compounds for BNCT purpose.

The delivery of  $^{10}\text{B}$  into tumors for BNCT requires the production and evaluation of biocompatible and water-soluble vectors, with no or only marginal and reversible toxicity, and preferential tumor accumulation while clearing from the blood and tumor micro-environment. As recently reported, some SWIR-WAZABY compounds possess a strong, time-dependent tumor uptake, and weak muscle accumulation [29]. Contrariwise,  $^{10}\text{B}$ -BSH, a molecule approved for BNCT, is rapidly washed out from the body and should be administrated at high dose [8,53]. Here, the tumor uptake kinetics and the elemental imaging indicated that the  $^{10}\text{B}$ -BSH part of the novel aza-SWIR-BSH compound advantageously followed the BNCT-compatible kinetics of the SWIR-WAZABY vector, rather than that of the  $^{10}\text{B}$ -BSH moiety itself. Therefore, the engraftment of the small  $^{10}\text{B}$ -BSH entity did not impact the tumor accumulation capacity and water-solubility of the SWIR-WAZABY, even when administered at high concentrations (200  $\mu\text{L}$  at 2 mM as a bolus intravenous administration). The substitution of the fluorine atoms on the boron allowing to increase the water-solubility is a key factor for efficient distribution and tumor targeting.

To evaluate the properties of the theranostic aza-SWIR-BSH compound *in vivo*, the CAM model was used. This model is particularly interesting for drug evaluation as (i) the tumors grow rapidly due to the nutrients-rich environment of the CAM, (ii) the vasculature is well developed and accessible, allowing an efficient tumor vascularization, (iii) the absence of a well-established immune system at this point of embryo development contributes to the tumor growth, even from patient-derived cells, and (iv) the utilization of this experimental model contributes to the reduction of animal's use in an ethical aspect of the research [54]. Therefore, this model has been widely used for the evaluation of anti-angiogenic or antitumor compounds [54–56], the evaluation of sensitizers for radiotherapy and photodynamic therapy [57,58], and imaging using MRI and PET/CT [59,60]; however, the CAM model has never been reported to demonstrate the potential of boron compounds for BNCT application. Using optical imaging, the distribution of aza-SWIR-BSH compound in this CAM model indicated an optimized tumor uptake after prolonged exposure time (24 h, Figure 5), while the 1-h administration followed by neutron exposure was already able to reduce tumor growth; all these results suggested that BNCT could increase tumor shrinkage after prolonged incubations with these compounds and neutron exposure.

#### 5. Conclusions

Altogether, we demonstrated that water-soluble aza-BODIPYs can be used as theranostic vectors for boron complexes, opening a new perspective for compound development for BNCT applications.

#### 6. Patents

To be added during the reviewing process when official patent numbers will be known.

**Supplementary Materials:** The following are available online at <http://www.mdpi.com/2073-4409/9/9/1953/s1>, Table S1: HPLC analytical gradient. Table S2: Detailed of gradient. Scheme S1: Synthetic pathway of

aza-SWIR-BSH-01. Figure S1: Analytical HPLC of SWIR-WAZABY-02. Figure S2:  $^1\text{H}$  NMR of SWIR-WAZABY-02 (500 MHz, 298 K, MeOD- $d_4$ ). Figure S3:  $^{13}\text{C}$  NMR of SWIR-WAZABY-02 (125 MHz, 298 K, MeOD- $d_4$ ). Figure S4: Analytical HPLC of aza-SWIR-03. Figure S5:  $^1\text{H}$  NMR of aza-SWIR-03 (500 MHz, 298 K, DMSO- $d_6$ ). Figure S6:  $^{13}\text{C}$  NMR of aza-SWIR-03 (150 MHz, 298 K, DMSO- $d_6$ ). Figure S7:  $^1\text{H}$  NMR of aza-SWIR-BSH-01 (500 MHz, 298 K, DMSO- $d_6$ ). Figure S8:  $^{13}\text{C}$  NMR of aza-SWIR-BSH-01 (150 MHz, 343 K, DMSO- $d_6$ ). Figure S9: U-251 cells incubated with aza-SWIR-BSH-01 before (a) and after (b) 10 min of neutron exposure colored with Trypan blue.

**Author Contributions:** Conceptualization, F.D., J.-L.C., and L.S.; methodology, G.K., A.G., V.M.-R., M.B., and U.K.; validation, A.G., J.P., C.G., and E.B.; formal analysis, G.K., B.B., M.B., and L.S.; investigation, G.K., A.G., B.B., J.P., K.D.W., U.R.-G., and L.S.; resources, U.K.; writing—original draft preparation, G.K., A.G., B.B., E.B., C.G., and L.S.; writing—review and editing, all the authors; supervision, E.B., C.G., and L.S.; funding acquisition, F.D., E.B., C.G., and L.S. All authors have read and agreed to the published version of the manuscript.

**Funding:** This work was supported by the GEFLUC Grenoble Dauphiné Savoie, and the French funding agencies: FLI (France Life Imaging) for the project Thera-BODIPY, the CNRS Mission for Transversal and Interdisciplinary Initiatives for the project BREVET-ISOTOP, the Fondation pour la Recherche Médicale (FRM) for the specific support of G.K. (FRM ECO201806006861). This research was funded by The Ministère de l'Enseignement Supérieur et de la Recherche, the Centre National de la Recherche Scientifique (CNRS), the Conseil Régional de Bourgogne (PhD JCE Grant # 2015-9205AAO033S04139/BG0003203), and the French Research National Agency (ANR) via project JCJC "SPID" ANR-16-CE07-0020 and project JCJC "WazaBY" ANR-18-CE18-0012. This work is part of the projects "Pharmacoimagerie et agents théranostiques" et "Chimie durable, environnement et agroalimentaire" supported by the Université de Bourgogne and the Conseil Régional de Bourgogne through the Plan d'Actions Régional pour l'Innovation (PARI) and the European Union through the PO FEDER-FSE Bourgogne 2014/2020 programs. It was performed within the Dijon's pharmaco-imaging consortium, a regional center of excellence in pharmaco-imaging.

**Acknowledgments:** G.K. and L.S. would like to thank F. Trichard from Ablatom SAS for LIBS experiments and M. Couvet and A. Grichine ( $\mu\text{Cell}$  platform IAB, Grenoble, France) for technical advice. The authors are grateful to V. Josserand from OPTIMAL platform (platform responsible) for technical access and optical experiments. We also thank the ISTERre facility (S.B., Grenoble, France) for ICP measurements. We are grateful to T. Soldner (ILL, PF1b instrument responsible) for invaluable help with the setup of the beam line. A.G., J.P., F.D., E.B., and C.G. gratefully acknowledge the Université de Bourgogne, SATT Sayens, Conseil Régional de Bourgogne Franche-Comté and the French Ministère de l'Enseignement Supérieur et de la Recherche for financial support of the analytical platform PACSMUB.

**Conflicts of Interest:** The authors declare no conflict of interest.

## References

1. Locher, G. Biological effects and therapeutic possibilities of neutrons. *Am. J. Roentgenol. Radium Ther.* **1936**, *36*, 1–13.
2. Barth, R.F.; Coderre, J.A.; Vicente, M.G.; Blue, T.E. Boron neutron capture therapy of cancer: Current status and future prospects. *Clin. Cancer Res.* **2005**, *11*, 3987–4002. [[CrossRef](#)] [[PubMed](#)]
3. Aihara, T.; Morita, N.; Kamitani, N.; Kumada, H.; Ono, K.; Hiratsuka, J.; Harada, T. BNCT for advanced or recurrent head and neck cancer. *Appl. Radiat. Isot.* **2014**, *88*, 12–15. [[CrossRef](#)] [[PubMed](#)]
4. Aiyama, H.; Nakai, K.; Yamamoto, T.; Nariai, T.; Kumada, H.; Ishikawa, E.; Isobe, T.; Endo, K.; Takada, T.; Yoshida, F.; et al. A clinical trial protocol for second line treatment of malignant brain tumors with BNCT at University of Tsukuba. *Appl. Radiat. Isot.* **2011**, *69*, 1819–1822. [[CrossRef](#)]
5. Kato, I.; Ono, K.; Sakurai, Y.; Ohmae, M.; Maruhashi, A.; Imahori, Y.; Kirihata, M.; Nakazawa, M.; Yura, Y. Effectiveness of BNCT for recurrent head and neck malignancies. *Appl. Radiat. Isot.* **2004**, *61*, 1069–1073. [[CrossRef](#)]
6. Sauerwein, W.; Moss, R.; Rassow, J.; Stecher-Rasmussen, F.; Hideghety, K.; Wolbers, J.G.; Sack, H. Organisation and management of the first clinical trial of BNCT in Europe (EORTC protocol 11961). EORTC BNCT study group. *Strahlenther. Onkol.* **1999**, *175* (Suppl. 2), 108–111. [[CrossRef](#)]
7. Wang, L.W.; Chen, Y.W.; Ho, C.Y.; Hsueh Liu, Y.W.; Chou, F.I.; Liu, Y.H.; Liu, H.M.; Peir, J.J.; Jiang, S.H.; Chang, C.W.; et al. Fractionated BNCT for locally recurrent head and neck cancer: Experience from a phase I/II clinical trial at Tsing Hua Open-Pool Reactor. *Appl. Radiat. Isot.* **2014**, *88*, 23–27. [[CrossRef](#)]
8. Haritz, D.; Gabel, D.; Huiskamp, R. Clinical phase-I study of Na $^{235}\text{U}$  (BSH) in patients with malignant glioma as precondition for boron neutron capture therapy (BNCT). *Int. J. Radiat. Oncol. Biol. Phys.* **1994**, *28*, 1175–1181. [[CrossRef](#)]

9. Takagaki, M.; Oda, Y.; Miyatake, S.; Kikuchi, H.; Kobayashi, T.; Sakurai, Y.; Osawa, M.; Mori, K.; Ono, K. Boron neutron capture therapy: Preliminary study of BNCT with sodium borocaptate (Na<sup>2</sup>B<sup>12</sup>H<sub>11</sub>SH) on glioblastoma. *J. Neurooncol.* **1997**, *35*, 177–185. [[CrossRef](#)]
10. Gonzalez, S.J.; Bonomi, M.R.; Santa Cruz, G.A.; Blaumann, H.R.; Calzetta Larriue, O.A.; Menendez, P.; Jimenez Rebagliati, R.; Longhino, J.; Feld, D.B.; Dagrosa, M.A.; et al. First BNCT treatment of a skin melanoma in Argentina: Dosimetric analysis and clinical outcome. *Appl. Radiat. Isot.* **2004**, *61*, 1101–1105. [[CrossRef](#)]
11. Mishima, Y.; Honda, C.; Ichihashi, M.; Obara, H.; Hiratsuka, J.; Fukuda, H.; Karashima, H.; Kobayashi, T.; Kanda, K.; Yoshino, K. Treatment of malignant melanoma by single thermal neutron capture therapy with melanoma-seeking 10B-compound. *Lancet* **1989**, *2*, 388–389. [[CrossRef](#)]
12. Kato, T.; Hirose, K.; Tanaka, H.; Mitsumoto, T.; Motoyanagi, T.; Arai, K.; Harada, T.; Takeuchi, A.; Kato, R.; Yajima, S.; et al. Design and construction of an accelerator-based boron neutron capture therapy (AB-BNCT) facility with multiple treatment rooms at the Southern Tohoku BNCT Research Center. *Appl. Radiat. Isot.* **2020**, *156*, 108961. [[CrossRef](#)] [[PubMed](#)]
13. Kreiner, A.J.; Baldo, M.; Bergueiro, J.R.; Cartelli, D.; Castell, W.; Thatar Vento, V.; Gomez Asoia, J.; Mercuri, D.; Padulo, J.; Suarez Sandin, J.C.; et al. Accelerator-based BNCT. *Appl. Radiat. Isot.* **2014**, *88*, 185–189. [[CrossRef](#)] [[PubMed](#)]
14. Barth, R.F.; Mi, P.; Yang, W. Boron delivery agents for neutron capture therapy of cancer. *Cancer Commun.* **2018**, *38*, 35. [[CrossRef](#)] [[PubMed](#)]
15. Slatkin, D.N. A history of boron neutron capture therapy of brain tumours. Postulation of a brain radiation dose tolerance limit. *Brain* **1991**, *114 Pt 4*, 1609–1629. [[CrossRef](#)]
16. Chandra, S.; Barth, R.F.; Haider, S.A.; Yang, W.; Huo, T.; Shaikh, A.L.; Kabalka, G.W. Biodistribution and subcellular localization of an unnatural boron-containing amino acid (cis-ABCPC) by imaging secondary ion mass spectrometry for neutron capture therapy of melanomas and gliomas. *PLoS ONE* **2013**, *8*, e75377. [[CrossRef](#)]
17. Kabalka, G.W.; Shaikh, A.L.; Barth, R.F.; Huo, T.; Yang, W.; Gordnier, P.M.; Chandra, S. Boronated unnatural cyclic amino acids as potential delivery agents for neutron capture therapy. *Appl. Radiat. Isot.* **2011**, *69*, 1778–1781. [[CrossRef](#)]
18. Futamura, G.; Kawabata, S.; Nonoguchi, N.; Hiramatsu, R.; Toho, T.; Tanaka, H.; Masunaga, S.I.; Hattori, Y.; Kirihaata, M.; Ono, K.; et al. Evaluation of a novel sodium borocaptate-containing unnatural amino acid as a boron delivery agent for neutron capture therapy of the F98 rat glioma. *Radiat. Oncol.* **2017**, *12*, 26. [[CrossRef](#)]
19. Kimura, S.; Masunaga, S.; Harada, T.; Kawamura, Y.; Ueda, S.; Okuda, K.; Nagasawa, H. Synthesis and evaluation of cyclic RGD-boron cluster conjugates to develop tumor-selective boron carriers for boron neutron capture therapy. *Bioorg. Med. Chem.* **2011**, *19*, 1721–1728. [[CrossRef](#)]
20. Hoppenz, P.; Els-Heindl, S.; Kellert, M.; Kuhnert, R.; Saretz, S.; Lerchen, H.G.; Kobberling, J.; Riedl, B.; Hey-Hawkins, E.; Beck-Sickinger, A.G. A Selective Carborane-Functionalized Gastrin-Releasing Peptide Receptor Agonist as Boron Delivery Agent for Boron Neutron Capture Therapy. *J. Org. Chem.* **2020**, *85*, 1446–1457. [[CrossRef](#)]
21. Kellert, M.; Hoppenz, P.; Lonneck, P.; Worm, D.J.; Riedl, B.; Koebberling, J.; Beck-Sickinger, A.G.; Hey-Hawkins, E. Tuning a modular system-synthesis and characterisation of a boron-rich s-triazine-based carboxylic acid and amine bearing a galactopyranosyl moiety. *Dalton Trans.* **2020**, *49*, 57–69. [[CrossRef](#)] [[PubMed](#)]
22. Kellert, M.; Worm, D.J.; Hoppenz, P.; Sarosi, M.B.; Lonneck, P.; Riedl, B.; Koebberling, J.; Beck-Sickinger, A.G.; Hey-Hawkins, E. Modular triazine-based carborane-containing carboxylic acids-synthesis and characterisation of potential boron neutron capture therapy agents made of readily accessible building blocks. *Dalton Trans.* **2019**, *48*, 10834–10844. [[CrossRef](#)] [[PubMed](#)]
23. Savolainen, S.; Kortensniemi, M.; Timonen, M.; Reijonen, V.; Kuusela, L.; Uusi-Simola, J.; Salli, E.; Koivunoro, H.; Seppala, T.; Lonroth, N.; et al. Boron neutron capture therapy (BNCT) in Finland: Technological and physical prospects after 20 years of experiences. *Phys. Med.* **2013**, *29*, 233–248. [[CrossRef](#)] [[PubMed](#)]
24. Koivunoro, H.; Hippelainen, E.; Auterinen, I.; Kankaanranta, L.; Kulvik, M.; Laakso, J.; Seppala, T.; Savolainen, S.; Joensuu, H. Biokinetic analysis of tissue boron ((1)(0)B) concentrations of glioma patients treated with BNCT in Finland. *Appl. Radiat. Isot.* **2015**, *106*, 189–194. [[CrossRef](#)]

25. Atallah, I.; Milet, C.; Henry, M.; Jossierand, V.; Reyt, E.; Coll, J.L.; Hurbin, A.; Righini, C.A. Near-infrared fluorescence imaging-guided surgery improves recurrence-free survival rate in novel orthotopic animal model of head and neck squamous cell carcinoma. *Head Neck* **2016**, *38* (Suppl. 1), E246–E255. [[CrossRef](#)]
26. Jacquart, A.; Keramidias, M.; Vollaie, J.; Boisgard, R.; Pottier, G.; Rustique, E.; Mittler, F.; Navarro, F.P.; Boutet, J.; Coll, J.L.; et al. LipImage 815: Novel dye-loaded lipid nanoparticles for long-term and sensitive in vivo near-infrared fluorescence imaging. *J. Biomed. Opt.* **2013**, *18*, 101311. [[CrossRef](#)]
27. Bai, L.; Sun, P.; Liu, Y.; Zhang, H.; Hu, W.; Zhang, W.; Liu, Z.; Fan, Q.; Li, L.; Huang, W. Novel aza-BODIPY based small molecular NIR-II fluorophores for in vivo imaging. *Chem. Commun.* **2019**, *55*, 10920–10923. [[CrossRef](#)]
28. Ge, Y.; O’Shea, D.F. Azadipyromethenes: From traditional dye chemistry to leading edge applications. *Chem. Soc. Rev.* **2016**, *45*, 3846–3864. [[CrossRef](#)] [[PubMed](#)]
29. Godard, A.; Kalot, G.; Pliquet, J.; Busser, B.; Le Guevel, X.; Wegner, K.D.; Resch-Genger, U.; Rousselin, Y.; Coll, J.L.; Denat, F.; et al. Water-Soluble Aza-BODIPYs: Biocompatible Organic Dyes for High Contrast In Vivo NIR-II Imaging. *Bioconj. Chem.* **2020**, *31*, 1088–1092. [[CrossRef](#)] [[PubMed](#)]
30. Bodio, E.; Denat, F.; Goze, C. BODIPYS and aza-BODIPY derivatives as promising fluorophores for in vivo molecular imaging and theranostic applications. *J. Porphyr. Phthalocyanines* **2019**, *23*, 1159–1183. [[CrossRef](#)]
31. Bertrand, B.; Passador, K.; Goze, C.; Denat, F.; Bodio, E.; Salmain, M. Metal-based BODIPY derivatives as multimodal tools for life sciences. *Coord. Chem. Rev.* **2018**, *358*, 108–124. [[CrossRef](#)]
32. Lhenry, D.; Larrouy, M.; Bernhard, C.; Goncalves, V.; Raguin, O.; Provent, P.; Moreau, M.; Collin, B.; Oudot, A.; Vrigneaud, J.M.; et al. BODIPY: A Highly Versatile Platform for the Design of Bimodal Imaging Probes. *Chem. Eur. J.* **2015**, *21*, 13091–13099. [[CrossRef](#)] [[PubMed](#)]
33. Bernhard, C.; Goze, C.; Rousselin, Y.; Denat, F. First bodipy-DOTA derivatives as probes for bimodal imaging. *Chem. Commun.* **2010**, *46*, 8267–8269. [[CrossRef](#)] [[PubMed](#)]
34. Bodio, E.; Goze, C. Investigation of B-F substitution on BODIPY and aza-BODIPY dyes: Development of B-O and B-C BODIPYs. *Dye. Pigment* **2019**, *160*, 700–710. [[CrossRef](#)]
35. Flores, O.; Pliquet, J.; Abad Galan, L.; Lescure, R.; Denat, F.; Maury, O.; Pallier, A.; Bellaye, P.S.; Collin, B.; Meme, S.; et al. Aza-BODIPY Platform: Toward an Efficient Water-Soluble Bimodal Imaging Probe for MRI and Near-Infrared Fluorescence. *Inorg. Chem.* **2020**, *59*, 1306–1314. [[CrossRef](#)] [[PubMed](#)]
36. Pliquet, J.; Amor, S.; Ponce-Vargas, M.; Laly, M.; Racœur, C.; Rousselin, Y.; Denat, F.; Bettaieb, A.; Fleurat-Lessard, P.; Paul, C.; et al. Design of a multifunctionalizable BODIPY platform for the facile elaboration of a large series of gold(i)-based optical theranostics. *Dalton Trans.* **2018**, *47*, 11203–11218. [[CrossRef](#)]
37. Flores, O.; Trommenschlager, A.; Amor, S.; Marques, F.; Silva, F.; Gano, L.; Denat, F.; Cabral Campello, M.; Goze, C.; Bodio, E.; et al. In vitro and in vivo trackable titanocene-based complexes using optical imaging or SPECT. *Dalton Trans.* **2017**, *46*, 14548–14555. [[CrossRef](#)]
38. Xuan, S.; Zhao, N.; Zhou, Z.; Fronczek, F.R.; Vicente, M.G. Synthesis and in Vitro Studies of a Series of Carborane-Containing Boron Dipyrromethenes (BODIPYs). *J. Med. Chem.* **2016**, *59*, 2109–2117. [[CrossRef](#)]
39. Nakase, I.; Katayama, M.; Hattori, Y.; Ishimura, M.; Inaura, S.; Fujiwara, D.; Takatani-Nakase, T.; Fujii, I.; Futaki, S.; Kiriwata, M. Intracellular target delivery of cell-penetrating peptide-conjugated dodecaborate for boron neutron capture therapy (BNCT). *Chem. Commun.* **2019**, *55*, 13955–13958. [[CrossRef](#)]
40. Gibbs, J.H.; Wang, H.; Bhupathiraju, N.V.; Fronczek, F.R.; Smith, K.M.; Vicente, M.G. Synthesis and properties of a series of carboranyl-BODIPYs. *J. Organomet. Chem.* **2015**, *798*, 209–213. [[CrossRef](#)]
41. Nakata, E.; Koizumi, M.; Yamashita, Y.; Onaka, K.; Sakurai, Y.; Kondo, N.; Ono, K.; Uto, Y.; Hori, H. Design, synthesis and destructive dynamic effects of BODIPY-containing and curcuminoid boron tracedrugs for neutron dynamic therapy. *Anticancer Res.* **2011**, *31*, 2477–2481. [[PubMed](#)]
42. Musnier, B.; Wegner, K.D.; Comby-Zerbino, C.; Trouillet, V.; Jourdan, M.; Hausler, I.; Antoine, R.; Coll, J.L.; Resch-Genger, U.; Le Guevel, X. High photoluminescence of shortwave infrared-emitting anisotropic surface charged gold nanoclusters. *Nanoscale* **2019**, *11*, 12092–12096. [[CrossRef](#)] [[PubMed](#)]
43. Shen, Q.; Wang, S.; Yang, N.D.; Zhang, C.; Wu, Q.; Yu, C. Recent development of small-molecule organic fluorophores for multifunctional bioimaging in the second near-infrared window. *J. Lumin.* **2020**, *225*, 117338. [[CrossRef](#)]

44. Sancey, L.; Motto-Ros, V.; Kotb, S.; Wang, X.; Lux, F.; Panczer, G.; Yu, J.; Tillement, O. Laser-induced breakdown spectroscopy: A new approach for nanoparticle's mapping and quantification in organ tissue. *J. Vis. Exp.* **2014**. [[CrossRef](#)] [[PubMed](#)]
45. Sancey, L.; Motto-Ros, V.; Busser, B.; Kotb, S.; Benoit, J.M.; Piednoir, A.; Lux, F.; Tillement, O.; Panczer, G.; Yu, J. Laser spectrometry for multi-elemental imaging of biological tissues. *Sci. Rep.* **2014**, *4*, 6065. [[CrossRef](#)] [[PubMed](#)]
46. Gimenez, Y.; Busser, B.; Trichard, F.; Kulesza, A.; Laurent, J.M.; Zaun, V.; Lux, F.; Benoit, J.M.; Panczer, G.; Dugourd, P.; et al. 3D Imaging of Nanoparticle Distribution in Biological Tissue by Laser-Induced Breakdown Spectroscopy. *Sci. Rep.* **2016**, *6*, 29936. [[CrossRef](#)]
47. Busser, B.; Moncayo, S.; Trichard, F.; Bonnetterre, V.; Pinel, N.; Pelascini, F.; Dugourd, P.; Coll, J.L.; D'Incan, M.; Charles, J.; et al. Characterization of foreign materials in paraffin-embedded pathological specimens using in situ multi-elemental imaging with laser spectroscopy. *Mod. Pathol.* **2018**, *31*, 378–384. [[CrossRef](#)]
48. Pliquet, J.; Dubois, A.; Racœur, C.; Mabrouk, N.; Amor, S.; Lescure, R.; Bettaieb, A.; Collin, B.; Bernhard, C.; Denat, F.; et al. A Promising Family of Fluorescent Water-Soluble aza-BODIPY Dyes for in Vivo Molecular Imaging. *Bioconj. Chem.* **2019**, *30*, 1061–1066. [[CrossRef](#)]
49. Abele, H.; Dubbers, D.; Haese, H.; Klein, M.; Knoepfler, A.; Kreuz, M.; Lauer, T.; Maerkisch, B.; Mund, D.; Nesvizhevsky, V.; et al. Characterization of a ballistic supermirror neutron guide. *Nucl. Instrum. Methods Phys. Res. Sect. A* **2006**, *562*, 407–417. [[CrossRef](#)]
50. Pedrosa-Rivera, M.; Ruiz-Magana, M.J.; Porroas, I.; Praena, J.; Torres-Sanchez, P.; Sabariego, M.P.; Köester, U.; Forsyth, T.; Solden, T.; Haertlein, M.; et al. Neutron radiobiology studies with a pure cold neutron beam. *Nucl. Instrum. Methods Phys. Res. Sect. B* **2020**, *462*, 24–31. [[CrossRef](#)]
51. Hideghety, K.; Sauerwein, W.; Wittig, A.; Gotz, C.; Paquis, P.; Grochulla, F.; Haselsberger, K.; Wolbers, J.; Moss, R.; Huiskamp, R.; et al. Tissue uptake of BSH in patients with glioblastoma in the EORTC 11961 phase I BNCT trial. *J. Neurooncol.* **2003**, *62*, 145–156. [[CrossRef](#)]
52. Busser, B.; Moncayo, S.; Coll, J.L.; Sancey, L.; Motto-Ros, V. Elemental imaging using laser-induced breakdown spectroscopy: A new and promising approach for biological and medical applications. *Coord. Chem. Rev.* **2018**, *358*, 70–79. [[CrossRef](#)]
53. Yokoyama, K.; Miyatake, S.; Kajimoto, Y.; Kawabata, S.; Doi, A.; Yoshida, T.; Asano, T.; Kirihata, M.; Ono, K.; Kuroiwa, T. Pharmacokinetic study of BSH and BPA in simultaneous use for BNCT. *J. Neurooncol.* **2006**, *78*, 227–232. [[CrossRef](#)] [[PubMed](#)]
54. Tamanoi, F. Recent excitements in the study of the CAM assay. *Enzymes* **2019**, *46*, 1–9. [[CrossRef](#)]
55. Steiner, R. Angiostatic activity of anticancer agents in the chick embryo chorioallantoic membrane (CHE-CAM) assay. *EXS* **1992**, *61*, 449–454. [[CrossRef](#)]
56. Tanaka, N.G.; Sakamoto, N.; Tohgo, A.; Nishiyama, Y.; Ogawa, H. Inhibitory effects of anti-angiogenic agents on neovascularization and growth of the chorioallantoic membrane (CAM). The possibility of a new CAM assay for angiogenesis inhibition. *Exp. Pathol.* **1986**, *30*, 143–150. [[CrossRef](#)]
57. Dunker, N.; Jendrossek, V. Implementation of the Chick Chorioallantoic Membrane (CAM) Model in Radiation Biology and Experimental Radiation Oncology Research. *Cancers* **2019**, *11*, 1499. [[CrossRef](#)] [[PubMed](#)]
58. Park, J.H.; Moon, Y.H.; Kim, D.J.; Kim, S.A.; Lee, J.B.; Ahn, S.G.; Yoon, J.H. Photodynamic therapy with hexenyl ester of 5-aminolevulinic acid induces necrotic cell death in salivary gland adenocarcinoma cells. *Oncol. Rep.* **2010**, *24*, 177–181.
59. Zuo, Z.; Syrovets, T.; Wu, Y.; Hafner, S.; Vernikouskaya, I.; Liu, W.; Ma, G.; Weil, T.; Simmet, T.; Rasche, V. The CAM cancer xenograft as a model for initial evaluation of MR labelled compounds. *Sci. Rep.* **2017**, *7*, 46690. [[CrossRef](#)]
60. Warnock, G.; Turtoi, A.; Blomme, A.; Bretin, F.; Bahri, M.A.; Lemaire, C.; Libert, L.C.; Seret, A.E.; Luxen, A.; Castronovo, V.; et al. In vivo PET/CT in a human glioblastoma chicken chorioallantoic membrane model: A new tool for oncology and radiotracer development. *J. Nucl. Med.* **2013**, *54*, 1782–1788. [[CrossRef](#)]



1 *Supplementary information*

## 2 **Theranostic aza-BODIPY as vector for enhanced** 3 **Boron Neutron Capture Therapy applications**

4 Ghadir Kalot <sup>1,†</sup>, Amélie Godard <sup>2,†</sup>, Benoît Busser <sup>1,3</sup>, Jacques Pliquett <sup>2</sup>, Mans Broekgaarden <sup>1</sup>,  
5 Vincent Motto-Ros <sup>4</sup>, K. David Wegner <sup>5</sup>, Ute Resch-Genger <sup>5</sup>, Ulli Köster <sup>6</sup>, Franck Denat <sup>2</sup>, Jean-  
6 Luc Coll <sup>1</sup>, Ewen Bodio <sup>2\*</sup>, Christine Goze <sup>2,\*</sup> and Lucie Sancey <sup>1,\*</sup>

7

### 8 **Materials and methods for chemical synthesis and characterization**

9 Reactions were carried out in analytical reagent grade solvents from Carlo Erba under normal  
10 atmosphere. Dry solvents, purchased from Carlo Erba, were non-stabilized and dried using a MB-  
11 SPS-800 (MBraun) or PureSolv-MD-5 (Inert®). All reagents purchased from Sigma Aldrich™,  
12 Thermo Fisher Scientific™ or ACROS Organics™ were used as received without further purification.  
13 Sodium mercaptododecaborate (<sup>10</sup>B) was purchased from Katchem™. Reactions were monitored by  
14 thin-layer chromatography and RP-HPLC-MS. Analytical thin-layer chromatography was performed  
15 with Merck 60 F254 silica gel (precoated sheets, 0.2 mm thick). Column chromatography was carried  
16 out using silica gel (Sigma Aldrich; 40-63 μm 230-400 mesh 60Å). Ion exchange was executed using  
17 an Amberlite™ IRA410Cl ion-exchange resin.

18 (<sup>1</sup>H, <sup>11</sup>B, <sup>13</sup>C, <sup>19</sup>F)-NMR spectra were recorded at 298 or 343 K on Bruker 500 Avance III or 600  
19 Avance III spectrometers. Chemical shifts are given relative to TMS (<sup>1</sup>H, <sup>13</sup>C), BF<sub>3</sub>\*Et<sub>2</sub>O (<sup>11</sup>B, <sup>10</sup>B), CFC<sub>3</sub>  
20 (<sup>19</sup>F), and were referenced to the residual solvent signal. High resolution mass spectra (HR-MS) were  
21 recorded on a Thermo LTQ Orbitrap XL ESIMS spectrometer. NMR and mass-analyses were  
22 performed at the "Plateforme d'Analyse Chimique et de Synthèse Moléculaire de l'Université de  
23 Bourgogne" (PACSMUB).

24 HPLC-MS analyses were obtained from a Thermo-Dionex Ultimate 3000 instrument (pump +  
25 autosampler at 20 °C + column oven at 25 °C) equipped with a diode array detector (Thermo-Dionex  
26 DAD 3000-RS) and a MSQ Plus single quadrupole mass spectrometer equipped with Phenomenex  
27 Kinetex® column (2.6 μm C18 100 Å, LC Column 50 x 2.1 mm).

28 The employed gradient for analyses was as follows:

29

Time [min]	% H <sub>2</sub> O + 0.1% formic acid	% ACN + 0.1% formic acid	Flow [mL/min]
0	95	5	0.5
5	0	100	0.5
6.5	0	100	0.5
6.6	95	5	0.5
8.5	95	5	0.5
8.51	95	5	0.05

30 **Table S1:** HPLC analytical gradient.

31

32

33 Semi-preparative separations were executed on a HPLC-system, from Shimadzu, that was  
 34 equipped with 2 LC-20AT pumps, a SPD-20A UV/Vis detector, a FRC-10A fraction collector, a SIL-  
 35 10AP sampler and a CBM-20A control unit. The column was a Shim-Pack GIST 5  $\mu$ m C18 10x250 mm  
 36 column obtained from Shimadzu too. The gradient using a mixture of ACN and water with 0.1% TFA  
 37 and a flow rate of 5 mL/min was as follows:

38

39

40

41

42

43

44

45

46

47

Time [min]	% H <sub>2</sub> O + 0.1 %TFA	% ACN + 0.1 %TFA	Flow [mL/min]
0	75	25	5
5	75	25	5
25	0	100	5
28	0	100	5
30	75	25	5

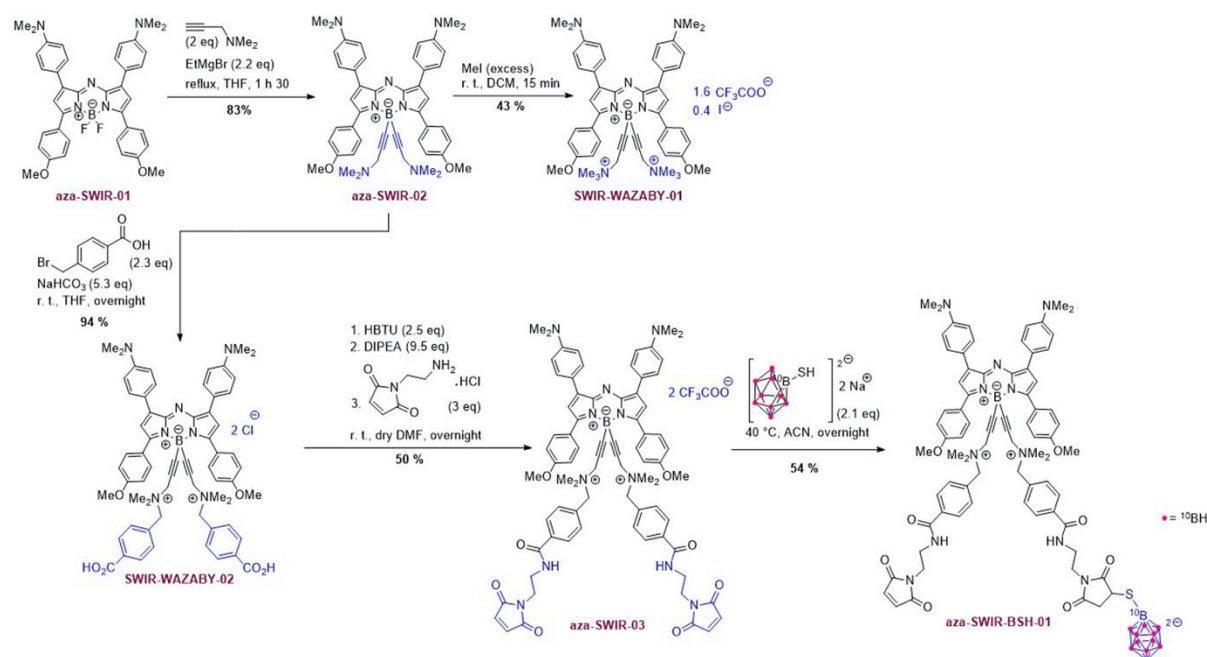
48

Table S2: Detailed of gradients.

49

50

### Synthesis and characterization



51

52

Scheme S1: Synthetic pathways of aza-SWIR-BSH-01.

53 Aza-SWIR-01, aza-SWIR-02, and SWIR-WAZABY-01 were synthesized according to procedures,  
 54 we previously reported [1].

55

56 • Compound **SWIR-WAZABY-02**:

57

58

59

60

61

62

63

64

65

66

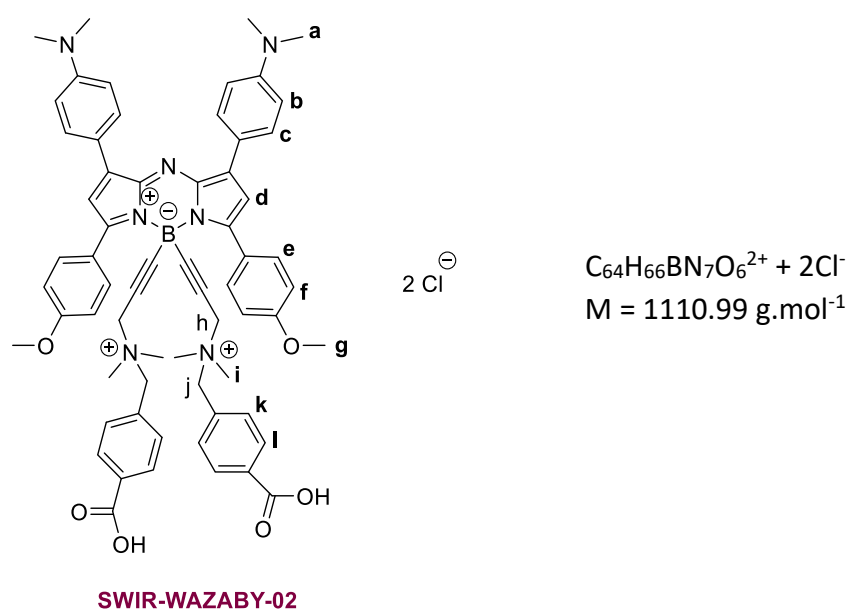
67

68

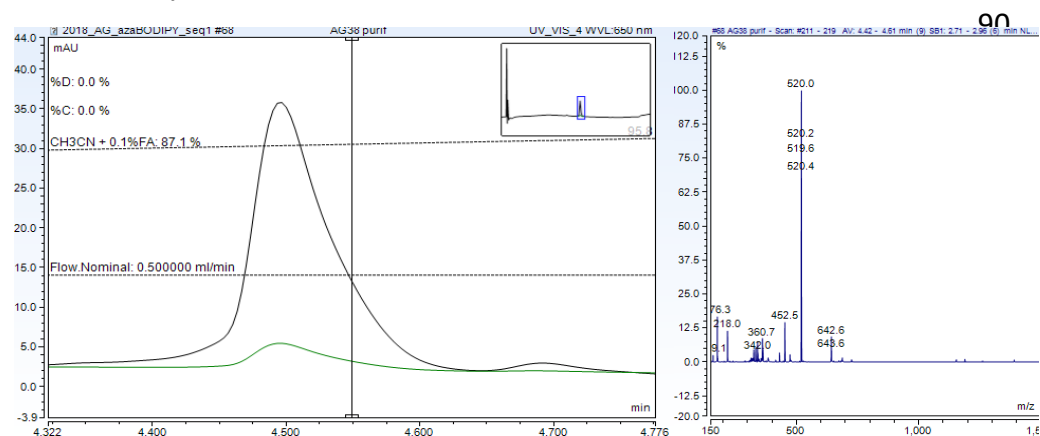
69

70

71



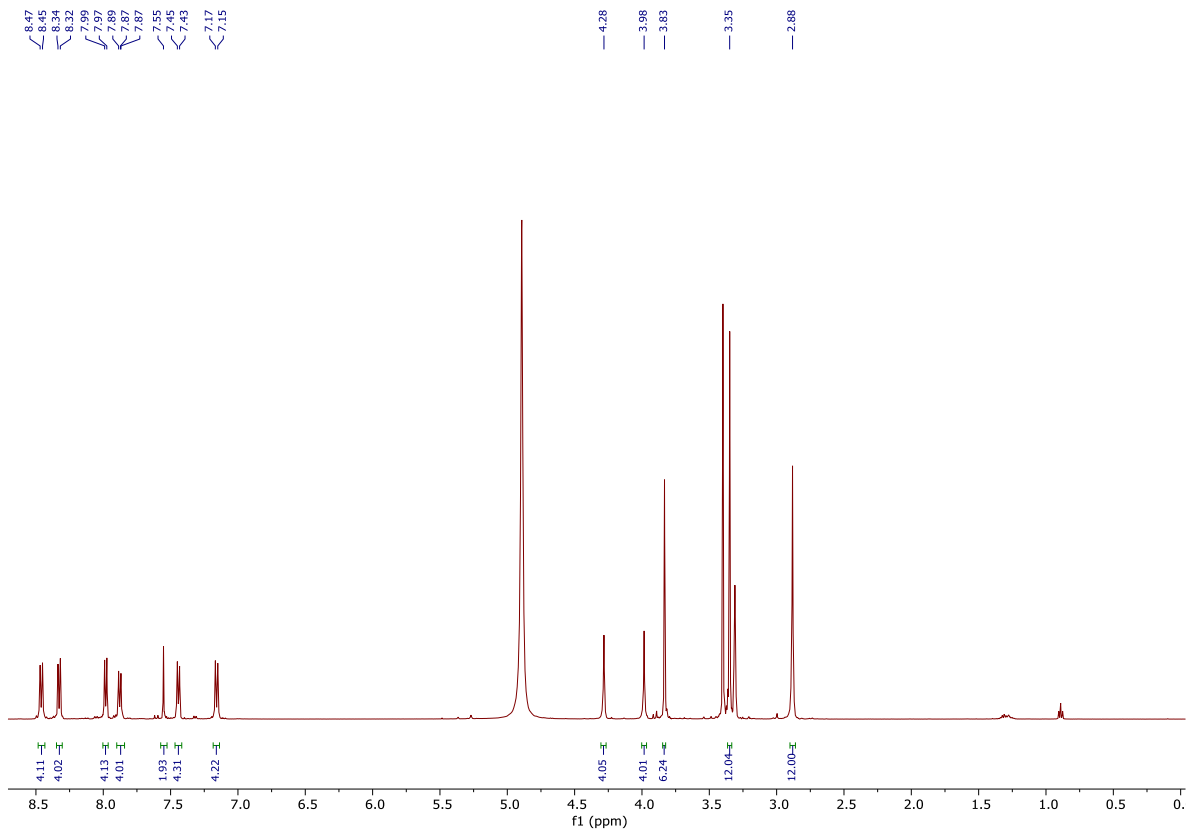
72 **Aza-SWIR-02** (250 mg, 0.3 mmol, 1 eq) was added in a 100 mL round bottom flask and dissolved  
 73 in a mixture of THF and water (50 mL / 8 mL). NaHCO<sub>3</sub> (137 mg; 1.6 mmol; 5.3 eq) and 4-  
 74 bromomethylbenzoic acid (144 mg; 0.7 mmol; 2.3 eq) were added successively. The resulting solution  
 75 was stirred at room temperature (RT) overnight and transferred to a separating funnel. Then, 90 mL  
 76 of Et<sub>2</sub>O and 90 mL of water were added and the two layers were separated. The aqueous layer was  
 77 washed with Et<sub>2</sub>O (6 × 60 mL) to remove the remaining traces of 4-bromomethylbenzoic acid. Then,  
 78 the aqueous layer was evaporated at 35 °C to 2/3<sup>th</sup> of the volume and 10 mL of HCl<sub>aq</sub> (3M) were added  
 79 to precipitate the compound (via protonation of the carboxylate groups). The mixture was  
 80 centrifuged during 5 min at 6 000 RPM. The supernatant was removed and the sediment was  
 81 suspended in Et<sub>2</sub>O (15 mL) and centrifuged. The process was repeated 3 times and the solid was dried  
 82 under vacuum to give pure **SWIR-WAZABY-02** as a crystalline dark powder (336 mg; 0.3 mmol; 94%  
 83 yield). <sup>1</sup>H NMR (500 MHz, 298 K, MeOD-d<sub>4</sub>) δ (ppm) = 2.88 (s, 12H), 3.35 (s, 12H), 3.83 (s, 6H), 3.98 (s,  
 84 4H), 4.28 (s, 4H), 7.16 (d, J = 9.0 Hz, 4H), 7.44 (d, J = 8.2 Hz, 4H), 7.55 (s, 2H), 7.88 (d, J = 9.0, 4H), 7.98  
 85 (d, J = 8.2 Hz, 4H), 8.33 (d, J = 9.0 Hz, 4H), 8.46 (d, J = 9.0 Hz, 4H). <sup>13</sup>C NMR (125 MHz, 298 K, MeOD-  
 86 d<sub>4</sub>) δ (ppm) = 48.0, 50.7, 52.1, 56.7, 57.5, 67.8, 89.6, 116.5, 123.1, 123.3, 125.8, 131.9, 132.2, 133.1, 133.6,  
 87 134.9, 135.2, 135.7, 142.3, 145.1, 145.6, 160.2, 164.9, 169.2. <sup>11</sup>B NMR (193 MHz, 298K, MeOD-d<sub>4</sub>) δ (ppm)  
 88 = -11.63 (bs). HR-MS (ESI): m/z calculated for <sup>12</sup>C<sub>64</sub><sup>1</sup>H<sub>66</sub><sup>11</sup>B<sup>14</sup>N<sub>7</sub><sup>16</sup>O<sub>6</sub><sup>2+</sup> [M]<sup>2+</sup> 519.75783 Th; found  
 89 519.75905 Th. Analytical HPLC: Tr = 4.50 min.



91

**Figure S1:** Analytical HPLC of **SWIR-WAZABY-02**

92

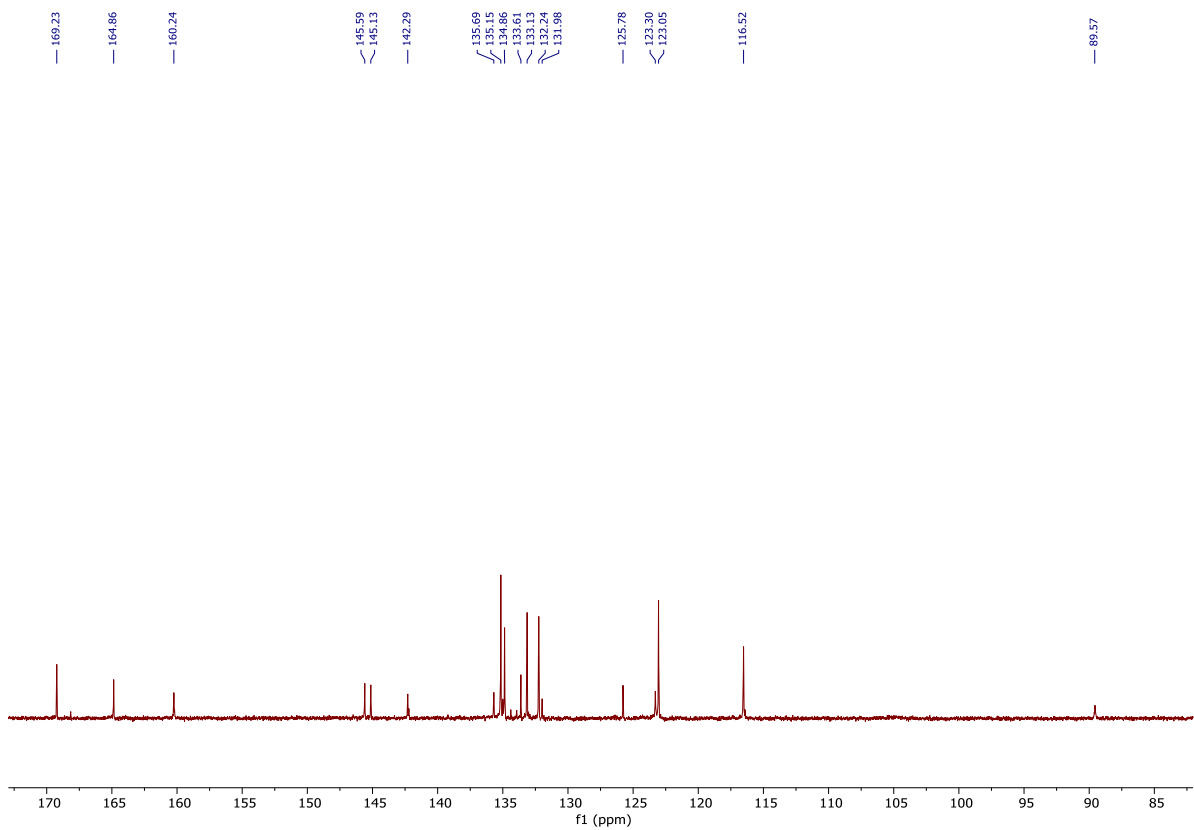


93

94

95

Figure S2: <sup>1</sup>H NMR of SWIR-WAZABY-02 (500 MHz, 298 K, MeOD-d<sub>4</sub>)



96

97

98 **Figure S3:**  $^{13}\text{C}$  NMR of SWIR-WAZABY-02 (125 MHz, 298 K, MeOD- $d_4$ )

99

100 • Compound **aza-SWIR-03**:

101

102

103

104

105

106

107

108

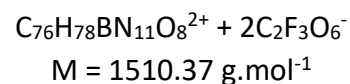
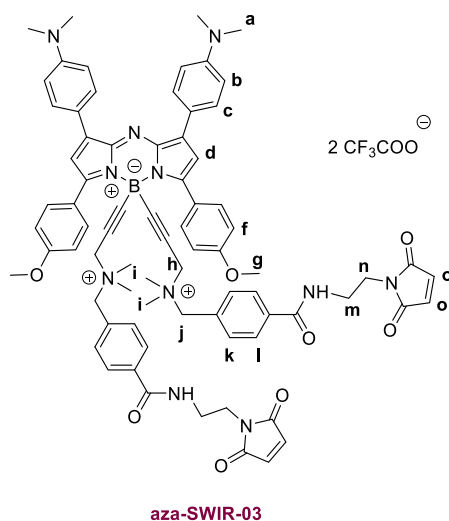
109

110

111

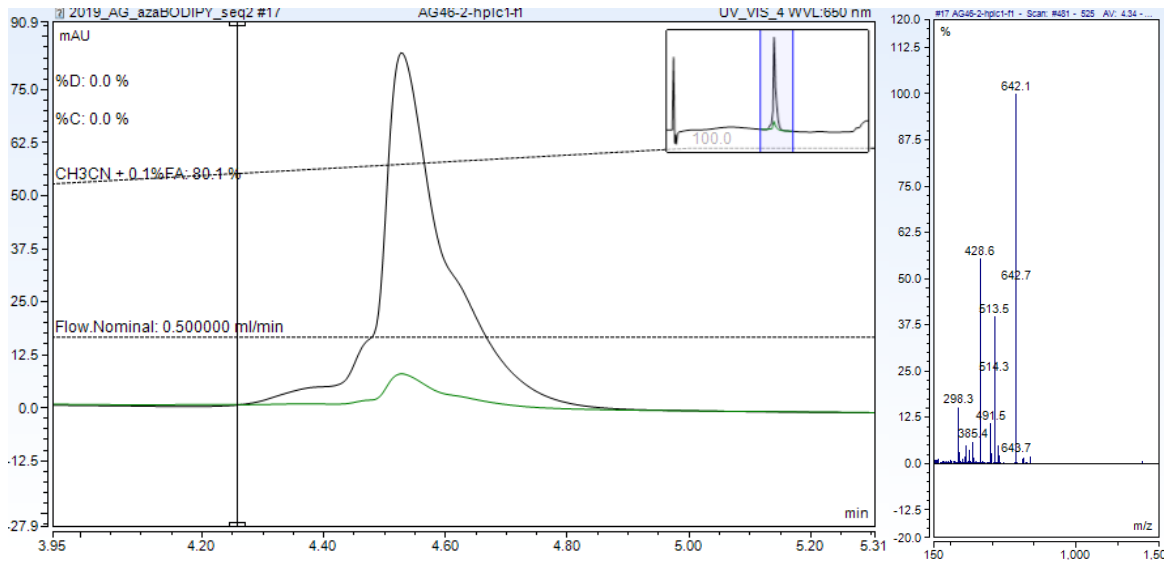
112

113



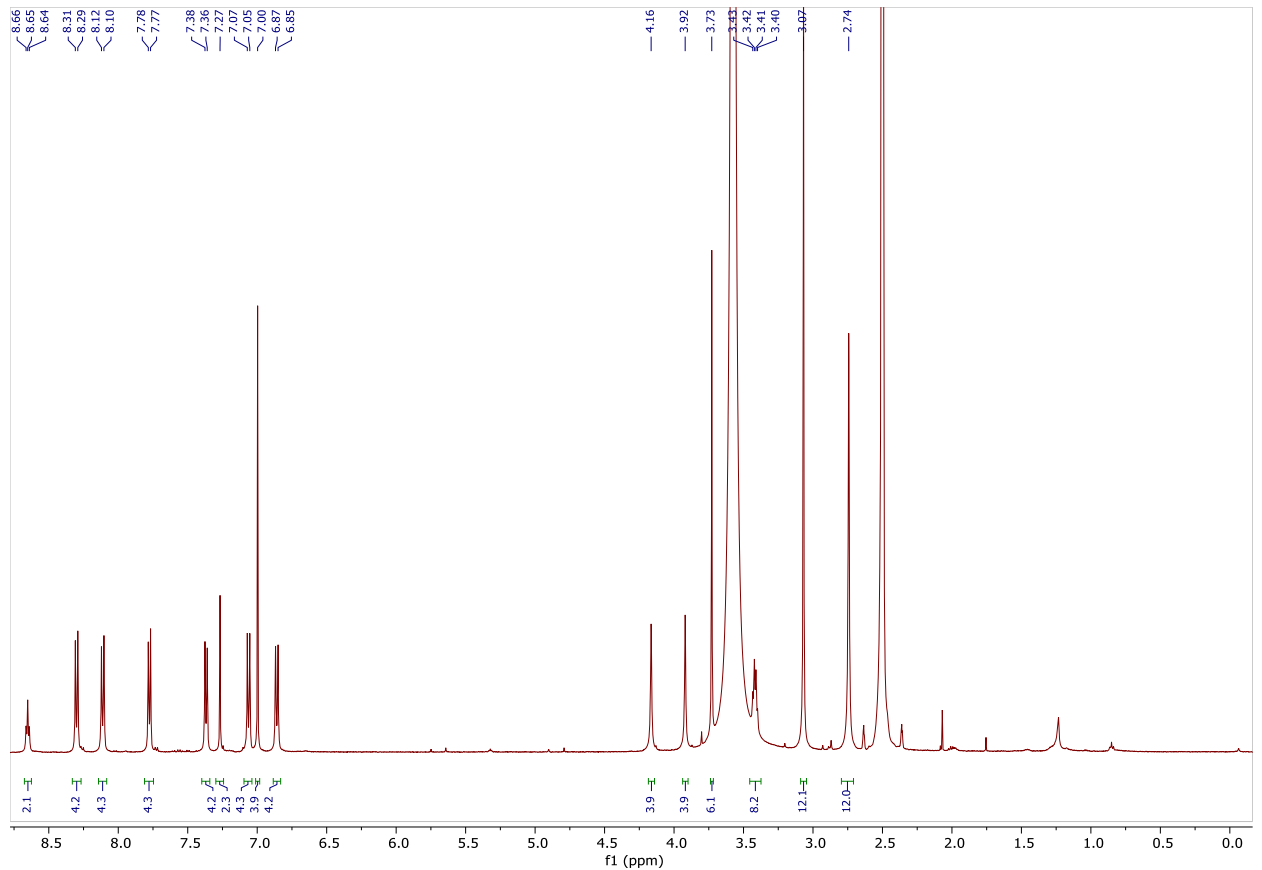
114 **SWIR-WAZABY-02** (250 mg, 0.2 mmol, 1 eq) was dissolved in 10 mL of dry DMF. HBTU (208  
 115 mg; 0.5 mmol; 2.5 eq) solubilized in dry DMF (10 mL) was added to the reaction medium. DIPEA  
 116 (340  $\mu\text{L}$ ; 1.9 mmol; 9.5 eq) was then added and the reaction mixture was stirred at RT for 1 h. *N*-(2-  
 117 aminoethyl)maleimide hydrochloride (0.6 mg, 0.6 mmol, 3 eq) was solubilized in dry DMF (10 mL)  
 118 and added to the medium. The reaction mixture was stirred at RT overnight. The solvent was  
 119 removed at 45°C under vacuum. The crude was purified by semi-preparative HPLC to obtain **aza-**  
 120 **SWIR-03** as a green solid (151 mg, 50 % yield).  $^1\text{H}$  NMR (500 MHz, 298 K, DMSO- $d_6$ )  $\delta$  = 2.74 (s, 12H),  
 121 3.07 (s, 12H), 3.40-3.43 (m, 8H), 3.73 (s, 6H), 3.92 (s, 4H), 4.16 (s, 4H), 6.86 (d,  $J$  = 9.0 Hz, 4H), 7.00 (s,  
 122 4H), 7.06 (d,  $J$  = 9.0 Hz, 4H), 7.27 (s, 2H), 7.37 (d,  $J$  = 8.0 Hz, 4H), 7.78 (d,  $J$  = 8.0 Hz, 4H), 8.11 (d,  $J$  = 9.0  
 123 Hz, 4H), 8.30 (d,  $J$  = 9.0 Hz, 4H), 8.65 (t,  $J$  = 5.9 Hz, 2H).  $^{13}\text{C}$  NMR (150 MHz, 298 K, DMSO- $d_6$ )  $\delta$  (ppm)  
 124 = 37.1, 37.8, 49.1, 54.0, 55.4, 64.7, 86.7, 112.1, 112.8, 113.8, 114.7, 116.0, 116.7, 118.6, 119.8, 124.3, 127.6,  
 125 130.1, 130.5, 132.0, 132.5, 134.6, 136.0, 141.6, 142.1, 151.0, 155.9, 157.9, 158.1, 158.3, 158.6, 160.9, 165.6,  
 126 171.1. HR-MS (ESI):  $m/z$  calculated for  $^{12}\text{C}_{76}^{1}\text{H}_{78}^{11}\text{B}^{14}\text{N}_{11}^{16}\text{O}_8^{2+}$   $[\text{M}]^{2+}$  641.80585 Th; found 641.80752 Th.  
 127 Analytical HPLC: Tr = 4.56 min.

128



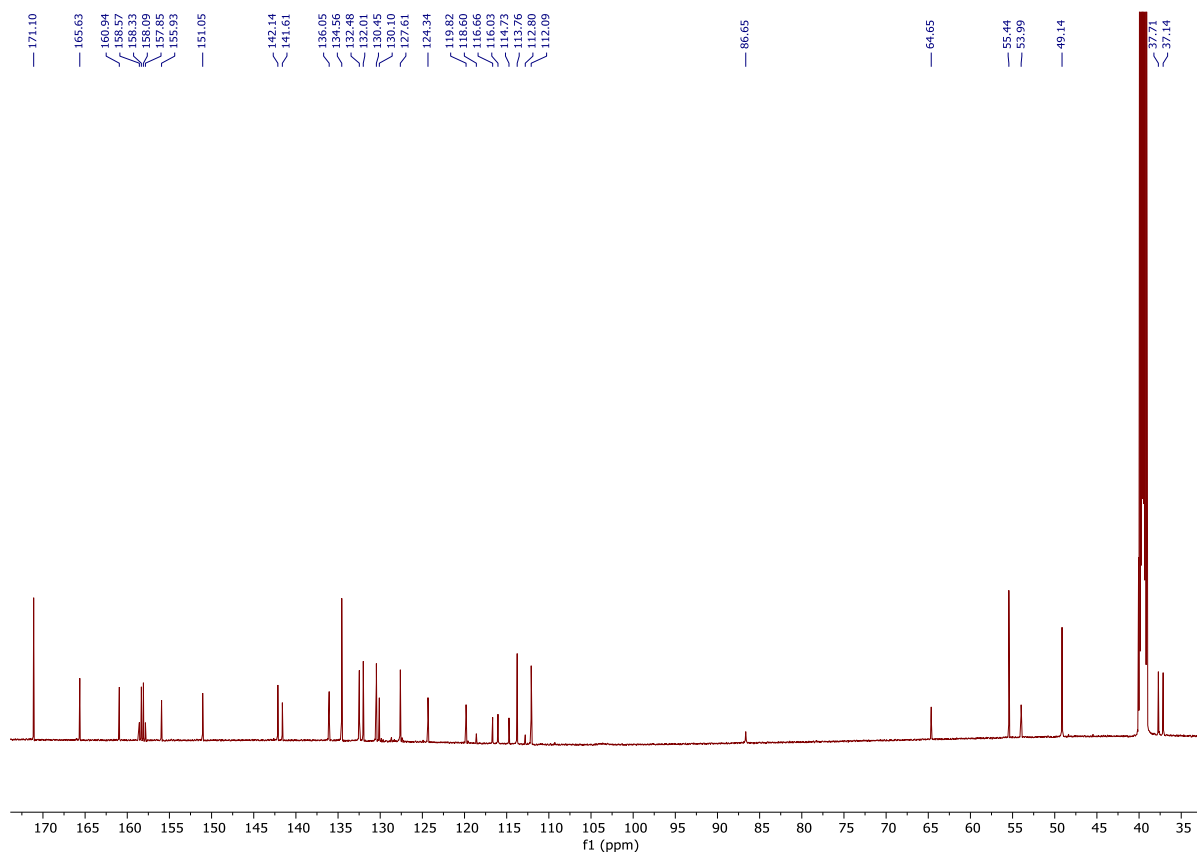
129

Figure S4: Analytical HPLC of aza-SWIR-03



130  
131

Figure S5: <sup>1</sup>H NMR of aza-SWIR-03 (500 MHz, 298 K, DMSO-d<sub>6</sub>)



132

133

134 **Figure S6:**  $^{13}\text{C}$  NMR of aza-SWIR-03 (150 MHz, 298 K, DMSO- $d_6$ )

135

- 136 • Compound aza-SWIR-BSH-01:

137

138

139

140

141

142

143

144

145

146

147

148

149

150

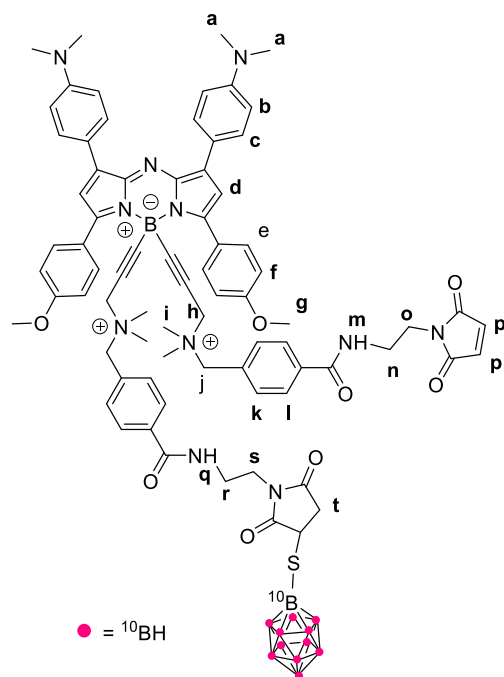
151

152

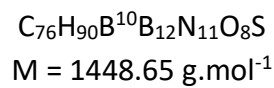
153

154

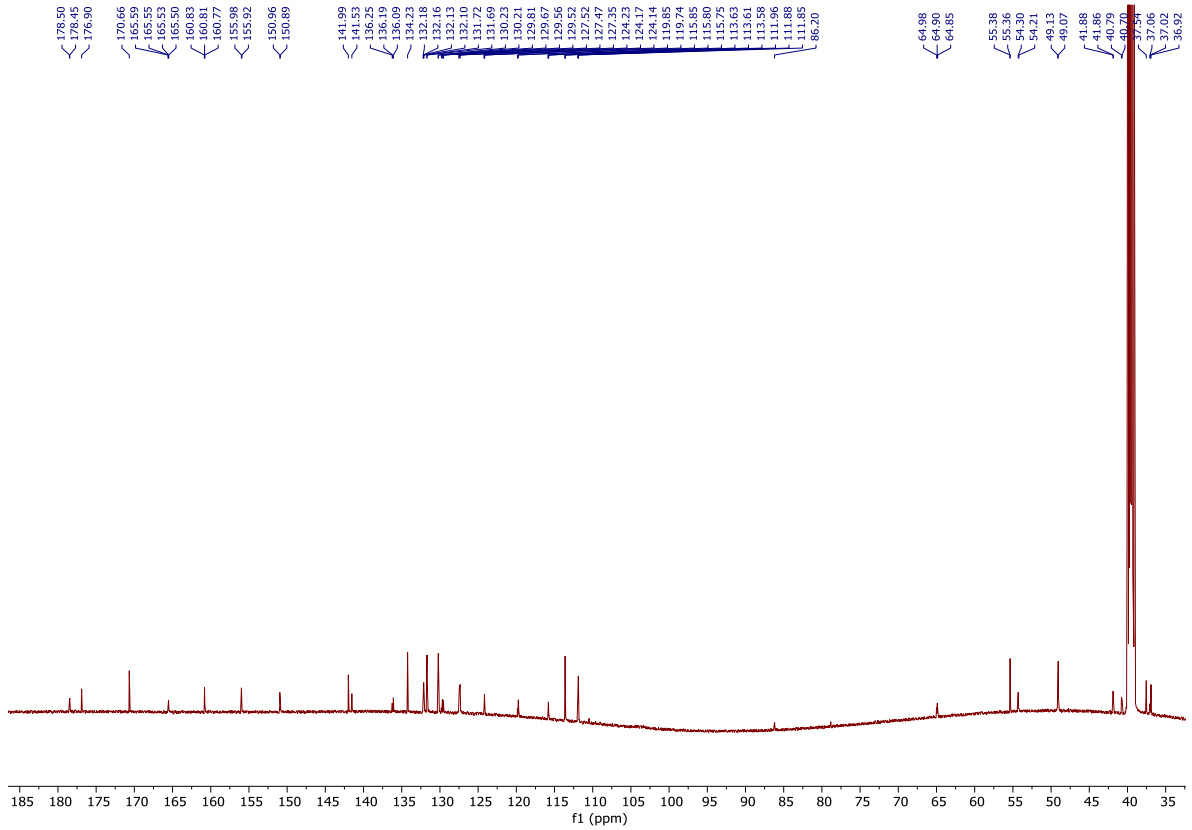
155



**Aza-SWIR-BSH-01**



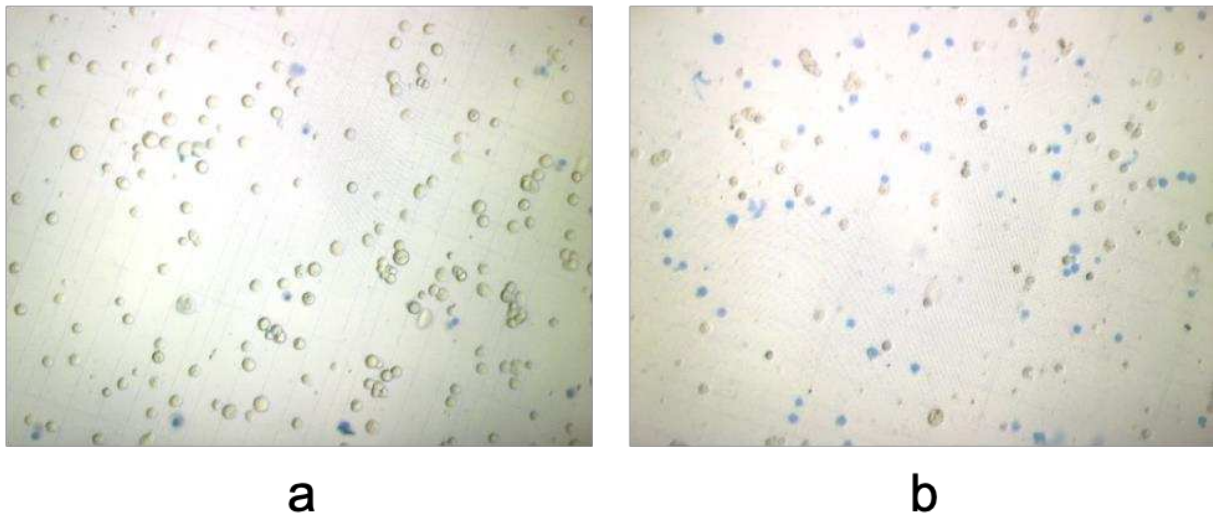




181  
182

183 **Figure S8:** <sup>13</sup>C NMR of *aza-SWIR-BSH-01* (150 MHz, 343 K, DMSO-d<sub>6</sub>).

184



185

186 **Figure S9:** U-251 cells incubated with *aza-SWIR-BSH-01* before (a) and after (b) 10 min of neutron  
187 exposure. The clichés were taken from microscopy observation. Cells were diluted with Trypan blue  
188 to count the viable cells and exclude the dead cells (in blue) on Malassez slides. The presence of huge  
189 number of blue cells in (b) evidences the strong and immediate impact of the neutron exposure on  
190 cells incubated with *aza-SWIR-BSH-01*.

191

192 **Reference**

193

- 194 1. Godard, A.; Kalot, G.; Pliquett, J.; Busser, B.; Le Guevel, X.; Wegner, K.D.; Resch-Genger, U.;  
195 Rousselin, Y.; Coll, J.L.; Denat, F., et al. Water-Soluble Aza-BODIPYs: Biocompatible  
196 Organic Dyes for High Contrast In Vivo NIR-II Imaging. *Bioconjug. Chem.* **2020**, *31*,  
197 1088-1092, doi:10.1021/acs.bioconjchem.0c00175.

198

## Discussion and perspectives

Our primary theranostic boron vector based on aza-BODIPYs, *i.e.* aza-SWIR-BSH-01, demonstrated a great potential for BNCT application in preclinical tumor models. Yet, further improvements of the aza-BODIPY/ $^{10}\text{B}$ -BSH compound and the bioevaluation techniques are required to address some encountered issues. In particular, water-solubility, and whole-body imaging and quantification that are necessary for any potential clinical use.

Accordingly, our chemist colleagues modified aza-SWIR-BSH-01 synthesis leading to the development of aza-SWIR-BSH-02 (Figure 75a), an aza-BODIPY/ $^{10}\text{B}$ -BSH that is structurally similar to aza-SWIR-BSH-01, except for a single modification of its free arm, necessary for the coupling of a chelating group, and further improvement of water-solubility. Aza-SWIR-BSH-02 possessed enhanced fluorescence properties as compared to aza-SWIR-BSH-01 (Figure 75b), which allowed easier visualization *in vitro* (Figure 75c) and *in vivo* (Figure 75d), using microscopy and NIR-II fluorescence imaging respectively. The imaging investigations confirmed the tumor accumulation of the compound, similarly to previous experiments using the analog aza-SWIR-BSH-01.

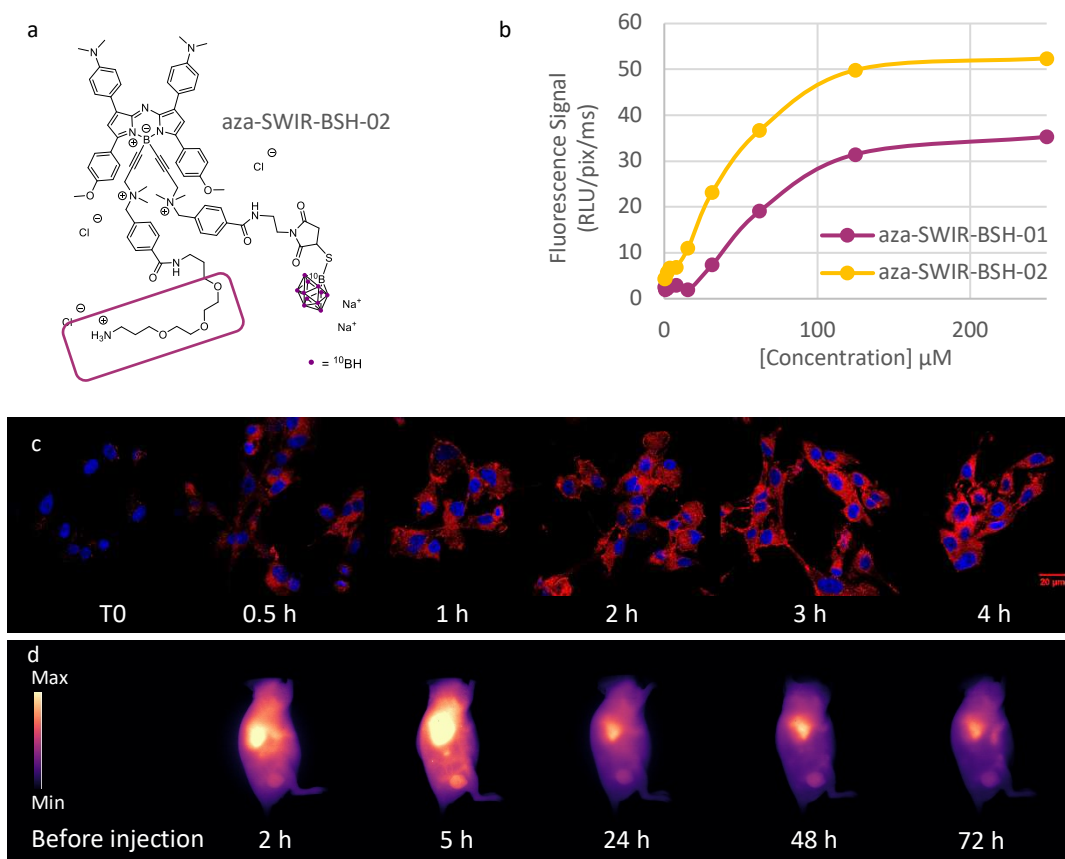


Figure 75: (a) Chemical structure of aza-SWIR-BSH-02, the purple box indicates the modified arm. (b) Quantification of aza-SWIR-BSH-01 and aza-SWIR-BSH-02 fluorescence signal following their serial dilution in blood plasma. (c) Confocal images of U-87 MG cells before and at certain time points following incubation with  $10 \mu\text{M}$  of aza-SWIR-BSH-02. Aza-SWIR-BSH-02 is presented in red and the nuclei are counterstained in blue. The scale bar represents  $20 \mu\text{m}$ . (d) NIR-II fluorescence images of mice bearing subcutaneous U-87 MG tumors before and until 72 h post aza-SWIR-BSH-02 administration ( $200 \mu\text{L}$  of  $600 \mu\text{M}$ ).

To assess the BNCT efficacy of aza-SWIR-BSH-02 under neutron field exposure, an *in ovo* U-87 MG tumor model was used. Compared to the *in ovo* workflow applied in the paper, the protocol was modified to implant tumor cells on day 10 instead of day 7 (Figure 76a). This procedure resulted in tumors of larger size and increased vasculature as compared to tumors implanted at day 7 (Figure 76b,c). Three days following tumor cells implantation, aza-SWIR-BSH-02 was incubated and its tumor accumulation was assessed using NIR-II fluorescence imaging. The time point 24 h was selected as the optimal time required for ideal aza-SWIR-BSH-02 tumor uptake prior to neutron exposure (Figure 76d,e). Accordingly, the embryos were sacrificed at day 19 instead of day 16, and a 50 % reduction in tumor growth was achieved using aza-SWIR-BSH-02 compared to the 30% reduction attained by BSH (Figure 77d). These results demonstrated the aza-SWIR-BSH-02 better anti-tumor effect compared to BSH.

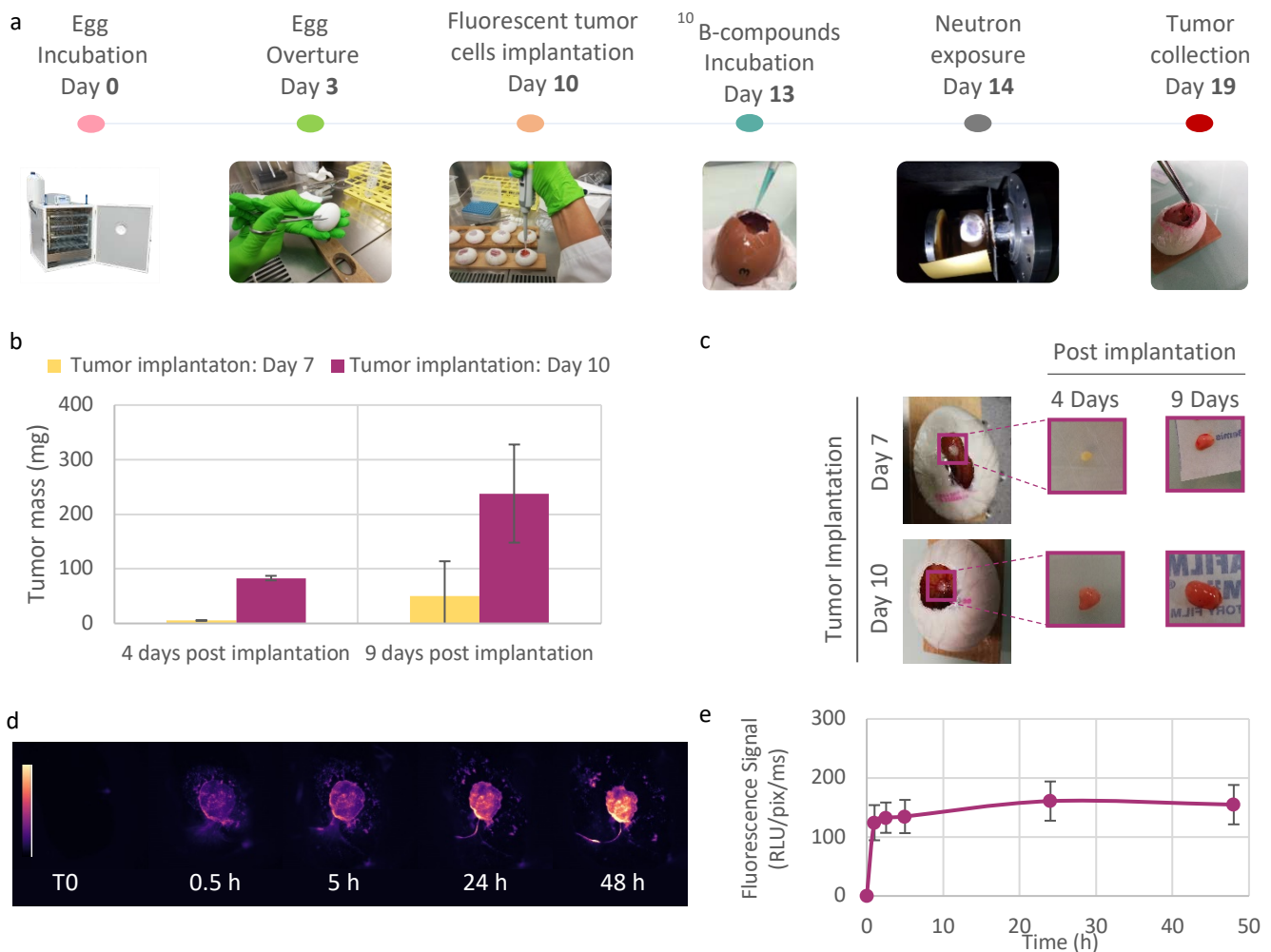


Figure 76: (a) New protocol for BNCT *in ovo* tumor model. (b) Quantification of tumor masses resected 4 or 9 days following their implantation at day 7 or day 10. (c) Images revealing the differences in size and vasculature between tumors implanted at day 7 and those implanted at day 10. (d) NIR-II fluorescence images of U-87MG *in ovo* tumor before and until 48 h post-incubation with aza-SWIR-BSH-02. (e) Quantification of aza-SWIR-BSH-02 fluorescence signal in U-87 MG *in ovo* tumors as a function of time. Results are expressed as the mean of tumor fluorescence  $\pm$  S.D (n=3).

In a clinical perspective, the aza-BODIPY/<sup>10</sup>B-BSH compound was coupled to DOTA, a chelator for indium and <sup>111</sup>In in particular that can be detected by SPECT imaging, resulting in the synthesis of aza-SWIR-BSH-03 (Figure 77a). This latter can provide an appropriate boron vector for human BNCT application as it can be monitored and quantified using SPECT imaging. Due to time restrictions, aza-SWIR-BSH-03 was only studied for its *in ovo* tumor accumulation and anti-tumor effect post neutron exposure. Similar to aza-SWIR-BSH-02, 24 h was selected as the optimal time required for tumor uptake prior to neutron irradiation (Figure 77b,c). It is important to note that aza-SWIR-BSH-03 possessed a further improved fluorescence signal as compared to aza-SWIR-BSH-02, using the same imaging settings (Figure 76e, Figure 77c). Additionally, a superior reduction in tumor growth was observed using aza-SWIR-BSH-03 (-60 %), however, this difference was not significant as compared to aza-SWIR-BSH-02 (Figure 77d).

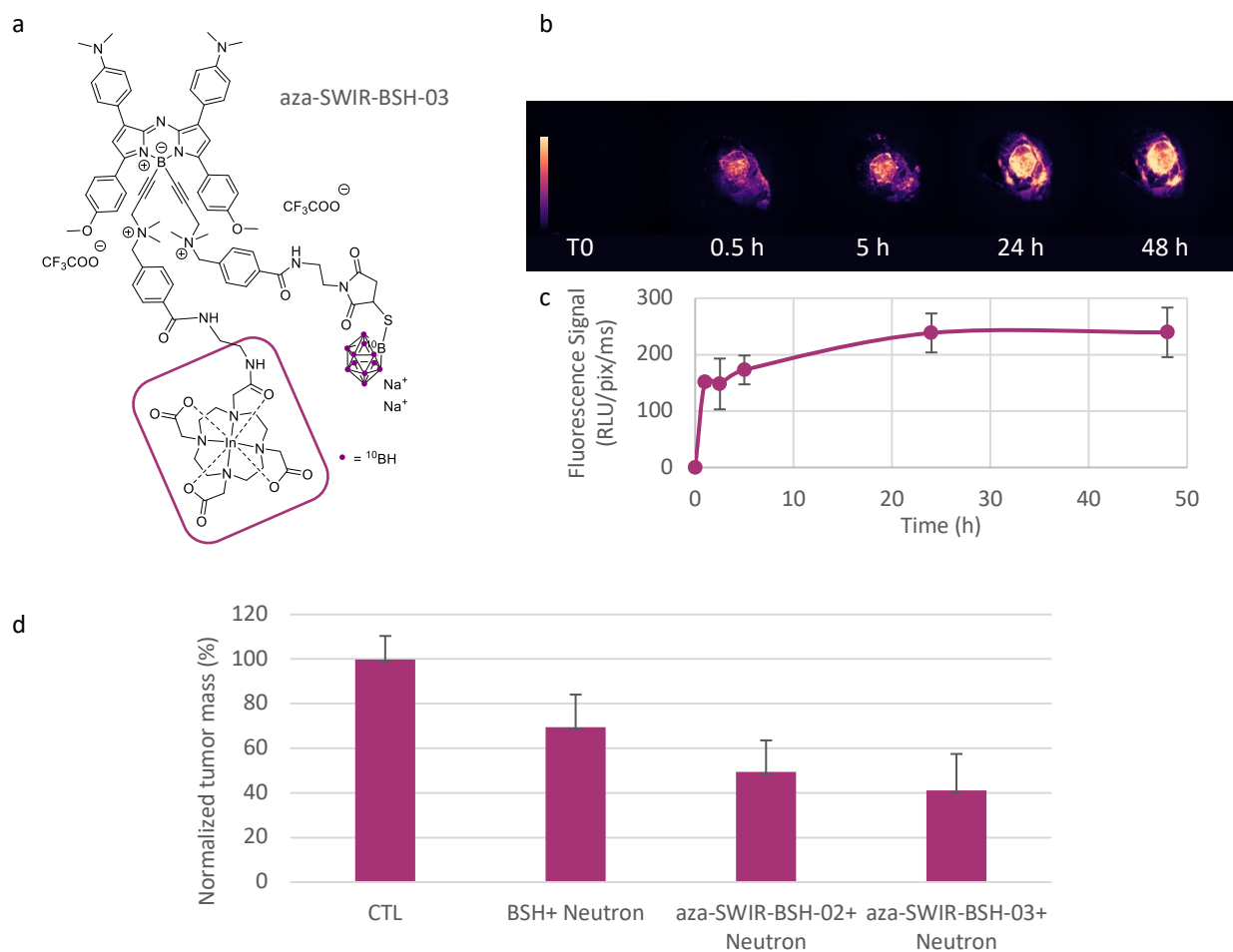


Figure 77: (a) Chemical structure of the bimodal theranostic compound aza-SWIR-BSH-03, the purple square indicates indium-DOTA. (b) NIR-II fluorescence images of U-87MG *in ovo* tumor before and until 48 h post-incubation with aza-SWIR-BSH-03. (c) Quantification of the aza-SWIR-BSH-03 fluorescence signal in U-87 MG *in ovo* tumors as a function of time. Results are expressed as the mean of tumors fluorescence  $\pm$  S.D (n=3). (d) Tumor development was measured at day 19, i.e., 6 days after the addition of the different compounds and 5 days following neutron irradiation.

Considering these promising therapeutic results and the bimodal imaging properties of aza-SWIR-BSH-03, further investigations of its *in vivo* distribution using fluorescence and SPECT imaging, and additional assessment of its *in vivo* BNCT efficacy in rodents, will demonstrate its potential for clinical application.

## General Conclusion

Along the thesis work, the first water-soluble aza-BODIPY emitting in the NIR-II window was developed from a library of aza-BODIPY derivatives. The aza-BODIPY tumor-targeting capacity and primary safety were demonstrated *in vivo* in tumor-bearing mice. Its favorable tumor uptake was attributed to its interaction with plasma lipoproteins, which act as vectors selectively targeting the aza-BODIPY towards tumors overexpressing lipoprotein receptors. To target tumors possessing low or absent lipoprotein receptors expression, coupling the aza-BODIPY to antibodies enabled its specific vectorization in those tumors, which wasn't the case using free aza-BODIPY. These promising data provided a concrete base for a planned fluorescence-guided surgery (FGS) proof of concept of the NIR-II antibody bioconjugated aza-BODIPY as compared to gold standard FGS fluorophores.

As the developed aza-BODIPY was able to accumulate strongly in lipoprotein receptor-expressing tumors, we used this property to vectorize a small drug into those tumors for boron neutron capture therapy application. Coupling the aza-BODIPY to clinically used sodium borocaptate (BSH), permitted an enhanced tumor accumulation of BSH *in vivo*. After neutron exposure, the complex aza-BODIPY/BSH induced a significant anti-tumor efficacy, compared to BSH alone. Furthermore, the aza-BODIPY/BSH complex was visualized using fluorescence imaging in a preclinical theranostic approach. These findings proved the efficacy of this compound in preclinical tumor models. Yet, further adjustments of the water-solubility and the imaging properties, by adding radioisotopes for nuclear imaging, will facilitate its potential clinical translation. The quantification using nuclear imaging (PET/SPECT) is a crucial step. Additionally, the aza-BODIPY multimodal imaging could be spread to other pathological situations beyond oncology, including lipidemic disorders.

This thesis work presented a step-by-step workflow that required close collaboration between the chemists and the biologists to achieve the compounds of interest. The deep collaboration between chemists, biologists, and physicists is key in advancing cancer diagnostic and therapeutic approaches.

## References

1. Mattiuzzi, C. and G. Lippi, *Current Cancer Epidemiology*. J Epidemiol Glob Health, 2019. **9**(4): p. 217-222.
2. McCormick, P.J., *Cancer Tsunami: Emerging Trends, Economic Burden, and Perioperative Implications*. Curr Anesthesiol Rep, 2018. **8**(4): p. 348-354.
3. Ferlay, J., et al. *Global Cancer Observatory: Cancer Today*. International Agency for Research on Cancer. 2020 May 1, 2021]; Available from: <https://gco.iarc.fr/today>.
4. Ferlay, J., et al. *Global Cancer Observatory: Cancer Tomorrow*. International Agency for Research on Cancer. 2020 May 1, 2021]; Available from: <https://gco.iarc.fr/tomorrow>.
5. van Rooij, J., et al., *Social consequences of advanced cancer in patients and their informal caregivers: a qualitative study*. Support Care Cancer, 2019. **27**(4): p. 1187-1195.
6. NATIONAL CANCER INSTITUTE NIH. *What Is Cancer?* May 5, 2021; Available from: <https://www.cancer.gov/about-cancer/understanding/what-is-cancer>.
7. Hanahan, D. and R.A. Weinberg, *The hallmarks of cancer*. Cell, 2000. **100**(1): p. 57-70.
8. Hanahan, D. and R.A. Weinberg, *Hallmarks of cancer: the next generation*. Cell, 2011. **144**(5): p. 646-74.
9. Bhowmick, N.A., E.G. Neilson, and H.L. Moses, *Stromal fibroblasts in cancer initiation and progression*. Nature, 2004. **432**(7015): p. 332-7.
10. Jiang, B.H. and L.Z. Liu, *PI3K/PTEN signaling in angiogenesis and tumorigenesis*. Adv Cancer Res, 2009. **102**: p. 19-65.
11. Burkhart, D.L. and J. Sage, *Cellular mechanisms of tumour suppression by the retinoblastoma gene*. Nat Rev Cancer, 2008. **8**(9): p. 671-82.
12. Junttila, M.R. and G.I. Evan, *p53--a Jack of all trades but master of none*. Nat Rev Cancer, 2009. **9**(11): p. 821-9.
13. Lowe, S.W., E. Cepero, and G. Evan, *Intrinsic tumour suppression*. Nature, 2004. **432**(7015): p. 307-15.
14. Blasco, M.A., *Telomeres and human disease: ageing, cancer and beyond*. Nat Rev Genet, 2005. **6**(8): p. 611-22.
15. Genentech Oncology. *Hallmarks of Cancer*. Enabling replicative immortality; Available from: <https://www.genentechoncology.com/pathways/cancer-tumor-targets/hallmarks-of-cancer.html>.
16. Hanahan, D. and J. Folkman, *Patterns and emerging mechanisms of the angiogenic switch during tumorigenesis*. Cell, 1996. **86**(3): p. 353-64.
17. Baluk, P., H. Hashizume, and D.M. McDonald, *Cellular abnormalities of blood vessels as targets in cancer*. Curr Opin Genet Dev, 2005. **15**(1): p. 102-11.
18. Klymkowsky, M.W. and P. Savagner, *Epithelial-mesenchymal transition: a cancer researcher's conceptual friend and foe*. Am J Pathol, 2009. **174**(5): p. 1588-93.
19. Talmadge, J.E. and I.J. Fidler, *AACR centennial series: the biology of cancer metastasis: historical perspective*. Cancer Res, 2010. **70**(14): p. 5649-69.
20. BioRender.com. *Overview of Metastatic Cascade*. Available from: <https://app.biorender.com/biorender-templates/t-5f46e7082c321c00b3f65e38-overview-of-metastatic-cascade>.
21. Weinhouse, S., *On respiratory impairment in cancer cells*. Science, 1956. **124**(3215): p. 267-9.
22. Jones, R.G. and C.B. Thompson, *Tumor suppressors and cell metabolism: a recipe for cancer growth*. Genes Dev, 2009. **23**(5): p. 537-48.
23. Vander Heiden, M.G., L.C. Cantley, and C.B. Thompson, *Understanding the Warburg effect: the metabolic requirements of cell proliferation*. Science, 2009. **324**(5930): p. 1029-33.
24. Keating, E. and F. Martel, *Antimetabolic Effects of Polyphenols in Breast Cancer Cells: Focus on Glucose Uptake and Metabolism*. Front Nutr, 2018. **5**: p. 25.
25. Mouggiakakos, D., et al., *Regulatory T cells in cancer*. Adv Cancer Res, 2010. **107**: p. 57-117.
26. Yang, L., Y. Pang, and H.L. Moses, *TGF-beta and immune cells: an important regulatory axis in the tumor microenvironment and progression*. Trends Immunol, 2010. **31**(6): p. 220-7.
27. Genentech Oncology. *Hallmarks of Cancer*. Evading immune destruction; Available from: <https://www.genentechoncology.com/pathways/cancer-tumor-targets/hallmarks-of-cancer.html>.

28. Matsumura, Y. and H. Maeda, *A new concept for macromolecular therapeutics in cancer chemotherapy: mechanism of tumoritropic accumulation of proteins and the antitumor agent smancs*. *Cancer Res*, 1986. **46**(12 Pt 1): p. 6387-92.
29. Li, R., et al., *Be Active or Not: the Relative Contribution of Active and Passive Tumor Targeting of Nanomaterials*. *Nanotheranostics*, 2017. **1**(4): p. 346-357.
30. BioRender.com, *Features of Tumor Blood Vessels*.
31. Kobayashi, H., R. Watanabe, and P.L. Choyke, *Improving conventional enhanced permeability and retention (EPR) effects; what is the appropriate target?* *Theranostics*, 2013. **4**(1): p. 81-9.
32. Maeda, H., *Toward a full understanding of the EPR effect in primary and metastatic tumors as well as issues related to its heterogeneity*. *Adv Drug Deliv Rev*, 2015. **91**: p. 3-6.
33. Røslund, G.V. and A.S. Engelsen, *Novel points of attack for targeted cancer therapy*. *Basic Clin Pharmacol Toxicol*, 2015. **116**(1): p. 9-18.
34. Moasser, M.M., *The oncogene HER2: its signaling and transforming functions and its role in human cancer pathogenesis*. *Oncogene*, 2007. **26**(45): p. 6469-87.
35. Slamon, D.J., et al., *Studies of the HER-2/neu proto-oncogene in human breast and ovarian cancer*. *Science*, 1989. **244**(4905): p. 707-12.
36. Massicano, A.V.F., B.V. Marquez-Nostra, and S.E. Lapi, *Targeting HER2 in Nuclear Medicine for Imaging and Therapy*. *Mol Imaging*, 2018. **17**: p. 1536012117745386.
37. Seebacher, N.A., et al., *Clinical development of targeted and immune based anti-cancer therapies*. *J Exp Clin Cancer Res*, 2019. **38**(1): p. 156.
38. Vu, T. and F.X. Claret, *Trastuzumab: updated mechanisms of action and resistance in breast cancer*. *Front Oncol*, 2012. **2**: p. 62.
39. Junttila, T.T., et al., *Ligand-independent HER2/HER3/PI3K complex is disrupted by trastuzumab and is effectively inhibited by the PI3K inhibitor GDC-0941*. *Cancer Cell*, 2009. **15**(5): p. 429-40.
40. Arnould, L., et al., *Trastuzumab-based treatment of HER2-positive breast cancer: an antibody-dependent cellular cytotoxicity mechanism?* *Br J Cancer*, 2006. **94**(2): p. 259-67.
41. Krop, I. and E.P. Winer, *Trastuzumab emtansine: a novel antibody-drug conjugate for HER2-positive breast cancer*. *Clin Cancer Res*, 2014. **20**(1): p. 15-20.
42. D'Amato, V., et al., *Mechanisms of lapatinib resistance in HER2-driven breast cancer*. *Cancer Treat Rev*, 2015. **41**(10): p. 877-83.
43. BioRender.com. *Mechanisms of Action of Trastuzumab*. Available from: <https://app.biorender.com/biorender-templates/t-5f2c56e5b9908c00b11d86cf-4-mechanisms-of-action-of-trastuzumab>.
44. Phillips, K.A., et al., *Clinical practice patterns and cost effectiveness of human epidermal growth receptor 2 testing strategies in breast cancer patients*. *Cancer*, 2009. **115**(22): p. 5166-74.
45. Dijkers, E.C., et al., *Biodistribution of 89Zr-trastuzumab and PET imaging of HER2-positive lesions in patients with metastatic breast cancer*. *Clin Pharmacol Ther*, 2010. **87**(5): p. 586-92.
46. Aggarwal, B.B., et al., *Models for prevention and treatment of cancer: problems vs promises*. *Biochem Pharmacol*, 2009. **78**(9): p. 1083-94.
47. Kapałczyńska, M., et al., *2D and 3D cell cultures - a comparison of different types of cancer cell cultures*. *Arch Med Sci*, 2018. **14**(4): p. 910-919.
48. Duval, K., et al., *Modeling Physiological Events in 2D vs. 3D Cell Culture*. *Physiology (Bethesda)*, 2017. **32**(4): p. 266-277.
49. Komatsu, A., et al., *Patient Derived Chicken Egg Tumor Model (PDcE Model): Current Status and Critical Issues*. *Cells*, 2019. **8**(5).
50. Victorelli, F.D., et al., *Chick embryo chorioallantoic membrane as a suitable in vivo model to evaluate drug delivery systems for cancer treatment: A review*. *Eur J Pharm Biopharm*, 2020. **153**: p. 273-284.
51. Dünker, N. and V. Jendrossek, *Implementation of the Chick Chorioallantoic Membrane (CAM) Model in Radiation Biology and Experimental Radiation Oncology Research*. *Cancers (Basel)*, 2019. **11**(10).
52. Cheon, D.J. and S. Orsulic, *Mouse models of cancer*. *Annu Rev Pathol*, 2011. **6**: p. 95-119.
53. Kahn, J., P.J. Tofilon, and K. Camphausen, *Preclinical models in radiation oncology*. *Radiat Oncol*, 2012. **7**: p. 223.

54. Ruggeri, B.A., F. Camp, and S. Miknyoczki, *Animal models of disease: pre-clinical animal models of cancer and their applications and utility in drug discovery*. *Biochem Pharmacol*, 2014. **87**(1): p. 150-61.
55. Siolas, D. and G.J. Hannon, *Patient-derived tumor xenografts: transforming clinical samples into mouse models*. *Cancer Res*, 2013. **73**(17): p. 5315-9.
56. Khaled, W.T. and P. Liu, *Cancer mouse models: past, present and future*. *Semin Cell Dev Biol*, 2014. **27**: p. 54-60.
57. Teicher, B.A., *Tumor models for efficacy determination*. *Mol Cancer Ther*, 2006. **5**(10): p. 2435-43.
58. Cekanova, M. and K. Rathore, *Animal models and therapeutic molecular targets of cancer: utility and limitations*. *Drug Des Devel Ther*, 2014. **8**: p. 1911-21.
59. Xia, H.J. and C.S. Chen, *Progress of non-human primate animal models of cancers*. *Dongwuxue Yanjiu*, 2011. **32**(1): p. 70-80.
60. WHO. *Promoting Cancer Early Diagnosis*. Available from: <https://www.who.int/activities/promoting-cancer-early-diagnosis>.
61. Weissleder, R. and M.J. Pittet, *Imaging in the era of molecular oncology*. *Nature*, 2008. **452**(7187): p. 580-9.
62. Wang, C., et al., *Optical molecular imaging for tumor detection and image-guided surgery*. *Biomaterials*, 2018. **157**: p. 62-75.
63. Joshi, B.P. and T.D. Wang, *Targeted Optical Imaging Agents in Cancer: Focus on Clinical Applications*. *Contrast Media Mol Imaging*, 2018. **2018**: p. 2015237.
64. Wallyn, J., et al., *Biomedical Imaging: Principles, Technologies, Clinical Aspects, Contrast Agents, Limitations and Future Trends in Nanomedicines*. *Pharm Res*, 2019. **36**(6): p. 78.
65. Valeur, B. and M.N. Berberan-Santos, *Characteristics of Fluorescence Emission*, in *Molecular Fluorescence: Principles and Applications, Second Edition*. 2012. p. 53-74.
66. Pirovano, G., et al., *Optical Imaging Modalities: Principles and Applications in Preclinical Research and Clinical Settings*. *J Nucl Med*, 2020. **61**(10): p. 1419-1427.
67. Hong, G., A.L. Antaris, and H. Dai, *Near-infrared fluorophores for biomedical imaging*. *Nature Biomedical Engineering*, 2017. **1**(1): p. 0010.
68. Boschi, F. and F. De Sanctis, *Overview of the optical properties of fluorescent nanoparticles for optical imaging*. *Eur J Histochem*, 2017. **61**(3): p. 2830.
69. Upputuri, P.K. and M. Pramanik, *Photoacoustic imaging in the second near-infrared window: a review*. *J Biomed Opt*, 2019. **24**(4): p. 1-20.
70. Monici, M., *Cell and tissue autofluorescence research and diagnostic applications*. *Biotechnol Annu Rev*, 2005. **11**: p. 227-56.
71. Frangioni, J.V., *In vivo near-infrared fluorescence imaging*. *Curr Opin Chem Biol*, 2003. **7**(5): p. 626-34.
72. Teraphongphom, N., et al., *Specimen mapping in head and neck cancer using fluorescence imaging*. *Laryngoscope Investig Otolaryngol*, 2017. **2**(6): p. 447-452.
73. Schaafsma, B.E., et al., *The clinical use of indocyanine green as a near-infrared fluorescent contrast agent for image-guided oncologic surgery*. *J Surg Oncol*, 2011. **104**(3): p. 323-32.
74. Gotoh, K., et al., *A novel image-guided surgery of hepatocellular carcinoma by indocyanine green fluorescence imaging navigation*. *J Surg Oncol*, 2009. **100**(1): p. 75-9.
75. Watanabe, M., et al., *Colonic tattooing using fluorescence imaging with light-emitting diode-activated indocyanine green: a feasibility study*. *Surg Today*, 2009. **39**(3): p. 214-8.
76. Poellinger, A., et al., *Breast cancer: early- and late-fluorescence near-infrared imaging with indocyanine green--a preliminary study*. *Radiology*, 2011. **258**(2): p. 409-16.
77. Kimura, T., et al., *Infrared fluorescence endoscopy for the diagnosis of superficial gastric tumors*. *Gastrointest Endosc*, 2007. **66**(1): p. 37-43.
78. Ishizawa, T., et al., *Real-time identification of liver cancers by using indocyanine green fluorescent imaging*. *Cancer*, 2009. **115**(11): p. 2491-504.
79. Aoki, T., et al., *Determination of the surgical margin in laparoscopic liver resections using infrared indocyanine green fluorescence*. *Langenbecks Arch Surg*, 2018. **403**(5): p. 671-680.
80. Rosenthal, E.L., et al., *Safety and Tumor Specificity of Cetuximab-IRDye800 for Surgical Navigation in Head and Neck Cancer*. *Clin Cancer Res*, 2015. **21**(16): p. 3658-66.

81. ClinicalTrials.gov. *Image Guided Surgery for Margin Assessment of Head and Neck Cancer Using Cetuximab-IRDye800CW cONjugate (ICON)*. NCT03134846. Available from: <https://clinicaltrials.gov/ct2/show/NCT03134846?term=Cetuximab-IRDye800&draw=2&rank=1>
82. Ma, Z., et al., *Deep learning for in vivo near-infrared imaging*. Proc Natl Acad Sci U S A, 2021. **118**(1).
83. Whitley, M.J., et al., *A mouse-human phase 1 co-clinical trial of a protease-activated fluorescent probe for imaging cancer*. Sci Transl Med, 2016. **8**(320): p. 320ra4.
84. ClinicalTrials.gov. *Intraoperative Detection of Residual Cancer in Breast Cancer*. NCT03321929. Available from: <https://clinicaltrials.gov/ct2/show/NCT03321929?term=LUM015&draw=2&rank=7>.
85. Lanahan, C.R., et al., *Performance of a novel protease-activated fluorescent imaging system for intraoperative detection of residual breast cancer during breast conserving surgery*. Breast Cancer Res Treat, 2021. **187**(1): p. 145-153.
86. Hong, G., et al., *Carbon Nanomaterials for Biological Imaging and Nanomedicinal Therapy*. Chem Rev, 2015. **115**(19): p. 10816-906.
87. Diao, S., et al., *Biological imaging without autofluorescence in the second near-infrared region*. Nano Research, 2015. **8**(9): p. 3027-3034.
88. Welsher, K., et al., *A route to brightly fluorescent carbon nanotubes for near-infrared imaging in mice*. Nat Nanotechnol, 2009. **4**(11): p. 773-80.
89. Hong, G., et al., *Through-skull fluorescence imaging of the brain in a new near-infrared window*. Nat Photonics, 2014. **8**(9): p. 723-730.
90. Smith, A.M., M.C. Mancini, and S. Nie, *Bioimaging: second window for in vivo imaging*. Nat Nanotechnol, 2009. **4**(11): p. 710-1.
91. Rogalski, A., *Infrared Detectors (2nd ed.)*. 2010: CRC Press.
92. O'Connell, M.J., et al., *Band gap fluorescence from individual single-walled carbon nanotubes*. Science, 2002. **297**(5581): p. 593-6.
93. Ghosh, D., et al., *Deep, noninvasive imaging and surgical guidance of submillimeter tumors using targeted M13-stabilized single-walled carbon nanotubes*. Proc Natl Acad Sci U S A, 2014. **111**(38): p. 13948-53.
94. Cao, J., et al., *Recent Progress in NIR-II Contrast Agent for Biological Imaging*. Front Bioeng Biotechnol, 2019. **7**: p. 487.
95. Zhang, Y., et al., *Ag2S quantum dot: a bright and biocompatible fluorescent nanoprobe in the second near-infrared window*. ACS Nano, 2012. **6**(5): p. 3695-702.
96. Hong, G., et al., *In vivo fluorescence imaging with Ag2S quantum dots in the second near-infrared region*. Angew Chem Int Ed Engl, 2012. **51**(39): p. 9818-21.
97. Zhang, J.J., et al., *Cell Membrane-Camouflaged NIR II Fluorescent Ag(2) Te Quantum Dots-Based Nanobioprobes for Enhanced In Vivo Homotypic Tumor Imaging*. Adv Healthc Mater, 2019. **8**(14): p. e1900341.
98. Naczynski, D.J., et al., *Rare-earth-doped biological composites as in vivo shortwave infrared reporters*. Nat Commun, 2013. **4**: p. 2199.
99. Yu, Z., C. Eich, and L.J. Cruz, *Recent Advances in Rare-Earth-Doped Nanoparticles for NIR-II Imaging and Cancer Theranostics*. Frontiers in Chemistry, 2020. **8**(496).
100. Wang, P., et al., *NIR-II nanoprobes in-vivo assembly to improve image-guided surgery for metastatic ovarian cancer*. Nat Commun, 2018. **9**(1): p. 2898.
101. Liu, Z., et al., *Circulation and long-term fate of functionalized, biocompatible single-walled carbon nanotubes in mice probed by Raman spectroscopy*. Proc Natl Acad Sci U S A, 2008. **105**(5): p. 1410-5.
102. Zhang, Y., et al., *Biodistribution, pharmacokinetics and toxicology of Ag2S near-infrared quantum dots in mice*. Biomaterials, 2013. **34**(14): p. 3639-46.
103. Zhong, Y. and H. Dai, *A mini-review on rare-earth down-conversion nanoparticles for NIR-II imaging of biological systems*. Nano Research, 2020. **13**(5): p. 1281-1294.
104. Antaris, A.L., et al., *A small-molecule dye for NIR-II imaging*. Nat Mater, 2016. **15**(2): p. 235-42.
105. Zhu, S., et al., *Near-Infrared-II Molecular Dyes for Cancer Imaging and Surgery*. Adv Mater, 2019. **31**(24): p. e1900321.
106. Meng, X., et al., *Hypoxia-triggered single molecule probe for high-contrast NIR II/PA tumor imaging and robust photothermal therapy*. Theranostics, 2018. **8**(21): p. 6025-6034.

107. Starosolski, Z., et al., *Indocyanine green fluorescence in second near-infrared (NIR-II) window*. PLoS One, 2017. **12**(11): p. e0187563.
108. Suo, Y., et al., *NIR-II Fluorescence Endoscopy for Targeted Imaging of Colorectal Cancer*. Adv Healthc Mater, 2019. **8**(23): p. e1900974.
109. He, S., et al., *Crucial breakthrough of second near-infrared biological window fluorophores: design and synthesis toward multimodal imaging and theranostics*. Chem Soc Rev, 2018. **47**(12): p. 4258-4278.
110. Vahrmeijer, A.L., et al., *Image-guided cancer surgery using near-infrared fluorescence*. Nat Rev Clin Oncol, 2013. **10**(9): p. 507-18.
111. Schuck, A., et al., *Microscopic residual disease is a risk factor in the primary treatment of breast cancer*. Strahlenther Onkol, 2002. **178**(6): p. 307-13.
112. Malhotra, V. and M.C. Perry, *Classical chemotherapy: mechanisms, toxicities and the therapeutic window*. Cancer Biol Ther, 2003. **2**(4 Suppl 1): p. S2-4.
113. Thariat, J., et al., *Past, present, and future of radiotherapy for the benefit of patients*. Nat Rev Clin Oncol, 2013. **10**(1): p. 52-60.
114. Baskar, R., et al., *Cancer and radiation therapy: current advances and future directions*. Int J Med Sci, 2012. **9**(3): p. 193-9.
115. Barth, R.F., et al., *Boron neutron capture therapy for cancer. Realities and prospects*. Cancer, 1992. **70**(12): p. 2995-3007.
116. Suzuki, M., *Boron neutron capture therapy (BNCT): a unique role in radiotherapy with a view to entering the accelerator-based BNCT era*. Int J Clin Oncol, 2020. **25**(1): p. 43-50.
117. Locher, G.L. and A.J. Roentgenol, *Biological effects and therapeutic possibilities of neutrons*. Radium Ther., 1936. **36**(1): p. 1-13.
118. Slatkin, D.N., *A history of boron neutron capture therapy of brain tumours. Postulation of a brain radiation dose tolerance limit*. Brain, 1991. **114** ( Pt 4): p. 1609-29.
119. Moss, R.L., *Critical review, with an optimistic outlook, on Boron Neutron Capture Therapy (BNCT)*. Appl Radiat Isot, 2014. **88**: p. 2-11.
120. Barth, R.F., P. Mi, and W. Yang, *Boron delivery agents for neutron capture therapy of cancer*. Cancer Commun (Lond), 2018. **38**(1): p. 35.
121. Miller, H.C., N.E. Miller, and E.L. Muetterties, *Chemistry of Boranes. XX. Syntheses of Polyhedral Boranes*. Inorg. Chem., 1964. **3**(10): p. 1456-1463.
122. Soloway, A.H., H. Hatanaka, and M.A. Davis, *Penetration of brain and brain tumor. VII. Tumor-binding sulfhydryl boron compounds*. J Med Chem, 1967. **10**(4): p. 714-7.
123. Snyder, H.R., A.J. Reedy, and W.J. Lennarz, *Synthesis of Aromatic Boronic Acids. Aldehyde Boronic Acids and a Boronic Acid Analog of Tyrosine1*. Journal of the American Chemical Society, 1958. **80**(4): p. 835-838.
124. Mishima, Y., et al., *TREATMENT OF MALIGNANT MELANOMA BY SINGLE THERMAL NEUTRON CAPTURE THERAPY WITH MELANOMA-SEEKING 10B-COMPOUND*. The Lancet, 1989. **334**(8659): p. 388-389.
125. Coderre, J.A., et al., *Selective Delivery of Boron by the Melanin Precursor Analogue *p*-boronophenylalanine to Tumors Other than Melanoma*. Cancer Research, 1990. **50**(1): p. 138-141.
126. Wittig, A., W.A. Sauerwein, and J.A. Coderre, *Mechanisms of transport of *p*-borono-phenylalanine through the cell membrane in vitro*. Radiat Res, 2000. **153**(2): p. 173-80.
127. Detta, A. and G.S. Cruickshank, *L-amino acid transporter-1 and boronophenylalanine-based boron neutron capture therapy of human brain tumors*. Cancer Res, 2009. **69**(5): p. 2126-32.
128. Wongthai, P., et al., *Boronophenylalanine, a boron delivery agent for boron neutron capture therapy, is transported by ATB0+, LAT1 and LAT2*. Cancer Sci, 2015. **106**(3): p. 279-86.
129. Yoshino, K., et al., *Improvement of solubility of *p*-boronophenylalanine by complex formation with monosaccharides*. Strahlenther Onkol, 1989. **165**(2-3): p. 127-9.
130. Yoshida, F., et al., *Enhancement of sodium borocaptate (BSH) uptake by tumor cells induced by glutathione depletion and its radiobiological effect*. Cancer Letters, 2004. **215**(1): p. 61-67.
131. Yokoyama, K., et al., *Pharmacokinetic study of BSH and BPA in simultaneous use for BNCT*. J Neurooncol, 2006. **78**(3): p. 227-32.
132. Coderre, J.A., et al., *Selective targeting of boronophenylalanine to melanoma in BALB/c mice for neutron capture therapy*. Cancer Res, 1987. **47**(23): p. 6377-83.

133. Ono, K., et al., *Radiobiological evidence suggesting heterogeneous microdistribution of boron compounds in tumors: Its relation to quiescent cell population and tumor cure in neutron capture therapy*. International Journal of Radiation Oncology\*Biophysics, 1996. **34**(5): p. 1081-1086.
134. Koivunoro, H., et al., *Biokinetic analysis of tissue boron (10B) concentrations of glioma patients treated with BNCT in Finland*. Applied Radiation and Isotopes, 2015. **106**: p. 189-194.
135. Goodman, J.H., et al., *Boron neutron capture therapy of brain tumors: biodistribution, pharmacokinetics, and radiation dosimetry sodium borocaptate in patients with gliomas*. Neurosurgery, 2000. **47**(3): p. 608-21; discussion 621-2.
136. Miyatake, S.-I., et al., *Modified boron neutron capture therapy for malignant gliomas performed using epithermal neutron and two boron compounds with different accumulation mechanisms: an efficacy study based on findings on neuroimages*. Journal of Neurosurgery, 2005. **103**(6): p. 1000.
137. Ono, K., et al., *The combined effect of boronophenylalanine and borocaptate in boron neutron capture therapy for SCCVII tumors in mice*. International Journal of Radiation Oncology\*Biophysics, 1999. **43**(2): p. 431-436.
138. Sköld, K., et al., *Boron Neutron Capture Therapy for glioblastoma multiforme: advantage of prolonged infusion of BPA-f*. Acta Neurol Scand, 2010. **122**(1): p. 58-62.
139. Choudhury, P. and M. Gupta, *Personalized & Precision Medicine in Cancer: A Theranostic Approach*. Curr Radiopharm, 2017. **10**(3): p. 166-170.
140. Ishiwata, K., et al., *Synthesis and radiation dosimetry of 4-borono-2-[18F]fluoro-D,L-phenylalanine: a target compound for PET and boron neutron capture therapy*. Int J Rad Appl Instrum A, 1991. **42**(4): p. 325-8.
141. Imahori, Y., et al., *Fluorine-18-labeled fluoroboronophenylalanine PET in patients with glioma*. J Nucl Med, 1998. **39**(2): p. 325-33.
142. Imahori, Y., et al., *Positron emission tomography-based boron neutron capture therapy using boronophenylalanine for high-grade gliomas: part I*. Clin Cancer Res, 1998. **4**(8): p. 1825-32.
143. Imahori, Y., et al., *Positron emission tomography-based boron neutron capture therapy using boronophenylalanine for high-grade gliomas: part II*. Clin Cancer Res, 1998. **4**(8): p. 1833-41.
144. Kabalka, G.W., et al., *The use of positron emission tomography to develop boron neutron capture therapy treatment plans for metastatic malignant melanoma*. J Neurooncol, 2003. **62**(1-2): p. 187-95.
145. Aihara, T., et al., *First clinical case of boron neutron capture therapy for head and neck malignancies using 18F-BPA PET*. Head Neck, 2006. **28**(9): p. 850-5.
146. Ariyoshi, Y., et al., *Boron neutron capture therapy using epithermal neutrons for recurrent cancer in the oral cavity and cervical lymph node metastasis*. Oncol Rep, 2007. **18**(4): p. 861-6.
147. Miyatake, S., et al., *Boron neutron capture therapy with bevacizumab may prolong the survival of recurrent malignant glioma patients: four cases*. Radiat Oncol, 2014. **9**: p. 6.
148. Li, J., et al., *A Metabolically Stable Boron-Derived Tyrosine Serves as a Theranostic Agent for Positron Emission Tomography Guided Boron Neutron Capture Therapy*. Bioconjug Chem, 2019. **30**(11): p. 2870-2878.
149. García-Toraño, E., V.P. Medina, and M.R. Ibarra, *The half-life of 18F*. Applied Radiation and Isotopes, 2010. **68**(7): p. 1561-1565.
150. Ishiwata, K., *4-Borono-2-(18)F-fluoro-L-phenylalanine PET for boron neutron capture therapy-oriented diagnosis: overview of a quarter century of research*. Ann Nucl Med, 2019. **33**(4): p. 223-236.
151. Hattori, Y., et al., *Study on the compounds containing 19F and 10B atoms in a single molecule for the application to MRI and BNCT*. Bioorg Med Chem, 2006. **14**(10): p. 3258-62.
152. Hattori, Y., et al., *Synthesis and evaluation as MRI probe of the trifluoromethylated p-boronophenylalanine and its alcohol derivative*. Bioorg Med Chem, 2007. **15**(5): p. 2198-205.
153. Porcari, P., et al., *In vivo 19F MR imaging and spectroscopy for the BNCT optimization*. Appl Radiat Isot, 2009. **67**(7-8 Suppl): p. S365-8.
154. Dubey, R., et al., *Tumor targeting, trifunctional dendritic wedge*. Bioconjug Chem, 2015. **26**(1): p. 78-89.
155. Sauerwein, W.A.G., et al., *Theranostics in Boron Neutron Capture Therapy*. Life (Basel), 2021. **11**(4).
156. Iguchi, Y., et al., *Tumor-specific delivery of BSH-3R for boron neutron capture therapy and positron emission tomography imaging in a mouse brain tumor model*. Biomaterials, 2015. **56**: p. 10-7.
157. Pulagam, K.R., et al., *Gold Nanoparticles as Boron Carriers for Boron Neutron Capture Therapy: Synthesis, Radiolabelling and In vivo Evaluation*. Molecules, 2019. **24**(19).

158. Wu, C.Y., et al., *Development of theranostic active-targeting boron-containing gold nanoparticles for boron neutron capture therapy (BNCT)*. Colloids Surf B Biointerfaces, 2019. **183**: p. 110387.
159. Shi, Y., et al., *Tracing Boron with Fluorescence and Positron Emission Tomography Imaging of Boronated Porphyrin Nanocomplex for Imaging-Guided Boron Neutron Capture Therapy*. ACS Appl Mater Interfaces, 2018. **10**(50): p. 43387-43395.
160. Li, L., et al., *On-Demand Biodegradable Boron Nitride Nanoparticles for Treating Triple Negative Breast Cancer with Boron Neutron Capture Therapy*. ACS Nano, 2019. **13**(12): p. 13843-13852.
161. Alberti, D., et al., *A theranostic approach based on the use of a dual boron/Gd agent to improve the efficacy of Boron Neutron Capture Therapy in the lung cancer treatment*. Nanomedicine, 2015. **11**(3): p. 741-50.
162. Kuthala, N., et al., *Engineering Novel Targeted Boron-10-Enriched Theranostic Nanomedicine to Combat against Murine Brain Tumors via MR Imaging-Guided Boron Neutron Capture Therapy*. Adv Mater, 2017. **29**(31).
163. Icten, O., et al., *Gadolinium borate and iron oxide bioconjugates: Nanocomposites of next generation with multifunctional applications*. Mater Sci Eng C Mater Biol Appl, 2018. **92**: p. 317-328.
164. Alberti, D., et al., *Synthesis of a carborane-containing cholesterol derivative and evaluation as a potential dual agent for MRI/BNCT applications*. Org Biomol Chem, 2014. **12**(15): p. 2457-67.
165. Bendel, P., N. Koudinova, and Y. Salomon, *In vivo imaging of the neutron capture therapy agent BSH in mice using (10)B MRI*. Magn Reson Med, 2001. **46**(1): p. 13-7.
166. Bendel, P., et al., *Boron-11 NMR of borocaptate: relaxation and in vivo detection in melanoma-bearing mice*. Magn Reson Med, 1998. **39**(3): p. 439-47.
167. Geninatti-Crich, S., et al., *Boronated compounds for imaging guided BNCT applications*. Anticancer Agents Med Chem, 2012. **12**(5): p. 543-53.
168. Timonen, M., et al., *<sup>1</sup>H MRS studies in the Finnish boron neutron capture therapy project: detection of 10B-carrier, L-p-boronophenylalanine-fructose*. Eur J Radiol, 2005. **56**(2): p. 154-9.
169. Zuo, C.S., et al., *Proton nuclear magnetic resonance measurement of p-boronophenylalanine (BPA): a therapeutic agent for boron neutron capture therapy*. Med Phys, 1999. **26**(7): p. 1230-6.
170. Miyatake, S.I., et al., *Boron neutron capture therapy for malignant brain tumors*. J Neurooncol, 2020. **149**(1): p. 1-11.
171. Sumitomo Heavy Industries, L. Sumitomo Heavy Industries, Ltd. obtains medical device approval for manufacturing and sales of accelerator based BNCT system and the dose calculation program in Japan. - *World's first BNCT systems as medical device* -. 2020, March 12; Available from: <https://www.shi.co.jp/english/info/2019/6kgpsq0000002ji0.html>.
172. Kawabata, S., et al., *Boron neutron capture therapy for newly diagnosed glioblastoma*. J Radiat Res, 2009. **50**(1): p. 51-60.
173. Kato, I., et al., *Effectiveness of BNCT for recurrent head and neck malignancies*. Appl Radiat Isot, 2004. **61**(5): p. 1069-73.
174. Kato, I., et al., *Effectiveness of boron neutron capture therapy for recurrent head and neck malignancies*. Appl Radiat Isot, 2009. **67**(7-8 Suppl): p. S37-42.
175. Kawabata, S., et al., *Boron neutron capture therapy for recurrent high-grade meningiomas*. J Neurosurg, 2013. **119**(4): p. 837-44.
176. Miyatake, S., et al., *Survival benefit of Boron neutron capture therapy for recurrent malignant gliomas*. J Neurooncol, 2009. **91**(2): p. 199-206.
177. Treibs, A. and F.-H. Kreuzer, *Difluorboryl-Komplexe von Di- und Tripyrrylmethenen*. Justus Liebigs Annalen der Chemie, 1968. **718**(1): p. 208-223.
178. Bodio, E., F. Denat, and C. Goze, *BODIPYS and aza-BODIPY derivatives as promising fluorophores for in vivo molecular imaging and theranostic applications*. Journal of Porphyrins and Phthalocyanines, 2019. **23**(11n12): p. 1159-1183.
179. Shi, Z., et al., *Bioapplications of small molecule Aza-BODIPY: from rational structural design to in vivo investigations*. Chem Soc Rev, 2020. **49**(21): p. 7533-7567.
180. Ni, Y. and J. Wu, *Far-red and near infrared BODIPY dyes: synthesis and applications for fluorescent pH probes and bio-imaging*. Org Biomol Chem, 2014. **12**(23): p. 3774-91.
181. Schellhammer, K.S., et al., *Tuning Near-Infrared Absorbing Donor Materials: A Study of Electronic, Optical, and Charge-Transport Properties of aza-BODIPYs*. Chemistry of Materials, 2017. **29**(13): p. 5525-5536.

182. Grossi, M., et al., *Lysosome triggered near-infrared fluorescence imaging of cellular trafficking processes in real time*. Nat Commun, 2016. **7**: p. 10855.
183. Daly, H.C., et al., *BF(2)-azadipyromethene NIR-emissive fluorophores with research and clinical potential*. Eur J Med Chem, 2017. **135**: p. 392-400.
184. Bai, L., et al., *Novel aza-BODIPY based small molecular NIR-II fluorophores for in vivo imaging*. Chem Commun (Camb), 2019. **55**(73): p. 10920-10923.
185. Zhao, M., et al., *NIR-II pH Sensor with a FRET Adjustable Transition Point for In Situ Dynamic Tumor Microenvironment Visualization*. Angew Chem Int Ed Engl, 2021. **60**(10): p. 5091-5095.
186. Gibbs, J.H., et al., *Synthesis and properties of a series of carboranyl-BODIPYs*. J Organomet Chem, 2015. **798**(Pt 1): p. 209-213.
187. Xuan, S., et al., *Synthesis and in Vitro Studies of a Series of Carborane-Containing Boron Dipyrromethenes (BODIPYs)*. J Med Chem, 2016. **59**(5): p. 2109-17.
188. Labra-Vázquez, P., et al., *Tuning the Cell Uptake and Subcellular Distribution in BODIPY-Carboranyl Dyads: An Experimental and Theoretical Study*. Chemistry, 2020. **26**(69): p. 16530-16540.
189. Smith, L.C., H.J. Pownall, and A.M. Gotto, Jr., *The plasma lipoproteins: structure and metabolism*. Annu Rev Biochem, 1978. **47**: p. 751-7.
190. Feingold, K.R., *Introduction to Lipids and Lipoproteins*, in *Endotext*, K.R. Feingold, et al., Editors. 2000, MDText.com, Inc. Copyright © 2000-2021, MDText.com, Inc.: South Dartmouth (MA).
191. van Leeuwen, E.M., et al., *A new perspective on lipid research in age-related macular degeneration*. Prog Retin Eye Res, 2018. **67**: p. 56-86.
192. Goldstein, J.L. and M.S. Brown, *The LDL receptor*. Arterioscler Thromb Vasc Biol, 2009. **29**(4): p. 431-8.
193. van de Sluis, B., M. Wijers, and J. Herz, *News on the molecular regulation and function of hepatic low-density lipoprotein receptor and LDLR-related protein 1*. Curr Opin Lipidol, 2017. **28**(3): p. 241-247.
194. Shen, W.J., S. Azhar, and F.B. Kraemer, *SR-B1: A Unique Multifunctional Receptor for Cholesterol Influx and Efflux*. Annu Rev Physiol, 2018. **80**: p. 95-116.
195. Mooberry, L.K., et al., *Targeting the SR-B1 Receptor as a Gateway for Cancer Therapy and Imaging*. Front Pharmacol, 2016. **7**: p. 466.
196. Wang, S. and J.D. Smith, *ABCA1 and nascent HDL biogenesis*. Biofactors, 2014. **40**(6): p. 547-54.
197. Baldán, A., et al., *ATP-binding cassette transporter G1 and lipid homeostasis*. Curr Opin Lipidol, 2006. **17**(3): p. 227-32.
198. Rudling, M.J., et al., *Content of low density lipoprotein receptors in breast cancer tissue related to survival of patients*. Br Med J (Clin Res Ed), 1986. **292**(6520): p. 580-2.
199. Versluis, A.J., et al., *Receptor-mediated uptake of low-density lipoprotein by B16 melanoma cells in vitro and in vivo in mice*. Br J Cancer, 1996. **74**(4): p. 525-32.
200. Champion, O., et al., *Contribution of the Low-Density Lipoprotein Receptor Family to Breast Cancer Progression*. Front Oncol, 2020. **10**: p. 882.
201. Gutierrez-Pajares, J.L., et al., *SR-BI: Linking Cholesterol and Lipoprotein Metabolism with Breast and Prostate Cancer*. Front Pharmacol, 2016. **7**: p. 338.
202. Yuan, B., et al., *High scavenger receptor class B type I expression is related to tumor aggressiveness and poor prognosis in breast cancer*. Tumour Biol, 2016. **37**(3): p. 3581-8.
203. Pawar, S., et al., *LDL receptors and their role in targeted therapy for glioma: a review*. Drug Discov Today, 2021. **26**(5): p. 1212-1225.
204. Maletínská, L., et al., *Human glioblastoma cell lines: levels of low-density lipoprotein receptor and low-density lipoprotein receptor-related protein*. Cancer Res, 2000. **60**(8): p. 2300-3.
205. Li, H., et al., *Carbocyanine labeled LDL for optical imaging of tumors*. Acad Radiol, 2004. **11**(6): p. 669-77.
206. Cao, W., et al., *Synthesis and evaluation of a stable bacteriochlorophyll-analog and its incorporation into high-density lipoprotein nanoparticles for tumor imaging*. Bioconjug Chem, 2009. **20**(11): p. 2023-31.
207. Gal, D., et al., *Low-density lipoprotein as a potential vehicle for chemotherapeutic agents and radionucleotides in the management of gynecologic neoplasms*. Am J Obstet Gynecol, 1981. **139**(8): p. 877-85.
208. Mooberry, L.K., et al., *Receptor mediated uptake of paclitaxel from a synthetic high density lipoprotein nanocarrier*. J Drug Target, 2010. **18**(1): p. 53-8.

209. Thaxton, C.S., et al., *Lipoproteins and lipoprotein mimetics for imaging and drug delivery*. *Adv Drug Deliv Rev*, 2016. **106**(Pt A): p. 116-131.
210. Busatto, S., et al., *Lipoprotein-based drug delivery*. *Adv Drug Deliv Rev*, 2020. **159**: p. 377-390.
211. Privat, M., et al., *Development of an Easily Bioconjugatable Water-Soluble Single-Photon Emission-Computed Tomography/Optical Imaging Bimodal Imaging Probe Based on the aza-BODIPY Fluorophore*. *J Med Chem*, 2021. **64**(15): p. 11063-11073.
212. Nagengast, W.B., et al., *Near-infrared fluorescence molecular endoscopy detects dysplastic oesophageal lesions using topical and systemic tracer of vascular endothelial growth factor A*. *Gut*, 2019. **68**(1): p. 7-10.

## Résumé

L'imagerie de fluorescence dans le NIR-II (1000 – 17000 nm) s'est développée depuis une vingtaine d'années. Avec une diffusion de photons limitée et une autofluorescence des tissus diminuée, l'imagerie NIR-II surpasse l'imagerie NIR-I (700-900 nm), en fournissant des images *in vivo* plus nettes, et un rapport signal/bruit amélioré. Depuis son émergence, plusieurs fluorophores NIR-II ont été décrits, mais aucun d'entre eux n'est évalué en essais cliniques actuellement en raison de leurs toxicités potentielles à long terme, de leurs faibles rendements quantiques ou de leurs faibles solubilités. Dans ce contexte, nous avons cherché à concevoir et évaluer des fluorophores évitant ces pièges et présentant des propriétés adaptées à l'imagerie tumorale NIR-II. Un premier dérivé d'aza-BODIPY soluble possédant des propriétés de fluorescence NIR-II uniques a ainsi été développé. Chez le rongeur, il présente une forte accumulation dans les glioblastomes, sans toxicité, avec des ratios tumeur/muscle élevés : ces propriétés lui confèrent donc un grand potentiel pour l'application clinique.

L'étude de son mécanisme d'accumulation tumorale a démontré son interaction avec les lipoprotéines de la circulation sanguine. Ces interactions améliorent les propriétés de fluorescence de l'aza-BODIPY et lui assurent un transport spécifique aux tumeurs surexprimant les récepteurs des lipoprotéines (LDLR et SR-B1). En parallèle, pour cibler les tumeurs possédant une faible expression de ces récepteurs, telles que les tumeurs ovariennes HER2-positives, l'aza-BODIPY a été couplé à un anticorps spécifique de HER, le Trastuzumab. Un ciblage sélectif des tumeurs HER2 positives a été réalisé *in vivo* en utilisant Trastuzumab bioconjugué aza-BODIPY fournissant ainsi une preuve de concept de la stratégie de vectorisation développée pour le ciblage tumoral, quelle que soit l'expression des récepteurs lipoprotéiques.

De par leur polyvalence et leurs propriétés d'accumulation tumorale, les aza-BODIPYs ont également été utilisés pour transporter des atomes de bore vers les tumeurs, en perspective à la thérapie par capture neutronique du bore (BNCT). La BNCT est une modalité radiothérapeutique ciblée basée sur l'accumulation sélective d'atomes de bore-10 dans les tissus tumoraux, suivie d'une exposition à un flux de neutrons qui conduit à la destruction spécifique des cellules tumorales chargées en bore. Il est actuellement nécessaire de développer de nouveaux composés riches en bore possédant un profil de sécurité approprié, une délivrance de bore sélective et adéquate, et des propriétés d'imagerie intrinsèques qui permettent sa quantification et une planification optimale du protocole thérapeutique. À cette fin, nous avons développé un composé théranostique basé sur le fluorophore aza-BODIPY couplé à un composé de bore utilisé en clinique, à savoir le borocaptate de sodium (BSH). Le complexe aza-BODIPY-BSH cible les tumeurs avec des ratios tumeur/muscle favorables à la BNCT. Une réduction significative de la croissance tumorale *in ovo* a été mesurée après exposition aux neutrons, par rapport à la BSH seule, démontrant l'efficacité du complexe aza-BODIPY-BSH dans des modèles tumoraux précliniques en BNCT. De plus, ce composé peut être modifié afin d'intégrer un radio-isotope permettant sa visualisation et sa quantification par imagerie nucléaire (TEP ou TEMP). Cette étape sera évaluée prochainement pour un potentiel transfert en clinique.

De manière générale, ces résultats ont démontré la grande polyvalence des aza-BODIPYs et leur fort potentiel pour la chirurgie guidée par l'imagerie optique NIR-II, et la thérapie par BNCT.

**Mot-clé :** Imagerie de fluorescence NIR-II, Imagerie des cancers, BNCT, Thérapie des cancers, aza-BODIPYs, composés théranostiques



## Abstract

Twenty years ago, fluorescence imaging in the NIR-II window (1000-1700 nm) has emerged. Providing less photon scattering and diminished tissues autofluorescence, NIR-II imaging has surpassed NIR-I imaging (700-900 nm), resulting in clearer images *in vivo*, with enhanced signal-to-noise ratio. Since its emergence, several NIR-II fluorophores have been reported, yet none of them passed to clinical assessment due to long-term toxicities, low quantum yields or poor solubilities. In this context, we aimed to design and evaluate NIR-II emitting fluorophores avoiding these pitfalls and exhibiting suitable properties for NIR-II tumor imaging *in vivo*. Accordingly, the first water-soluble aza-BODIPY possessing unique NIR-II fluorescence properties was developed. A favorable accumulation in glioblastoma tumors was observed in rodents, with high tumor to muscle ratios and no adverse events, presenting the aza-BODIPY great potential for clinical NIR-II tumor imaging application. Assessing the aza-BODIPY mechanism of tumor uptake proved its interaction with lipoproteins in the blood circulation. Lipoproteins enhanced the aza-BODIPY fluorescence properties, and acted as trojan horses targeting the aza-BODIPY specifically towards tumors overexpressing lipoproteins receptors. In parallel, to target tumors possessing low lipoprotein receptors expression, as HER2-positive ovarian tumors, the aza-BODIPY was coupled to HER-specific antibody i.e. Trastuzumab. A selective targeting of HER2 positive tumors was achieved *in vivo* using Trastuzumab bioconjugated aza-BODIPY, thus providing a proof of concept of the developed vectorization strategy to target tumors regardless of their lipoprotein receptors expression.

Considering the high versatility of the aza-BODIPYs, it was also used to carry boron atoms to tumors, for Boron Neutron Capture Therapy (BNCT). BNCT defines a targeted radiotherapeutic modality based on the sufficient and selective boron-10 atoms accumulation in tumor tissues, followed by neutron field exposure, that leads to specific destruction of boron-loaded tumor cells. Regardless of BNCT clinical efficacy, there is a need for a boron-rich compound possessing suitable safety profile, selective and adequate boron delivery, and intrinsic imaging properties that allow its quantification and optimal planning of neutron radiation dosing. To this end, we developed a theranostic boron compound based on the aza-BODIPY fluorophore coupled to the clinically used boron compound i.e. sodium borocaptate (BSH). The aza-BODIPY-BSH complex targeted the tumors with BNCT favorable tumor to muscle ratios, as visualized by fluorescence imaging. A significant reduction in tumor growth *in ovo* was measured following neutron exposure as compared to BSH alone, demonstrating the BNCT efficacy of aza-BODIPY-BSH complex in preclinical tumor models. Coupling the aza-BODIPY-BSH compound to radioisotopes, that allow accurate quantification, is currently under evaluation for potential human translation.

Altogether these findings demonstrated the high versatility of aza-BODIPY and its great potential for clinical NIR-II tumor imaging and BNCT application.

**Keywords :** NIR-II fluorescence Imaging, Cancer imaging, BNCT, Cancer therapy, aza-BODIPYs, Theranostic compounds

